EXPERIMENTAL METHODS FOR EVALUATING STRAIN RATE DEPENDENCY OF SHAPE MEMORY ALLOY MATERIALS UNDER QUASISTATIC AND IMPULSIVE LOADING

A Thesis
Presented to
The Academic Faculty

by

Nan Gao

In Partial Fulfillment
of the Requirements for the Degree
Doctor of Philosophy in the
School of Civil and Environmental Engineering

Georgia Institute of Technology
December 2017

EXPERIMENTAL METHODS FOR EVALUATING STRAIN RATE DEPENDENCY OF SHAPE MEMORY ALLOY MATERIALS UNDER QUASISTATIC AND IMPULSIVE LOADING

Approved by:

Dr. Lauren Stewart, Advisor
School of Civil and Environmental Engineering
Georgia Institute of Technology

Dr. Laurence J. Jacobs
School of Civil and Environmental Engineering
Georgia Institute of Technology

Dr. Reginald DesRoches, Co-advisor
Department of Civil and Environmental Engineering
Rice University

Dr. Russell Gentry
School of Architecture
Georgia Institute of Technology

Dr. Lawrence F. Kahn
School of Civil and Environmental Engineering
Georgia Institute of Technology

Date Approved: November 2017

ACKNOWLEDGEMENTS

I would like to express my deepest appreciation to my advisors Dr. Lauren Stewart and Dr. Reginald DesRoches. The completion of this dissertation would not have been possible without their ingenious guidance and invaluable contribution. I am extremely grateful to Dr. Lawrence Kahn who provided me with relentless encouragement. I would also like to extend my deepest gratitude to Dr. Laurence Jacobs and Dr. Russell Gentry for their critical support.

I would like to thank Dr. Jong-Su Jeon, Dr. Chuang-Sheng Yang, and Dr. Darel Hodgson, whose productive collaboration are so crucial to this research. I would like to extend my sincere thanks to Dr. Giovanni Loreto who helped and inspired me so much. I wish to thank my colleague graduate students Genevieve Pezzola, Marc Sanborn, and Kathryn Sanborn for their enthusiastic support and generous help. I also wish to thank Dr. Álvaro Paul, Dr. Bradley Dolphyn, Dr. Laura Redmond, and Dr. Timothy Wright for their precious advices.

I am deeply indebted to Jeremy Mitchell for his exceptional lab support. I must also thank Andrew Udell and Blake Baklini for their incredible contributions to fabrication works. I would like to acknowledge the valuable assistance from Brian Riser, Zachary Wilson, Lawrence Wolffis, Clifford Tribble, Camila Bergamo, Alix Nail, Donny Otwell, and Billy Plum. I also had a great pleasure of working with Seo-Hun Lee, Jiuk Shin, Javaid Anwar, and Xi Liu.

I would like to recognize the support and assistance I received from all faculty and staff members of School of Civil and Environmental Engineering at Georgia Tech. I am particularly grateful to Dr. David Scott and Dr. Donald Webster for their support during my graduate study. I also greatly appreciate Kurt Belgum for his help on academic writing.

Additionally, I would like to thank my parents for their endless support and encouragement. I would also like to thank my grandparents, my cousins, my parents-in-law, and my

other family members.

Finally and most importantly, I would like to thank my beloved wife Dr. Ruiting Lin. She was my high school sweetheart fifteen years ago and she has been supporting me since then. She makes my life so delightful and meaningful and she keeps inspiring me to become a better person. I could not complete my graduate study without her tremendous support and deep love. I would like to thank her for everything she did for me.

TABLE OF CONTENTS

LIST OF TABLES

LIST OF FIGURES

SUMMARY

Shape memory alloys (SMAs) are innovative materials that have great potential in structural engineering because they can provide significant energy dissipation capacity and introduce considerable re-centering ability to structures. The stress-strain relations of SMAs are dependent on loading rates, and the responses of SMAs under intermediate strain rates are hard to obtain using conventional experimental techniques. This research developed an innovative high-loading-rate tensile testing system to test specimens under intermediate strain rates, bridging the gap between quasistatic strain rates from conventional servo-hydraulic techniques and high strain rates from typical Kolsky bar techniques. This testing system converted impacts from a high-speed actuator into high-loading-rate tensile forces and elongated specimens under relatively constant deformation rates. This testing system is capable of testing not only prismatic material specimens to evaluate stress-strain behavior but also non-prismatic structural components composed of different materials to evaluate force-deformation behavior. The testing system was verified and calibrated through a series of validation tests on aluminum tensile specimens. Experimental results were compared with theoretical estimations and finite element simulations to confirm this system obtained reliable force-deformation measurements in a repeatable and controllable manner. This research conducted two types of experimental tests on SMA specimens: a quasistatic cyclic loading test on a seismic bracing system based on an SMA ring and a series of high-loading-rate tensile tests on various SMA tensile specimens. The test results corroborated that this new testing system is capable of assessing the behavior of material specimens and structural components under intermediate strain rates.

CHAPTER I

INTRODUCTION

1.1 Problem statement

Discoveries in material science have improved the field of structural engineering for thousands of years. For example, the emergence of modern concrete and steel in the 19th century changed structural engineering dramatically. Modern infrastructures based on these materials became more reliable and efficient as researchers investigated the properties of engineering materials more deeply [60, 94]. The pursuit of lighter, stronger, more durable, and more environmentally friendly materials has been the focus of many researchers for many decades. In this relentless pursuit, numerous materials with extraordinary properties have been studied, modified, or even built from the bottom up using state-of-the-art nanotechnology [69, 143]. Although these innovative materials have great potential in engineering applications, proper understanding of their behaviors remains a challenge to researchers and engineers.

Among these innovative materials, shape memory alloys (SMAs) have been attracting the attention of engineers for years [12, 62]. Because of their remarkable properties such as shape memory effects, superelasticity, and biocompatibility, SMAs are utilized in several engineering fields, including biomedical engineering [36, 82], mechanical engineering [99, 133], and aerospace engineering [52].

To apply SMAs in structural engineering, researchers focus on two properties: the capacity to dissipate energy and the ability to spontaneously restore original shapes. Because of these two properties, SMAs are studied for potential applications such as energy dissipation, vibration control, and smart systems in the field of structural engineering [63, 120].

Nevertheless, actual SMA-based applications in structural engineering are very rare. One reason is the high cost of SMA materials. Since applications in structural engineering generally require larger volume of materials than those in biomedical or mechanical

engineering, structural engineering practices usually compromise between performance and cost. Because of the high cost of raw materials and fabrications, SMAs are currently seen as excessively expensive for general applications in structural engineering even though they are capable of delivering extraordinary performance [63]. However, recent improvements in material science and fabrication techniques have reduced the price of NiTi SMAs, one of the major types of SMAs, by 90% in the past few years [3]. Moreover, a comprehensive socioeconomic evaluation conducted by Bruno et al. [14] shows that large-scale applications of SMAs in seismic engineering are actually cost-effective if considering the overall life-cycle cost of infrastructure systems. Although initial direct costs of SMA-based systems are higher than conventional seismic resisting systems, the potential socioeconomic losses are reduced significantly because of the high performance of SMAs. As a result, the total costs of SMA-based seismic systems remain in the same order as conventional seismic systems.

Another reason restraining the implementation of SMAs in structural engineering is that the responses of SMAs under seismic or blast events are not yet fully understood. For example, the thermal-coupled mechanical properties of SMAs result in complex temperature-dependent and strain-rate-dependent behaviors. These unique properties of SMAs are discussed in Section 2.1. Proper understanding of these properties is the prerequisite of actual large-scale applications of SMAs in structural engineering.

This research focuses on strain rate dependency of SMA materials in the scenarios of seismic and blast events. Although stress waves caused by seismic or blast events transmit through structures in velocities of approximately 2,000 to 5,000 m/s, the structural components deform in much lower rates because of the large volume and weight of typical structures. These rates are estimated at the order of 100 s^{-1} for blast loading on relatively large structures [51]. For the responses of structural components, previous studies suggested the average strain rates under seismic events are between 0.1 to 10 s^{-1} and the average strain rates under blast events are between 1 to 100 s^{-1} [118]. Orton et al. conducted actual blast tests on reinforced concrete slabs strengthened with carbon fiber reinforced polymer (CFRP) and found that the strain rates of CFRP material were 0.75 to 3 s^{-1} during blast loading [101]. Cadoni et al. reported that the strain rates in concrete of

a bridge under blast loading were up to 10 s^{-1} [16].

Based on these previous studies, this research aims to investigate the behavior of structural components under the strain rates of 1 to 100 s^{-1}. This range of strain rates is usually defined as *intermediate strain rates* and is relatively difficult to study [108]. The deformations of critical structural components in seismic or blast events correspond to average strain rates in this intermediate range. Therefore, the behaviors of materials and components under intermediate strain rates clearly need to be evaluated.

Previous researchers have developed several experimental techniques to test specimens under intermediate strain rates. One common experimental technique is the Kolsky bar tests, also known as Split-Hopkinson pressure bar (SHPB) tests [19]. SMA specimens were tested under different strain rates in several previous Kolsky bar tests [20, 96, 97, 119]. Nevertheless, one limitation of the Kolsky bar technique is that it is based on one-dimensional stress wave theory. The force and deformation of the specimens are not directly measured but indirectly derived with the assumption that stress and strain are uniformly distributed throughout the specimens. To ensure this assumption is valid, Kolsky bar tests are limited to prismatic and homogeneous specimens such as cylinders or rods cut from bulk volume of materials. The sizes of the specimens in these Kolsky bar tests are also limited. The diameters of the SMA cylinder specimens tested in most of the previous Kolsky bar tensile tests were no more than 10 mm, significantly smaller than the typical sizes of proof-of-concept structural component. Besides the size limitation, the strain rates achieved in most of these tests are usually higher than 100 s^{-1}, which belong to the range of high strain rates and are too high for the purpose of assessing behaviors of materials and components in seismic and blast events. Therefore, the existing Kolsky bar technique does not have the ability to test larger scale specimens under intermediate strain rates.

Another experimental technique tests specimens with servo-hydraulic testing machines. The sizes of specimens in this type of tests are usually larger than those in Kolsky bar tests. For example, DesRoches et al. tested SMA rod specimens with diameters up to 25.4 mm (1 inch) [31]. However, because of the limitation of the loading rates in servo-hydraulic techniques, the strain rates achieved in this study were less than 0.15 s^{-1}. Specimens in

this type of tests are still deforming under quasistatic strain rates. Existing servo-hydraulic experimental technique does not have the ability to load specimens fast enough to reach the range of intermediate strain rates.

Compared with the target range of intermediate strain rates from 1 to 100 s^{-1}, the strain rates achieved in Kolsky bar tests are too high while the strain rates achieved in servo-hydraulic tests are too low. Therefore, to evaluate the responses of SMA specimens under intermediate strain rates, a new experimental technique that is capable of testing large scale components under intermediate strain rates is required.

1.2 Research objectives and rationales

To overcome the limitations of current experimental techniques, this research focuses on developing a new high-loading-rate tensile testing system that is capable of testing large scale components under intermediate strain rates in a repeatable and controllable manner. This new testing system directly measures force and deformation of specimens with different shapes, sizes, and materials. Besides SMA specimens, this test system has the ability to test other structural materials and components after minor modification.

This research aims to bridge the gap between tests on prismatic material specimens and tests on full scale structure systems. Tests on small scale prismatic specimens such as Kolsky bar tests are limited to obtain only stress and strain results on the material level. On the other hand, tests on full scale structure systems such as shaking table tests and actual blast tests can obtain more information on the system level but are usually expensive and time-consuming. In contrast to these existing experimental methods, the new method in this research provides the ability to test various large scale structural components and directly measure force and deformation results of non-prismatic components. The new experimental method is capable of evaluating behaviors related to sizes and shapes of structural components rather than only assessing stress-strain responses of prismatic specimens as in current material tests. Compared with current system tests, this new method is more time-effective and cost-effective because it focuses on testing critical structural components rather than the entire structure.

This research also aims to bridge the gap between quasistatic strain rates achieved by conventional servo-hydraulic techniques and high strain rates achieved by typical Kolsky bar techniques. The quasistatic strain rates generated in conventional servo-hydraulic tests are usually below 1 s^{-1} while the high strain rates generated in most of Kolsky bar tests are above 100 s^{-1}. Intermediate strain rates between 1 s^{-1} and 100 s^{-1} are very difficult to achieve [19]. However, evaluation of the responses of materials and components under this range of intermediate strain rates is critical to applications in seismic mitigation and blast protection. With appropriate experimental design, the new tensile testing system in this research can successfully test specimens of SMAs and other materials in this range of intermediate strain rates.

1.3 Research contributions and significances

The major contribution of this research is the new high-loading-rate tensile testing system that can test both material specimens and structural components under constant intermediate strain rates (1 to 100 s^{-1}). This new testing system can deform large scale specimens under intermediate strain rates in a controllable manner, which has not been achieved by any other existing techniques. As a result, this new testing system contributes in filling the gap between quasistatic strain rates lower than 1 s^{-1} obtained from conventional servo-hydraulic techniques and high strain rates higher than 100 s^{-1} obtained from typical Kolsky bar techniques. This tensile testing system is capable of testing both prismatic specimens and non-prismatic components in a repeatable manner. The force and deformation of specimens and components are directly measured in this testing system. Therefore, this testing system provides experimental techniques for both characterizing material properties and assessing structural components.

This new tensile testing system has great potential to perform various types of experimental tests because it can accommodate specimens with different sizes, shapes, and materials. Adaptivity is one of the major design objectives of this testing system. As a result, researchers can adopt this new experimental method in various tests with different research objectives. For example, with minor modification, this system can test pull-out

strength of reinforcing steel in concrete, tensile strength of welded and bolted connections in steel structures, and bonding strength between fiber-reinforced polymer components.

1.4 Outline of this dissertation

1.4.1 Chapter 2: Literature review

This chapter includes the introduction and background of the research and focuses on the material properties of SMAs and the relation between material properties and potential applications. The martensitic phase transformation and the corresponding reverse transformation are introduced in detail. Several temperature-induced, stress-induced, and thermal-mechanical coupled behaviors of SMAs are explained by phase transformations.

This chapter also includes the overview of numerical modeling of SMA materials in finite element simulations. The Auricchio-Taylor model, the built-in superelastic model in Abaqus, is adopted in this research and is discussed in detail. In addition, this chapter covers the introduction of existing high-loading-rate experimental techniques such as the Kolsky bar tests. Experiments conducted on SMAs using these techniques in previous studies are reviewed.

1.4.2 Chapter 3: Quasistatic cyclic loading tests of an SMA-based seismic bracing system

This chapter investigates the performance of a seismic bracing system based on a shape memory alloy ring, which is capable of both re-centering and dissipating energy. Part of this chapter is adopted from published articles [46, 47, 48] and is reused with permission from the publishers. This lateral force resisting system is a cross-braced frame consisting of a shape memory alloy ring and four tension-only cable assemblies and is applicable to both new constructions and seismic retrofits. The mechanical responses of this SMA-based system are evaluated under quasistatic strain rates induced by cyclic loading. Performances such as strength, stiffness, energy dissipation, damping ratio, and re-centering ability of this SMA-based seismic bracing system are examined based on experimental results. This chapter describes the experimental design in detail, presents and discusses the experimental results, and compares the performance of this system with other SMA-based bracing systems from

previous studies [122].

This chapter also presents a numerical model of SMA materials which is based on Abaqus built-in Auricchio-Taylor model. The subroutine defining the material properties is updated based on the experimental observations, and the simulated results are compared with the experimental results to validate the finite element model for quasistatic loading rates. After that, a parametric study on the performances of SMA rings with different sizes is conducted numerically using the updated material model. This numerical analysis can be utilized in proof-of-concept studies on potential SMA-based applications.

1.4.3 Chapter 4: Development of a high loading rate tensile testing system for structural components

This chapter focuses on the design, fabrication, and validation of an innovative high-loading-rate tensile testing system. This new tensile testing system utilizes an existing high-speed actuator of the Blast, Shock, and Impact Laboratory at Georgia Tech to generate high speed impact force [126]. An inverter mechanism inverts the direction of the impact force through a specially designed motion, resulting in high speed tensile force onto the specimen. With proper instrumentation and data acquisition, this testing system is able to capture the responses of specimens under intermediate strain rates.

This chapter includes the validation tests of this testing system after it was built. Experimental results from different instruments are verified by each other and are compared with theoretical estimation to ensure this system is obtaining reasonable experimental data in a repeatable and controllable manner as expected. Since this testing system is designed not only for SMA specimens but also for general structural components within a certain limit of size and strength, the validation and calibration are significantly important for the accuracy and reliability of future tests. Therefore, this chapter documents all these validation tests as well as all the design and fabrication information in order to serve as a reference for any future high-loading-rate tensile test involving this testing system.

This chapter also includes a finite element (FE) simulation for the tensile testing system. The FE simulation is calibrated by comparing FE simulated results with corresponding experimental results. This calibrated FE simulation can be utilized to estimate the results

of tests with various initial conditions and, thus, replace some experimental tests. Therefore, it can help reducing the required number of iterations in the entire testing process.

1.4.4 Chapter 5: High-loading-rate tensile tests of SMA specimens

Using the high-loading-rate tensile testing system developed in Chapter 4, this chapter conducts a series of tensile tests on three types of SMA specimens including round tensile specimens, threaded-end bar, and ring. The experimental design, setup, and results are presented in this chapter, and these results are compared with the results from the quasistatic test in Chapter 3. Analysis of experimental results shows that this new testing system is capable of testing various SMA specimens in intermediate strain rates. The differences between SMA rods, threaded-end bars, and rings are also discussed in this chapter.

1.4.5 Chapter 6: Conclusions and recommended future research

Chapter 6 summaries the primary conclusions of the research. Conclusions from both the development of the high-loading-rate tensile testing system and the investigation of properties and potential applications of SMAs are presented. This chapter also discusses potential improvements and implementations of the new high-loading-rate tensile testing system and provided recommended directions on future research regarding the material properties and applications of SMAs.

CHAPTER II

LITERATURE REVIEW

2.1 Material properties of Shape memory alloys (SMAs)

2.1.1 Brief introduction

The shape memory effect of NiTi alloys was first discovered by Buehler et al. at the Naval Ordnance Laboratory in 1963 [15]. NiTi alloys was named as Nitinol in honor of the name of the laboratory. Since then, researchers have discovered numerous shape memory alloys (SMAs), including copper-based SMAs [56, 125], iron-based SMAs [132], and other types of SMAs such as CoNiGa, NiMnGa, and NiCoMnIn [21, 65, 138].

SMAs are named after the shape memory effect (SME), which indicates that these materials can recover their original shapes through thermal-mechanical coupled behaviors. For example, under a certain temperature, a specimen made of SMAs deforms under external loading. After unloading, the specimen remains in the deformed shape. However, if the temperature is increased, the specimen spontaneously returns to its original shape almost as if it "remembers" its original shape.

Because of this unique thermal-mechanical coupled behavior, SMAs can be used as active materials that function as both sensors and actuators simultaneously [112]. For example, a valve in a rice cooker is required to be opened to release the excess steam when the cooking chamber reaches a certain temperature. Traditionally, a sensor monitors the temperature, and a processor collects the data from the sensor. When the temperature reaches the preset level, an actuator, such as an electric motor, receives a signal from the processor and then opens the valve. However, with proper design, an SMA component is able to replace the sensor, the processor, and the actuator altogether [6]. When the temperature reaches a preset level, the SMA component deforms spontaneously because of its thermal-mechanical coupled behavior. Through a mechanism connected to the valve, this deformation of the SMA component opens the valve automatically. When the temperature drops below that

preset level, the SMA component recovers its shape and closes the valve automatically. For this reason, SMAs are usually considered as smart materials that have great potential in applications of active control.

The temperature-induced deformation is just one example of the unique properties of SMAs. Another extraordinary property is called *superelasticity* or *pseudoelasticity*. If the temperature of an SMA specimen is above a certain level and if an external mechanical loading is applied, the specimen deforms into a new shape. After this external loading is removed, the specimen recovers its original shape spontaneously. Even if the deformation under loading is up to 6% to 8% strain, SMA specimens are still capable of returning to the original shape with little or no residual deformation [57]. The term superelasticity is misleading to some extent since the stress-strain relation during loading and unloading cycles is not a typical elastic curve but rather a flag-shaped closed loop, which can provide both energy dissipation and re-centering ability. Because of this flag-shaped hysteresis behavior, superelasticity is the focus of many researchers in structural engineering, especially in the field of seismic mitigation [30, 103, 137].

2.1.2 Phase transformations

These unique thermal-mechanical coupled behaviors of SMAs are caused by the reversible martensitic phase transformation that occurs in the crystalline structures of the materials [11, 140]. Typically, most of SMAs have two phases: *martensite* (M) and *austenite* (A). When the temperature is high and the stress is low, SMAs tend to change into austenite. In contrast, when the temperature is low and the stress is high, SMAs tend to change into martensite. Figure 1 shows the schematic phase diagram of SMAs with respect to temperature and stress. Each point on this diagram represents a certain state of the material under the corresponding temperature and stress.

The austenite phase usually has a cubic crystal system with high symmetry, while the martensite phase usually has a monoclinic system with low symmetry. The monoclinic martensite phase has two forms with different variants which relate to the orientations

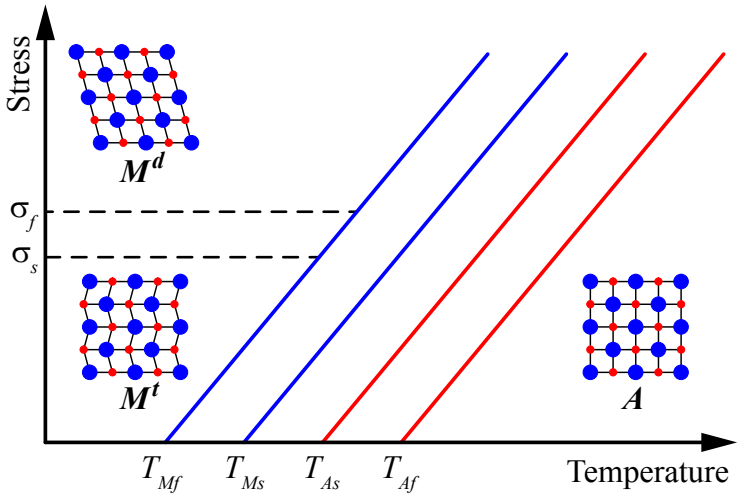

Figure 1: Stress-temperature phase diagram of SMAs.

of the crystal structures. One form is called *twinned martensite* (M^t) which has a self-accommodated variant. The other form is called *detwinned martensite* (M^d) which has a specific variant. These crystal structures of different phases are also illustrated schematically in Figure 1. The transformations between these phases are related to shear lattice distortions which are induced by stress, temperature, or both.

Under constant stress, when temperature decreases, the phase transformation from austenite (A) to martensite (M) starts at the temperature T_{Ms} and finishes at the temperature T_{Mf}. In contrast, when temperature increases, the reversed phase transformation from martensite (M) to austenite (A) starts at the temperature T_{As} and finishes at the temperature T_{Af}. These transformation temperatures are not constant values but functions of stress. As shown in Figure 1, the relations between transformation temperatures and stress are simplified as linear functions [33, 77]. Transformation temperature generally increases as stress increases.

Under a constant temperature below T_{Mf}, if stress increases from σ_s to σ_f, SMA material transforms from twinned martensite (M^t) phase into detwinned martensite (M^d) phase.

These thermal-mechanical coupled behaviors can be represented as curves on the phase diagram connecting the original states and the new states. These unique behaviors of SMAs are discussed in detail in the following sections.

2.1.3 Shape memory effect (SME)

Because of these thermal-mechanical coupled properties, instead of 2D stress-strain diagrams for conventional engineering materials, the behaviors of SMAs are usually described by 3D stress-strain-temperature diagrams. The shape memory effect (SME) is associated with the temperature-induced transformations. Generally, the stress remains constant while the strain changes as the temperature changes.

Figure 2 illustrates the paths of temperature-induced phase transformations under stress-free conditions as the horizontal arrows on the phase diagram. The transformation temperatures $T_{Mf}^{[0]}$, $T_{Ms}^{[0]}$, $T_{As}^{[0]}$, and $T_{Af}^{[0]}$ corresponding to the phase transformations under no mechanical loading are important characteristics of SMA materials. These transformation temperatures can be measured by differential scanning calorimetry (DSC) tests [7, 115].

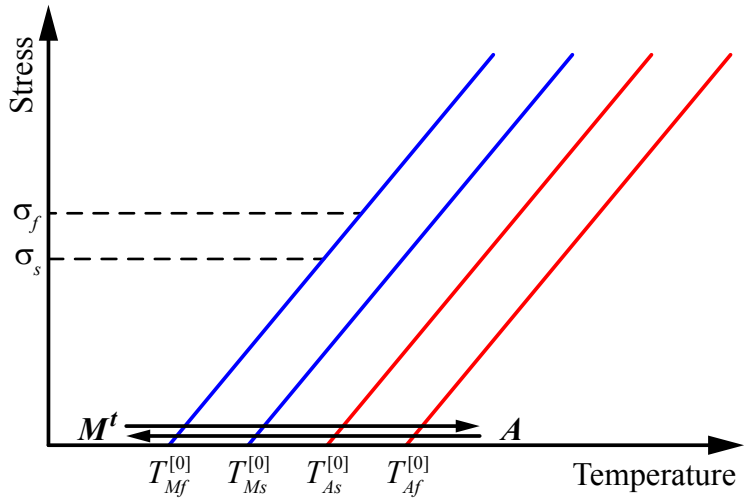

Figure 2: Temperature-induced phase transformations without mechanical loading.

The micro phase transformation and corresponding macro shape changes imply that the strain of SMA materials changes as the temperature changes. The full shape recovery occurs after the external mechanical loading is removed. The entire loading-unloading and heating-cooling cycle forms a closed loop in the stress-temperature phase diagram as shown in Figure 3.

The closed loop starts at the twinned martensite phase under T_{Mf} with no external mechanical loading. This phase is denoted as $(1)M^t$ in Figure 3. If external loads are

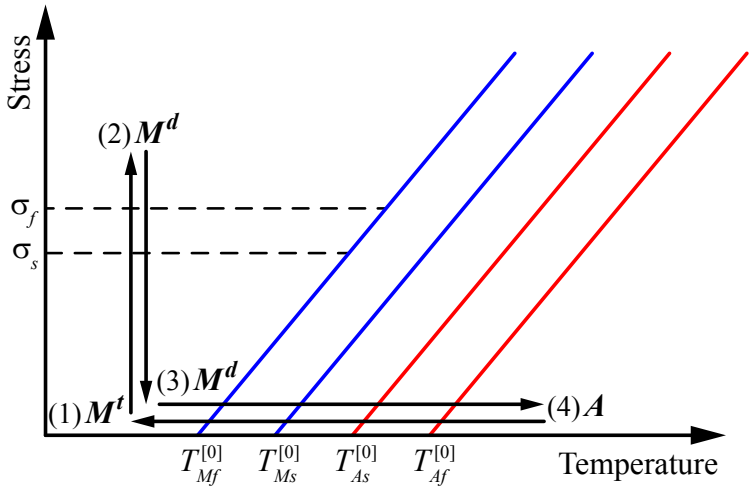

Figure 3: Thermal-mechanical coupled phase transformations in shape memory effect.

applied to this phase, the material transforms to detwinned martensite phase, which is denoted as $(2)M^d$. This detwinned martensite is stressed and is in its deformed shape. After that, if the external loads are removed while the temperature is still under T_{Mf}, SMAs remain in detwinned martensite phase, denoted as $(3)M^d$, which is still in deformed shape but is unstressed. From this phase, if temperature increases, the temperature-induced deformation occurs, and the material transfers from $(3)M^d$ into $(4)A$, which represents austenite phase in the original undeformed shape. When the temperatures reaches the austenite start temperature T_{As}, the material starts to transform from $(3)M^d$ into $(4)A$. When the temperature reaches the austenite finish temperature T_{Af}, the material completes the phase transformation and recovers its original shape. Then the specimen can return to its original unstressed and undeformed $(1)M^t$ phase by just cooling to a temperature below T_{Mf}. This transformation from $(4)A$ to $(1)M^t$ causes no shape change. Therefore, the specimen is still in its original shape after this transformation. The entire cycle of SME is composed of these four phase transformations which are represented by four arrows in Figure 3.

The temperature-induced phase transformations also occur under applied mechanical loading, resulting in not only shape recovery but also energy transfer from thermal energy into mechanical energy. As shown in Figure 4, an SMA specimen is loaded under a certain temperature below T_{Mf}. Before loading, the specimen is in twinned martensite phase (M^t)

under the original undeformed shape. After the specimen is loaded above the stress of σ_f, the material transforms into detwinned martensite phase (M^d) under the new deformed shape. This mechanical loading process is the same as that in Figure 3 represented by the vertical upward arrow.

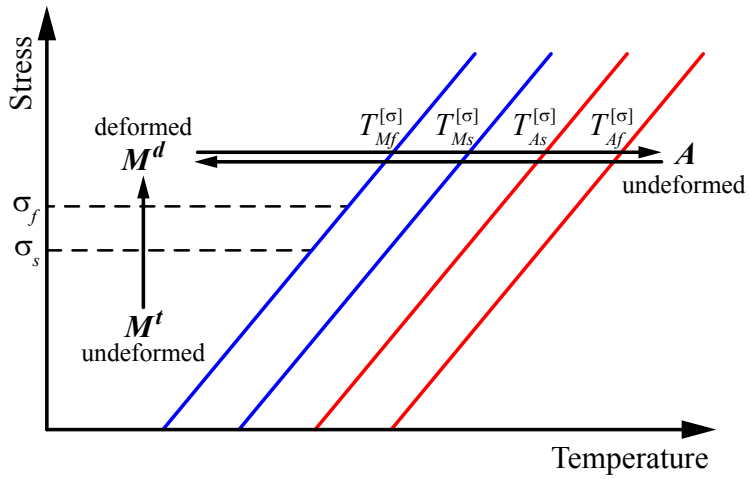

Figure 4: Temperature-induced phase transformations under a constant stress.

After loading the SMA specimen above the stress of σ_f, the temperature-induced phase transformation occurs under that constant stress level if the external mechanical force is maintained and the temperature is increased. As a result of this phase transformation, the shape of the specimen also changes as the temperature changes. This phase transformation is represented by the horizontal arrow pointing from left to right in Figure 4. When the temperature of the specimen reaches the transformation temperature $T^{[\sigma]}_{As}$, which indicates the start of the martensite-to-austenite transformation under a certain stress,$[\sigma]$, the SMA material begins to change back to its original shape. When the temperature reaches $T^{[\sigma]}_{Af}$, this phase transformation is completed, and the specimen fully recovers its original undeformed shape. After that, if the temperature decreases, the SMA specimen transforms from austenite in the undeformed shape back into the detwinned martensite in deformed shape. Temperature $T^{[\sigma]}_{Ms}$ and $T^{[\sigma]}_{Mf}$ indicate the start and finish temperature of this reverse transformation, respectively.

Figure 5 schematically shows the strain-temperature relation of this shape memory effect assuming the stress is constant. This 2D strain-temperature diagram can be considered as

a section cut from the actual 3D stress-strain-temperature diagram perpendicular to the axis representing stresses.

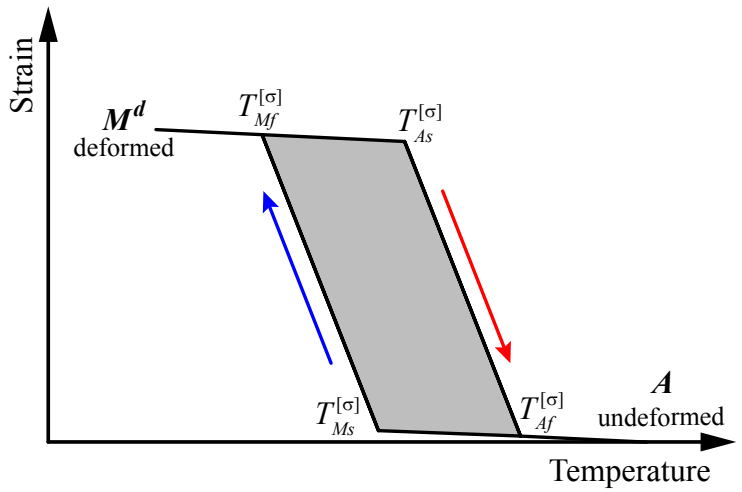

Figure 5: Strain-temperature diagram of shape memory effect under a constant stress.

The shape memory effect implies that, even under external mechanical loading, an SMA specimen still changes its shape as temperatures changes. As a result, the SMA specimen is actually doing work as an actuator transferring thermal energy into mechanical energy. For most types of SMAs, the available work output per unit mass is approximately 10^3 J/kg, which is one of the highest among all the current smart materials [72]. The available work per unit volume of SMAs is generally around 10 J/cm^3. In contrast, the available work per unit volume of typical piezoelectric materials is only around 0.035 J/cm^3. Human muscles, which can also be considered as smart active materials, have similar capacities to piezoelectric materials. As a result of the reversible temperature-induced phase transformation and the high energy capacity related to this transformation, SMAs have great potential as smart actuators [62]. This unique property of SMAs is the basis of many applications in mechanical engineering and aerospace engineering. Additional examples are discussed in Section 2.2.2.

2.1.4 Superelasticity

The superelasticity of SMAs is associated with the stress-induced phase transformations under a constant temperature. These transformations are represented by vertical arrows in

the stress-temperature diagram. As shown in Figure 6, if this constant temperature, $[T]$, remains above T_{Af}, an SMA specimen under no external loading is in austenite phase. When external mechanical loading is applied and the stress reaches $\sigma_{Ms}^{[T]}$, the SMA material starts to transform from austenite into detwinned martensite. This transformation completes when the stress reaches $\sigma_{Mf}^{[T]}$. After that, the material is in the detwinned martensite phase, and the specimen is in the deformed shape. If the external load is gradually removed and the temperature remains the same, when the stress drops below $\sigma_{As}^{[T]}$, the reverse transformation starts spontaneously and immediately. This reverse transformation completes when the stress drops below $\sigma_{Af}^{[T]}$. After that, the material is in the austenite phase again, and the specimen recovers its original shape with little or no residual deformation.

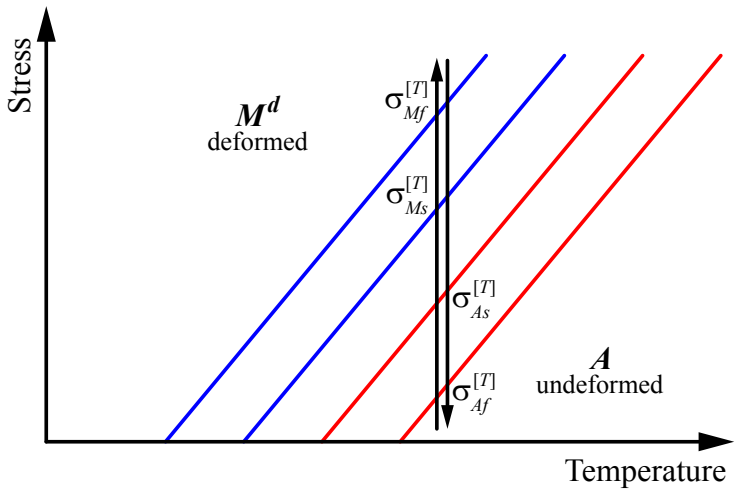

Figure 6: Stress-induced phase transformations under a constant temperature.

The stress-strain relation of the superelastic loading-unloading cycle is illustrated in Figure 7. The loading-unloading curve forms a closed loop crossing the origin point, indicating a re-centering behavior with little or no residual strain. The shaded area enclosed by the loading-unloading curve as shown in Figure 7 represents the dissipated energy during this loading-unloading cycle. This flag-shaped stress-strain curve shows the abilities of both re-centering and energy dissipation, which are the major reasons that superelastic SMAs have great potential in structural engineering.

If the external loading increases to an excessive level, the SMA material starts to exhibit plastic behavior. The martensite yield strain of typical NiTi SMAs is approximately 8%

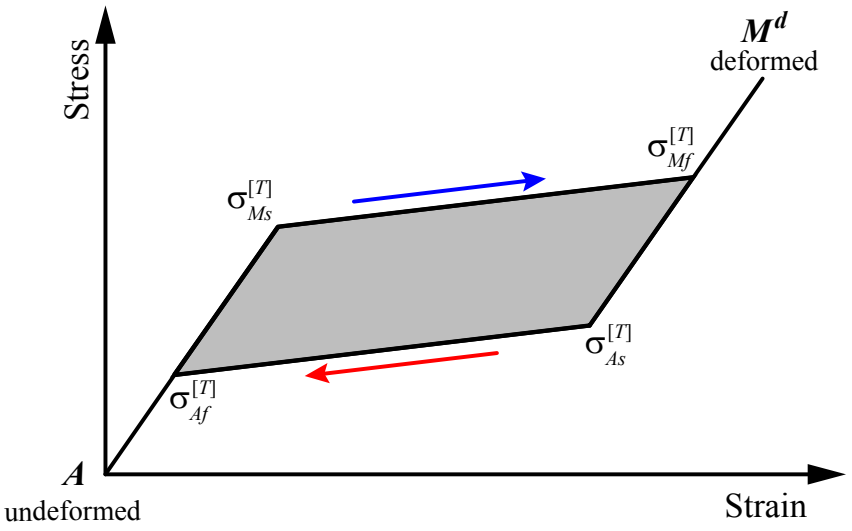

Figure 7: Stress-strain diagram of superelasticity under a constant temperature.

[54]. If a specimen is loaded beyond this yield strain, irreversible plastic deformation occurs, and the specimen is no longer able to fully recover its original shape when unloaded. As a result, permanent residual deformation occurs in the specimen.

In structural engineering, most of the construction materials are passive materials, which are not considered to have thermal-coupled behaviors, and most of the designs are passive systems, which respond to external forces passively without active actuation. Therefore, superelasticity has been the focus of studies on SMAs in the field of structural engineering. In contrast, applications of thermal-coupled shape memory effect in structural engineering are rare. Examples of superelastic SMAs in structural applications are discussed in Section 2.2.1.

2.1.5 Strain rate and temperature dependency

Because of the thermal-mechanical coupled behaviors as discussed above, the mechanical responses of SMAs are dependent on temperature [18]. The experimental results of a series of tests conducted at deferent temperatures prove that the superelastic behavior and the ability of full recovery are significantly influenced by temperature [33]. If the temperature is above T_{Af} during the loading and unloading process, SMA specimens can fully recover their original shapes after unloading as long as they are not loaded beyond the martensite yield

point. However, if the temperature is below T_{Ms}, partial recoveries occurs, and residual deformations are observed after unloading. The transformation stress and damping ratio are also affected by temperatures [33].

Besides temperature, the behaviors of SMAs are also affected by strain rate. Several previous studies investigated the rate dependency of SMAs both analytically [38, 73, 75] and experimentally [1, 20, 79, 96, 97]. The strain rates of SMA specimens in these experimental studies ranged from 10^{-3} s^{-1} to 10^{4} s^{-1}. Responses under strain rates below 1 s^{-1} were obtained by conventional quasistatic loading tests while responses under high strain rates from around 100 s^{-1} to around 5,000 s^{-1} were obtained by Kolsky bar tests. Extremely high strain rates such as those above 10^{4} s^{-1} were achieved by special miniature Kolsky bar systems [96]. The details of these Kolsky bar tests are discussed in Section 2.4.1.

Previous experimental results conclude that, similar to dynamic transit behaviors, the cyclic behaviors are also highly dependent on strain rate. DesRoches et al. tested SMA wires and bars cyclically at different loading frequencies from 0.025 to 1.0 Hz. The test results show that the plateau stresses of both loading and unloading, the dissipated energy, and the equivalent damping ratio are all affected by loading rates [31].

According to the analytical models proposed by Mirzaeifar et al. [89], the responses of SMA materials are actually determined by the combination of specimen sizes, boundary conditions, and loading rates. Thermodynamic behaviors such as latent heat and heat flux in the cross section are affected by size and boundary conditions of specimens. In other words, the strain rate dependency of SMA materials is not independent of size or boundary conditions. Therefore, tests on not only prismatic specimens but also non-prismatic specimens and components with different sizes and boundary conditions are required to investigate the strain rate dependency of SMA materials.

2.1.6 Tension-compression asymmetry

Another notable property of SMAs is the asymmetry between tensile and compressive behaviors [80]. The main reason for this asymmetry is the differences between the crystal

mechanisms for deformations under tension and compression. The deformation under tension is dominated by reorientation of martensite variants while the deformation under compression is affected by dislocations. As a result of these differences at the micro level, the stress-strain behaviors at the macro level are different. The stress-strain curves under tensile force usually have flat plateaus corresponding to the process of phase transformation. In contrast, the stress-strain curves under compressive force exhibit early strain hardening without obvious stress plateaus.

Several previous studies investigated numerical models on the tension-compression asymmetry of SMAs [75, 105]. Experimental tests on tension-compression asymmetry under high strain rates were also conducted by Adharapurapu et al. [1]. The results of these studies suggest that the compressive stress is generally higher than tensile stress subject to the same magnitude of strain. This tensile-compressive asymmetry is significantly influenced by temperature as shown in previous research [105]. At lower temperature, the increase from static strength to dynamic strength is more rapid in compression than in tension. At higher temperature, the increases of strength in both tension and compression are almost negligible. As a result, the responses of SMA specimens under bending, which involve both tension and compression in the same section, are required to be analyzed by more complex models [90].

2.2 Engineering applications of SMAs

Because of the distinctive behaviors such as shape memory effect and superelasticity as discussed in Section 2.1, SMAs have unsurprisingly become the key components of numerous engineering applications. Currently, most of the commercial applications of SMAs occur in the field of biomedical engineering [91]. The utilization of SMA-based smart actuators is increasing in the field of automobile, mechanical, and aerospace engineering. In contrast, actual applications in civil engineering are not common as mentioned in Section 1.1. Most of the studies of SMAs in civil engineering are experimental proof-of-concept research rather than actual applications. Nevertheless, with decreasing costs of SMA materials and increasing demands of high-performance infrastructures [3, 14], SMAs have bright prospects in the

future of civil engineering.

2.2.1 Applications in structural engineering

Since superelastic behavior of SMAs provides both energy dissipation and re-centering ability with sufficient ductility and strength, SMAs are among the most suitable materials for seismic applications as suggested by previous overviews [30, 63, 103].

Because of the high performance per unit volume as compared with conventional materials such as steel, SMAs are more preferred in seismic retrofit projects of historical buildings. Examples among the few actual seismic engineering applications include the retrofits of the S. Giorgio Church bell tower [61], the Basilica of St Francesco of Assisi [24], and the Sherith Israel Synagogue [106].

SMA-based devices can be utilized as the key uniaxial components of seismic resisting systems [13, 34, 35, 123]. For example, the full-scale prototype tested by Dolce et al. [35] was a brace member based on pre-tensioned superelastic SMA wires. The uniaxial device tested by Speicher et al. [123] utilized SMA helical springs and Belleville washers.

SMAs are also able to work together with other materials in a hybrid seismic resisting system. Ideally, the re-centering ability of this hybrid systems is provided by SMAs while additional energy dissipation and restoring force are supplemented by other materials such as steel. An articulated quadrilateral hybrid bracing system composed of SMA wires and steel plates was designed and tested by Speicher et al. [122]. Another example was the hybrid bracing system proposed by Yang et al. [139]. In this bracing system with high strength steel tubes as key components, SMA wires and steel struts were enclosed inside these tubes and were designed to deform together to provide re-centering ability and energy dissipation.

Other seismic applications include SMA-based beam column connections for both steel structures [32, 124] and reinforced concrete structures [2, 141], base isolation [49, 55, 136], dampers, restrainers, expansion joints in bridge structures [4, 64, 85, 113], and external retrofit for concrete members [5, 22, 29, 117].

Besides applications in seismic resisting and retrofit systems, SMAs are also investigated

in other fields of structural engineering such as reinforced concrete and prestressed concrete structures. SMA wires directly utilized as reinforcements embedded inside concrete were tested in previous studies [25]. Active control on deflections of concrete members was achieved by heating up embedded SMA wires using electrical power [28]. Through thermal-mechanical coupled responses, SMA wires and rods were capable of working as external prestressing tendons both in new constructions and retrofit applications [84].

SMAs can also be utilized to combine with other engineering materials and form new composite materials. The behavior of SMAs as part of composite materials was evaluated by various previous studies. One example was high performance concrete reinforced with SMA short fibers [92]. Another example was utilizing SMA wires as fibers to construct Fiber-reinforced polymer (FRP) materials. The SMA-embedded FRP material was able to be actively controlled because of temperature-induced deformations of SMA fibers [107]. The superelasticity of SMAs also enhanced the mechanical performance of the FRP material [135].

2.2.2 Applications in other engineering fields

Because of extraordinary biocompatibility [37] and unique mechanical properties discussed above, SMAs are currently widely used in biomedical engineering. Examples include guidewires in angiography, stents for treatment of peripheral vascular disease, stent grafts, inferior vena cava filters, and clinical instruments [91].

Applications in mechanical engineering are mostly smart actuators based on the thermal-mechanical coupled phase transformations. Examples include the air valve in rice cooker mentioned previously [6], small actuators of robots [62], and extensive applications in the automobile industry, such as wipers, fuel injectors, air vents, and absorbers [128].

As a result of the unique mechanical properties, relatively light weight, and good corrosion resistance, SMAs also have critical applications in aerospace engineering. The first successful application of SMAs was the coupling of hydraulic lines in the F-14 jets in the 1970s [52]. Since then, SMA-based connectors, dampers, sealers, release mechanisms, as well as many other applications emerged in the field of aerospace engineering [62].

Other miscellaneous applications of SMAs include eyeglass frames [133], clothing [134], sports equipment, and mobile-phone antennae [62].

2.3 Phenomenological superelasticity models

Several researchers proposed phenomenological constitutive laws of SMAs to construct analytical material models. An overview of these studies and resultant models can be found in references [72, 104].

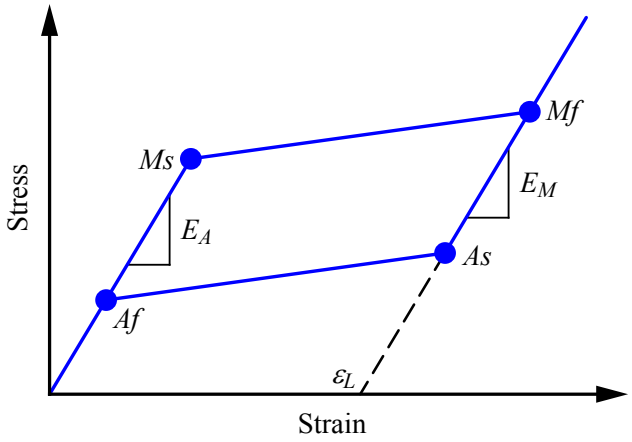

Figure 8: Idealized stress-strain curve of superelastic SMAs.

This research adopted the Auricchio-Taylor model developed by Auricchio et al. [8, 9] to simulate the superelastic and thermal-mechanical coupled behaviors. This material model is derived from the concept of generalized plasticity [81]. The mathematical method is similar to plasticity theory but the physical meanings of variables are different. Figure 8 shows an idealized 1-D stress-strain curve of this material model. The points M_s, M_f, A_s, and A_f denote the start and finish of the martensitic phase transformation and the reversed transformation from martensite back to austenite, respectively.

The corresponding strain of these four critical points are determined as

$$\varepsilon_{Ms} = \frac{\sigma_{Ms}}{E_A} \tag{1}$$

$$\varepsilon_{Mf} = \varepsilon_L + \frac{\sigma_{Mf}}{E_M} \tag{2}$$

$$\varepsilon_{Af} = \frac{\sigma_{Af}}{E_A} \tag{3}$$

$$\varepsilon_{As} = \varepsilon_L + \frac{\sigma_{As}}{E_M} \tag{4}$$

where ε_L is a material property constant and is defined as the transformation strain which corresponds to the maximum possible strain associated with the phase transformation.

As shown in Figure 9, the phase transformation of SMAs is taken into account by an internal variable ξ_s, which represents the volume fraction of martensite phase. If the material is in austenite phase, ξ_s equals zero; if the material is in martensite phase, ξ_s equals one; if the material undergoes the phase transformation from austenite to martensite, ξ_s changes from zero to one.

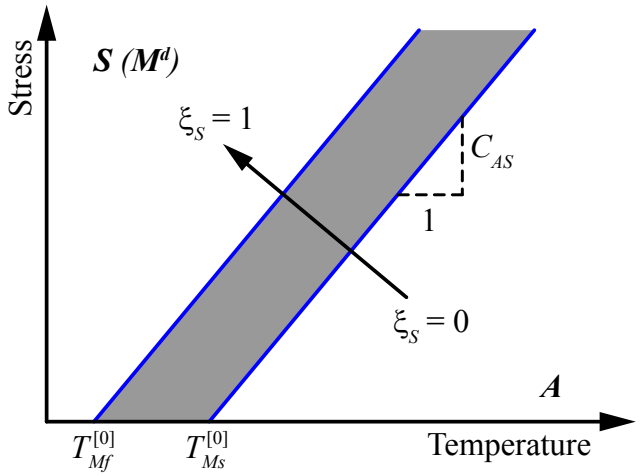

Figure 9: Idealized stress-temperature diagram of superelastic SMAs under increased loading.

The total strain is defined as the summary of strain associated with both elastic behavior and phase transformation.

$$\varepsilon = \varepsilon^e + \xi_s \varepsilon_L \tag{5}$$

where ε^e is the elastic strain.

Before the start of phase transformation from austenite to martensite, ξ_s equals zero. Therefore, the material behavior remains pure elastic since the total strain, ε, equals the elastic strain, ε^e. During the phase transformation, which is denoted as the shaded region in Figure 9, ξ_s increases from zero to one. As a result, the total strain, ε, is the combination of elastic strain, ε^e, and phase transformation strain, $\xi_s \varepsilon_L$. After the completion of phase transformation, ξ_s equals one. Therefore, the total strain, ε, equals the elastic strain, ε^e, and the full phase transformation strain, ε_L. Since the phase transformation strain reaches

ε_L and does not increase any more, all the increases in total strain, ε, are associated with elastic strain, ε^e. Therefore, the material returns to pure elastic behavior again.

To simulate the thermal-mechanical coupled behaviors, the relations between transformation stresses and temperatures are simplified as linear functions with a material property constant, C_{AS}, which corresponds to the slope of the inclined lines dividing the phase diagram as shown in Figure 9. As a result, the statues of the material on this stress-temperature diagram are described by forcing functions defined as follows:

$$F^{As} = \sigma - C_{AS}T \tag{6}$$

$$F_s^{As} = F^{As} - C_{AS}T_{Ms}^{[0]} = \sigma - C_{AS}\left(T - T_{Ms}^{[0]}\right) \tag{7}$$

$$F_f^{As} = F^{As} - C_{AS}T_{Mf}^{[0]} = \sigma - C_{AS}\left(T - T_{Mf}^{[0]}\right) \tag{8}$$

For a certain combination of stress, σ, and temperature, T, the criteria of the forcing functions are these following conditions:

$$\dot{F}^{As} > 0 \tag{9}$$

$$F_s^{As} > 0 \tag{10}$$

$$F_f^{As} < 0 \tag{11}$$

If the stress, σ, and the temperature, T, do not satisfy all three conditions listed above, this indicates that the material is not undergoing phase transformation. Therefore, the internal variable, ξ_s, is either zero or one and is not changing. As a result, the rate of ξ_s remains zero.

$$\dot{\xi}_s^{AS} = 0 \tag{12}$$

where $\dot{\xi}_s^{AS}$ is the rate of ξ_s during the phase transformation from austenite to martensite.

If the stress, σ, and the temperature, T, satisfy all three conditions listed above, this indicates that the material is under increasing load and is undergoing the phase transformation represented by the shaded region in Figure 9. For this case, an evolutionary equation between the rate of the internal variable, $\dot{\xi}_s$, and the rate of the forcing function, $\dot{F}^{AS}$, is constructed as

$$\dot{\xi}_s^{AS} = K_1^{AS}\dot{F}^{AS} \tag{13}$$

where K_1^{AS} is the flow rule of the evolutionary equation and is a function of ξ_s.

This flow rule, K_1^{AS}, can be chosen either as a linear model or an exponential model. The linear model is defined as

$$K_1^{AS} = -\frac{1-\xi_s}{F_f^{AS}} \tag{14}$$

while the exponential model is defined as

$$K_1^{AS} = \beta^{AS} \frac{1-\xi_s}{\left(F_f^{AS}\right)^2} \tag{15}$$

where β^{AS} is a material property constant.

The unloading process from martensite phase to austenite phase can be analyzed similarly. The evolutionary equation between $\dot{\xi}_s^{SA}$ and $\dot{F}^{SA}$ is defined as

$$\dot{\xi}_s^{SA} = K_1^{SA}\left(-\dot{F}^{SA}\right) \tag{16}$$

where $\dot{\xi}_s^{SA}$ is the rate of ξ_s during the phase transformation from martensite phase to austenite phase.

The flow rule K_1^{SA} as a function of ξ_s is constructed as

$$K_1^{SA} = \xi_s F_f^{SA} \tag{17}$$

for the linear model and

$$K_1^{SA} = \beta^{SA} \frac{\xi_s}{\left(F_f^{SA}\right)^2} \tag{18}$$

for the exponential model.

The overall rate of ξ_s is determined as

$$\dot{\xi}_s = \dot{\xi}_s^{AS} + \dot{\xi}_s^{SA} \tag{19}$$

This 1D material model can be expanded to a 3D version. The 3D model has two internal variables: the martensite fraction scalar, ξ_s, and the scaled transformation strain tensor, $\mathbf{u}$. The total strain tensor is considered as the summary of elastic part and the transformation part. The forcing functions, the evolutionary equations, and the flow rules are constructed similarly to the 1D version.

Since this material constitutive model is built upon a mathematical method that is similar to plasticity theory, the plastic behavior after yielding can be added by defining isotropic plastic behavior after martensite yielding. As a result, the material model can have a superelastic-plastic behavior. Figure 10 shows the stress-strain results of SMAs from a numerical simulation of an uniaxial tensile test using the superelastic-plastic material model assuming perfect plastic behavior after martensite yielding without strain hardening.

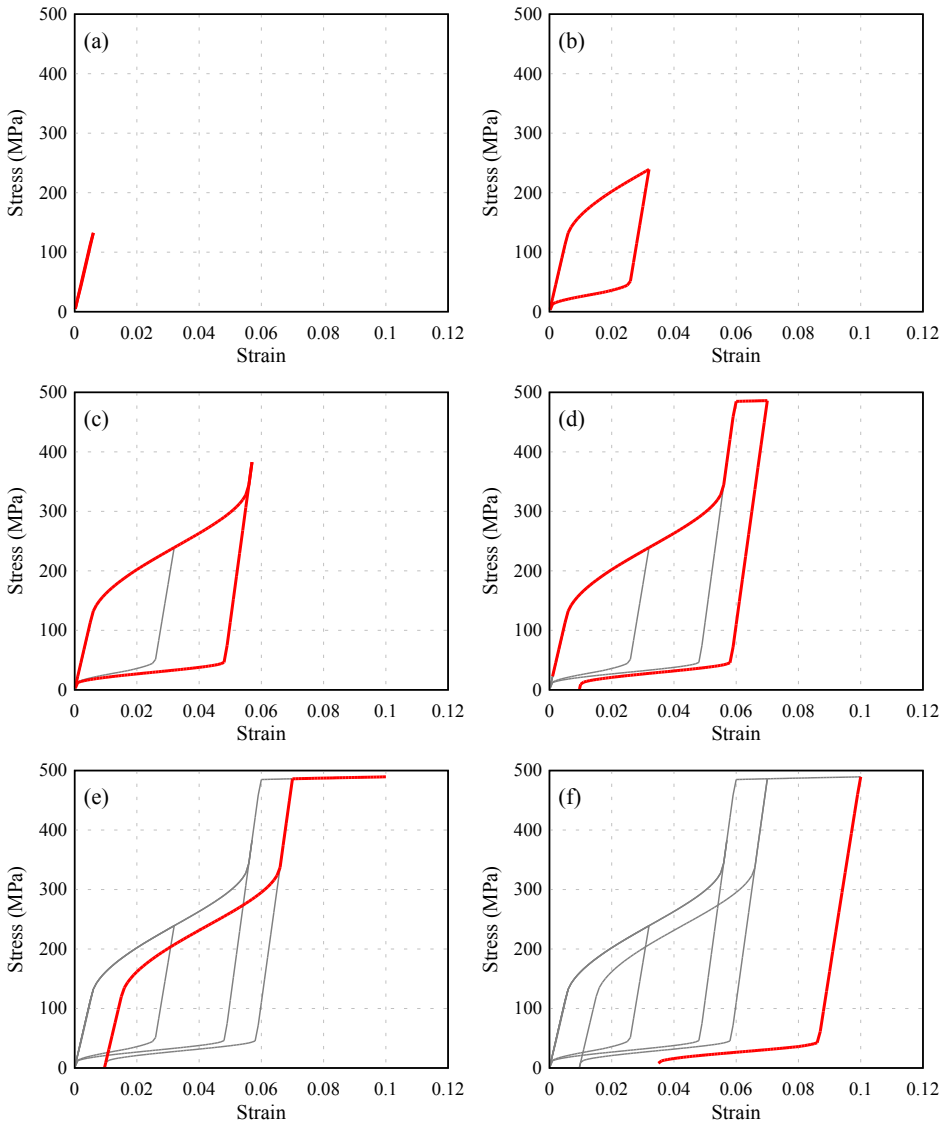

Figure 10: Simulated stress-strain curves for cyclic uniaxial tensile tests of SMAs.

When the specimen is loaded to a stress below σ_{Ms} and then unloaded, the material is

still in austenite phase without any phase transformation, indicating a linear elastic behavior as shown in Figure 10(a). If the specimen is loaded to a stress between σ_{Ms} and σ_{Mf} and then unloaded, the response of the material is a flag-shaped closed loop as shown in Figure 10(b), exhibiting superelasticity with full recovery to the original shape. The specimen is then loaded to a stress between σ_{Mf} and the martensite yield point. The response of this loading and unloading cycle is shown in Figure 10(c). The specimen is still able to return to the original shape without any residual strain. However, if the specimen is loaded beyond the martensite yield point as the case in Figure 10(d), plastic deformation occurs and the specimen does not fully recover to zero strain. Figure 10(e) shows the response of the specimen if it is loaded again and Figure 10(f) shows the final unloading process. This loading and unloading cycle is similar to typical plastic behavior except that the loading curve is in three segments corresponding to before, during, and after the martensite phase deformation, respectively.

2.4 High loading rate experimental techniques

To evaluate the mechanical responses under high speed loading, researchers developed various experimental techniques covering different ranges of strain rates. A detailed overview of these experimental techniques can be found in references [44, 114]. Based on the magnitude from low to high, strain rates are divided into several ranges which occur under different scenarios from creep to ultra-high speed impact. The behaviors under different strain rates can be obtained by different experimental techniques. Table 1 lists these ranges of strain rates and their corresponding experimental techniques.

Table 1: Strain rate ranges and corresponding experimental techniques

Strain rate (s^{-1})	Range	Experimental techniques
Below 10^{-6}	Creep	Creep-testing machine
$10^{-6} \sim 10^{0}$	Quasistatic	Conventional servo-hydraulic testing machine
$10^{0} \sim 10^{2}$	Intermediate	Specialized testing machine
$10^{2} \sim 10^{4}$	High	Conventional Kolsky bars
$10^{4} \sim 10^{6}$	Very high	Special Kolsky bars or Taylor impact
$10^{6} \sim 10^{8}$	Ultra high	Pressure-shear plate impact

Generally, strain rates of interest for structural engineering applications are lower than $100\,\mathrm{s}^{-1}$, which is the boundary between intermediate stain rates and high range rates. Conventional servo-hydraulic testing machines, which are capable of generating strain rates up to $1\,\mathrm{s}^{-1}$, are widely used in structural experimental tests. Specially designed servo-hydraulic systems can achieve strain rates up to $10\,\mathrm{s}^{-1}$ on small scale specimens [109]. Strain rates above $10\,\mathrm{s}^{-1}$ are beyond the capacity of servo-hydraulic systems. As a result, other experimental techniques need to be adopted to evaluate the responses of materials and components under intermediate strain rates.

2.4.1 Kolsky bar test

One of the most common techniques for high-loading-rate experiments is the Kolsky bar test, also know as Split-Hopkinson pressure bar (SHPB) test [19]. Although these two names can be used interchangeably, sometimes the term *Split-Hopkinson pressure bar* refers to compression tests, while the term *Kolsky bar* covers the more general concepts including compression, tension, and torsion tests [114].

Figure 11 shows the basic configuration of a compression Kolsky bar test. A specimen is attached between two bars, which are usually cylindrical metal bars with the same diameters. The initial cross sectional area of the specimen is A_s and the initial length of the specimen is l_0.

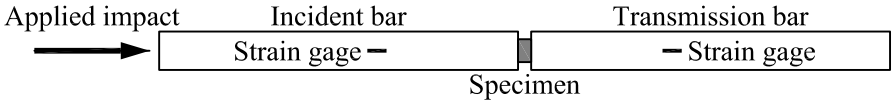

Figure 11: Schematic drawing of a compression Kolsky bar test setup.

The elastic modulus, E_b, and the density, ρ_b, of the bars are determined by other experiments. The stress wave velocity in the bars is derived as

$$c_b = \sqrt{\frac{E_b}{\rho_b}} \tag{20}$$

The longitudinal axes of the bars and the specimen are aligned in a straight line. The friction between the bars and the supports is assumed to be negligible, and the bars are able to slide along the longitudinal axis. The bars are designed to remain elastic during

the tests and, therefore, are usually made of high strength steel or aluminum. The total strength of the specimen is required to remain below a certain level in order to ensure that the bars remain elastic during the test.

To perform the test, an external impact applies onto the outer end of one bar, which is called the *incident* bar. The stress wave generated by this impact travels through the incident bar and reaches the interface between the incident bar and the specimen. From this interface, one part of the stress wave transmits through the specimen and then into the other bar, which is called the *transmission* bar. The other part of the stress wave reflects back into the incident bar. Strain gages, which monitors the strain changes with high sampling frequency, are attached to the surface of both the incident bar and the transmission bar. These stain gages capture three impulse signals: the incident pulse, ε_I, the reflected pulse, ε_R, and the transmitted pulse, ε_T. The incident pulse, ε_I, and reflected pulse, ε_R, are measured by the strain gages on the incident bar, while the transmitted pulse, ε_T, is measured by the strain gages on the transmitted bar. The distance between the strain gages on the incident bar and the specimen is selected to be sufficiently long so that the incident pulse, ε_I, and the reflected pulse, ε_R, do not overlap.

The compressive Kolsky bar tests are usually achieved by directly applying a compressive impulse onto the input end of the incident bar. This compressive impulse is either from an impact of a striker bar, which is accelerated by pressurized gas, or from the suddenly release of a static preloading. The tension and torsional Kolsky bar tests share the same basic concepts as compressive tests but require different setups to achieve different stress states. Tension Kolsky bar tests generally require special threaded connections between the specimen and the bars. The geometry of the specimen is usually dog-bone shape or dumbbell shape to achieve uniformly distributed tensile stress at the gage section of the specimen. The initial tensile impulse is applied either by an impact onto the incident bar in the tensile direction from mechanisms such as rotating-disk [66, 76] or by a direct loading onto the incident bar through a striker tube [98, 102]. Torsional Kolsky bar tests usually evaluate specimens in tubular shapes [10]. The initial torsional impulse is generated by a torquing device and an associated clamp to suddenly release the restored energy.

Based on measurements from strain gages and known properties of the bar materials, the stress and strain history of the specimen can be derived if the stress and strain are assumed to be uniformly distributed in the gage section of the specimen.

The stress in the incident bar and in the transmission bar are determined by the following equations based on the assumption that the bars remain linear elastic during the test:

$$\sigma_1 = E_b \left(\varepsilon_I + \varepsilon_R\right) \tag{21}$$

$$\sigma_2 = E_b \varepsilon_T \tag{22}$$

where E_b is the elastic modulus of the bars as mentioned before.

The normal forces at the two contacting surfaces between bars and the specimen are

$$P_1 = \sigma_1 A_b = E_b \left(\varepsilon_I + \varepsilon_R\right) A_b \tag{23}$$

$$P_2 = \sigma_2 A_b = E_b \varepsilon_T A_b \tag{24}$$

To ensure that the test results are valid, dynamic stress equilibrium should be achieved during the time of interest. For stress equilibrium, the criterion is

$$P_1 = P_2 \tag{25}$$

which implies that

$$\varepsilon_I + \varepsilon_R = \varepsilon_T \tag{26}$$

At this condition of stress equilibrium, the magnitude of the force applied onto the specimen equals to the same magnitude of P_1 and P_2. Therefore, the nominal stress of the specimen can be determined by the following equation:

$$s_s = \frac{P_2}{A_s} = \frac{E_b A_b}{A_s} \varepsilon_T \tag{27}$$

To obtain stress-strain relation, the strain is also derived from the test results. Based on the strain gage measurements, the particle velocities at the two interfaces between the specimen and the bars are calculated as

$$v_1 = c_b \left(\varepsilon_I - \varepsilon_R\right) \tag{28}$$

$$v_2 = c_b \varepsilon_T \tag{29}$$

where c_b is the stress wave velocity in the bars.

Then the average nominal strain rate of the specimen is determined as

$$\dot{e}_s = \frac{v_1 - v_2}{l_0} = \frac{c_b}{l_0}\left(\varepsilon_I - \varepsilon_R - \varepsilon_T\right) \tag{30}$$

Under the condition of stress equilibrium, substitute Equation 26 into Equation 30, the average nominal strain rate is derived as

$$\dot{e}_s = \frac{c_b}{l_0}\left[\varepsilon_I - \varepsilon_R - (\varepsilon_I + \varepsilon_R)\right] = -\frac{2c_b}{l_0}\varepsilon_R \tag{31}$$

The strain rate $\dot{e}_s$ is a function of time since ε_R is the time history of measured strain of reflected pulse.

$$\dot{e}_s(t) = -\frac{2c_b}{l_0}\varepsilon_R(t) \tag{32}$$

The nominal strain is calculated as the integration of the nominal strain rate.

$$e_s = \int_0^t \dot{e}_s(\tau)d\tau \tag{33}$$

After the nominal stress and strain are obtained from Equation 27 and Equation 33, assigning positive sign to compression, the true stress and strain are derived as

$$\sigma_s = s_s\left(1 - e_s\right) \tag{34}$$

$$\varepsilon_s = -\ln\left(1 - e_s\right) \tag{35}$$

The true strain rate are calculated as the derivative of true strain.

$$\dot{\varepsilon}_s = \frac{\dot{e}_s}{1 - e_s} \tag{36}$$

A critical requirement of a valid Kolsky bar test is the condition of a constant strain rate because the main purpose of the test is to obtain the stress-strain relation under a certain strain rate. Ideally, the strain rate should remain constant during the entire test. This may not be practical for most of the tests because of the limited stiffness of the bars and lack of closed-loop feedback control. However, a constant strain rate during the time of interest can still be achieved by an iterative approach in which the initial trial test is conducted, the results are analyzed, and then the test setup is modified for the next trial

test. Another method to improve the test is pulse shaping techniques. Through iterations of several tests and proper pulse shaping techniques, constant strain rates can be achieved for most of the tests [19].

2.4.2 Other high speed tensile tests

Besides tensile Kolsky bar tests, researchers also developed several other experimental techniques to assess the high-loading-rate responses of materials under tensile force. Generally, the two ends of the tensile specimen in these tests are connected to shuttles which can slide along the longitudinal axis of the specimen. Through specially designed mechanisms, either the two shuttles simultaneously move away from each other at the same velocity or one shuttle is fixed while the other shuttle moves at a certain velocity, elongating the specimen rapidly. As a result, the specimen is subject to a high-loading-rate tensile force. Using proper instruments, the force and deformation of the specimen can be directly measured rather than derived from strain measurements as in Kolsky bar tests. High speed cameras can be utilized to monitor the deformation of the specimen.

One method to apply high-loading-rate tensile force is to modify conventional servo-hydraulic testing machines to achieve higher loading speed. Huh et al. tested steel sheets with a modified servo-hydraulic tensile testing machine [58]. The maximum velocity of the loading grip was 7.8 m/s, and the strain rates of the steel specimens with a width of 6 mm were up to 200 s^{-1}. Sun and Khaleel evaluated the strength of riveted and welding joints using a special servo-hydraulic testing instrument [129]. The maximum velocity of the moving end of the specimen was 8.94 m/s.

Another method to apply high-loading-rate tensile force is to utilize a force inverter mechanism to convert the impact from a striking mass into tensile force. For example, Fatt and Bekar developed a high speed tensile instrument on the basis of a Charpy impact machine [43]. The shuttle at each end of the specimen was connected to a copper cable. The cable was wrapped around a pulley and then attached to a sliding bar, which slided horizontally at a high speed. The two cables and two shuttles formed a symmetric configuration in a plane parallel to the ground. To start the test, the pendulum of a Charpy

impact machine struck onto the sliding bar and provided the initial impact energy. The sliding bar stretched the cables, and the cables drove the shuttles into a high speed. As a result of this mechanism, the specimen was elongated from the two ends symmetrically and simultaneously. This instrument successfully tested styrene butadiene rubber specimens with a section of 6.35 mm × 2.54 mm at strain rates varying from $10\,s^{-1}$ to 1,000s^{-1}.

Mott et al. improved this experimental technique by replacing the Charpy impact pendulum with a drop weight tower [93]. The whole test setup was installed vertically, and the motions of the mechanism occurred in the plane perpendicular to the ground. Two L-shaped levers were installed in a symmetric configuration. The output ends of the two levers were connected to the two ends of the specimen through tensile cables. During the test, the drop weight hit the input ends of the L-shaped levers. The levers rotated around their own pivots and pulled the cables at a high speed. The specimen was then elongated by the two moving cables at the two ends symmetrically. Because of the different lengths of the two legs of the L-shaped lever, the velocity and displacement caused by the drop weight were magnified. Elastomer specimens with a section of 4 mm × 1.5 mm were successfully tested using this system at strain rates up to $588\,s^{-1}$.

High speed tensile tests were also achieved by direct drop-weight method as demonstrated by Kleiner et al. [67]. A weight was attached to the lower side of a tensile specimen while a plunger with a larger diameter was attached to the upper side. The plunger, specimen, and weight fall together accelerated by gravity towards a hole in a rigid barrier. The diameters of the weight and specimen were smaller than the diameter of the hole. Thus, they went through the hole. However, the plunge had a diameter larger than that of the hole. Therefore, the plunge hit the barrier and stopped abruptly. As a result, the specimen was stretched by the dropping weight at the lower side. The displacement of the drop weight was measured by an optoelectronic transducer, and the force and deformation of the specimen were then derived. This method successfully tested aluminum specimens with a section of 3 mm × 2 mm at strain rates up to 2,200 s^{-1}.

CHAPTER III

QUASISTATIC CYCLIC LOADING TESTS OF AN SMA-BASED SEISMIC BRACING SYSTEM

Shape memory alloys have great potential in seismic applications because of their remarkable superelasticity. SMA-based seismic bracing systems, which are capable of both re-centering and dissipating energy, can mitigate the damage caused by earthquakes [30]. Nevertheless, actual applications of SMA-based bracing systems are very limited because of the high cost of SMA materials and the deficient understanding of the behavior of SMA-based systems. This research investigates an innovative seismic bracing system based on an SMA ring. The purpose of the study is to evaluate the responses of SMA rings under quasistatic cyclic loading and to test the system as a proof-of-concept model of SMA-based seismic applications, which are suitable for both new constructions and seismic retrofits.

This SMA-based seismic resisting system is a cross-braced frame consisting of a shape memory alloy ring and four tension-only cable assemblies. The performance of this system is examined through a quasistatic cyclic loading test and finite element analyses. This study also compares the performance of this new system with other SMA-based bracing systems, calibrates a finite element model in Abaqus/Standard on the basis of experimental results, performs a parametric study on the geometry of SMA rings, and presents an idealized estimation of the loading capacity of SMA rings. The results indicate that the seismic performance of this system is promising in terms of resisting force, energy dissipation, damping, and re-centering ability.

3.1 Introduction of SMA-based seismic bracing systems

A large number of welded steel moment resisting frames exhibited unexpected damage in the 1994 Northridge and 1995 Kobe earthquakes [83, 95]. The poor performance of these moment resisting frames resulted in the re-evaluation of other lateral force resisting systems, which can provide new options for seismic design. One of the main viable alternatives

to a moment resisting frame was a braced frame. To obtain higher ductility and energy dissipation, a resisting system with buckling restrained braces (BRB) became a practical option. However, these BRB systems generally had considerable residual deformations after earthquakes since they dissipated most of the seismic energy by plastic responses. These significant residual deformations not only caused structures to be practically unusable before repairing [17] but also increased the repair time and cost after earthquakes [39].

To reduce residual deformations of structures after earthquakes, some researchers inspected the benefits of re-centering braced systems based on SMAs in various configurations [13, 31, 34, 35, 122]. Research interests on experimental and numerical studies on SMA-based re-centering systems have been increased in recent years [41, 42, 121]. The results of these studies revealed that SMA-based braces provided excellent re-centering and energy dissipation abilities. For example, as shown in Figure 12, Speicher et al. [122] developed an SMA-based bracing system composed of SMA wires, articulated quadrilateral (AQ) steel components, and four cable assemblies. One primary merit of this system was that the elements inside the AQ were able to resist both tension and compression while all the elements outside the AQ were tension-only. The system had two configurations with different components installed. One was the AQ-S bracing system as shown in Figure 12(a) with only SMA wires inside the AQ, the other was the AQ-SC bracing system as shown in Figure 12(b) with SMA wires and two C-shape steel dissipaters installed inside the AQ. The performances of these bracing systems were investigated by quasistatic cyclic loading tests. The AQ-S bracing system showed great re-centering ability with a residual story drift of only 0.12% after the test frame was pushed to 3% story drift. The AQ-SC system exhibited higher damping capacity as well as satisfying re-centering capacity with a 0.47% residual story drift after the 3% story drift. As a result, these seismic bracing systems based on SMA wires exhibited satisfying performance.

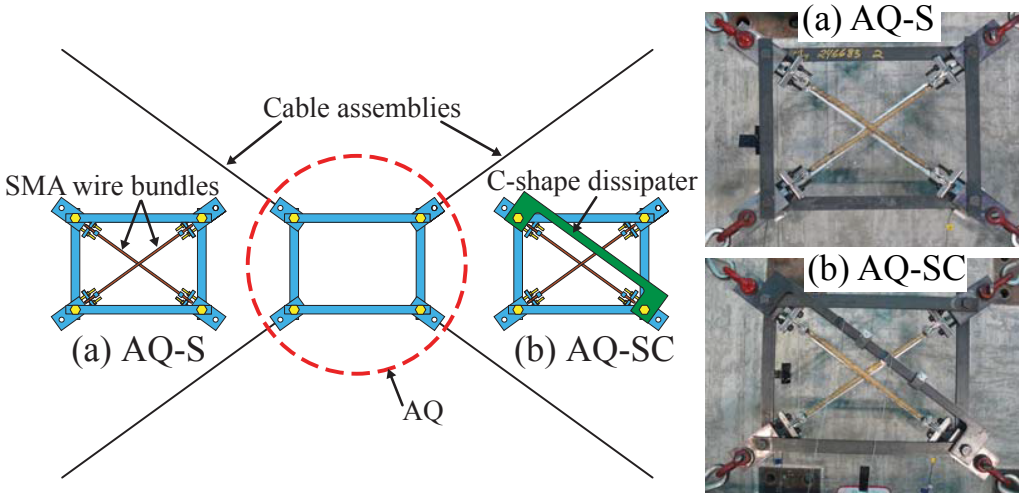

Figure 12: SMA-based AQ bracing system: (a) AQ-S configuration and (b) AQ-SC configuration

3.2 Experimental design

3.2.1 Design of the bracing system

Based on the SMA-based AQ system as shown in Figure 12, the current study replaced the AQ and SMA wire bundles with an SMA ring. As illustrated in Figure 13, the SMA ring was connected to four cable assemblies by custom-made steel connectors. The angle between the two inclined cable assemblies was 72 degrees.

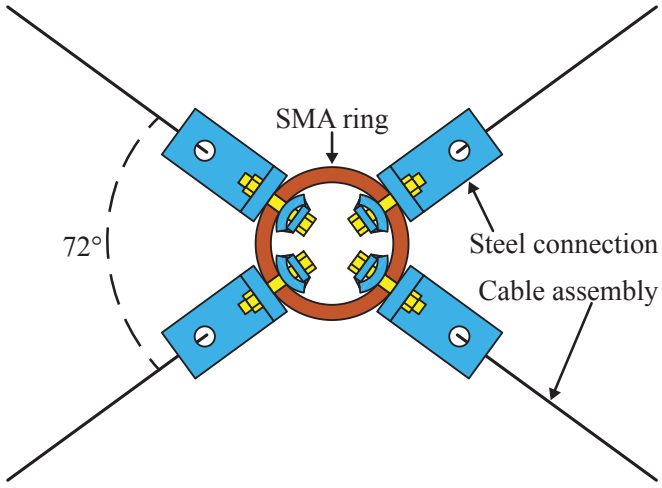

Figure 13: Cross-braced system based on an SMA ring.

As shown in Figure 14, the outer and inner diameters of the SMA ring were 257 mm

and 202 mm, respectively. The thickness of the ring was 57 mm. The SMA ring was manufactured by Nitinol Technology and was made of superelastic NiTi SMA (Alloy 508). First, an initial disk, which was 152 mm in diameter and 64 mm in thickness, was cut from a forged ingot. The disc was then heated to 750°C. After that, a center plug with 76 mm diameter was pushed onto the disk to form the center hole and create an initial rough ring. This rough ring was repeatedly heated to approximately 800°C and gently hammer forged on a cylindrical mandrel to shape it to an outer diameter of roughly 203 to 229 mm. Finally, the ring was reheated and then rolled on a ring rolling machine to achieve the final dimensions. During the entire process of fabrication, proprietary heat treatments were applied to provide optimal superelastic properties.

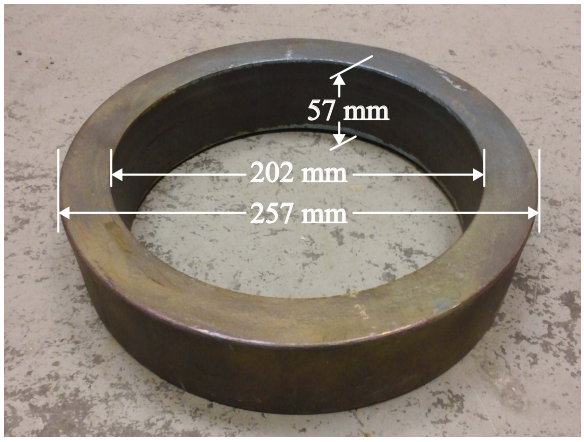

Figure 14: Dimensions of the SMA ring.

To design the steel connections and cable assemblies, the maximum required deformation and force of each component were estimated with a preliminary finite element (FE) simulation using Abaqus/Standard. Since available test results for the ring-shaped SMA specimen were scarce, its mechanical properties were assumed to be similar to the NiTi SMA dog-bone specimens tested by Speicher et al. [124]. Figure 15(a) shows the stress-strain curves of the dog-bone specimens along with the simplified tri-linear stress-strain curve used in this FE simulation. Figure 15(b) shows the simulated results for the force-deformation curve of the SMA ring under monotonic loading.

In this FE simulation, two tensile forces with the same amplitude but opposite directions were applied to the SMA ring. The loading points of these two forces were two end-points

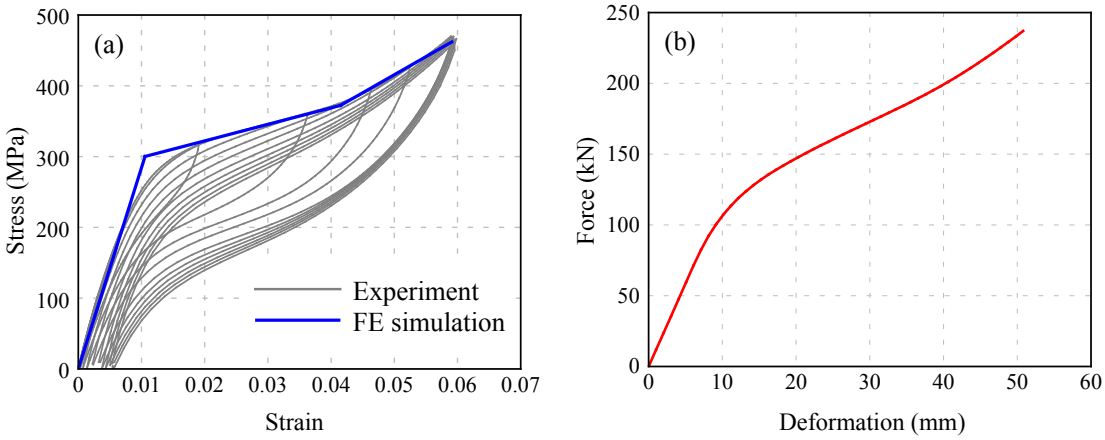

Figure 15: Preliminary FE simulated results: (a) Assumed stress-strain curve of the SMA material based on the experimental results of the SMA dog-bone specimen from Speicher et al. [124] and (b) resulting force-deformation curve of the SMA ring under monotonic loading.

of the inner diameter of the ring, and the deformation in Figure 15(b) was the displacement between these two loading points. The stiffness of the cable assemblies was estimated based on the cross-sectional area and elastic modulus of the cable. After they were connected together, the SMA ring and two cables in one diagonal direction can be treated as springs in series. The estimated maximum deformation in the diametric direction of the ring was approximately 50.0 mm at 3.5% story drift and the corresponding maximum tensile force was 237 kN as obtained from the Abaqus simulation. The drift of 3.5% was the maximum allowable deformation of the external loading frame.

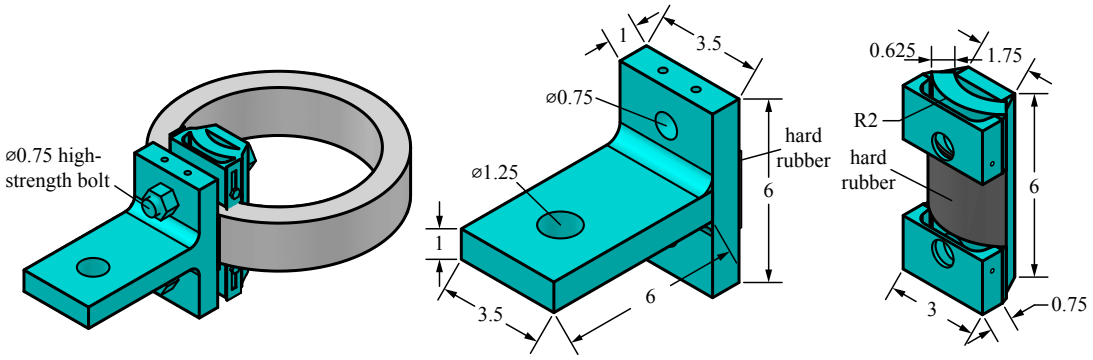

Figure 16: Design of the steel connections (unit: inch).

Based on this estimated maximum force, steel connections were designed and fabricated

to connect the SMA ring to the steel cable assemblies. As shown in Figure 16, each connection consisted of two steel pieces: one T-shaped piece on the outside of the ring and one circular piece on the inside of the ring. These two pieces were made of steel with minimum yield stress of 345 MPa and were connected with high-strength bolts with a minimum yield stress of 896 MPa. The steel pieces and bolts acted together as a clamp and transferred the tensile force from the cable assemblies to the ring.

3.2.2 Experimental setup

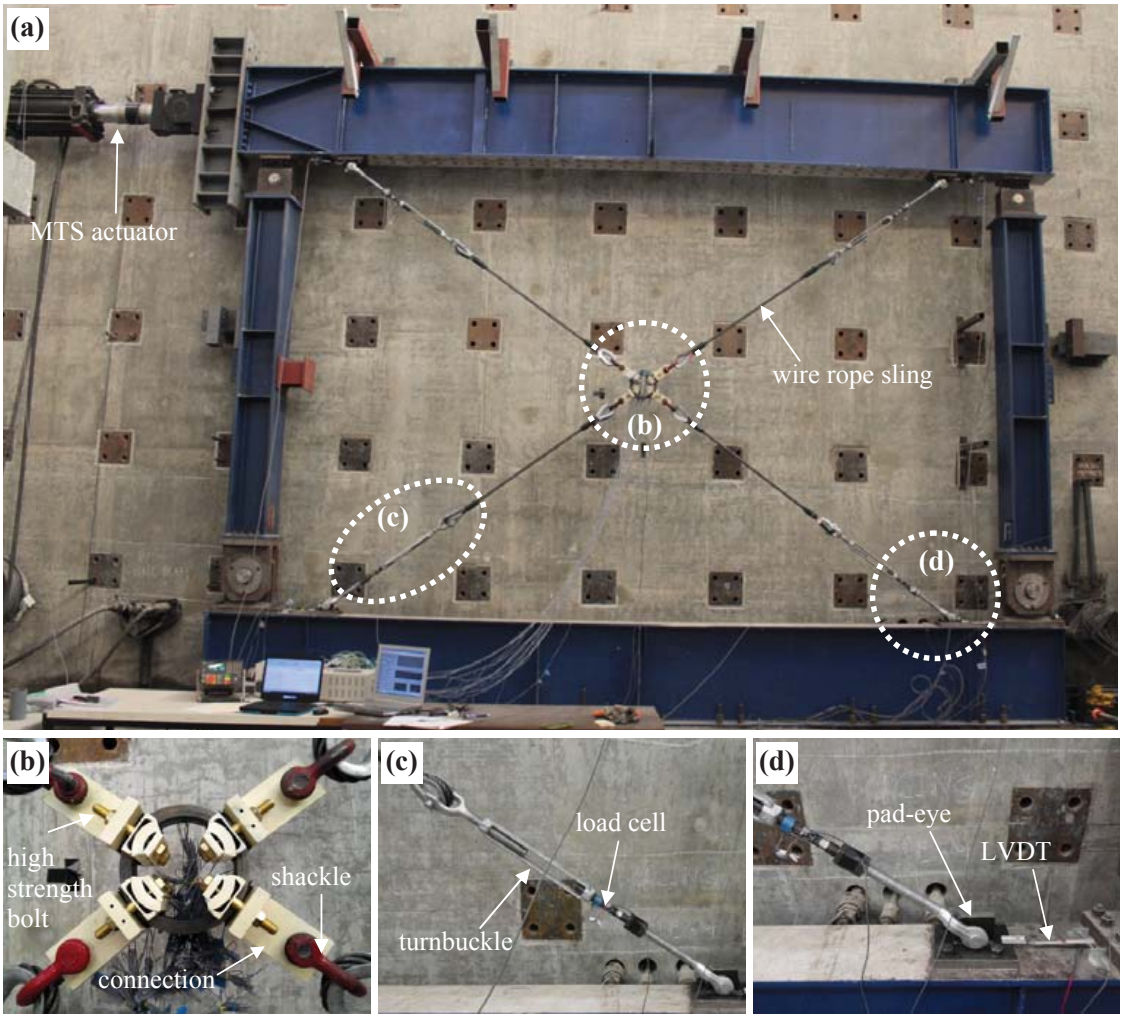

Figure 17: Experimental setup: (a) loading frame, (b) SMA ring and steel connections, (c) turnbuckle and custom-made load cell, and (d) pad-eye connection and LVDT.

Figure 17(a) shows the experimental setup including the existing loading frame [71] and the new cross-braced system built for the current study. The existing loading frame was

a steel portal frame with pins at each corner and had a story height of 4,394 mm. The bottom beam was post-tensioned to the strong floor by Dywidag threaded bars. Lateral braces on the top beam were installed to prevent out-of-plane deformation.

The cross-braced system consisted of an SMA ring in the middle and four cable assemblies connecting the SMA ring to the frame. Each cable assembly was composed of a 28.6 mm (1.125 inch) diameter wire rope sling with a breaking strength of 436 kN and a turnbuckle with a breaking strength of 476 kN. Wire rope thimbles and swage sleeves were installed ar both ends of the wire rope slings to protect the steel wires. Shackles with a breaking strength of 454 kN were used to connect the wire rope slings to the steel connections as shown in Figure 17(b). Custom-made load cells, which were fabricated from 38.1 mm (1.5 inch) diameter threaded rods made of ASTM A193 alloy steel with a yield stress of 720 MPa, were installed between the screw threads and one of the rods of the turnbuckles as shown in Figure 17(c). To construct the load cell, four foil strain gages, which formed a full Wheatstone bridge to monitor the axial forces, were attached to the machine finished surfaces on the lateral sides of the steel threaded rods. Four custom-made steel pad-eyes were bolted to the both ends of the top and bottom beams as shown in Figure 17(d). The cable assemblies were connected to the steel frame with clevis pins through these pad-eyes. The cable assembles were pre-tensioned by manually turning the turnbuckles. Before the actual cyclic loading test, each pair of cable assemblies in the same diagonal direction were installed to the frame and then connected by an additional turnbuckle in the middle to identify the response of the braced frame with only cables installed. The initial lateral stiffness of this cable-only braced frame was 2.4 kN/mm.

An MTS hydraulic actuator with a capacity of 1,000 kN, controlled by a digital MTS 407 controller, was installed between the left end of the top beam and the existing strong wall. The built-in LVDT and load cell of the actuator monitored the lateral displacement and lateral force, respectively. The maximum stroke of the actuator was 173 mm, corresponding to 3.9% story drift. A string potentiometer was installed to the other end of the top beam to verify the measurement of lateral displacement. As shown in Figure 17(d), LVDTs were installed between the pad-eyes and the steel beams to monitor the potential slippage. Two

string potentiometers were bolted to the T-shapes steel connections on the outside of the SMA ring to measure the diametric deformation in two diagonal directions. Foil strain gages were attached to the surface of the ring to measure the strains in the hoop direction. The data acquisition system utilized an NI SCXI platform as the hardware and LabVIEW as the software.

3.2.3 Loading protocol

Seismic performance of structures depended on cumulative damage from previous applied loadings as shown in previous studies [70]. Therefore, the choice of loading protocols affected the effectiveness of evaluation for seismic performance. The cyclic loading protocol in this research was modified from the SAC protocol [110], which originally comprised six cycles of 0.375%, 0.50%, and 0.75% story drift, followed by four cycles of 1% story drift and then two cycles of 1.5%, 2%, 3%, and 4% story drift. As shown in Figure 18, two cycles of 2.5% and 3.5% story drift were added in this research to obtain more valuable information on the hysteretic responses of the SMA-based system. The maximum story drift was selected as 3.5% because of the stroke limitation of the actuator.

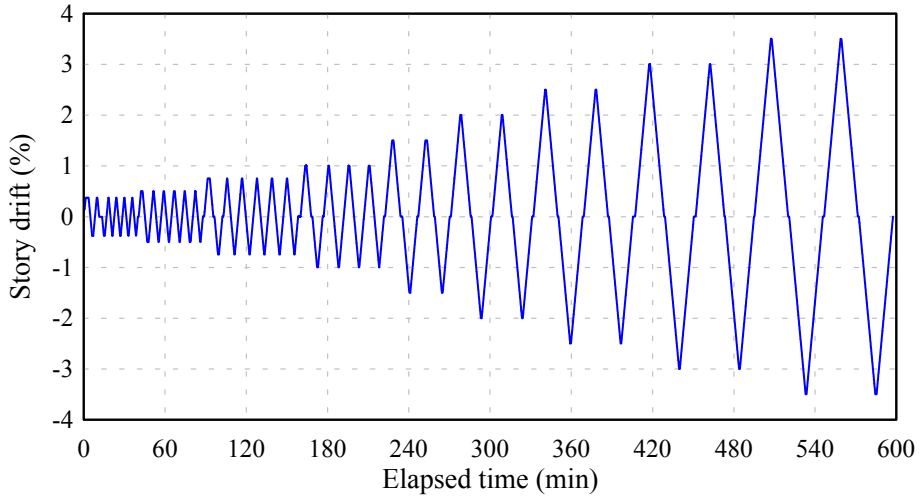

Figure 18: Loading protocol of the cyclic loading test.

Previous research suggested that the strain rates of quasistatic tests of SMAs should not exceed 0.0005 s^{-1} in order to ensure an isothermal condition and minimize temperature effects [116]. Therefore, the constant loading rate of the actuator during the entire cyclic

loading test was selected as 12.7 mm/min (0.5 inch/min), which corresponded to a strain rate of approximately 0.0001 s^{-1} at the SMA ring. The sampling rate of the data acquisition system was set as 1 Hz, which was sufficient for this quasistatic loading test. The test was performed at an ambient temperature of 20 to 21°C.

As mentioned before, this cross-braced system was designed as a tension-only bracing system. Generally, tension-only concentrically braced frames exhibited pinched hysteretic loops during higher story drifts because of the increased slackness of the bracing members after each loading cycle [45]. Therefore, diagonal bracing members were required to be pre-tensioned to minimize the slackness. Before the cyclic loading test, the turnbuckles were tightened to provide appropriate tensile forces to the cable assemblies. After several trial loading cycles of less than 0.375% story drifts, the turnbuckles were tightened again to induce pre-tension forces into the cable assemblies. Since the turnbuckles were manually tightened and the cable assemblies were installed and pre-tensioned in one diagonal direction after the other, the pre-tension forces in these two directions were not identical. To prevent damage of the SMA ring, the pre-tension forces were not applied to an excessive level. From the measurement of cable load cells during the pre-tension process, the pre-tension forces in the two diagonal directions were approximately 20 kN and 11 kN, respectively.

3.3 Discussion of experimental results

3.3.1 Experimental observations

Figure 19 shows photos of the deformed SMA ring under various story drifts. Figure 20(a) shows the force-deformation curve of the SMA ring, cable assemblies, and the system consisted of the SMA ring and the cable assemblies. The tensile force was averaged from measurements of the two load cells in each diagonal direction. The maximum tensile forces in the push (positive, from left to right) and pull (negative, from right to left) direction were 197 kN and 183 kN, respectively. The deformations of the SMA ring in the diagonal directions were directly measured by the two string potentiometers bolted diagonally across the SMA ring. The maximum ring deformations in the push and pull direction were 48 mm

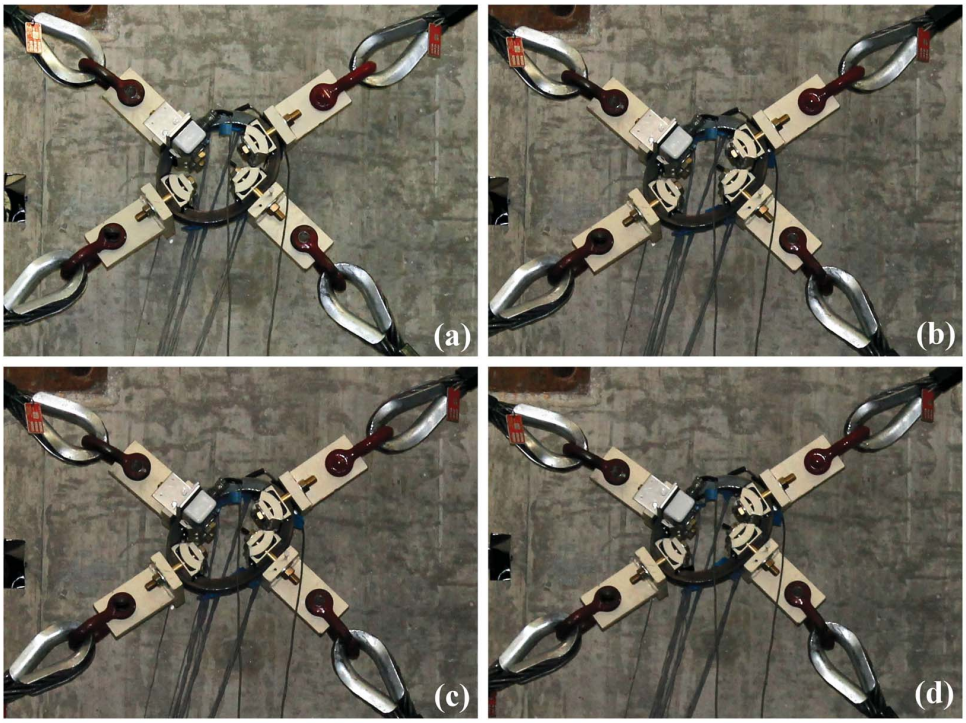

Figure 19: Deformed shape of the SMA ring at various story drifts in the positive direction: (a) 2% story drift, (b) 2.5% story drift, (c) 3% story drift, and (d) 3.5% story drift.

and 44 mm, respectively. The deformation of the system was derived from the frame geometry and the measured lateral displacement of the actuator. The deformation of the cable assemblies was calculated as the deformation of the system minus the deformation of the SMA ring. The slight differences of the peak force and deformation between push and pull directions were mainly caused by the difference in the initial pre-tension forces.

Figure 21 shows the hysteresis curves of the lateral force versus the story drift of the braced system. Since the SMA ring and the two steel cable assemblies in one diagonal direction can be treated as springs in series, the lateral displacement of the frame and associated story drift were divided into separate contributions from the SMA rings and from the cable assemblies. Therefore, the responses and performances of the SMA ring and the cable assemblies can be discussed separately. The experimental results were presented in three categories: SMA ring, cable, and system. The results labeled as *System* in Figure 21(c) were the measured responses of the actual tested braced frame consisting of the SMA ring and cable assemblies. The results labeled as *SMA* in Figure 21(a) were the response of

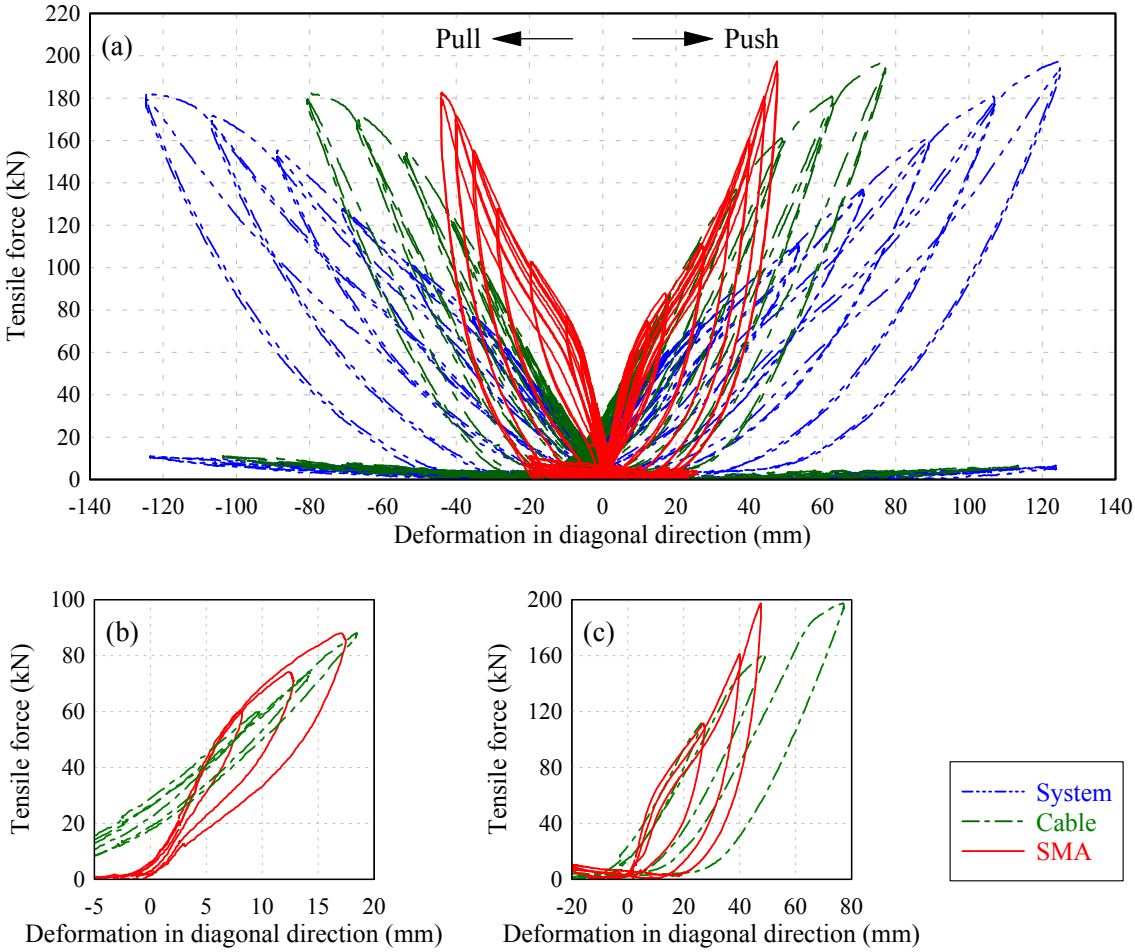

Figure 20: Hysteretic responses of the force-deformation in the diagonal direction: (a) tensile force versus deformation for all cycles, (b) tensile force versus deformation for the first cycles of 0.5%, 0.75%, and 1% story drift, and (c) tensile force versus deformation for the first cycles of 1.5%, 2.5%, and 3.5% story drift.

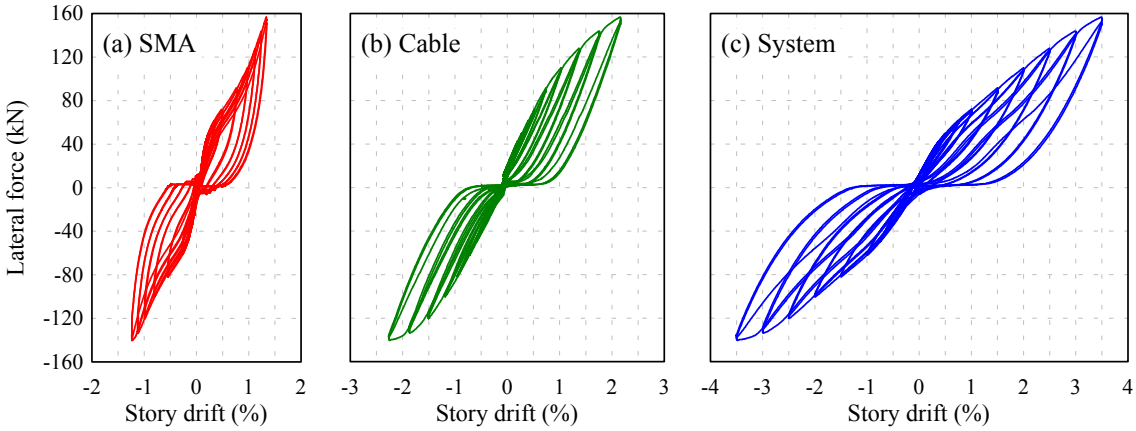

Figure 21: Lateral force versus story drift of sub-components and system.

a fictitious braced frame consisting of the actual SMA ring and fictitious rigid cables instead of the actual deformable steel cable assemblies. Therefore, in this fictitious braced frame, all the possible deformations and energy dissipation occurred in the SMA ring. By the same token, the results labeled as *Cable* in Figure 21(b) were the responses of the fictitious braced frame consisting of actual steel cable assemblies and a fictitious rigid ring instead of the actual deformable SMA ring. The deformation and energy dissipation of this fictitious braced frame were completely determined by the responses of the steel cable assemblies. As shown in Figure 21, at any time, the lateral story drift of the actual frame labeled as *System* always equaled the summation of the story drifts of the two fictitious frames labeled as *SMA* and *Cable*.

As shown in Figure 21(c), the hysteresis loops of the SMA-based system successfully exhibited the characteristics of tension-only re-centering systems. The lateral force and dissipated energy increased for each cycle of increased amplitudes of story drifts, and the residual story drifts were relatively small when the lateral force was around zero between two successive cycles.

Using the hysteretic responses of the actual tested frame and the two fictitious frames, dissipated energy, equivalent damping ratio, and residual story drift for *System*, *SMA*, and *Cable* were calculated. The performance of the actual tested frame, labeled as *System*, was the combination of these two fictitious frames. For example, under the same lateral force, the dissipated energy of *System* were the summation of those of *SMA* and *Cable*, while the equivalent damping ratio of *System* was approximately the average of the damping ratios of *SMA* and *Cable*.

The total input energy was dissipated by the SMA ring and cable assemblies. Energy dissipated by the SMA ring, cable assemblies, and entire system were computed as the area enclosed by the hysteresis curves in Figure 21 for each cycle. Figure 22(a) shows the dissipated energy E_D in the first and second cycles of each drift for the entire system and individual components. At 1% to 2.5% story drift, the SMA ring dissipated more than 60% of the total dissipated energy. This ratio decreased to 52% for the first cycle of 3.5% story drift. This decrease was possibly caused by the increased cable deformation, which

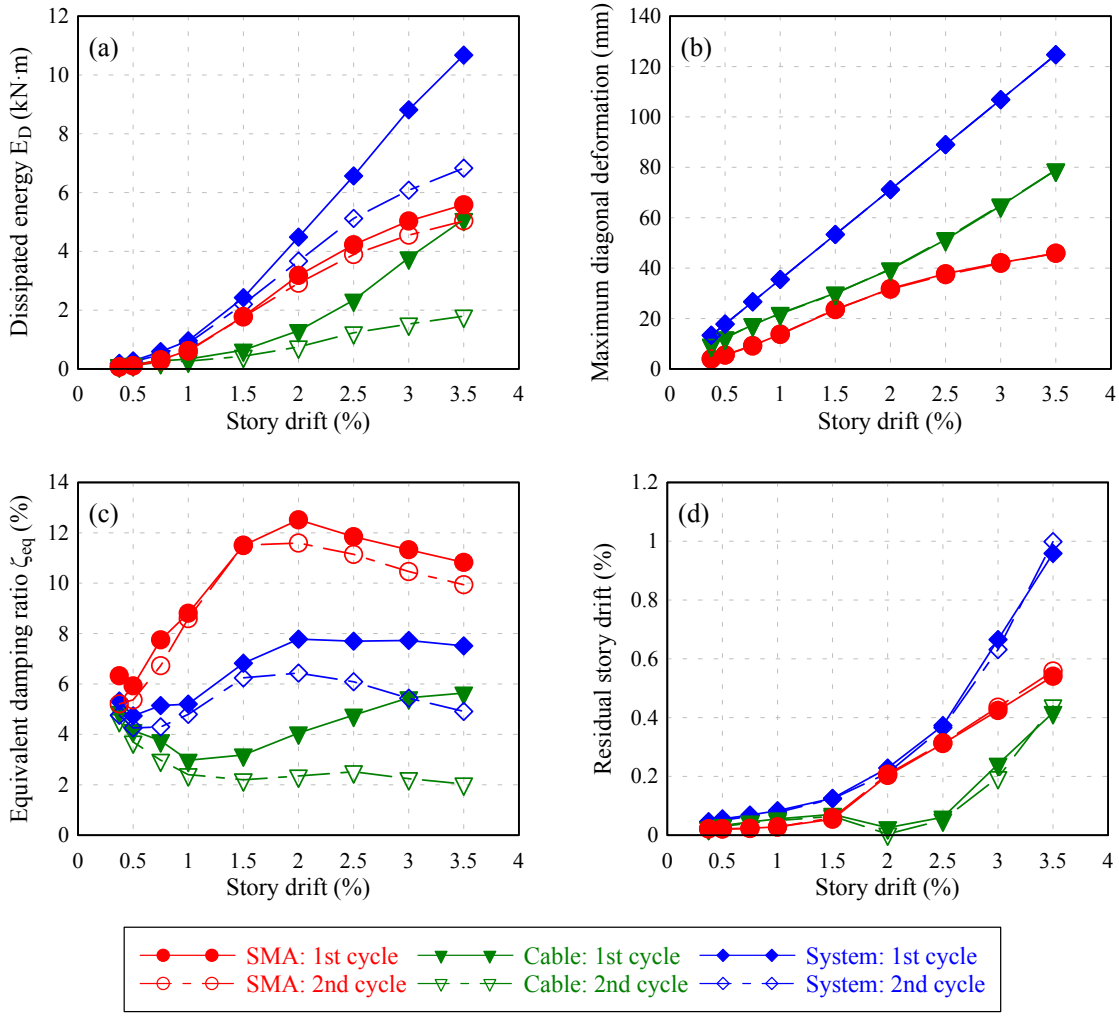

Figure 22: Responses of the 1st and 2nd cycles for each story drift for SMA, Cable, and System: (a) dissipated energy, (b) maximum diagonal deformation, (c) equivalent damping ratio, and (d) residual story drift.

contributed larger portion into the total deformation, as shown in Figure 22(b). Comparison of the dissipated energy between the first and second cycles of the same story drift indicated that the cable assemblies exhibited a dramatic reduction while the SMA ring exhibited a stable performance with slight deterioration. For example, at 3.5% story drift, the dissipated energy of the SMA ring of the second cycle was 10% less than that of the first cycle, while the dissipated energy of the cable assemblies of the second cycle was 65% less than that of the first cycle.

The equivalent damping ratio ζ_{eq} was associated with the ratio of the dissipated energy

to the maximum stored strain energy in each cycle and was calculated as:

$$\zeta_{eq} = \frac{E_D}{4\pi E_{SO}} \tag{37}$$

where E_D was the dissipated energy as defined previously and E_{SO} was the energy absorbed by an equivalent linear system loaded to the same maximum force and displacement. Figure 22(c) shows the calculated equivalent damping ratios for the first and second cycles of each story drift. For the first cycle of 2% story drift, the damping ratios of the entire system and SMA ring reached the peak values of 8% and 13%, respectively. As the story drift increased, a large amount of deformation occurred in the cable assemblies as shown in Figure 22(b). Therefore, at the first cycle of 3.5% story drift, the damping ratios of the system and SMA ring decreased to 7% and 11%, respectively. As shown in Figure 13(c), from the first cycle to the second cycle of the same story drift, the damping ratio of SMA ring decreased by less than 10% while the damping ratio of cable assemblies decreased by approximately 40% to 60%. In terms of damping ratio, SMA ring showed much less deteriorations compared with cable assemblies.

The re-centering ability of this bracing system was assessed by the residual story drift defined as the story drift at zero lateral force. McCormick et al. [86] concluded that a residual story drift larger than 1% was highly possible to cause occupants feel uncomfortable both physiologically and psychologically. Moreover, the repair costs of damaged structures with residual drift larger than 1% were significantly higher than those less than 1%. Figure 22(d) shows the residual story drift of the entire system and its distribution between the SMA ring and cable assemblies. The total residual drifts are 0.1% and 0.4% for story drifts of 1% and 2.5%, respectively. For small story drifts, the residual drifts were mainly caused by the residual deformations in the SMA ring. During large story drifts, the increases of residual drifts were mainly associated with the residual deformations in the cable assemblies around the cable thimbles as the thimbles started to yield. Another reason was that some regions of the SMA ring exceeded the martensite yield strain. The re-centering ability of SMA ring diminished as more regions were subject to excessive large strain beyond martensite yield point. Unlike the energy dissipation and the damping ratio, the residual

story drift was not significantly influenced by the repeated cyclic loading. The re-centering ability can be enhanced by optimizing dimensions of the SMA ring and improving the cable system such as adopting stiffer steel members and more reliable connections.

3.3.2 Comparison with previous SMA-based AQ bracing systems

The experimental results of this bracing system based on an SMA ring were compared with results of the SMA-based AQ-S and AQ-SC bracing systems tested by Speicher et al. [122]. This comparison was performed in terms of the lateral strength, dissipated energy, damping ratio, and residual story drift of the braced systems. This comparison only included the results for the first cycle of each story drift up to 3.0% because the AQ systems were tested up to this story drift.

As shown in Figure 23(a), as the story drift increased, the lateral strength of the SMA ring system almost linearly increased, while the lateral strength of the two AQ systems increased at a slower rate. Since the SMA ring had a larger cross section, the lateral strength of the ring system was the highest over the entire range of story drifts. Figure 23(b) shows that the dissipated energy of the ring system was also the highest. The dissipated energy of the AQ-SC system was higher than AQ-S system because of the additional energy dissipater, but still slightly lower than the ring system.

Figure 23(c) shows the comparison of the equivalent damping ratios of these bracing systems. At story drifts below 0.5%, the damping ratios of these bracing systems were very similar since deformations of SMAs under small story drifts were not sufficiently large to affect the damping ratios. The damping ratio of the SMA ring system dropped at 0.5% story drift and then began to increase. Similarly, for the AQ systems, the damping ratio continued to decrease until 1% story drift, and then started to increase rapidly. From 1% to 2% story drift, the damping ratios of both ring system and AQ systems increased significantly because SMAs began to deform into the phase transformation range. The damping ratios of the ring and the AQ-S system became constant and very similar to each other at story drifts greater than 1.5%, while the damping ratio of the AQ-SC system kept increasing up tp 3%. From 0.5% to 2% drift, the ring system had the largest damping

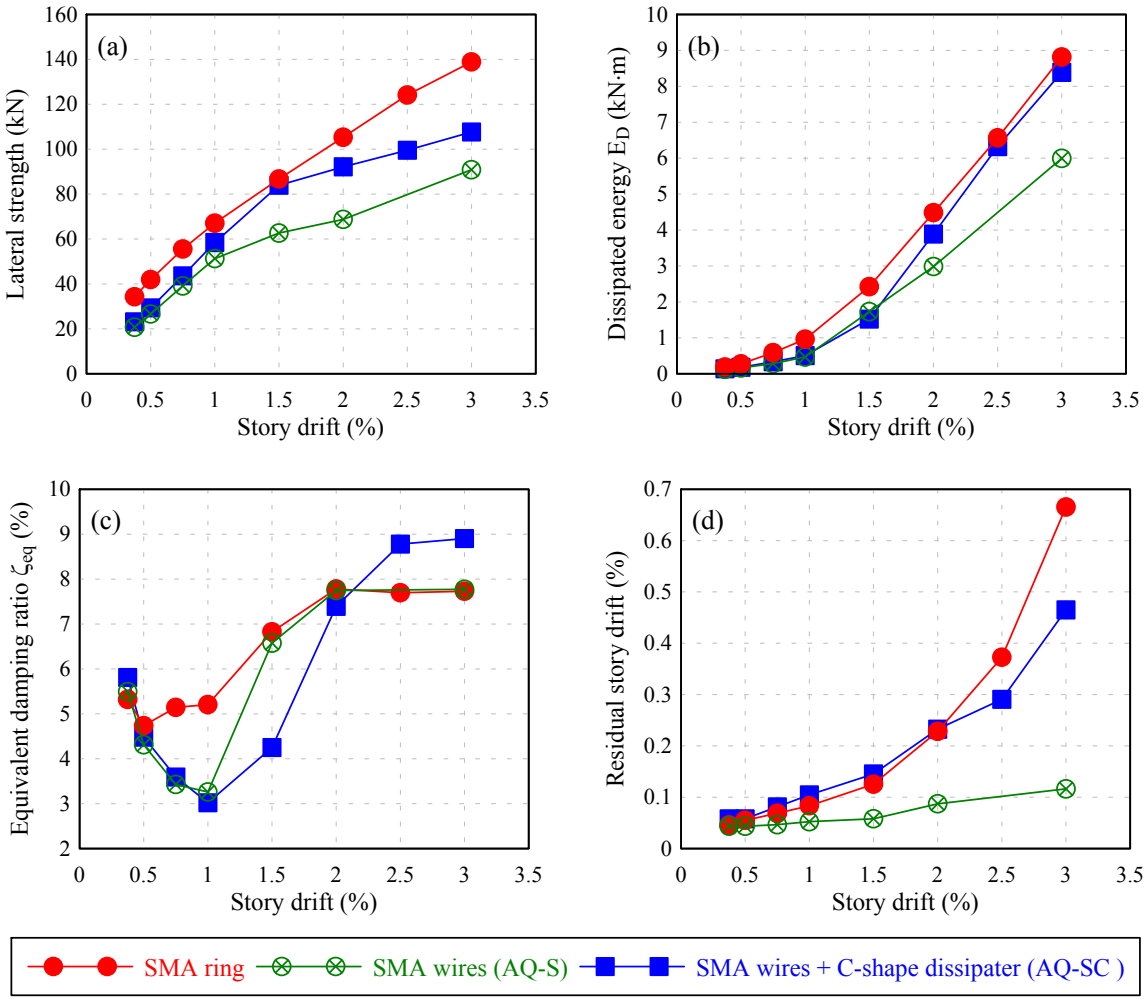

Figure 23: Responses of the first cycles for each story drift of the SMA ring system, the AQ-S system, and the AQ-SC system: (a) lateral strength, (b) dissipated energy, (c) equivalent damping ratio, and (d) residual story drift.

ratio. Beyond 2% story drift, the AQ-SC system had the largest damping ratio because of its additional energy dissipater.

The re-centering abilities of these systems were compared in Figure 23(d). The AQ-S system was the most effective in providing re-centering over the entire range of drifts. At story drifts below 2%, the AQ-SC system had the largest residual story drift because of the permanent deformation of the C-shape steel energy dissipater. At story drifts above 2%, the residual drift of the ring system was the largest because of the increase of slack in the cable assemblies and connections. At the story drift of 3%, the residual story drift in the ring system was approximately 5.7 times of that in the AQ-SC system. Possible

reasons included strain concentrations in the SMA ring caused by its non-prismatic shape and permanent deformations in the cable assemblies of the ring system.

3.4 Finite element simulation of SMA rings under static loading

3.4.1 Modeling methods

To expand the applications of this SMA-based bracing system, an FE model was established to simulate the mechanical properties of SMA rings. The FE model was calibrated on the basis of the experimental results obtained from the quasistatic cyclic loading test. This study adopted Abaqus/Standard to simulate SMA rings under cyclic loading and to perform a parametric study on the size effects the SMA rings. An idealized model was established from the parametric study to estimate the loading and deformation capacity of SMA rings with different sizes. This idealized model provided rough guidelines for the analysis of SMA rings.

This FE simulation applied an Abaqus built-in superelastic material constitutive model based on the Auricchio-Taylor model [8, 9]. The material model was created by a user-defined material (UMAT) subroutine called *ABQ_SUPER_ELASTIC_N3D*. This subroutine defined the material properties by 15 parameters, including elastic modulus and Poisson's ratios for both austenite and martensite phases, transformation strain, and stress values when phase transformations start and finish.

Since linear elements generally provided more robust solutions for very large deformations, this study adopted 8-node linear brick elements rather than 20-node quadratic brick elements. Element type *C3D8I* with incompatible modes was selected because the incompatible modes can alleviate the fictitious increase in stiffness associated with potential shear locking of the elements.

The SMA ring was modeled as a three-dimensional deformable solid body. Because of the relatively high stiffness of steel material compared with the SMA material, the steel connections inside the ring were simplified as analytical rigid bodies, which applied the external force to the SMA ring with a displacement-controlled procedure. The input displacement

history on the analytical rigid bodies was extracted from the experimental measured results. Since contact regions of the steel connections were cylindrical surfaces covered with hard rubber pads as shown in Figure 16, the contact property between the connections and SMA ring was simplified as a non-frictional surface contact. No additional constraint was modeled between the connections and the SMA ring. As a result, the steel connections inside the SMA ring can only push the ring outwards but not pull the SMA ring inwards, matching the tension-only bracing system during the experiments. The steel connections in the two diagonal directions moved cyclically in one direction and then the other following the sequences of the experiments.

Figure 24 shows the mesh of the SMA ring, which was locally refined for regions that underwent high strain during cyclic loading tests. These refined regions included the regions near the steel connections and the regions near the cross sections perpendicular to the directions of tensile forces. The refined regions were meshed with an element size of approximately 2.5 mm. To increase computational efficiency, regions not subjected to high strain were divided into a relatively coarse mesh. The total number of the elements for the SMA ring was 8,960.

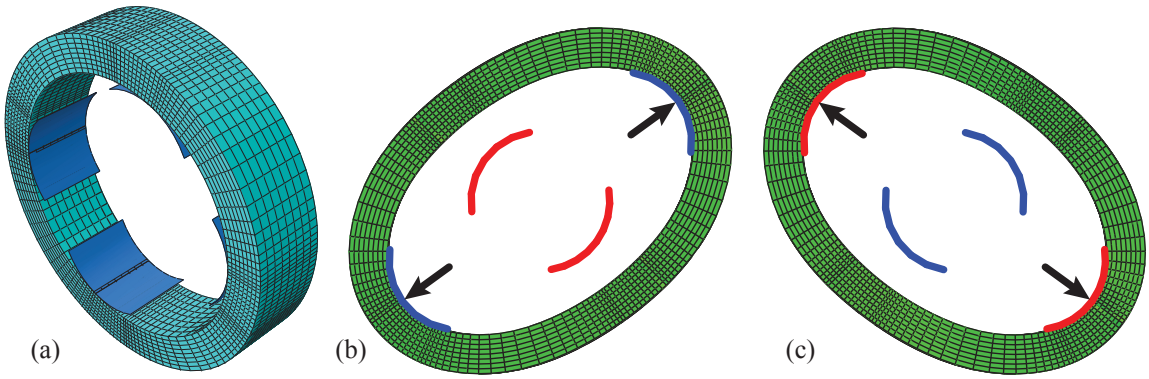

Figure 24: FE model of the SMA ring: (a) FE mesh, (b) applying tensile force in the forward slash diagonal direction, and (c) applying tensile force in the backward slash diagonal direction.

3.4.2 Validation of the simulated results

Input parameters of the material model used in the FE simulation are listed in Table 2. These parameters were determined by a trial-and-error method such that the simulated

force-deformation curves correlated with the experimental results within acceptable tolerances. The modulus, critical stress values, and Poisson's ratio in these parameters were in the same order as the parameters in previous studies [40, 111]. Since the current study focused mainly on superelastic behavior of the SMA ring rather than temperature-related behavior, the parameters related to temperature had minimal effects on the simulated results. These temperature-related parameters in Table 2 were adopted from previous studies [23, 68]. Because of different micro behaviors under monotonic tension and compression loadings, NiTi SMAs generally exhibited asymmetric stress-strain relations between tension and compression [80]. This asymmetric behavior became more complex for SMA components under bending [90]. For simplicity, the current study assumed a symmetric stress-strain relation between tension and compression.

Table 2: Input parameters of SMA material model in FE simulation.

Modeling parameter	Symbol	Value	Units
Modulus of elasticity for austenite	E_A	22,753	MPa
Poisson's ratio for austenite	ν_A	0.33	
Modulus of elasticity for martensite	E_M	42,748	MPa
Poisson's ratio for martensite	ν_M	0.33	
Transformation strain	ε_l	0.046	
$\frac{\delta\sigma}{\delta T}$ during loading	$\left(\frac{\delta\sigma}{\delta T}\right)_L$	6.7	MPa/°C
Stress at the start of phase transformation during loading	σ_{Ms}	124	MPa
Stress at the finish of phase transformation during loading	σ_{Mf}	359	MPa
Reference temperature	T_0	0	°C
$\frac{\delta\sigma}{\delta T}$ during unloading	$\left(\frac{\delta\sigma}{\delta T}\right)_U$	6.7	MPa/°C
Stress at the start of phase transformation during unloading	σ_{As}	48	MPa
Stress at the finish of phase transformation during unloading	σ_{Af}	1	MPa
Stress asymmetry at start of transformation during loading in compression	$\sigma_{CL,s}$	0	MPa
Volumetric transformation strain	ε_l^V	0	
Number of annealings to be performed during the simulation	N_A	0	

Figure 25(a) shows the stress-strain relation of the SMA material in FE simulations labeled with critical points related to phase transformations as shown in Figure 8. Figure 25(b) shows the comparison of the experimental and simulated force-deformation curves of the SMA ring under cyclic load. The simulated peak force results matched the experimental results within 3% differences during both the elastic range and the phase transformation range from austenite to martensite. For example, the differences between the simulated and experimental peak forces at 2.5%, 3.0%, and 3.5% story drifts were 0.8%, 2.5%, and 1.2%, respectively. After some regions of the SMA ring reached the AM_f point as defined in Figure 25(a), the simulated results started to slightly deviate from the experimental results. This deviation was possibly caused by the diminishing of re-centering ability of the SMA ring in experimental results. Another possible reason was that the input martensite elastic modulus, E_M, was a compromise between the reasonable fits of the loading segment before the AM_s point and the unloading segment after the AM_f point since E_M influenced both of these two segments. This idealized material model assumed a perfect superelastic relation. As a result, the FE simulation was not able to account for residual deformations and deteriorations between cycles. Because of this limitation, the unloading segments of the simulated results and experimental results did not match closely.

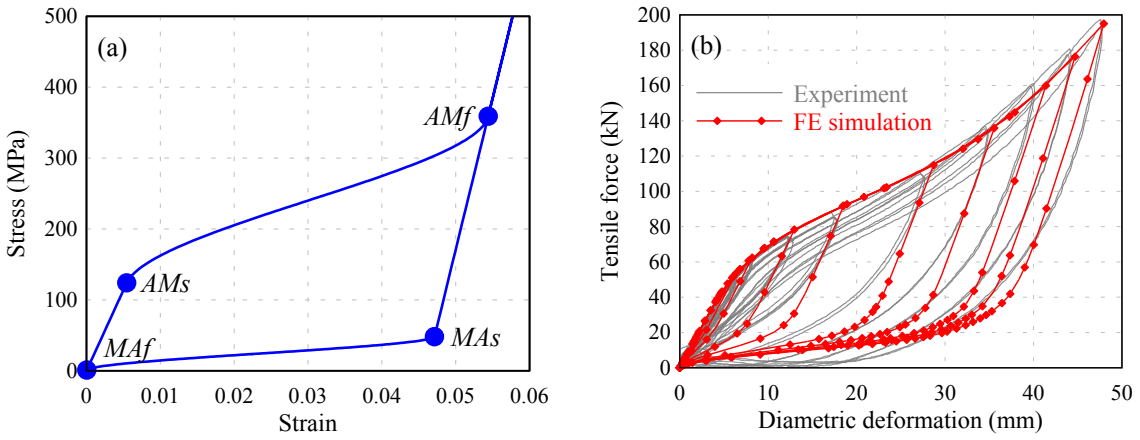

Figure 25: FE simulated results in Abaqus: (a) stress-strain curve of the SMA material and (b) comparison of the simulated and the experimental force-deformation curves.

Figure 26 shows the von Mises stress of the SMA ring under 1.5%, 2.5%, and 3.5% story drift. The stress contour was illustrated based on critical stress values of phase

transformations, Therefore, the stress contour identified the phase status of each location. Unlike SMA bars or wires that had nearly uniform stress distributions along the sections, the SMA ring had significant stress concentrations at certain regions. For example, in Figure 26(a), the von Mises stress at the contact locations between the SMA ring and the steel connections was higher than 359 MPa (σ_{Mf}), indicating that these regions already transformed into the martensite phase. In contrast, the von Mises stress at rest of the locations was below 359 MPa. As shown in Figure 26(b), at 2.5% story drift, the stress at the inner edge of the cross section perpendicular to the tensile force exceeded 359 MPa, and the peak stress of the SMA ring was higher than 800 MPa corresponding to a strain of 0.065. Figure 26(c) shows that the volume of the regions with stress values higher than 359 MPa increased as the story drift increased. Nevertheless, the stress at most regions of the ring was still between 124 MPa (σ_{Ms}) and 359 MPa (σ_{Mf}), indicating that majority materials of the ring was still during phase transformation between AM_s and AM_f.

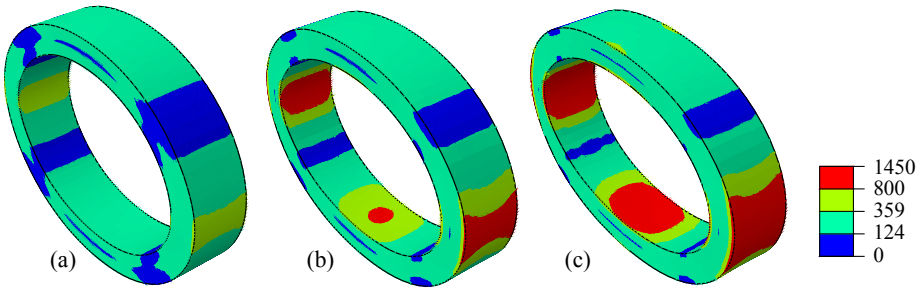

Figure 26: Von Mises stress of the SMA ring for (a) 1.5% story drift, (b) 2.5% story drift, and (c) 3.5% story drift (unit: MPa).

Since the deformation of the SMA ring was symmetric under the tensile forces applied from the steel connections in one direction, a quarter of the ring was taken as a free body to identify the stress distribution as illustrated in Figure 27(a). The cross section A was perpendicular to the tensile forces, and the cross section B was parallel to the tensile forces. Both sections exhibited stress concentrations towards the edges. Figure 27(b) depicts the axial stress distribution along section A. The inner edge was in compression, while the outer edge was in tension with a high concentration. The total resultant axial force was 95.6 kN, which was balanced by half of the peak tensile force in Figure 25(b). The axial

stress distribution along the section B is shown in Figure 27(c). The total resultant axial force was 26.6 kN, which was balanced by the vertical component of the contact force from the steel connection. Although this total resultant force was small, the stress near the edges was still high caused by stress concentration.

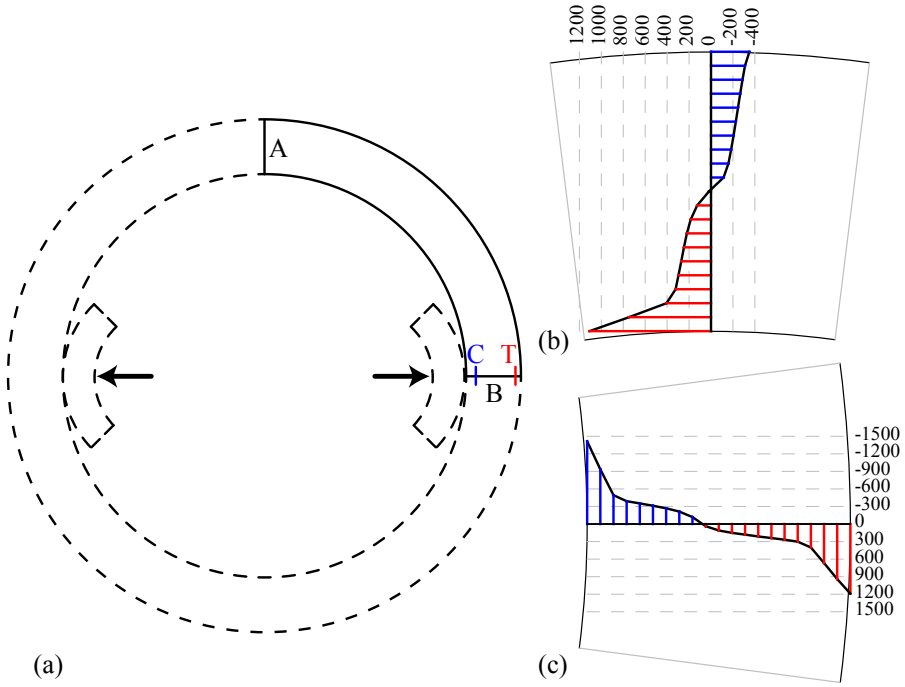

Figure 27: Stress distribution of the SMA ring at 3.5% story drift: (a) locations of sections and points, (b) axial stress distribution along section A, and (c) axial stress distribution along section B (unit: MPa).

Figure 28 shows the experimental strains measured from strain gages and the FE simulated strains at points C and T as indicated in Figure 27(a). Since the strain gages have a maximum measurable strain of 5%, the valid experimental strain results were limited to small story drifts. As shown in Figure 28(a), the FE simulated results for point C fit the experimental results within 5% difference for the loading segment up to 1% story drift. After that, the experimental results exhibited residual strains after each cycle, and the FE simulated results began to deviate from the experimental results. Figure 28(b) shows the comparison of the experimental and simulated strain results at point T. Since the strain gage failed at around 0.75% story drift, the FE results were only compared with the experimental results at 0.375% and 0.5% story drift.

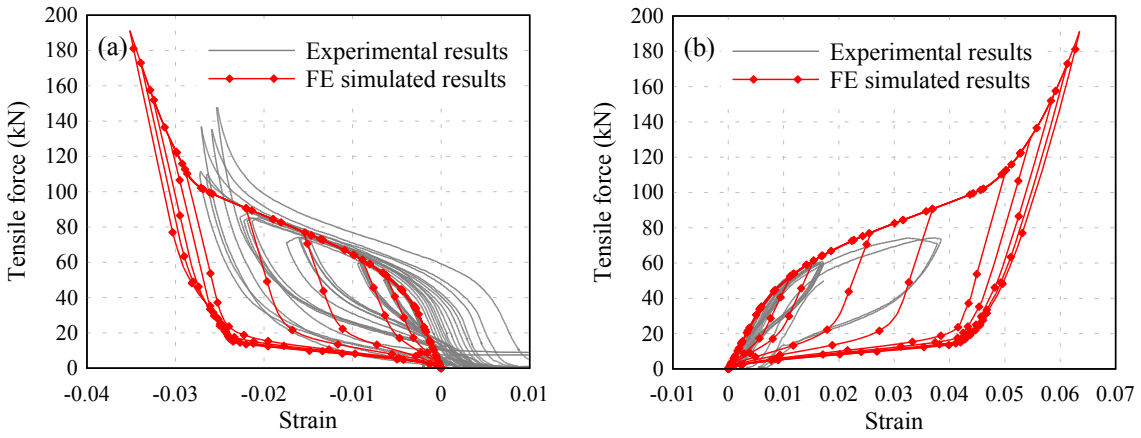

Figure 28: Comparison of the simulated and experimental force-strain curves.

The gage length of the strain gages in this study was 0.3 mm, which was one of the smallest in common strain gages for structural tests. Since the strain gages measured the average strain over the entire gage length, these average values may not represent the real strain distribution at regions subject to large strain gradients. Because of stress concentration, the strain gradient near the edge of the ring was large. As a result, the experimental measurements from strain gages were compromised. This partly explained the difference between FE simulated results and experimental results.

In conclusion, the simulated force-deformation results of the SMA ring matched the experimental results within 5% tolerance under loading. The FE simulated stress results balanced the measured tensile force and satisfied the equilibrium requirement. The FE simulated strain results were verified by measurements from strain gages at small story drifts. This FE model was able to estimate the performance of SMA rings under cyclic loading. However, the FE simulated results under unloading did not perfectly capture the residual deformation observed in the experiment. This limitation was because of the simplifications of material models in FE simulations.

3.4.3 Simplified loading curves for SMA rings

Based on the FE simulations discussed above, a parametric study was conducted to investigate the relation between the performance and the geometric sizes of SMA rings. The geometry of SMA rings was defined by three independent variables as shown in Figure 29:

width of the cross section (B), height of the cross section (T), and the outer diameter (OD).

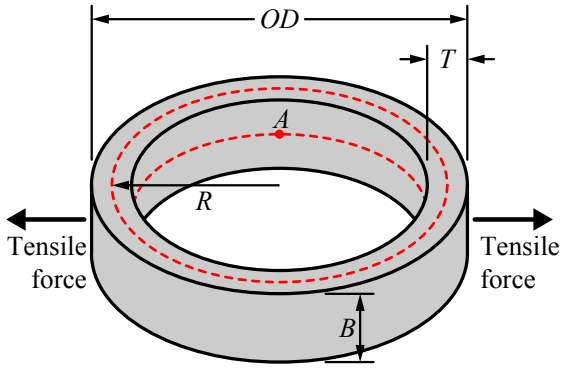

Figure 29: Design variables of SMA rings.

The reference values of these variables were selected as $B = 57.0\,\text{mm}$, $T = 27.5\,\text{mm}$, and $OD = 257.0\,\text{mm}$, which were the dimensions of the SMA ring in the experimental test.

The radius to the centroid of the cross section was calculated as

$$R = \frac{1}{2}(OD - T) \tag{38}$$

The total volume of the ring was calculated as

$$V = 2\pi RTB \tag{39}$$

In this parametric study, the values of these three variables, B, T, and OD, changed gradually around the reference values. Five values for width, B, were selected as 25.4 mm, 38.1 mm, 50.8 mm, 63.5 mm, and 76.2 mm; five values for height, T, were selected as 12.7 mm, 19.1 mm, 25.4 mm, 31.8 mm, and 38.1 mm; five values for outer diameter, OD, were selected as 203.2 mm, 228.6 mm, 254.0 mm, 279.4 mm, and 304.8 mm. As a result, a total of 125 cases with different ring dimensions were investigated in this study. For each ring, the radius of the rigid surface representing the steel connection inside the ring was chose as half of the inner radius of the ring.

The maximum principle strain ε_{max} at point A, which was at the middle of the inner edge of the cross section perpendicular to the direction of the external tensile forces as shown in Figure 29, was selected as the criterion to compare the performance of different cases. Each case was loaded monotonically until ε_{max} reached 0.1.

The stress-strain relation under monotonic loading was divided into three segments as shown in Figure 8: the austenite segment before AM_s, the transition segment between AM_s and AM_f, and the martensite segment after AM_f. Therefore, for simplicity, the nonlinear force-deformation relation of the ring was idealized as three linear segments. The goal of this idealization was to represent the nonlinear force-deformation relation by an simplified tri-linear relation as closely as possible.

The first method to idealize the nonlinear loading curves into tri-linear curves was to find the tri-linear curves with the least square errors. For example, for three randomly chosen cases, Figure 30 shows the FE simulated loading curves as solid lines with the asterisk markers corresponding to ε_{max} from 0.01 to 0.1 with an increment of 0.01. Figure 30 also plots the tri-linear simplified curves with the least square errors plotted as red dashed lines. The ending points of each loading curve were arbitrarily chosen as ε_{max} equals 0.1, and the results of these idealizations were affected by the choice of this ending point. If the criterion of the ending points was changed, the idealized results also changed since the points defining the idealized curves were completely derived from curve fitting without any clearly defined physical meanings.

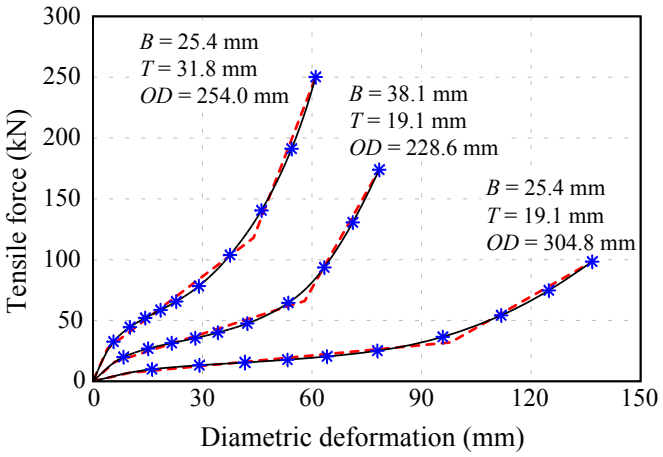

Figure 30: Examples of tri-linear idealization defined by least square errors.

The second method of idealization was to define the tri-linear curves by several critical points corresponding to certain ε_{max} values. The first turning point on a tri-linear idealized curve in Figure 30 was close to the point corresponding to ε_{max} equals 0.01 on the

comparable simulated curve. Similarly, the second and third points on a tri-linear idealized curve were close to the points corresponding to ε_{max} equals 0.07 and 0.10 on the comparable simulated curves, respectively.

The tri-linear curves were then simplified as straight lines connecting the points corresponding to ε_{max} equals 0, 0.01, 0.07, and 0.10. Figure 31 shows the idealized loading curves of three randomly chosen cases using this method. The results for the first and second segments fitted closely with the FE simulated results. The results for the third segment overestimated the tensile force.

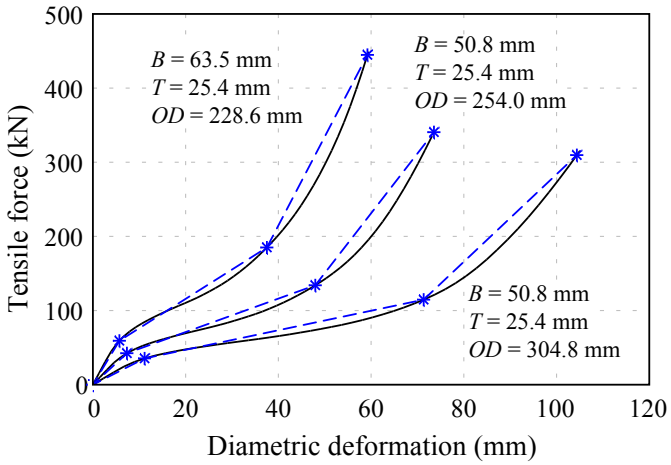

Figure 31: Examples of tri-linear idealizations defined by points corresponding to certain strain values.

The first idealization method based on least square errors produced results that were numerically closer to the FE simulated results while the second idealization method constructed the idealized loading curves by connecting clearly defined points which were correlated to certain ε_{max} values. The following discussion adopted the second method to investigate the relation between responses and dimensions of SMA rings.

The stiffnesses for the three segments during loading, k_1, k_2, and k_3, were determined as the slopes of the idealized loading curves discussed above. Miller et al. [88] proposed that the stiffness of an elastic ring under tensile forces applied at the two ends of a diameter was proportional to EI/R^3, where E was the elastic modulus of the material and I was the moment of inertia which equaled $BT^3/12$. Since SMA materials had different elastic

moduli for different phases, the elastic modulus of the austenite phase was chosen as the elastic modules value, E, used in the following calculations. The stiffnesses k_1, k_2, and k_3 versus EI/R^3 of each case were plotted in Figure 32.

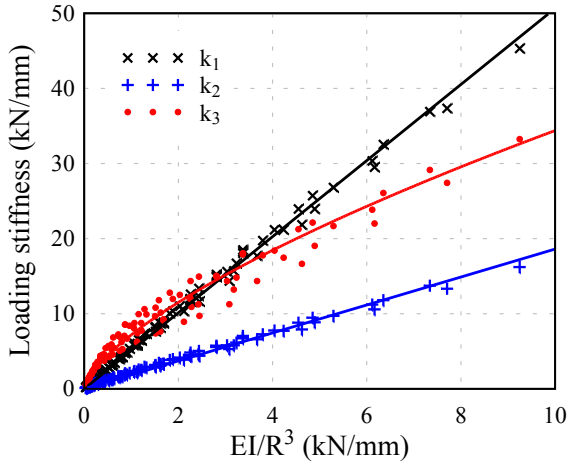

Figure 32: Loading stiffnesses of the three segments.

As shown in Figure 32, the stiffness k_1 and k_2 have linear relations with EI/R^3 . During the first segment, the whole SMA ring was in the austenite phase without any phase transformation. During the second segment, because the transformation from austenite into detwinned martensite started at a relatively low strain, most of the regions of the SMA ring reached that strain and started the phase transformation. As a result, nearly all the regions of the SMA ring were in the transition phase. Therefore, the stiffnesses, k_1 and k_2, were both linear with respect to EI/R^3 because materials of the entire ring behaved similarly. However, the stiffness for the third segment, k_3, was not linear with respect to EI/R^3. The main reason was that the materials from different regions of the ring no longer behave similarly. Because of the high strain caused by stress concentration, only the regions near the steel connections and the cross sections perpendicular to the force directions completed the phase transformation and were already in the martensite phase. The rest regions of the ring were still undergoing phase transformation. Therefore, different regions of the ring exhibited different stress-strain behaviors, and the stiffness of the ring was no longer linear to EI/R^3 .

Numerical expressions for k_1, k_2, and k_3 were established by curve fitting. The stiffnesses

for the first and the second segments of the tri-linear relation, k_1 and k_2, were estimated as linear expressions. The stiffness for the third segment, k_3, was fit into a power function. The coefficients of determination were 0.996, 0.991, and 0.967, respectively.

$$k_1 = 5.065 \left(\frac{EI}{R^3} \right) \tag{40}$$

$$k_2 = 1.867 \left(\frac{EI}{R^3} \right) \tag{41}$$

$$k_3 = 7.220 \left(\frac{EI}{R^3} \frac{1}{\text{kN/mm}} \right)^{0.68} \frac{\text{kN}}{\text{mm}} \tag{42}$$

Miller et al. [88] proposed that the elastic stiffness of a ring was estimated as

$$k = \frac{4\pi}{\pi^2 - 8} \left(\frac{EI}{R^3} \right) = 6.721 \left(\frac{EI}{R^3} \right) \tag{43}$$

which was based on the assumptions that the thickness of the ring, T, is negligible compared with the radius of the ring, R, and the external forces were idealized point loads. Since the thickness of the ring, T, for most of the cases examined in this study was not negligible, and the external forces were applied to the SMA ring through surface contact rather than idealized point loads, the elastic stiffness results obtained from Equation 40 was close but not identical to the estimation obtained from Equation 43.

The diametric deformations, u_1, u_2, and u_3, corresponding to ε_{max} equals 0.01, 0.07, and 0.10, respectively, were found to be linearly correlated to R^2/T as shown in Figure 33. Since the external forces were applied within the plane of the ring, the width of the cross section, B, which was the extrusion out of the plane, had little effect on the deformation. The relation between the deformation and the corresponding strain was geometric and, thus, independent of the elastic modulus, E.

The results of curve fitting for deformations, u_1, u_2, and u_3, were the following equations with coefficients of determination of 0.998, 0.991, and 0.990, respectively.

$$u_1 = 0.0147 \frac{R^2}{T} \tag{44}$$

$$u_2 = 7.29\,\text{mm} + 0.0771 \frac{R^2}{T} \tag{45}$$

$$u_3 = 18.26\,\text{mm} + 0.1037 \frac{R^2}{T} \tag{46}$$

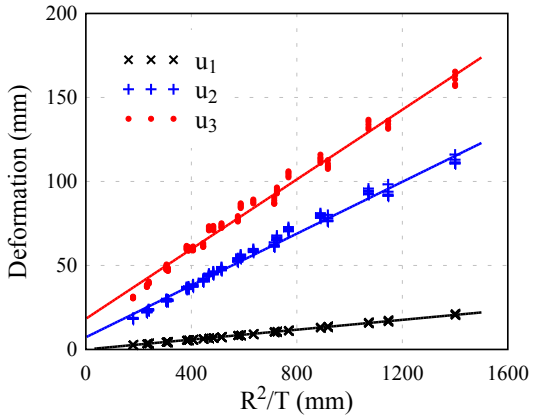

Figure 33: Deformations corresponding to the start and finish of the three segments

For an idealized tri-linear loading curve, the tensile forces, F_1, F_2, and F_3, of turning points corresponding to ε_{max} of 0.01, 0.07, and 0.10, were derived from the stiffnesses and deformations defined above.

$$F_1 = k_1 u_1 \tag{47}$$

$$F_2 = F_1 + k_2(u_2 - u_1) \tag{48}$$

$$F_3 = F_2 + k_3(u_3 - u_2) \tag{49}$$

As a result, the idealized tri-linear loading curve of a SMA ring with given dimensions was fully determined. For example, the dimensions of the SMA ring used in the cyclic loading test were $B = 57.0\,\text{mm}$, $T = 27.5\,\text{mm}$, and $OD = 257.0\,\text{mm}$. The elastic modulus of the austenite phase was $E = 22,753\,\text{MPa}$.

For this SMA ring,

$$R = \frac{1}{2}(OD - T) = \frac{1}{2} \times (257.0 - 27.5) = 114.75\,\text{mm} \tag{50}$$

$$I = \frac{1}{12}BT^3 = \frac{1}{12} \times 57.0 \times 27.5^3 = 98785.16\,\text{mm}^4 \tag{51}$$

$$\frac{EI}{R^3} = \frac{(22,753\,\text{MPa})\left(98785.16\,\text{mm}^4\right)}{(114.75\,\text{mm})^3} = 1.488\,\frac{\text{kN}}{\text{mm}} \tag{52}$$

$$\frac{R^2}{T} = \frac{(114.75\,\text{mm})^2}{(27.5\,\text{mm})} = 478.8\,\text{mm} \tag{53}$$

The stiffnesses for the three segments of the idealized tri-linear relation were calculated

as follows:

$$k_1 = 5.065\frac{EI}{R^3} = 5.065 \times 1.488\,\frac{\text{kN}}{\text{mm}} = 7.537\,\frac{\text{kN}}{\text{mm}} \tag{54}$$

$$k_2 = 1.867\frac{EI}{R^3} = 1.867 \times 1.488\,\frac{\text{kN}}{\text{mm}} = 2.778\,\frac{\text{kN}}{\text{mm}} \tag{55}$$

$$k_3 = 7.220\left(\frac{EI}{R^3}\frac{\text{mm}}{\text{kN}}\right)^{0.68}\,\frac{\text{kN}}{\text{mm}} = 7.220 \times \left(1.488^{0.68}\right)\,\frac{\text{kN}}{\text{mm}} = 9.460\,\frac{\text{kN}}{\text{mm}} \tag{56}$$

The deformations of the two turning points and the end point of the idealized tri-linear relation were calculated as follows:

$$u_1 = 0.0147\frac{R^2}{T} = 0.0147 \times 478.8\,\text{mm} = 7.04\,\text{mm} \tag{57}$$

$$u_2 = 7.29\,\text{mm} + 0.0771\frac{R^2}{T} = 7.29\,\text{mm} + 0.0771 \times 478.8\,\text{mm} = 44.21\,\text{mm} \tag{58}$$

$$u_3 = 18.26\,\text{mm} + 0.1037\frac{R^2}{T} = 18.26\,\text{mm} + 0.1037 \times 478.8\,\text{mm} = 67.91\,\text{mm} \tag{59}$$

The forces of the two turning points and the end point of the idealized tri-linear relation were calculated as follows:

$$F_1 = k_1 u_1 = 7.537 \times 7.04 = 53.06\,\text{kN} \tag{60}$$

$$F_2 = F_1 + k_2(u_2 - u_1) = 53.06 + 2.778 \times (44.21 - 7.04) = 156.32\,\text{kN} \tag{61}$$

$$F_3 = F_2 + k_3(u_3 - u_2) = 156.32 + 9.460 \times (67.91 - 44.21) = 380.52\,\text{kN} \tag{62}$$

Figure 34 shows the idealized tri-linear loading curve of this SMA ring as well as the experimental and FE simulated loading curves. As mentioned before, the maximum diametric deformation of the SMA ring during the experimental test was 47.6 mm. The material stayed within the first and second segments for most of the story drifts and only reached the third segment beyond 3.0% story drift. Therefore, the overestimation of tensile forces in the third segment had little effect on the overall results for this particular ring.

In conclusion, SMA rings with different dimensions were analyzed using the calibrated finite element simulation. Numerical expressions of force and deformation capacities were determined by curve fitting of FE simulated results. The idealized tri-linear expressions of loading curves properly captured the behavior of SMA rings under monotonic loading, especially for the first and second segment when the SMA material was prior to and during

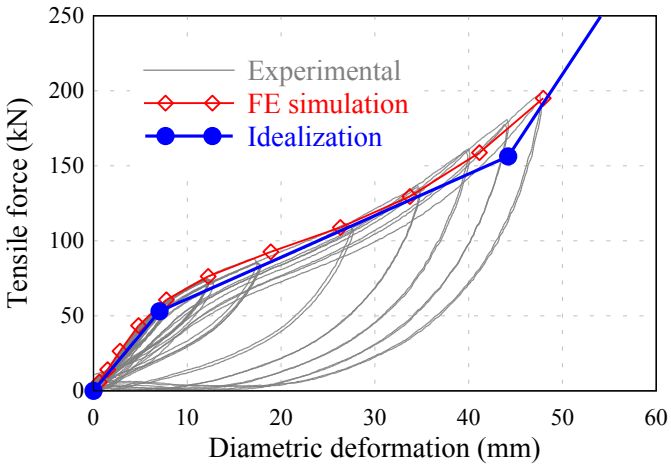

Figure 34: Idealized loading curve for the experimental tested SMA ring.

phase transformation. These idealized tri-linear expressions were suitable for preliminary analysis of SMA rings.

3.5 Summary

In this chapter, a seismic bracing system based on an SMA ring was designed, fabricated, and tested to examine its seismic performances, including resisting strength, energy dissipation, damping, and re-centering ability. The results of the quasistatic cyclic loading test demonstrated that the damping and energy dissipation of the SMA ring system were stable under various story drifts. SMA ring was able to dissipate considerable amount of energy and provide satisfying re-centering ability. The performances of this bracing system were compared with those of two SMA-based systems developed in a previous studies. The comparison of results indicated that the SMA ring system exhibited the highest lateral strength and energy dissipation, which are critical for large scale structural applications. The ring system also showed a reasonable damping ratio. The re-centering ability of the ring system was not as good as previously tested systems. One primarily reason was the yielding of sub-components in the cable assemblies. Another possible reason was the excessive strain in some regions of the SMA ring caused by stress concentration.

An FE model was established in Abaqus/Standard and calibrated on the basis of the

experimental results obtained from the cyclic loading test. In the loading part, the simulated force–deformation relation of the SMA ring matched the experimental results closely within 3% difference in terms of peak force. However, in the unloading part, the FE model did not perfectly capture the residual deformation as observed in the experiment. This was caused by the simplification of perfect superelasticity in the material model used in the FE simulation. The FE simulated stress results were verified by checking the equilibrium to experimental force results, and the FE simulated strain results were verified by comparing with experimental results from strain gages. Based on this FE model, this research also conducted a parametric study on the size effects of SMA rings. Idealized tri-linear expressions of the loading behavior of SMA rings were presented and were compared with experimental and FE simulated results.

In conclusion, this cross-braced seismic resisting system exhibited a promising seismic performance in terms of lateral strength, energy dissipation, damping, and re-centering ability, although improvements were needed. This bracing system was suitable for various structural configurations and design capacities.

CHAPTER IV

DEVELOPMENT OF A NEW HIGH-LOADING-RATE TENSILE TESTING SYSTEM

Since shape memory alloys are strain rate dependent materials, quasistatic testing in Chapter 3 is not sufficient to fully capture the responses of SMA-based specimens under various strain rates. Currently available techniques are able to test large-scale specimens under quasistatic strain rates as shown in Chapter 3 and test small-scale specimens under high strain rates using Kolsky bar tests as introduced in Section 2.4.1. However, experimental techniques for large-scale components under intermediate strain rates are not well established. The responses of an entire structure under high-loading-rate forces caused by blast events can be directly assessed by actual explosive tests, although this testing method is usually time-consuming and expensive [26]. However, the responses of a structural component under blast loading are difficult to test in a controllable and repeatable manner. Therefore, to understand the properties of rate-dependent materials like SMAs, a new experimental technique capable of testing large-scale specimens under intermediate strain rates is required.

The main purpose of this new tensile testing system is to capture the responses of relatively large-scale specimens when loaded in tension under intermediate strain rates. Several design measures are adopted to handle the challenges in developing such a system. The testing system is designed as a general testing method that is capable of testing specimens made of not only SMAs but also other materials. Adaptivity and versatility are among the design requirements of the testing system to ensure that this system is able to accommodate specimens of various materials, shapes, and sizes.

The key component of this system is an inverter mechanism that inverts the impact from a high-speed actuator into high-loading-rate tensile force which is then applied onto specimens. Since most of the high-loading-rate tests happens in a very short period of

time, usually less than 0.1 second, the deformation and force of specimens are monitored by DAQ instruments including high-speed cameras and piezoelectric load cell with adequate sampling rates.

Because the high-loading-rate testing system only has open-looped control, iterations of trial-and-error are needed to conduct successful tests which satisfy certain targets. To understand the characteristics and access the performances of this new high-loading-rate testing system, this research conducts a series of validation tests on aluminum alloy specimens before actually using this system to test SMAs and other rate-dependent materials. Experimental results from these validation tests corroborate that this system is capable of applying high-loading-rate tensile forces onto specimens and deforming the specimens under intermediate strain rates in a controllable and repeatable manner. Responses such as energy and impulse of the specimens are derived based on the time history of deformation and force from the measured data. The relations between the input initial conditions, such as the impact mass, impact velocity, and configuration of the inverter mechanism, and the output results, such loading rate, peak force, peak deformation, and peak energy, are also investigated to provide guidelines for adjusting initial condition for certain targets. These relations help researchers decide how to effectively adjust the input initial conditions for the next trial test if certain testing targets are desired.

This research also includes a finite element (FE) simulation of the new high-loading-rate tensile testing system in Abaqus/Explicit. This FE model is calibrated based on the comparison of simulated results and experimental results. As a result, this FE simulation provides guidelines on adjusting the input initial conditions to meet certain testing targets. This significantly reduces the number of experimental tests that are needed in the trial-and-error iterations.

4.1 Introduction of the high-loading-rate tensile testing system

4.1.1 Rationale

The force and deformation responses of an SMA component can be obtained using traditional servo-hydraulic testing machines as in tests of SMA tension/compression device

conducted by Speicher et al. [122] or using loading frames pushed and pulled by a servo-hydraulic actuator as in the test discussed in Chapter 3. The strain rates obtained in these tests are usually within the range of quasistatic strain rates because of the limitation in loading speed of servo-hydraulic systems. Generally speaking, strain rates in traditional servo-hydraulic testing system are usually below $1\,s^{-1}$.

To achieve higher strain rates, Kolsky bar tests are widely utilized to characterize mechanical properties of materials under high speed loading [44]. As mentioned in Section 2.4.1, the specimens in these tests are generally small disks for compressive tests and small cylinders for tensile tests. The diameters of these specimens are generally 2 to 10 mm for typical metal materials. The time history of the average stress and strain are obtained based on the assumption that the stress and strain are uniformly distributed along the section of the specimens. Because of this limitation, Kolsky bar tests can only obtain the averaged stress-strain relations for prismatic homogeneous material specimens [87]. As a result, the force-deformation relations of non-prismatic structural components are outside the scope of Kolsky bar tests. For example, Kolsky bar tests are not able to evaluate the differences between SMA rings and SMA springs, test a damping device made of multiple materials, or investigate the dynamic strength of bolted or welded connections.

Besides, the strain rates achieved in most Kolsky bar tests are usually above $100\ s^{-1}$ [19]. Such results are quite valuable to the field of mechanical engineering, which focuses on topics such as metalworking and shock-waves. However, typical components in civil engineering usually have larger volumes compared with those in mechanical engineering. Furthermore, most of the scenarios in civil engineering including seismic and blast events do not generate strain rates higher than $100\ s^{-1}$ [51]. As a result, a testing system that can achieve strain rates of 1 to $100\ s^{-1}$, lower than the high strain rates from Kolsky bar tests, is very valuable to the field of civil engineering.

To accomplish this target of intermediate strain rates within 1 to $100\ s^{-1}$, one method is to improve existing servo-hydraulic techniques. Specially modified servo-hydraulic testing machines are able to achieve strain rates higher than $10\ s^{-1}$, and the velocity of the loading grip at the moving end can reach 7 to 9 m/s [58, 129]. However, the peak forces of these

tests are limited to approximately 5 kN. Therefore, the maximum dimensions of specimens are also limited. These systems are ideal for small-scale specimens like metal sheets with thickness of less than 2 mm. Because of the low force capacity, although these modified servo-hydraulic systems can achieve higher loading rates, they are not suitable for large-scale specimens such as rods, bars, and rings in the field of structural engineering.

In this research, an innovative high-loading-rate test system is designed, built, validated, and calibrated to test relatively large-scale specimens under intermediate strain rates ranging from 1 to 100 s^{-1}. With proper instrumentation and competent data acquisition system, responses of specimens under intermediate strain rates are successfully captured by this testing system. Moreover, this system is designed for high-loading-rates tensile tests on not only SMA materials and SMA-based components but also other structural materials and components. For example, this system is capable of testing the pull-out strength of reinforcements in concrete or the tensile welding strength of steel connections.

4.1.2 Overall design concept

The high-loading-rate tensile testing system is composed of five components: a high-speed actuator with its own reaction wall, an impact mass, an inverter mechanism, a specimen assembly, and a reaction wall to anchor the specimen assembly. DAQ instruments, including piezoelectric load cell and high-speed cameras, are also included in the system design.

Figure 35 schematically illustrates the overall design of the testing system. On the far left, a fixed reaction wall is post-tensioned onto the existing strong wall, and the left end of the high-speed actuator is attached to this fixed reaction wall. On the right of the high-speed actuator, the inverter mechanism is installed with its input end facing the high-speed actuator and its output end connected to the specimen assembly. With one end connecting to the inverter mechanism, the other end of the specimen assembly is anchored to a second reaction wall, called the *movable reaction wall*. As the name indicated, the position of this movable reaction wall can be adjusted by an overhead crane to meet different experimental configurations. When a test begins, the high-speed actuator starts accelerating an impact mass to a desired velocity. After that, the high-speed actuator decelerates and detaches

from the impact mass, while the impact mass keeps moving until it strikes into the input end of the inverter mechanism. Through a specially designed motion mechanism, when the input end of the inverter mechanism moves along the direction of the impact, the output end of the inverter mechanism moves in the opposite direction and, thus, stretches the specimen assembly. As a result, the specimen is elongated by a high-loading-rate tensile force. By directly measuring force and deformation of the specimen, the responses of the specimen are acquired.

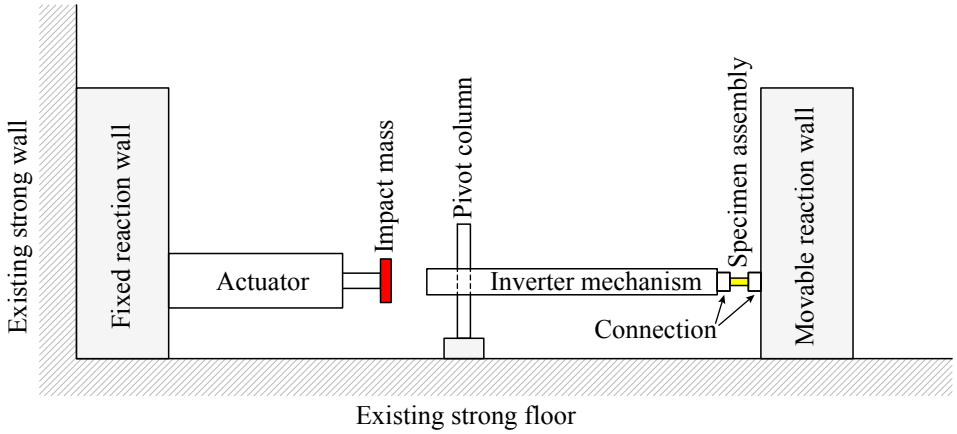

Figure 35: Schematic drawing of the overall design of the high-loading-rate tensile testing system.

4.2 Design challenges and methods

Although high-loading-rate tensile tests are important to evaluate the performances of material specimens and structural components under intermediate strain rates, these tests are not very common in previous research. Possible reasons include that high-loading-rate tensile tests currently do not have well-established standards as quasistatic tests, and they are generally more complicated than quasistatic tests in terms of experimental design and instrumentation. To perform a valid high-loading-rate tensile test, several challenges are required to be addressed properly in the experimental design.

4.2.1 Force inverter mechanism

Because of the tension-compression asymmetry of SMAs as discussed in Section 2.1.6, a comprehensive evaluation of the properties of SMA-based components cannot be achieved

without tensile tests. For quasistatic loading, tensile tests are generally straightforward. In contrast, compressive tests are more complex because they are subject to the risk of specimen buckling. However, for tests in the range of intermediate strain rates, tensile tests are usually more complicated than compressive tests because of the requirement to invert an impact force into a tensile force.

As discussed in Section 2.4.2, high-loading-rate tensile tests require inverter mechanisms to invert impacts into tensile forces. A high-loading-rate compressive test can be conducted by directly striking a mass onto the specimen. However, to conduct a high-loading-rate tensile test, the direction of the impact force has to be inverted so that the specimen is stretched instead of compressed. This can be achieved by using a specially designed force inverter mechanism. For example, in the tensile Kolsky bat tests conducted by Owens and Tippur[102], the impact mass was designed as a hollow cylinder around the incident bar. A flange was added at the input end of the incident bar and the tensile force was achieved by striking the hollow cylinder onto the flange of the incident bar at the direction moving away from the specimen as shown in Figure 36.

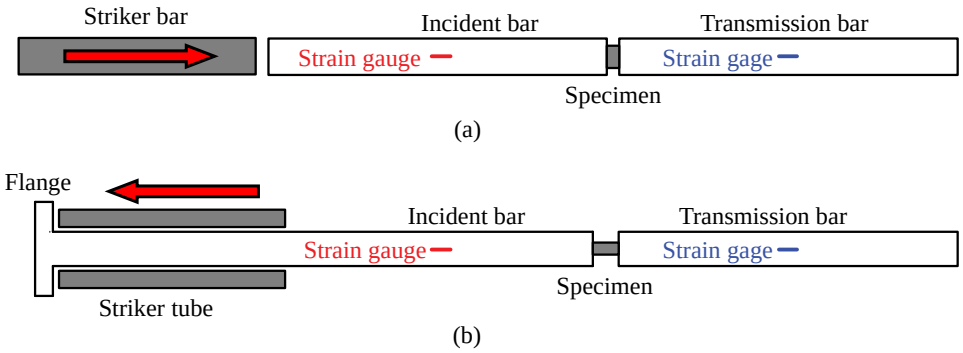

Figure 36: Schematic drawings of two Kolsky testing setups: (a) a typical compressive Kolsky bat test and (b) a tensile Kolsky test from Owens and Tippur[102]

Another example of an inverter mechanism is the two L-shaped levers with a symmetric configuration in the high-loading-rate tensile tests conducted by Mott et al. [93]. This mechanism converted the vertical impact from a drop weight into horizontal motions of loading grips as shown in Figure 37. The drop weight struck onto the L-shaped levers from above and pushed the L-shaped levers to rotate around the pivot point. As a result,

the cables were stretched in tension. With pulleys to transform the moving directions of the cables, the specimen was then elongated in the horizontal direction symmetrically and simultaneously from its two ends.

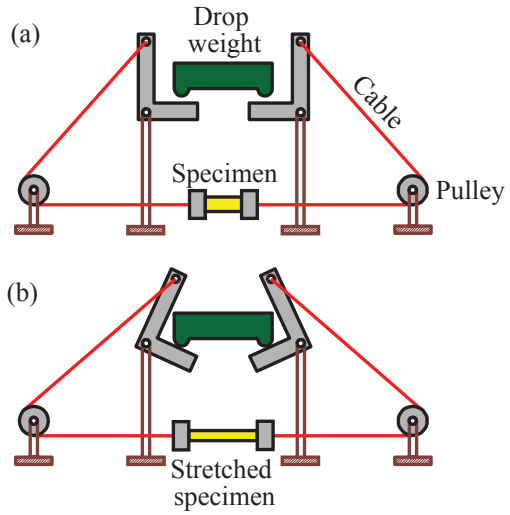

Figure 37: Schematic drawings of the high-loading-rate tensile tests conducted by Mott et al. [93]: (a) initial positions before tests and (b) positions during tests.

This type of inverter mechanism can be represented by a general design as exhibited in Figure 38. A high-loading-rate compressive test is directly performed by striking an impact mass onto the specimen as shown in Figure 38(a). In contrast, as illustrated in Figure 38(b), a high-loading-rate tensile test generally needs a force inverter between the impact mass and the specimen to invert the direction of the impact force. One of the simplest examples of a force inverter is a lever as shown in Figure 38(c). When one end of the lever is pushed downwards by the impact mass, the lever rotates around its pivot pin. As a result, the other end moves upwards, inverting the direction of the force and applying a tensile force onto the specimen.

To achieve higher loading rates from a limited impact mass with a limited striking velocity, the inverter mechanism is preferred to be able to magnify the movement caused by the impact. For a simple lever, this can be achieved by changing the position of the pivot pin and, therefore, changing the ratio between the lengths of the output arm and the input arm. Increasing the output-to-input ratio enlarges the displacement at the output end of the lever for a certain displacement at the input end. However, an inverter mechanism

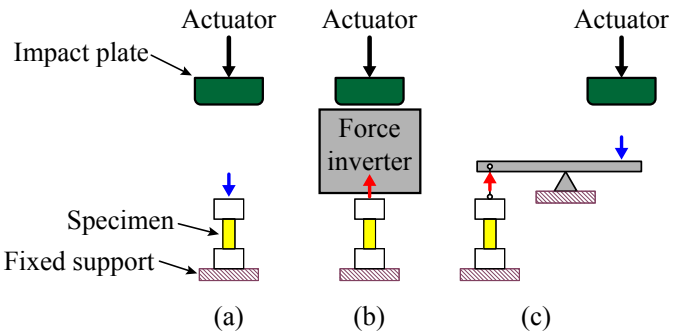

Figure 38: Schematic drawing of the concept of force inverters: (a) compressive test from a direct impact, (b) tensile test using a force inverter, and (c) a simple lever as a force inverter in a tensile test

is also required to have sufficient strength and stiffness to transfer the impact loading. Otherwise the mechanism itself may be deformed or even damaged by the impact force while the specimen is still stay intact. For this simple lever, which can be considered as a beam element, the stiffness of the beam, k, decreases significantly as the length of the output arm, L, increases. This is because the stiffness, k, is directly proportional to EI/L^3, where E is the elastic modulus of the lever material and I is the moment of inertia of the lever section. As a result, within a reasonable range of section sizes, the ability of the lever to magnify movements and the stiffness of the lever cannot be enhanced at the same time.

Another drawback of a simple lever is that the input impact force and the output tensile force are not aligned along the same straight line. As shown in Figure 38(c), the impact generates not only tensile force but also bending moment at the specimen. Although this can be mitigated by special connections such as universal joints, this still causes challenges in the data acquisition and interpolation since the specimens is both stretched and rotated at the same time during the tests.

To overcome these two drawbacks, this research adopted the conceptual design for the inverter mechanism as shown in Figure 39(a). Instead of a single beam as in the lever, the rotating parts in this design were frames with higher strength and stiffness. The output end of each frame was connected to a tensile link by a hinge joint and this tensile link was then connected to the specimen. The entire inverter mechanism, with one frame and one tensile link on each side, was symmetric to the axis which connected the center of the impacting

mass and the center of the specimen. This symmetric configuration eliminated any bending moment at the specimen and theoretically ensured pure tension of the specimen. As shown in Figure 39(b), when an impact mass struck onto the input location of the frame, the frame rotated around its pivot pin. The rotated frame then pulled the tensile link outwards in the lateral direction. Since the two tensile links were connected together at the other end along the symmetric axis, the specimen was then pulled by the tensile links and elongated along its longitudinal axis.

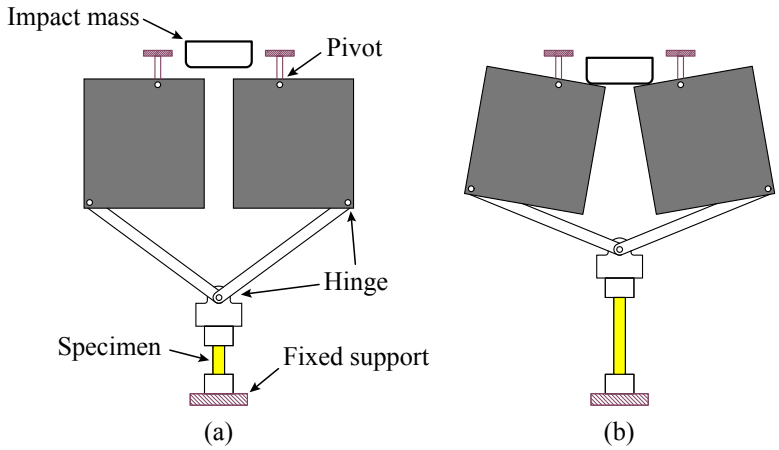

Figure 39: Schematic drawing of the proposed loading frame.

In this research, since the impact came from a high-speed actuator in the horizontal direction rather than a dropped weight in the vertical direction, the inverter mechanism was placed in the horizontal plane and directly connected to the specimen without the need of pulleys and cables as in previous research [93].

4.2.2 Open-loop control

Generally speaking, quasistatic tests are usually controlled in a real-time closed-loop manner while high-loading-rate tests are usually controlled in an open-loop manner. This means that controls during high-loading-rate tests are almost impossible because of the short time duration and the high loading rate. As a result, high-loading-rate tests are only determined by initial conditions, such as impact mass, striking velocity, and thickness and locations of pulse shapers such as neoprene pads.

Closed-loop control of loading rate in a quasistatic test can be analogized as driving

an automobile vehicle to maintain a certain speed. The operator has the opportunity to adjust the rate based on the current feedback from real-time measured data. In driving an automobile vehicle, this means the driver can adjust the driving speed by accelerating or braking based on the current speed read on the speedometer and the desired speed. For example, if the current speed on speedometer is higher than the desired speed, the operator can decelerate the vehicle by pressing the brake pedal to reduce the current speed and make it closer to the desired speed. By the same token, the operator of a quasistatic test can adjust the loading rate based on the feedback of the current loading speed. This loop of reading current feedback, adjusting control, and checking feedback again is a closed cycle and it iterates all the time during the quasistatic tests to achieve the desired constant loading rate.

On the other hand, the control of a high-loading-rate test can be compared to shooting a basket ball or hitting a golf ball. Once the ball is off, the operator cannot control it at all. What the operator can control is only the initial conditions. For example, in the case of shooting a basket, initial conditions include the location of hands touching the basketball, the pressure from the hands, the moving speed of the elbows, etc. The feedback is the result of this trial, and the operator has to figure out the relation between the result and the initial conditions. Then, the operator needs to adjust the initial conditions in the subsequent trial to get a more desired result. The cycles of getting feedback, adjusting control, and checking feedback again are actually the iterations of one test after another. As a result, this process is usually called an open-loop control and is usually performed using a trial-and-error process as shown in Figure 40.

For example, to achieve a target such as a certain deformation rate or a certain maximum deformation, the first trial test chooses guessed initial conditions. After that, the next trial improves the initial conditions based on the experimental observations of the previous trial. This trial-and-error process continues until the target of the tests is achieved. Although the actual time duration of each test is very short, the test setups and the preparation of specimens are usually time-consuming because of the large number of iterations that are required. Moreover, the relations between some of the initial conditions and the final

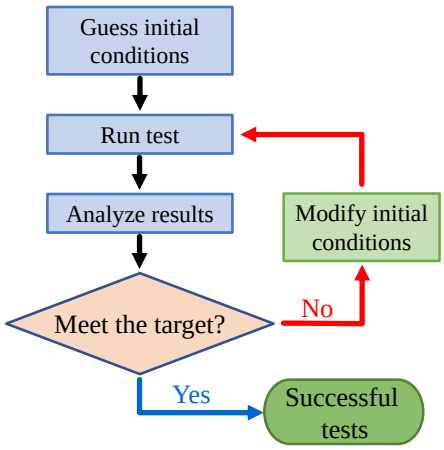

Figure 40: Schematic drawing of the open-looped control of high-speed dynamic tests.

targets are not straightforward as linear functions. To figure out these complex relations, even more iterations are required. Therefore, the number of iterations in the trial-and-error process cannot be easily optimized.

In this research, a finite element model including the inverter mechanism and the specimen assembly was simulated in Abaqus/Explicit. The actual number of tests during the trial-and-error process was minimized because some of the trial tests were replaced with finite element simulations. Additionally, a special connection between the inverter mechanism and the specimen assembly was designed with an adjustable intended slack. Different test conditions can be achieved by only adjusting the distance of this slack. This design of intended slack also provided more flexibility to the initial conditions as discussed later in Section 4.3.7.

4.2.3 Inertia effect

Unlike quasistatic tests in which stiffness of the loading mechanism is generally the only major concern, high-loading-rate tests are also dependent on the mass and damping of the loading mechanism. The inertia effect significantly affects the results of high-loading-rate tests and, therefore, is no longer negligible. For instance, if the natural frequency of the load cell itself is not high enough and its natural period is not significantly smaller than the total time duration of the test, the measured results are possibly to be dominated by the oscillations of the load cell itself instead of the overall responses of the specimen.

This phenomenon is called the load ringing. To mitigate load ringing, the load cell and the moving parts of the loading frame are required to have both high stiffness and low self-weight.

For example, experimental results from Huh et al. [58] showed that the measured force data from load cell were heavily affected by the self-weight and stiffness of the loading grips. Based on the mass and stiffness, the natural frequency of each type of loading grips was estimated. When using a heavier loading grip with a natural frequency of 2,500 Hz, the measured force data were dominated by the oscillation of the loading grip itself. As a result, the actual force history during the test was not captured accurately. However, by reducing unnecessary parts of the loading grip, the mass was reduced significantly. As a result, the natural frequency was increased to 13,000 Hz. With this loading grip, the measured data from the load cell were improved significantly, and the load ringing phenomenon diminished dramatically.

In this research, the moving parts of the inverter mechanism were mainly made of aluminum 6061 alloys to maintain a relatively high strength-to-weight ratio. High-strength bolts were also adopted to ensure adequate strength and stiffness at connections. The load cell was a piezoelectric force sensor with higher stiffness and lower mass compared with conventional load cells based on strain gages. These actions were expected to effectively control the load ringing phenomenon.

4.2.4 Adaptability for various specimens

One major objective of this research is to develop a universal high-loading-rate tensile testing system that can be applied to various types of specimens. To achieve that, the design of this system should be adaptive enough to accommodate specimens with different sizes, shapes, and materials. The adaptability of the testing system is established in three aspects: the adjustable initial position of the inverter mechanism, the versatility of the loading grips, and the flexibility in the overall test area configurations.

First of all, the initial positions of the inverter frame is adjustable to accommodate specimens with different sizes. The locations of the two pivot columns can be adjusted

along the direction of the symmetric axis. The inverter frames can be rotated around the pivot columns and set to different initial angles. As a result, both l_{impact}, which is the distance from the impacting mass to the input end of the inverter mechanism, and l_{specimen}, which is the distance from the output end of the inverter frame to the fixed reaction block, can be adjusted. Because of this flexibility in both l_{impact} and l_{specimen}, the system can have various initial parameters to accommodate the testing requirements of various specimens. These initial parameters include the distance for impact mass to travel, the position of the inverter frame, and the clear space to install the specimen assembly.

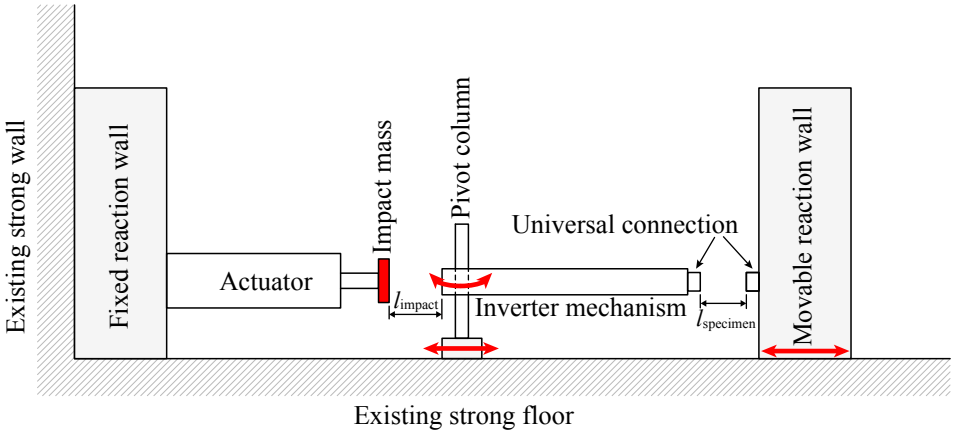

Figure 41: Schematic drawing of the adaptability of the testing system.

Secondly, the system is able to accommodate various types of specimens, such as flat tensile specimens, round tensile specimens, bars or rods, rings, etc. To achieve this versatility, both the connection from the inverter frame to the specimen assembly and the connection from the specimen assembly to the fixed support should be universal. In this research, these two universal connections were chosen as 31.75 mm (1.25 in.) diameter threaded connections. That is to say, various types of loading grips were designed and fabricated to accommodate various types of specimens, as long as these loading grips had the same 31.75 mm (1.25 in.) diameter threaded connections at both ends. The rest parts of the testing system, including the inverter mechanism and the fixed supports, remained the same for different specimens.

Finally, the reaction wall at the fixed end of the specimen assembly is designed as a movable modular reaction wall. This modular reaction wall consists of several identical

concrete modular blocks which can be post-tensioned together. The height of this movable reaction wall can be adjusted by using different quantity of modular blocks. Each of the modular block can be moved by an overhead crane. Therefore, l_{specimen} can be further adjusted by adjusting the location of the movable reaction wall.

4.3 Experimental Design

4.3.1 Overall configuration of testing area

This testing area is inside the Structural Engineering and Materials Laboratory of the Georgia Institute of Technology. Figure 42 shows the overall configuration of the testing area. The testing area is surrounded by polycarbonate safety walls and the operators control the tests remotely outside the safety walls. The laboratory is also equipped with an audio warning system and a CCTV monitoring system to ensure the safety of personnel during tests. Detailed information about the high-loading-rate testing facilities in this laboratory can be found in reference [126].

Both the existing strong floor and strong wall have a grid of embedded anchor points with center-to-center distances of 1219.2 mm (4 ft). Each anchor point on the strong floor and the strong wall has four holes to anchor 31.75 mm (1.25 inch) diameter Dywidag post-tensioning threaded bars. The center-to-center distance of these holes inside one anchor point is 203.2 mm (8 inch). The testing system is designed to have anchor locations matching the patterns of these existing anchor points on the strong floor and strong wall.

4.3.2 High-speed actuator and impact mass

The impact loading in this research is generated by an ultra-fast, hydraulically drive, computer-controlled actuator called Blast Generator (BG) [50, 127]. The existing high-speed actuator in the Structural Engineering and Materials Laboratory of Georgia Tech is a BG25 model, which can accelerate a 50 kg impact mass up to 34m/s.

Before a test, an impact mass was placed on top of the rails with the back surface firmly against the pushing plate of the high-speed actuator. Once the test began, the computer-controlled high-pressure hydraulic system of the actuator pushed a piston rod on the backside of the pushing plate outwards and, thus, pushed the impact mass towards the

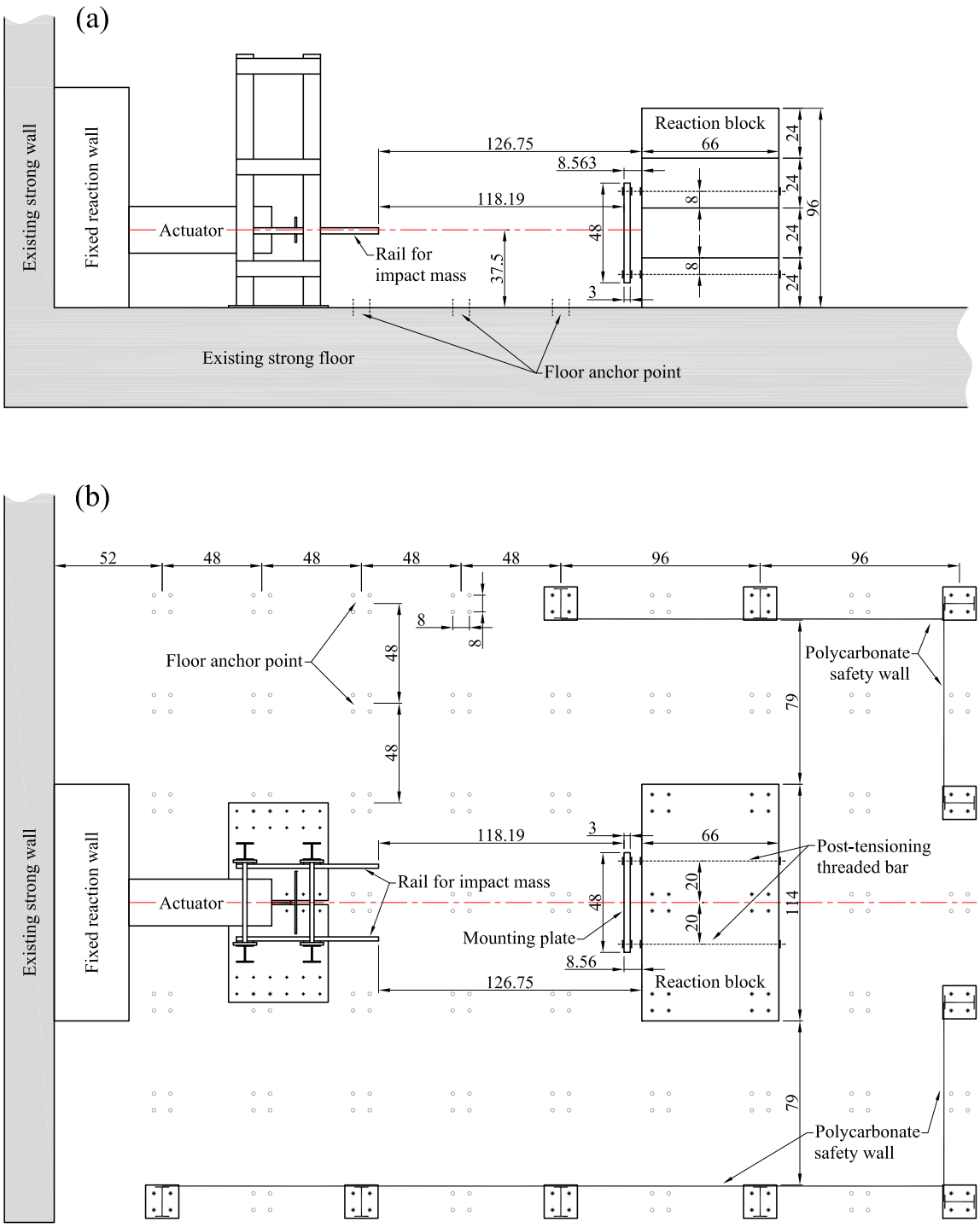

Figure 42: Overall configuration of the test area: (a) side view and (b) plan view (units: inch).

inverter mechanism. At a certain time, when the impact mass reached a targeting velocity, the actuator started to decelerate the piston rod so that the impact mass detached from the pushing plate. After that, the pistol rod and pushing plate retracted back to initial positions while the impact mass kept moving forward until struck onto the input end of the inverter mechanism. After the impact, the impact mass bounced back and fell onto the floor which was covered with a layer of sandbags. Both the impact speed and the impact duration can be tailored by the computer-controlled system to meet the requirements of various tests.

An adjustable impact mass composed of several modular steel blocks was used in this research. This impact mass was adopted from previous research projects conducted by Lee et al. [74]. As Figure 43 shows, this impact mass was composed of four types of blocks: front block, back block, support block, and infill block. These blocks were connected together by four 12.7 mm (0.5 inch) diameter high-strength steel threaded bars. The front ends of these threaded bars were anchored into the threaded holes in the front block. Then these threaded bars went through the holes in the support blocks and infill blocks and finally anchored to external nuts inside the countersink holes of the back block. The support blocks were 914.4 mm (36 inch) long, spanning between the rails which had a clear distance of 838.2 mm (33 inch). As a result, the whole impact mass was able to slide on the rails along the direction of the symmetric axis.

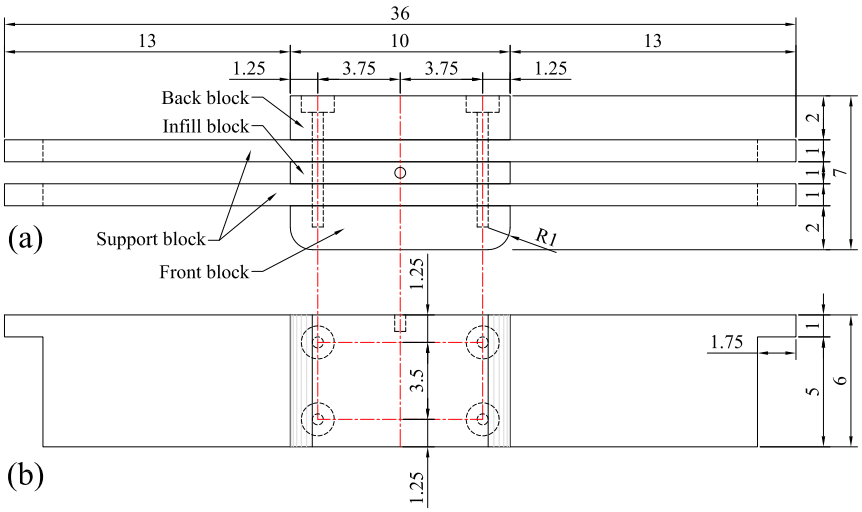

Figure 43: Design of the impact mass: (a) top view and (b) front view (units: inch).

The total mass and the dimension along the moving direction of the impact mass can be adjusted by adding or removing infill blocks. Figure 43 shows the assembly with one infill block, which was the configuration that had the minimum mass of 87.12 kg and was used in most of the tests. The top surface of the middle infill block had a threaded hole so that the whole impact mass can be lifted and positioned by an overhead crane connected to an eye bolt anchored into this threaded hole.

4.3.3 Concrete reaction walls

The two ends of the tensile testing system were anchored into two reaction walls, respectively. The fixed end of the high-speed actuator was bolted to the embedded steel plates of a fixed concrete reaction wall, which was post-tensioned onto the strong wall as illustrated in Figure 44(a). The fixed end of the specimen assembly was bolted to an external steel mounting plate attached to the movable reaction wall, which was composed of four concrete modular reaction blocks as illustrated in Figure 44(b). The 76.2 mm (3 inch) thick external mounting steel plate was anchored to the movable reaction wall by four 31.75 mm (1.25 inch) diameter Dywidag post-tensioning threaded bars running through the horizontal ducts of the concrete blocks.

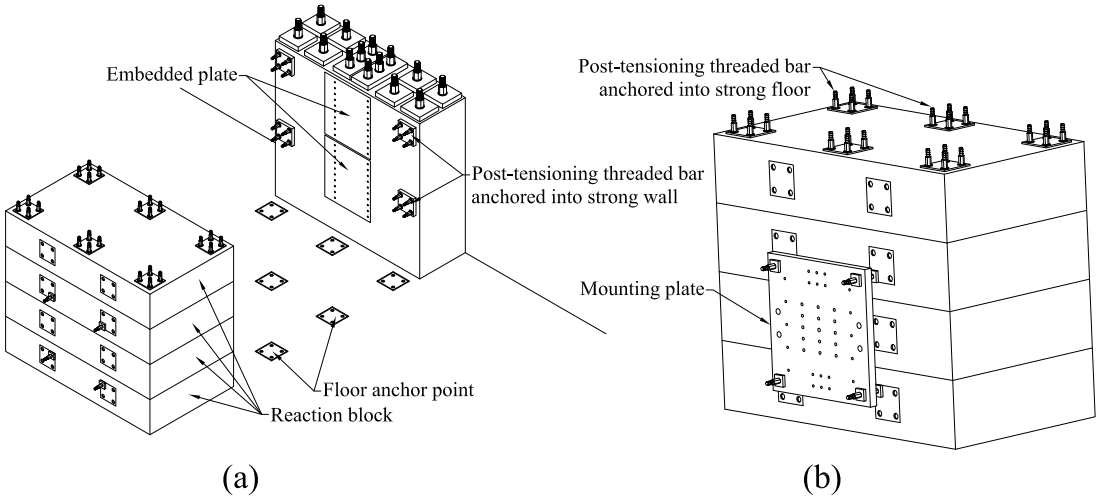

Figure 44: Reaction walls of the testing system: (a) view towards the front side of the fixed reaction wall (b) view towards the front side of the movable reaction wall.

Figure 45 shows the design and construction of an individual modular reaction block. PVC pipes were embedded inside the concrete to work as ducts for 31.75 mm (1.25 inch) diameter Dywidag post-tensioning threaded bars. Steel bearing plates with a thickness of 12.7 mm (0.5 inch) were also embedded in the concrete to increase the bearing strength around the post-tensioning bars.

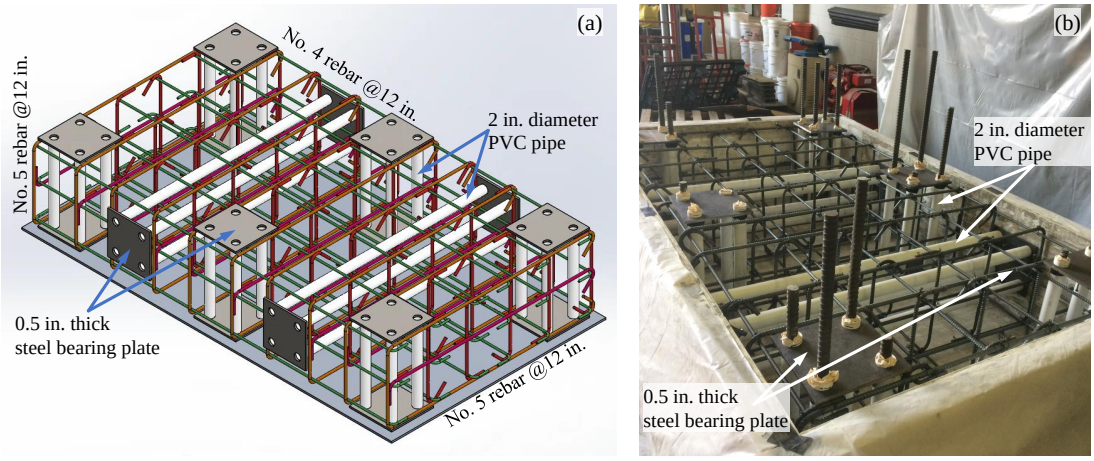

Figure 45: Modular concrete reaction block: (a) isometric view of design drawing (b) block during construction before pouring concrete.

4.3.4 Optimization of the inverter mechanism

The concept of the inverter mechanism in this research as shown in Figure 39 was similar to the force inverter discussed by De Leon et al. [27] and Liu et al. [78]. Nevertheless, the inverter designed in these previous research was a compliant mechanism in a very small scale with dimensions on the order of millimeters. In contrast, the size of the inverter mechanism in this research was in a much larger scale with dimensions on the order of meters. The forces that need to be inverted in this research were also larger by several orders of magnitude. Since high-loading-rate tests in this research were expected to have a total loading time less than 0.01 s, the inverted displacement was less important than that in the case of a compliant mechanism. On the other hand, the stiffness of the inverter in this research was extremely important, and it must be significantly higher than the specimens under investigation. Otherwise, the inverter mechanism itself may be deformed or even damaged by the impact force even before it started to load the specimen. As a result of

these differences, although the inverter mechanism in this research shared similar concepts to the mechanism in previous studies, their design were quite different in many aspects.

To determine the optimized shape and size of the inverter frame, this research utilized topology optimization techniques as guidelines. In short, the goal was to find an optimized design that had the highest stiffness for a certain load. At the same time, this inverter mechanism had to be designed within the limits of a certain geometric region and a certain amount of material. Half of the system was utilized in the optimization problem because of its symmetry. The design domain of this optimization problem was taken as the shaded area in Figure 46. This design domain included a pin support near the middle of the top edge, representing the pivot column of the rotating frame, and a hinge at the bottom right corner, representing the tensile link connected to the output end of the rotating frame. The impact force was applied at the top left corner as shown in Figure 46(a). Since the design objective was the stiffness, for simplicity, the problem was converted into the equivalent problem as shown in Figure 46(b). The applied force and a boundary condition with a single degree of freedom were interchanged between these two cases. For an estimated elastic analysis, these two cases were assumed to be equivalent.

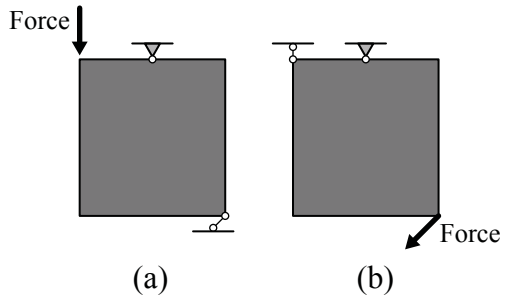

Figure 46: Simplified optimization problem for the dimension of inverter frame: (a) actual problem and (b) equivalent problem.

The 2D model of the inverter frame was meshed with PolyMesher, a MATLAB code for polygonal mesh generation[130]. The total number of elements was chosen as 5,000 and the volume ratio constraint was set as 0.2, which limited the maximum amount of material in the final optimized shape. The boundary conditions and the applied load were specified to the nodes at the related locations as shown in Figure 47(a). After that, the optimization

was conducted in PolyTop, a MATLAB code for structural topology optimization with a general finite element routine based on isoparametric polygonal elements [131]. The optimized results in Figure 47(b) exhibited the characteristics of a Michell truss [53].

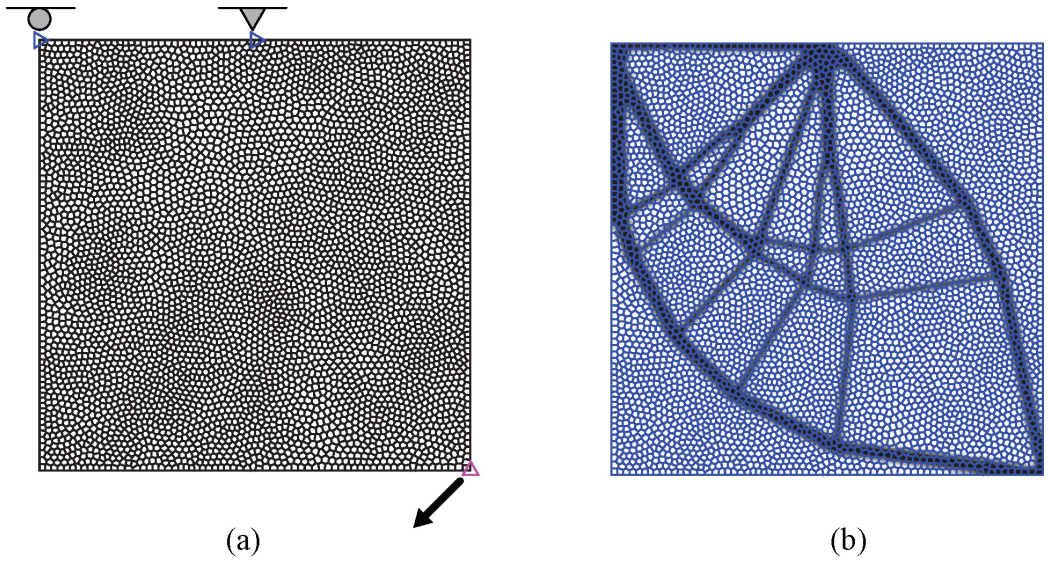

Figure 47: 2D optimization of the inverter frame: (a) mesh from PolyMesher and (b) optimized result from PolyTOP

The design domain for the inverter frame was then modeled in Modified Top3D, a MATLAB program that can find optimized structural shapes in 3D [78]. The mesh size was chosen as $80 \times 80 \times 10$. Since this inverter frame was designed to be fabricated with aluminum alloy, the volume fraction could not be excessively large. Otherwise, the frame would be too heavy and would cause problems in the process of fabrication and installation. With consideration of the dimension restraint caused by space limitation and the density of aluminum alloy, a volume ratio of 0.065 seemed to be a reasonable assumption. The boundary conditions near the pin connection were applied to four nodes around the location of the pin for each layer of nodes in the z-direction. As shown in Figure 48, the load was only applied to the surface nodes, simulating a double-shear connection with a clevis pin inside a hinge connection.

Figure 49 shows the passive zones defined in the design domain. To model the pivot of the inverter frame, a passive zone was defined around the location of the pivot to simulate the pivot hole and a passive-solid zone was defined around the pivot hole to represent a full

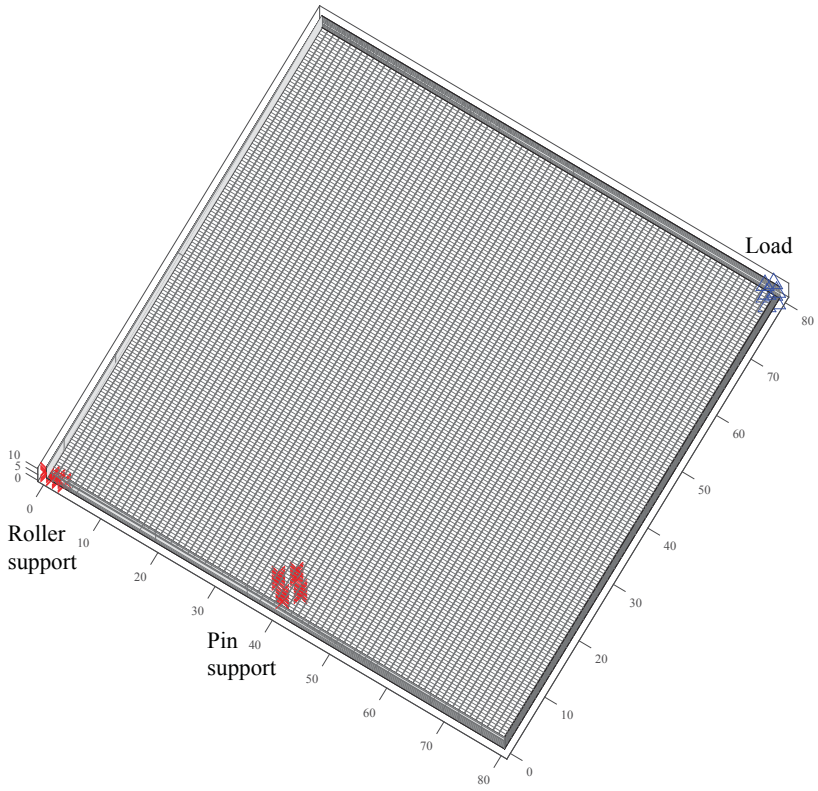

Figure 48: Mesh of the whole model in Modified TOP3D

circle of tube around the pivot. The passive-solid zone was set to occupy the entire height in order to minimize the contact stress in the pin connection.

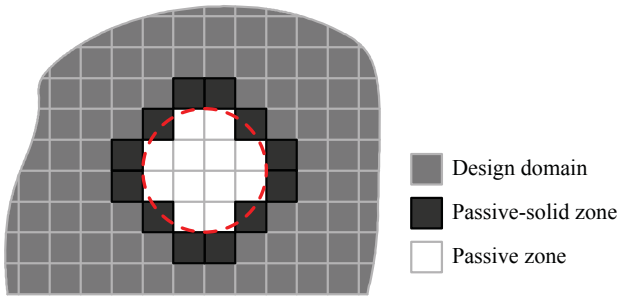

Figure 49: Passive zone and passive-solid zone around the pin connection defined in Modified TOP3D.

To make the optimization process more efficient, only the top half of the design domain was modeled in Modified Top3D because the force inverter was also symmetric in the vertical direction. Figure 50 shows the mesh of this model with constraints on z-direction to maintain the symmetry. The optimized process was set to run for 1,000 iterations.

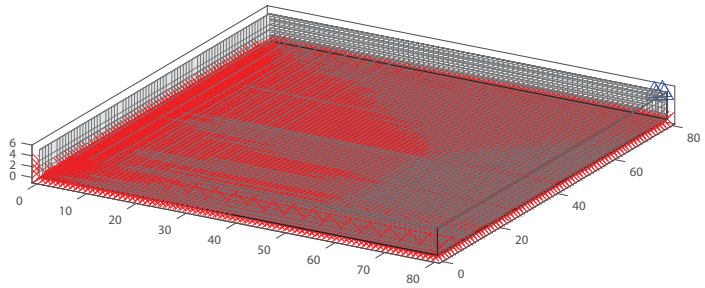

Figure 50: Mesh in 3D using Modified TOP3D.

The optimized results of the Modified TOP3D were then imported into TOPslicer, a post-process tool developed in MATLAB by Zegard and Paulino [142]. Since only the top half was modeled in Modified Top3D, the results were mirrored in TOPslicer to restore the whole model of one inverter frame. The optimized results provided a volume ratio for each element which indicated the amount of the material that was required inside this element in the final optimized results. The cutoff was selected as 0.4, meaning an element which had a volume ratio of less than 0.4 was deleted. Only elements that had a volume ratio of more than 0.4 were kept, and all these elements formed the final shape. Figure 51 shows the results in TOPslicer after mirroring the model.

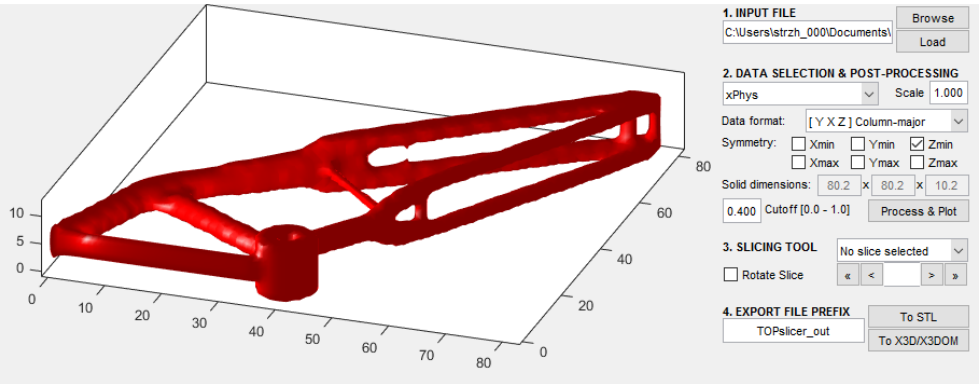

Figure 51: Optimized result of the inverter frame from Modified TOP3D processed in TOPslicer.

Compared with the Michell truss from PolyTop, the optimized result from Modified Top3D was much simpler. The basic shape was a triangular truss with optimized dimensions and angles. This may not be as efficient as the Michell truss from the point of stiffness-to-weight ratio. However, from the point of manufacturing, this triangular truss was easier to

construct using traditional manufacturing techniques.

The optimized results in TOPslicer were then converted into a STL file, which can be imported into other software for further use. For example, the STL file of the optimized force converter was imported into SOLIDWORKS and Figure 52 shows a conceptual model for the entire tensile testing system in SOLIDWORKS.

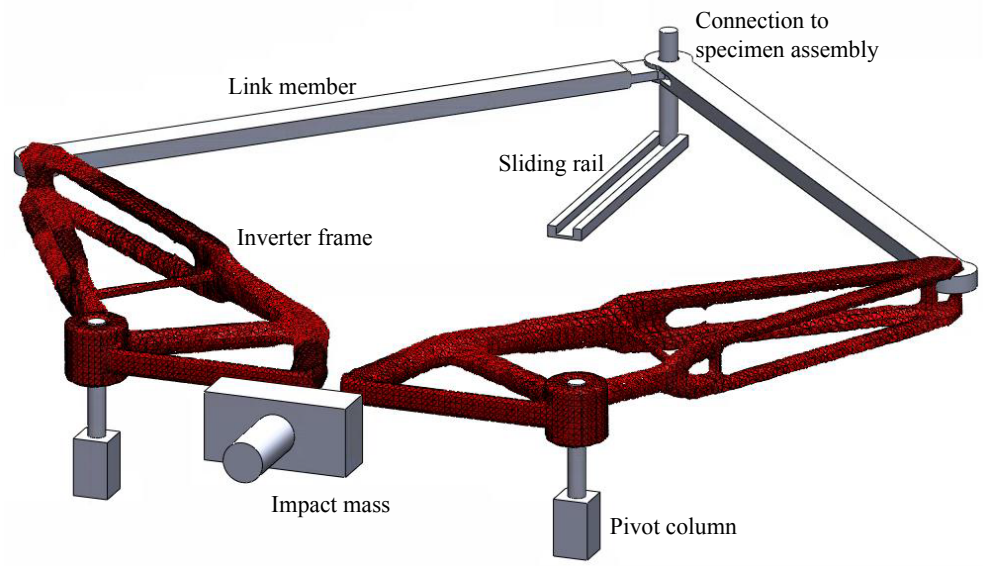

Figure 52: SolidWorks model of the test device with the optimized result of force inverter.

The final shape of the inverter frame was simplified based on the above optimization results to minimize the complexity in fabrication. As Figure 53 shows, the shape of the inverter frame was further simplified as a triangular by removing small section braces in the middle and changing the impact location to the joint at the corner of the triangle.

The final dimensions of this loading frame were selected based on the space limitation of the available testing area. As shown in Figure 54, the horizontal distance between the center of two pivot columns was selected as 2438.4 mm (96 inch), which was two times the distance between two adjacent existing anchor plates on the strong floor.

The ability of this mechanism to magnify the movement was related to the initial setup position of the inverter frame. In Figure 55, the angle between the initial position of the triangular frame and the symmetric axis was denoted as β. The relation between the amplification ratio of displacement and the angle β was evaluated by a rigid body

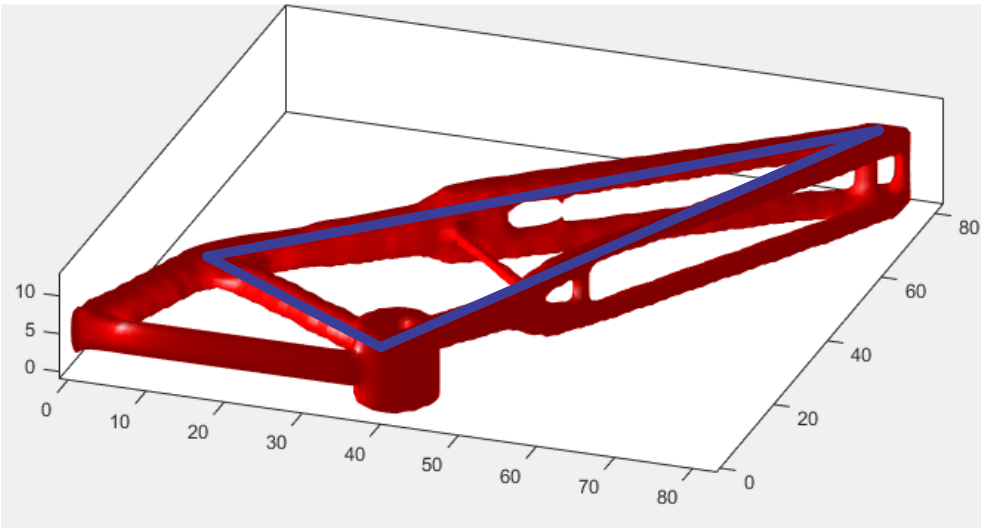

Figure 53: Final shape of the inverter frame simplified from optimization results.

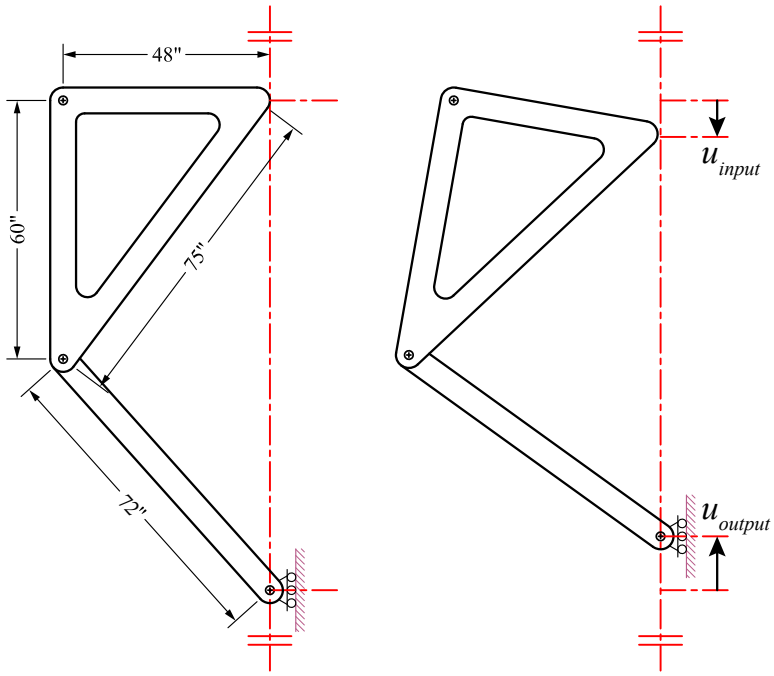

Figure 54: Schematic drawing of the dimension parameters of the loading frame.

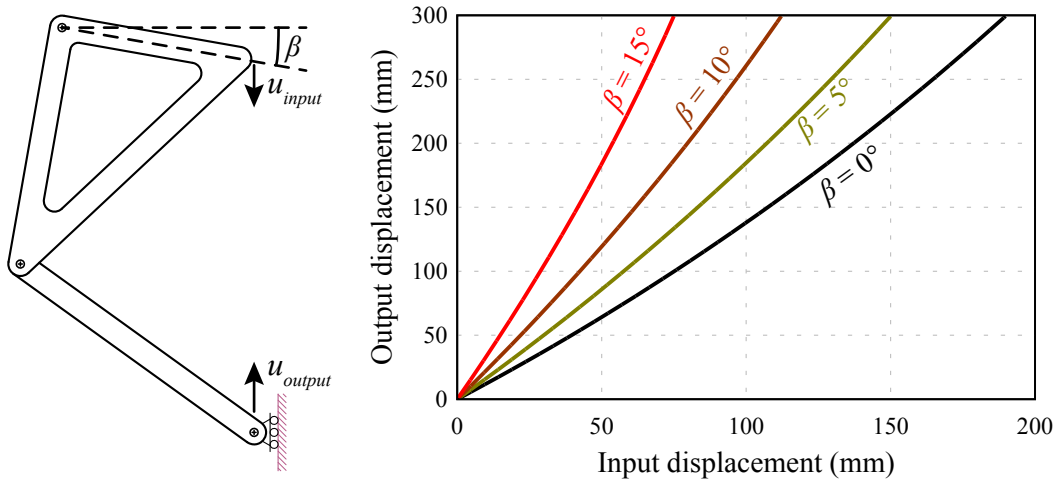

Figure 55: Ratio between the output and input displacements of the loading frame assuming rigid body motion.

motion analysis. Assuming the triangular frame and the link were ideally rigid bodies, the ratio between the magnitude of the output and the input displacements was obtained using motion analysis in SOLIDWORKS. As shown in Figure 55, the amplification ratio increased as the angle β increased. When β equals zero, which meant the initial position of the short leg of the triangular frame was perpendicular to the symmetric axis, the amplification ratio of displacement was around 1.25. When β equaled 15°, which was the maximum possible value because of the restriction of available testing areas, the amplification ratio reached around 3.5.

4.3.5 Inverter mechanism

As discussed in Section 4.2.3, the force inverter mechanism was preferred to have relatively low self-weight to reduce inertia effect and relatively high strength and stiffness to satisfy the performance requirement. The main material for the inverter frame was chosen as aluminum alloy 6061 for its high strength-to-weight ratio and easy workability. The members were designed as built-up sections with aluminum channels as web and batten plates as flanges. The joints were designed as welded joints with aluminum gusset plates and end plates. The members and joints were then bolted together to form the entire inverter mechanism. One of the reasons for bolted connection between joints and members rather than a monolith

welded connection was for easy repair or replacement. If a single joint or member was damaged during the test, it can be replaced with a new component relatively easily. In contrast, if the inverter frame was built as a monolith unit, the potential repair would be quite difficult and time-consuming..

The inverter mechanism consisted of two types of components: triangular frames and tensile links. On each side of the symmetric axis, one triangular frame and one tensile link were connected by a double shear connection with a high strength clevis pins as shown in the conceptual drawing in Figure 54. The other ends of the two tensile links were connected together using a third clevis pin, which also went through the connection to specimen assembly. The weights of a single triangular frame and a single link were 143 kg (316 lbs) and 37 kg (82 lbs), respectively. The total weight of the entire inverter mechanism was around 360 kg (800 lbs).

4.3.5.1 Pivot columns and foundation beams

The key part of a pivot column was a steel solid rod with a diameter of 101.6 mm (4 inch). This rod, surrounded by four stiffeners, was perpendicularly welded onto a steel bottom plate to ensure the longitudinal axis of the rod was as close to vertical as possible. A 25.4 mm (1 inch) thick steel flange plate with an inner diameter of 101.6 mm (4 inch) and an outer diameter of 228.6 mm (9 inch) was welded on top of the stiffeners. The top surface of the flange plate was machine finished to ensure it was flat and smooth. The cylindrical surface of the top part of the pivot rod was also machine finished to provide a smooth contact surface and, thus, minimize misalignment and reduce friction. A plastic washer was placed on top of the flange plate to further decrease friction.

Two identical pivot columns were required with one on each side of the symmetric axis. Bolt holes were drilled in the bottom plates of the pivot columns. Through these holes, each pivot columns was anchored to a foundation beam. The foundation beam was built-up I-sections with 50.8 mm (2 inch) thick flanges and web. Both of these two foundation beams were fixed to the strong floor with Dywidag post-tensioning threaded bars. Two lines of bolt holes were drilled on the top flange of each foundation beam, and the hole patterns

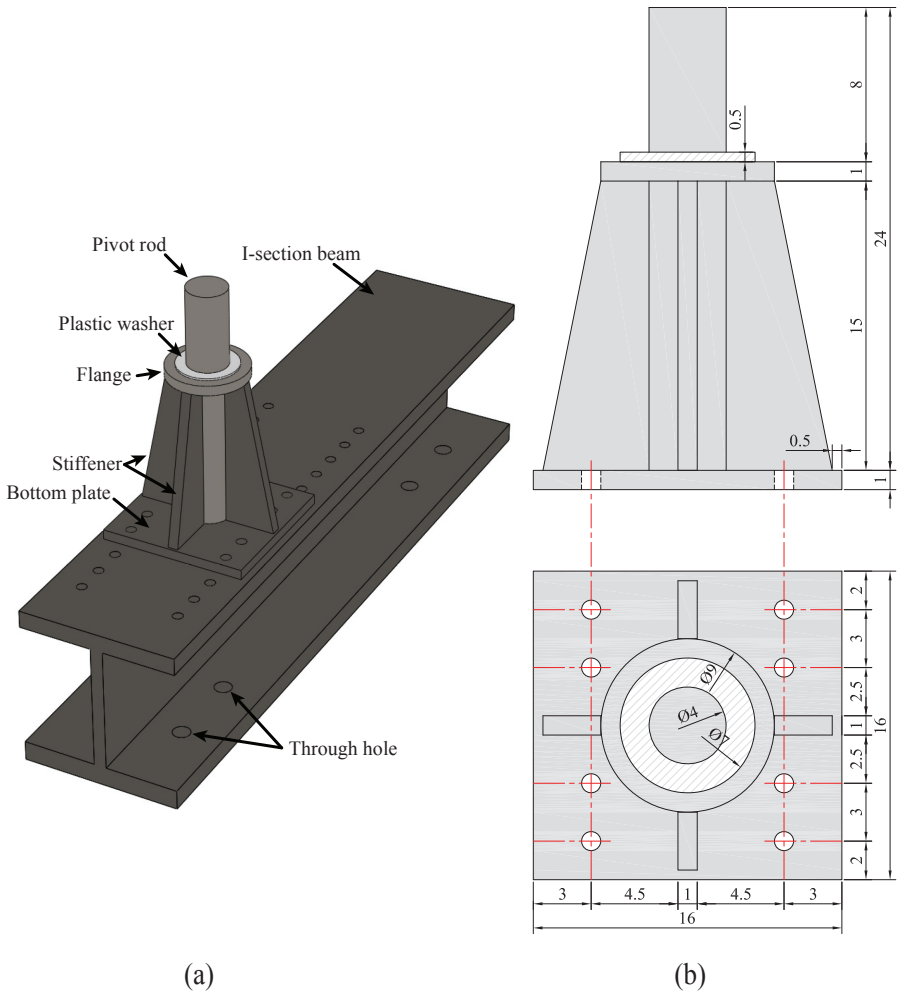

Figure 56: Design of the pivot column: (a) perspective view and (b) side view and plan view (units: inch).

matched with the bolt holes on the bottom plates of the pivot columns. As a result, the pivot column can be anchored to different sets of bolt holes, which resulted in different locations along the symmetric axis. This corresponded to the design concept of adaptivity as discussed in Section 4.2.4.

4.3.5.2 Triangular frames

Each triangular frame was composed of three joints and three members as shown in Figure 57. The lengths of the built-up members on three sides were 406.4 mm (16 inch), 660.4 mm (26 inch), and 1016 mm (40 inch), respectively. The flanges of these built-up members were 152.4 mm × 12.7 mm (6 inch × 0.5 inch) aluminum batten plates. The webs were Aluminum

Association (AA) CS 4×2.33 channels, which had a section height of 101.6 mm (4 inch), a section width of 57.15 mm (2.25 inch), a web thickness of 4.83 mm (0.19 inch), and a flange thickness of 7.37 mm (0.29 inch). The batten plates and channels were welded together along the longitudinal edges. Both ends of the built-up member had groups of bolt holes to connect with the joints.

Joint A was designed as the pivot point of the triangular frame. As shown in Figure 58, an aluminum tube with an outer diameter of 152.4 mm (6 inch) and an inner layer of 6.35 mm (0.25 inch) thick bronze sleeve bearing was designed to rotate around the pivot column smoothly. Two horizontal 25.4 mm (1 inch) thick gusset plates with a clear spacing of 76.2 mm (3 inch) were welded outside of the tube. End plates with attached flange plates and web plates were welded to the gusset plates so that the joint can be bolted to the adjacent built-up members through the groups of holes on the flange plates and web plates. Vertical stiffeners were welded between the gusset plates and around the outside surface of the tube to increase the stiffness of this joint.

The rotation mechanism between Joint A and the pivot column is shown in Figure 59. The outer diameter of the bronze bearing was machined to be slightly larger than the inner diameter of the aluminum tube. The bronze bearing was pushed into the aluminum tube with a servo-hydraulic testing machine. The inner diameter of the bronze bearing was then machined to be slightly larger than the outer diameter of the steel rod so that the tube can rotate around the rod smoothly without any considerable swaying or shaking. Grease fittings were added to the tube so that grease can be injected into the contacting surfaces between the bronze bearing and the steel rod. The friction around this rotation joint was well controlled by the precise match of machined surfaces and the additional lubricant provided by grease fittings.

Joint B was designed as the input end of the triangular frame. During tests, the impact mass directly struck onto this joint. As shown in Figure 60, an aluminum plate with dimensions of $254\,\text{mm} \times 177.8\,\text{mm} \times 25.4\,\text{mm}$ ($10\,\text{inch} \times 7\,\text{inch} \times 1\,\text{inch}$) was the actual impact location. Between two 25.4 mm (1 inch) thick gusset plates, two 25.4 mm (1 inch) thick stiffeners were welded to the back side of the impact plate. These two stiffeners were

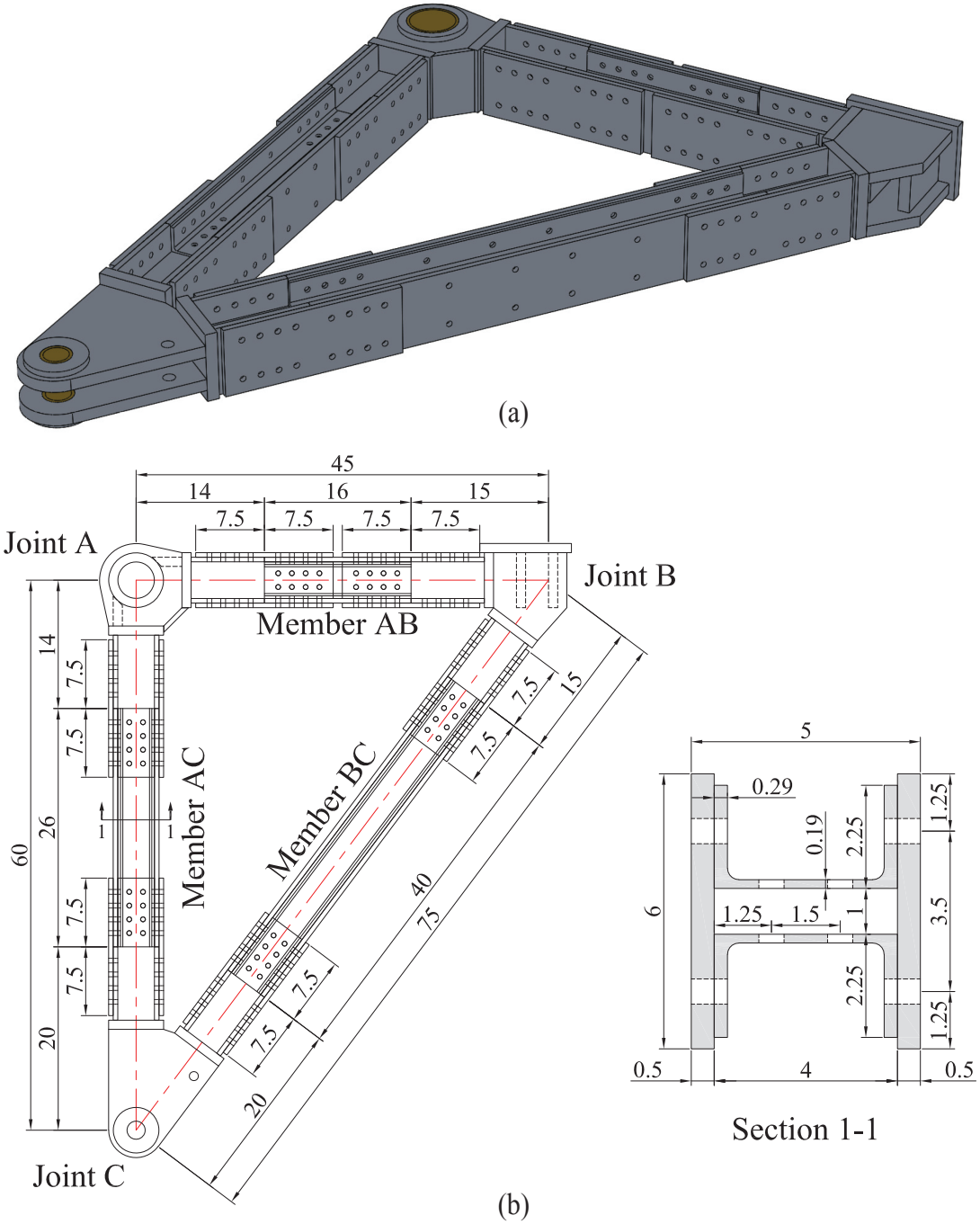

Figure 57: Design of the triangular frame of the inverter mechanism: (a) perspective view and (b) plan view and cross section of built-up members (units: inch).

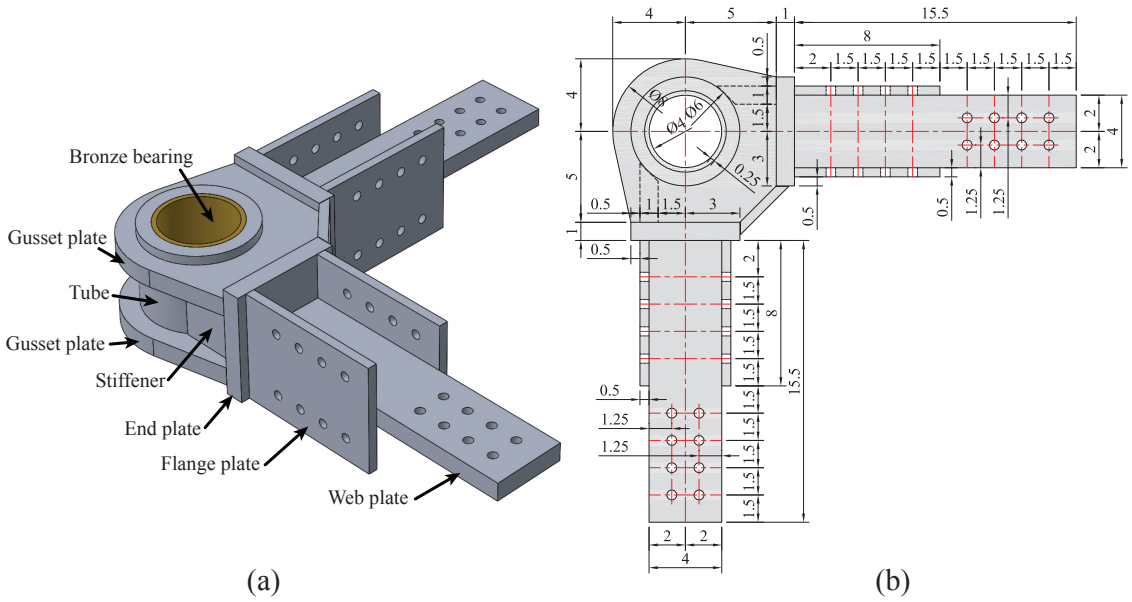

Figure 58: Design of Joint A of the inverter mechanism: (a) perspective view and (b) top view (units: inch).

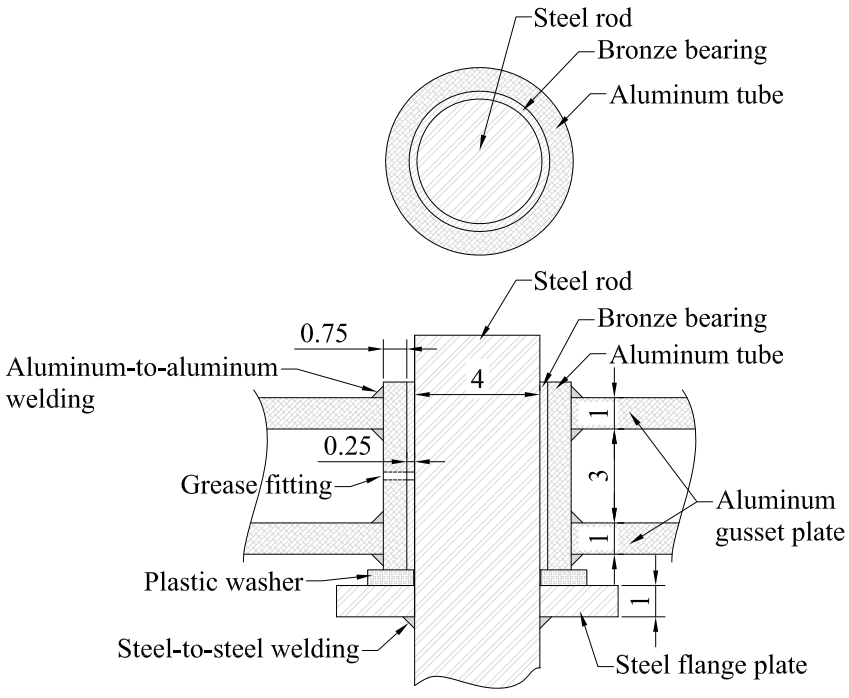

Figure 59: Design of the rotation mechanism between Joint A and pivot column (units: inch).

designed to distribute the concentrated impact force into the flange plates and web plates.

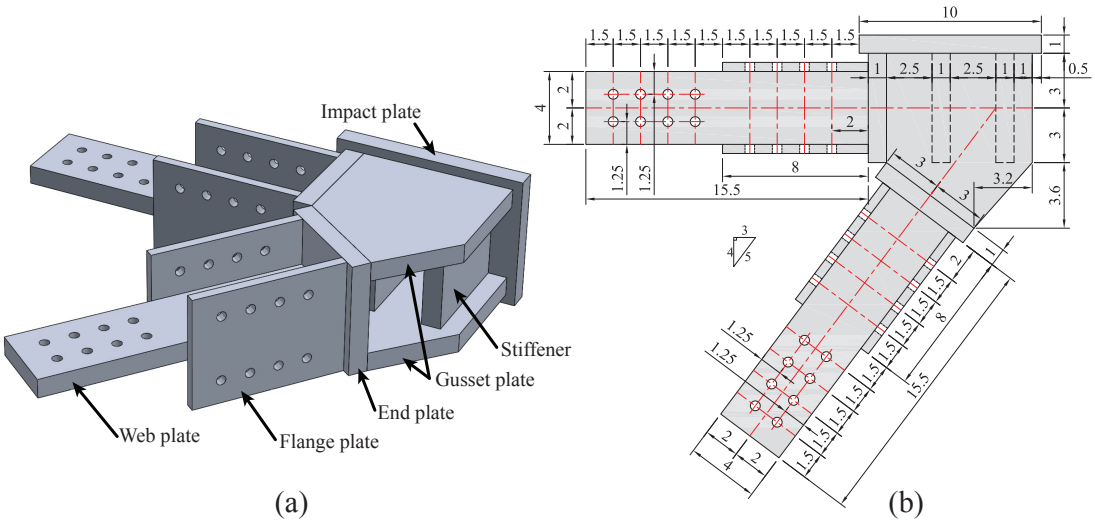

Figure 60: Design of Joint B of the inverter frame: (a) perspective view and (b) top view (units: inch).

Joint C was designed as the output end of the triangular frame. This joint was connected to the tensile link through a double shear connection with a clevis pin. Additional cheek plates were added around the pin hole to increase the contact area and connection strength. The pin connections also had bronze sleeve bearings and grease fittings similar to the rotating tube in Joint A. Bolt holes for safety cables were added to each gusset plate of this joint.

A typical connection between a joint and a built-up member is shown in Figure 62. The web plate of the joint was inserted into the middle opening of the built-up member. Then the web plate of the joint and the web of the built-up member were bolted together. After that, two splice plates were bolted onto both sides of the flanges.

4.3.5.3 Link members of the inverter mechanism

Each tensile link of the inverter mechanism was an aluminum built-up member with pad-eye plates at both ends. As shown in Figure 63, the flange and web of the built-up member were 152.4 mm × 25.4 mm (6 inch × 1 inch) plates and 7.62 mm × 101.6 mm (3 inch × 4 inch) rectangular tube, respectively. Each end of this built-up member was welded to a 25.4 mm (1 inch) thick end plate with a pad-eye plate on the other side. The pin hole on the pad-eye

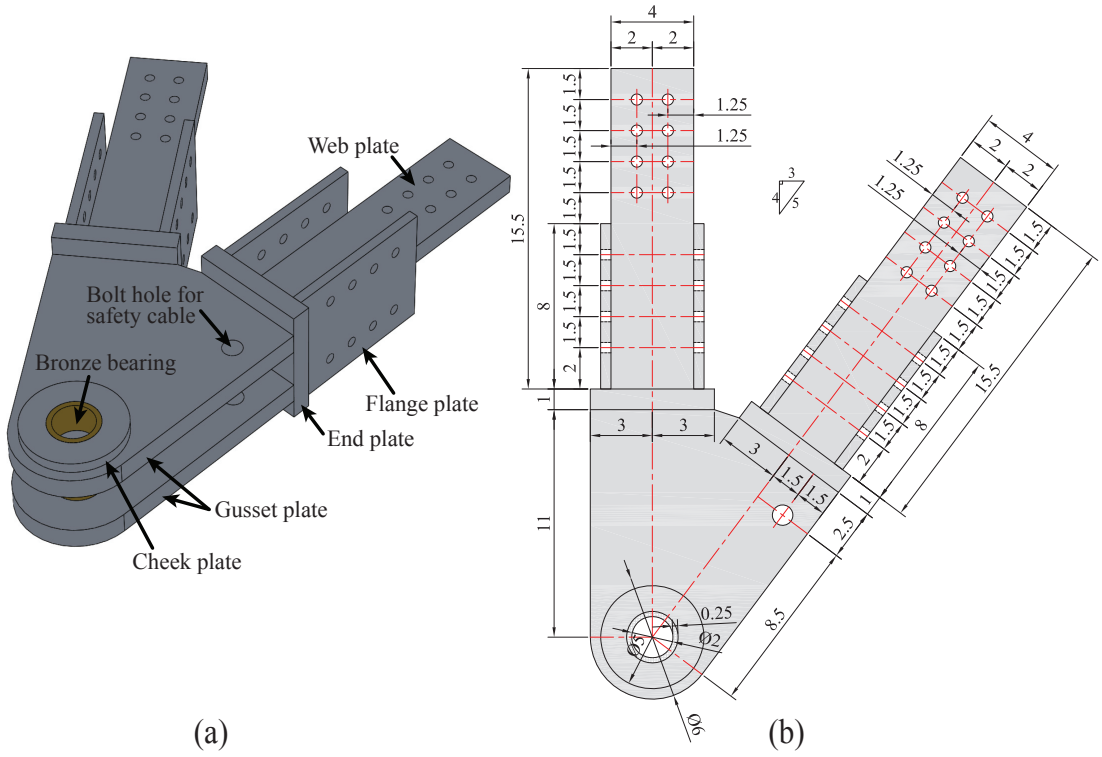

Figure 61: Design of Joint C of the inverter frame: (a) perspective view and (b) top view (units: inch).

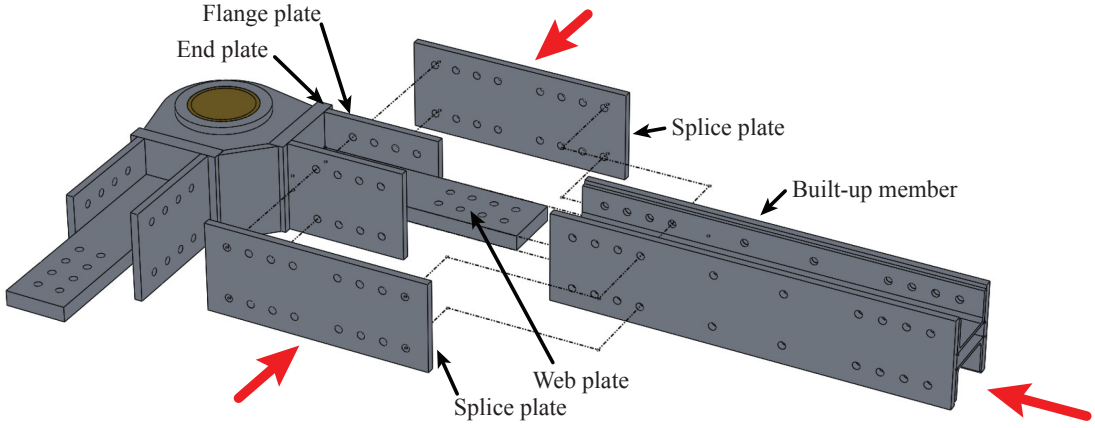

Figure 62: Typical connection between a frame joint and a frame member

plate also had bronze sleeve bearing and grease fitting. The centered pad-eye on the left side as shown in Figure 63 was the one connected to output end of the triangular frame while the eccentric pad-eye plate on the right side was the one connected to the input end of the specimen assembly. That is to say, during installation, the centered pad-eye plate was inserted into the middle of the two gusset plates of Joint C, and the two eccentric pad-eye plates from two tensile links were placed on top and bottom of a ball joint connector of the specimen assembly.

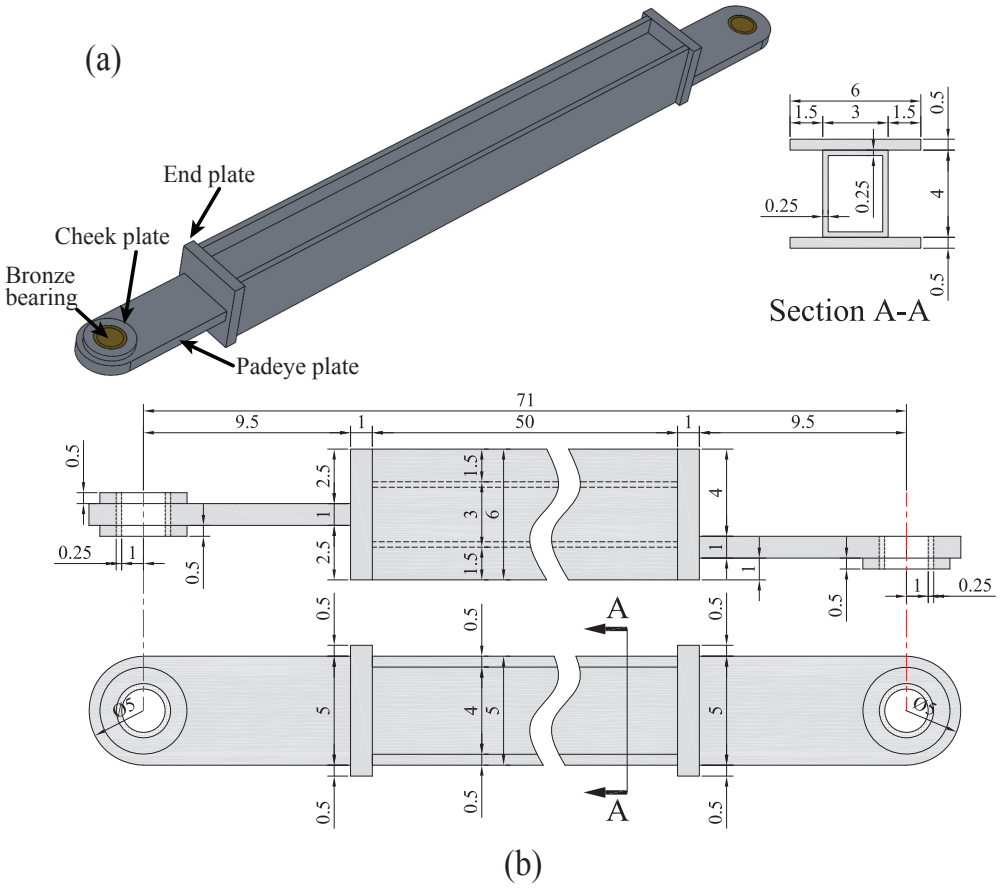

Figure 63: Design of the tensile link: (a) perspective view and (b) side view and section view (units: inch).

4.3.5.4 Roller supports

The self weight of the inverter mechanism was supported by six legs made of aluminum rectangle tubes. As illustrated in Figure 64, each leg was composed of three parts: a top connection, a main tube, and a bottom roller. The top connection was welded to the bottom

surface of the gusset plates of the joints. The 63.5 mm × 63.5 mm (2.5 inch × 2.5 inch) main tube was then bolted to the top connection. The bottom of the main tube was welded to an end plate with a through threaded hole. A stud-mounted ball transfer was threaded into this threaded hole. As a result, this leg can work as a roller support. By turning the ball transfer inwards or outwards of the threaded hole, the total height of this roller support can be slightly adjusted.

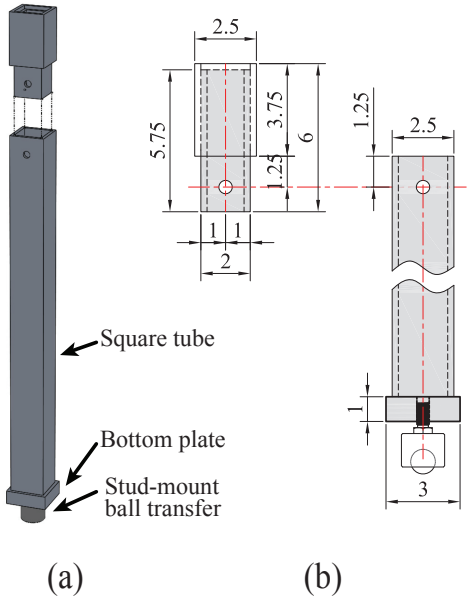

Figure 64: Design of the roller support: (a) perspective view and (b) side view (units: inch).

4.3.5.5 Assembly of the inverter mechanism

Figure 65 shows the final assembly of the inverter mechanism including two foundation beams, two pivot columns, two triangular frames, two tensile links, and six roller supports in a symmetric configuration. The centered pad-eye plates of the tensile links were inserted between the gussets plates of Joint C to form double shear connections. The eccentric pad-eye plates of the tensile links were placed in an asymmetric pattern with a gap in the middle for the input end of the specimen assembly to insert in. Each joint had its own roller supports except Joint A, which was firmly supported by the flange plate of the pivot column.

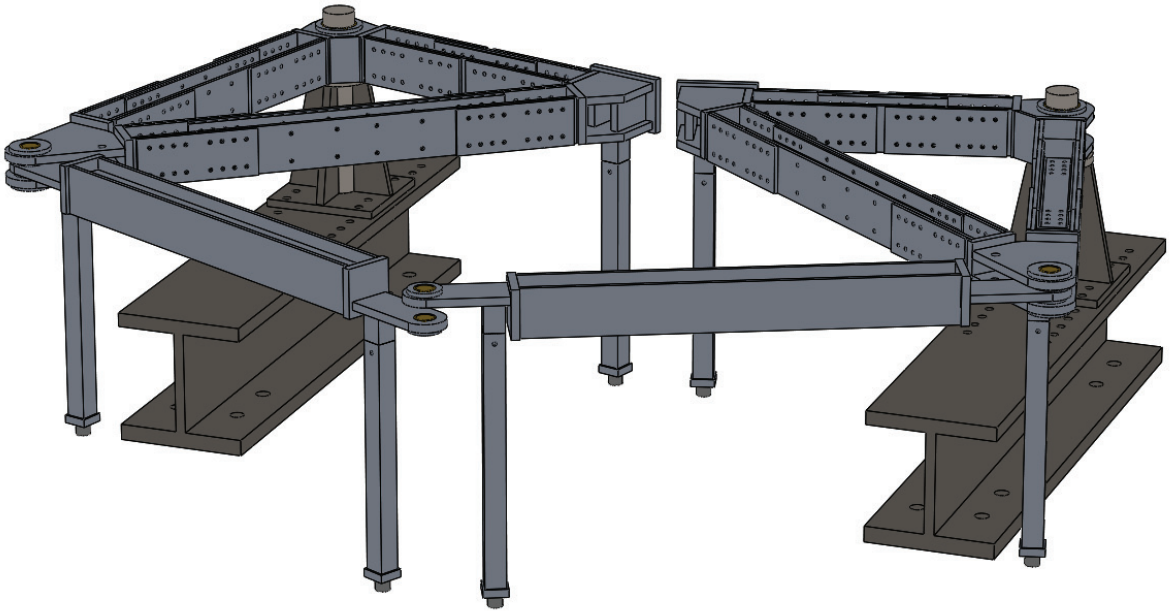

Figure 65: Assembly of the inverter mechanism.

4.3.6 Specimen assembly

The specimen assembly was composed of four parts: an universal ball joint connector, a sliding rail, a support of the rail, and a pair of loading grips to hold the specimens. As discussed in Section 4.2.4, the design of the specimen assembly was required to accommodate various types of specimens. For different types of specimens, only the loading grips needed to be modified. The rest of the assembly were universal for specimens of various materials, shapes, and sizes.

4.3.6.1 Ball joint connector

The ball joint connector attached the output end of the inverter mechanism to the input end of specimen assembly. As shown in Figure 66, two aluminum blocks were connected together by two 19.05 mm (0.75 inch) diameter threaded bars. At one side, a ball joint rod end was inserted through the center hole of the input block and anchored by a nut. The pin hole of the ball joint rod end had an inner diameter of 50.8 mm (2 inch). At the other side, similarly, a 31.75 mm (1.25 inch) diameter threaded bar was inserted through the center hole of the output block and anchored by a nut. The far end of this 31.75 mm (1.25 inch) diameter threaded bar was connected to a piezoelectric load cell, which had

31.75 mm (1.25 inch) diameter threaded holes at both ends.

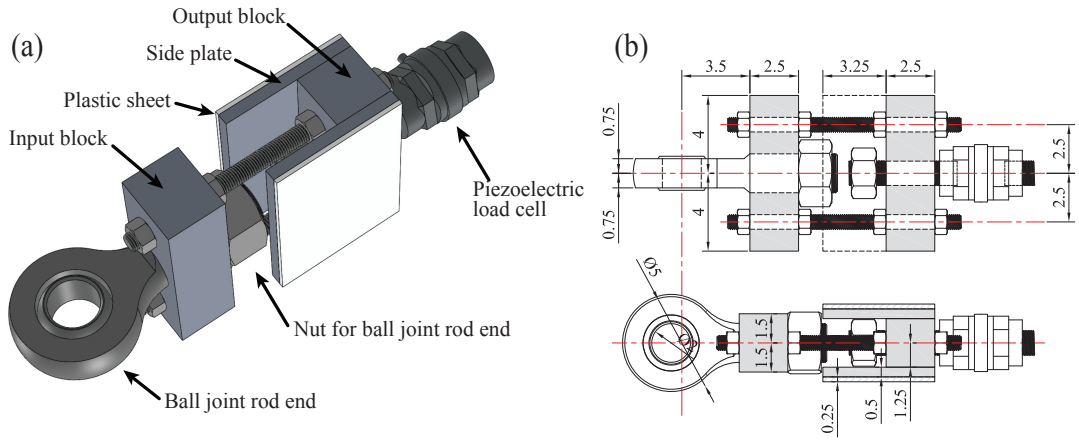

Figure 66: Design of the ball joint connector: (a) perspective view and (b) side view and top view (units: inch).

The connection also included an intended slack distance between the right surface of the nut for the threaded bar connecting to the load cell and the left surface of the output block as Figure 66(b) shown. The main purpose of this intended slack distance was to provide more flexibility in the testing setups as discussed in Section 4.2.4 and to achieve a more constant loading rate as discussed later in Section 4.3.7.

Each lateral surface of the output block was mounted with a 12.7 mm (0.5 inch) thick aluminum side plate. The outer surface of the side plate was then fully covered with a piece of low-friction plastic sheet.

4.3.6.2 Sliding rail

To ensure the specimens were stretched along the longitudinal direction without significant amount of bending moment or torsion, a sliding rail was designed to confine the movements of the ball joint connector. The bottom rail was a T-shaped steel plate with a piece of low-friction plastic sheet attached on its top surface. Two vertical steel plates were welded perpendicularly to the T-shaped plate as lateral rails. With two stiffeners connecting the top of these two vertical plates, a hollow box shape was formed. The ball joint connector fit inside this hollow box and slid against the plastic sheet on the T-shaped plate and the two lateral plates. Both vertical and lateral movements of the ball joint connector were

confined, and, theoretically, the only degree of freedom was along the longitudinal axis of the specimen. Therefore, the specimen was secured to be purely elongated without bending moment or torsion.

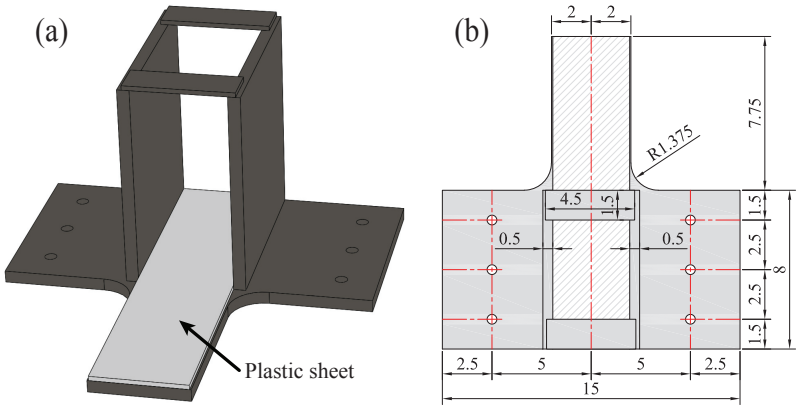

Figure 67: Design of the sliding rail of specimen assembly: (a) perspective view and (b) top view (units: inch).

4.3.6.3 Rail support

A stationary support, as shown in Figure 68, was fabricated to firmly bracing the sliding rail. This support worked as a cantilever beam with the fixed end bolted to the external steel mounting plate and the free end bracing the sliding rail. Each of the cantilever components was a 101.6 mm × 101.6 mm × 12.7 mm (4 inch × 4 inch × 0.5 inch) steel angle which had enough strength and stiffness to restrain both movement and rotation of the sliding rail.

A line of bolt holes was drilled on the top flange of each angle to match the hole patterns on the T-shaped plate of the sliding rail. The position of the sliding rail can be adjusted along the longitudinal axis by connecting to different group of bolt holes. This design feature also provided further flexibility to l_{specimen} as mentioned in Section 4.2.4.

4.3.6.4 Loading grips

As mentioned before, the specimen assembly can accommodate various specimens by only changing the loading grips as long as the loading grips had the same 31.75 mm (1.25 inch) diameter threaded bars at both ends to match the universal connections. Since aluminum

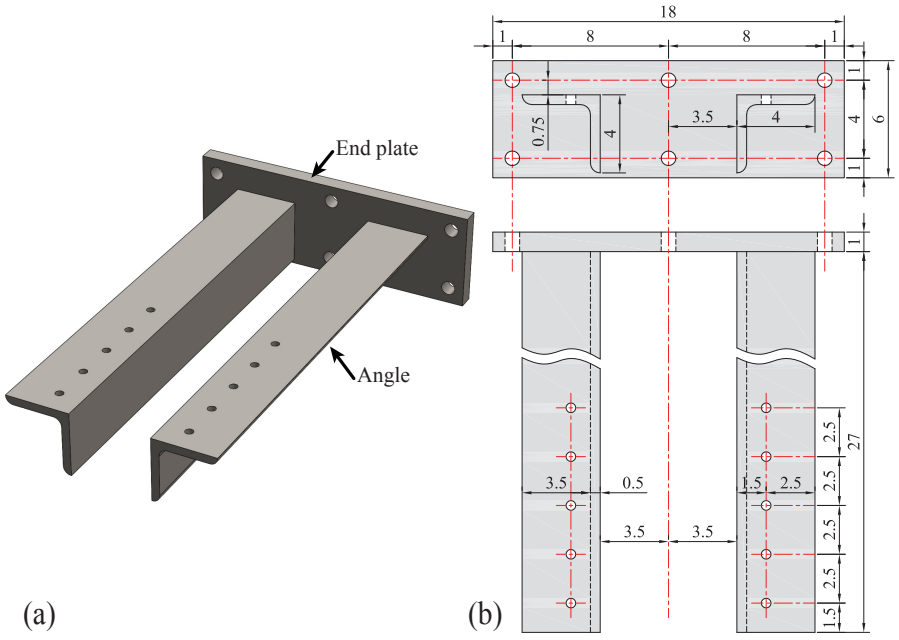

Figure 68: Design of the rail support: (a) perspective view and (b) top and front view (units: inch).

bolted flat tensile specimens were utilized in the validation tests of the system, the corresponding load grips were designed as shown in Figure 69 with a 31.75 mm (1.25 inch) diameter threaded blind hole at the end. The specimen was bolted to the main aluminum block with a 12.7 mm (0.5 inch) diameter high-strength bolt with a washer plate on the other side of the specimen. Two additional bolts, connecting the washer plate and the main block, reduced the stress concentration around bolt holes.

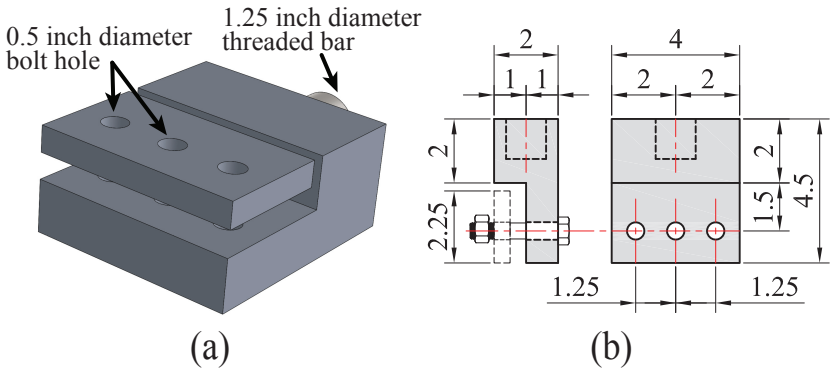

Figure 69: Design of the loading grip for bolted flat specimens: (a) perspective view and (b) top and side view (units: inch).

4.3.6.5 Installation of the specimen assembly

Figure 70 shows the whole specimen assembly after installation of all parts. The fixed parts included the rail support bolted to the external mounting plate, the sliding rail bolted to the rail support, and one loading grip fixed to the external mounting plate. The moving parts included the ball joint connector, the load cell, and the other loading grip installed between the load cell and the specimen. During tests, all fixed parts theoretically remained fixed while all moving parts moved away from the mounting plate.

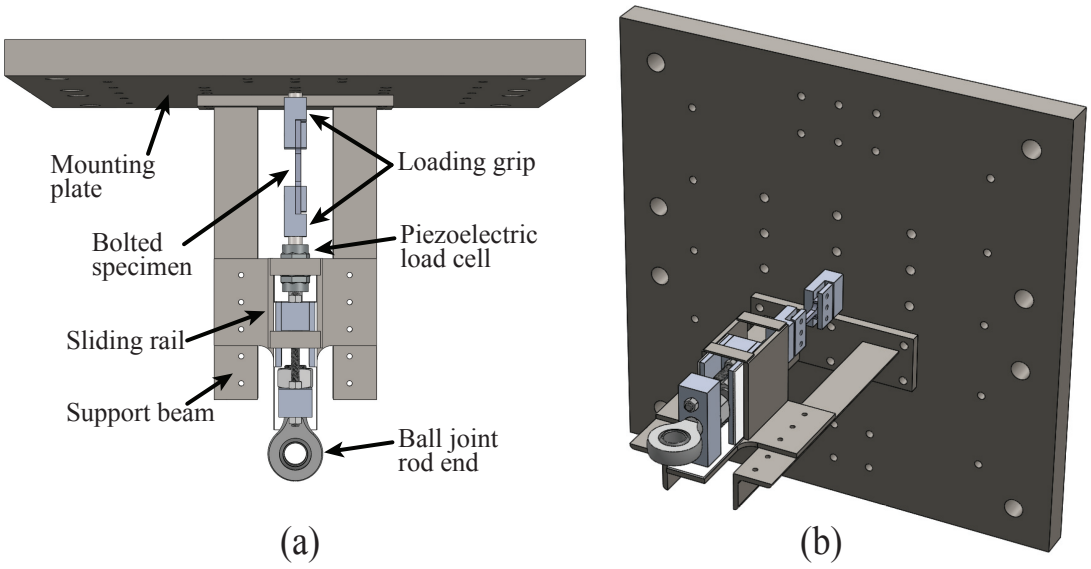

Figure 70: Specimen assembly: (a) top view and (b) perspective view.

4.3.7 Adjustable intended slack distance

The main purpose of adding an intended slack into the specimen assembly is to achieve a more constant loading rate and to provide more flexibility in testing setups. The demand of a nearly constant loading rate indicates that the loading grip at the moving end needs to travel at a nearly constant velocity. To achieve a certain high velocity corresponding to a certain strain rate, the loading grip has to be accelerated from an initial zero velocity to that target high velocity. During the time of this acceleration, the loading grip already starts to move, and the specimen already starts to deform. However, the loading rate is still relatively low since the loading grip has not reached the targeting velocity yet. As

a result, the beginning part of the deformation of the specimen occurs under a relatively low loading rate. After the loading grip has been fully accelerated, the later part of the deformation occurs under a relatively high loading rate. Therefore, the loading rate of the specimen is not constant. To mitigate this drawback, an intended slack is incorporated into the connection as shown in Figure 66 and Figure 71.

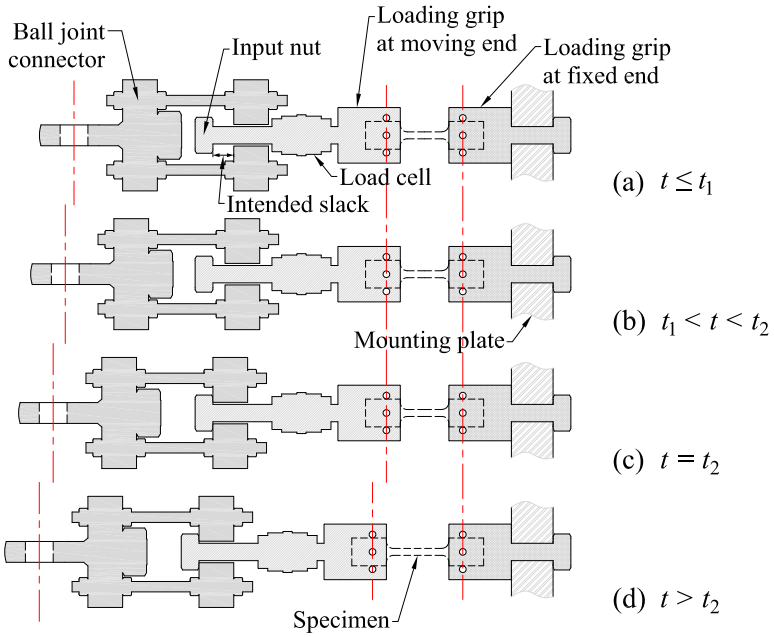

Figure 71: Mechanism of intended slack: (a) ball joint connector started to move, (b) ball joint connector moved freely through the slack distance, (c) ball joint connector engaged with the input nut, and (d) loading grip at moving end started to move.

Figure 72 schematically shows the movement of the components on the two sides of the intended slack: ball joint connector on one side and load cell plus loading grips on the other side. Time t_0 is defined as when the impacting mass hits the input end of the loading frame. At time t_1, the output end of the loading frame starts to move and the ball joint connector, which is connected to the output end, starts to be accelerated from zero velocity. Between time t_1 and t_2, the ball joint connector moves freely since the output block is not engaged to the input nut of the load cell with the intended slack in between. The ball joint connector keeps being accelerated and reaches a relatively high velocity after traveling the full distance of the slack. At time t_2, the ball joint connector contacts with the input nut of the load cell and starts to pull the load cell and specimen all together. At this time,

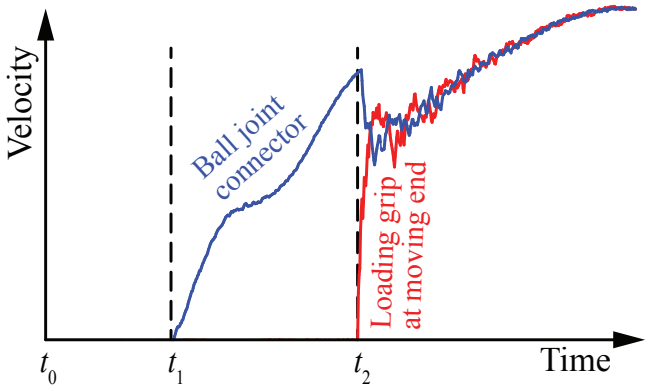

Figure 72: Schematic drawing of the change of velocity of ball joint connector and the loading grip at moving end.

because the ball joint connector is traveling at a high velocity and is striking onto the input nut, the specimen is being stretched at a relatively high initial loading rate instead of slowly accelerated from zero. Eventually, the connector and the load cell reach the same velocity and travel together until the specimen is loaded to its peak deformation.

This design of this intended slack distance also increases the flexibility of the tensile testing system. By adjusting the distance of this slack, the velocity at which the ball joint connector impacts onto the input nut changes accordingly. As a result, the loading rate of the specimen can be controlled by just adjusting the slack distance without changing other parts of the system. If needed, soft materials such as copper and rubber can also be placed inside the gap to tailor the duration time of the impact between the ball joint connector and the input nut.

4.3.8 Test instrumentations

The displacement, velocity, pressure, and the impact force of the high-speed actuator were monitored by its own instrumentation system consisting of position transducers, stroke transducer, pressure transducers, and accelerometers [127]. Additional instrumentation were added to measure the response of the specimen.

The deformation of the specimen was measured by high-speed cameras. A typical test utilized two high-speed cameras: Miro M310, which captured the response of the specimen assembly, and Miro C110, which captured the movements of the impact mass. The sampling

rates of Miro M310 and Miro C110 were set as 4100 fps and 1200 fps, respectively. The captured video were then post-processed by motion tracking software to reconstruct the displacement time history of the targets attached onto the impact mass and specimen assembly.

The force of the specimen was measured by a piezoelectric PCB 227C load cell. The maximum tensile capacity of this load cell was 133.4 kN (30 kip). A Synergy P portable data acquisition system with a maximum sampling frequency of 2 MHz was connected to the load cell. In this research, the sampling rate of the load cell was set as 500 kHz. The cameras and the load cell were activated by the same trigger so that the measured deformation and force results were synchronized with the same elapsed time.

4.4 Fabrication and installation

4.4.1 Fabrication of individual components

Figure 73: Photos of individual components of the inverter mechanism under fabrication.

All the structural components were fabricated at the machine shop of the School of Civil and Environmental Engineering at Georgia Tech. Aluminum plates were cut and drilled by a water jet as shown in Figure 73(a). All contact surfaces were machined to a snug fit to reduce friction and minimize misalignment as much as possible. For example, Figure 73(b) shows the rotation mechanism between the aluminum tube of Joint A and the steel pivot rod. When welding Joint A together as shown in Figure 73(c), a dummy rod was inserted into the bronze bearing as a template to reduce potential dimension changes caused by temperature effects of welding. Figure 73(d) shows the completed joints with bronze bearing, top connection of roller supports, and custom-made clevis pins attached.

4.4.2 Installation of the system

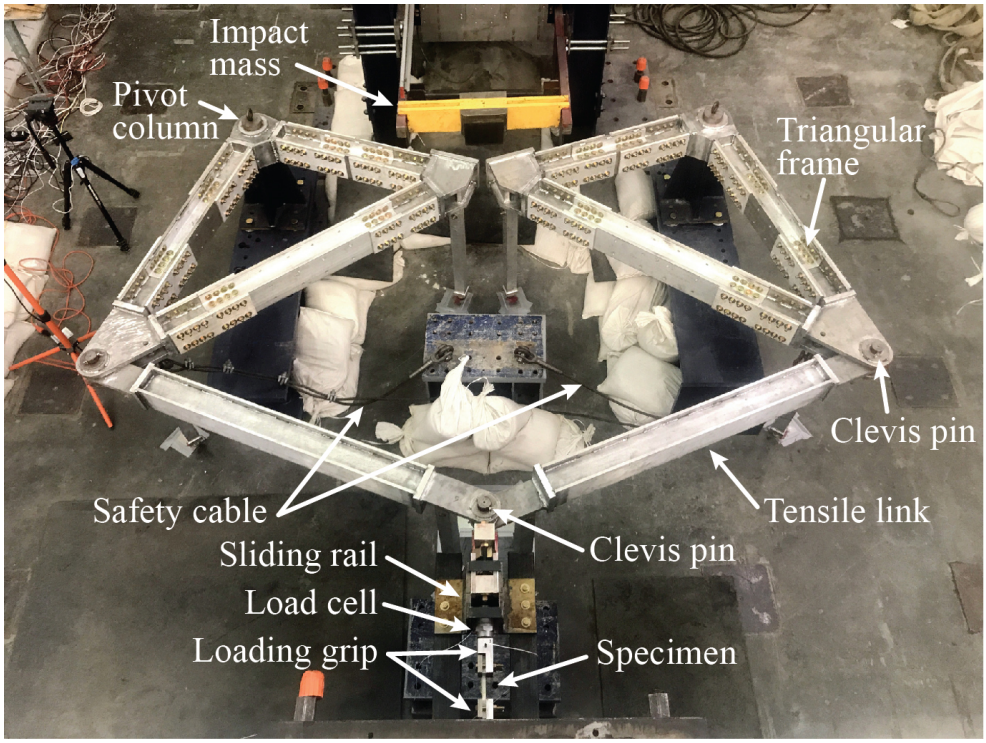

Figure 74: Photo of the whole testing system after assembly and installation.

The components were assembled on site of the testing area as shown in Figure 74 and Figure 75 . Two safety cables were installed to limit the maximum movement of the mechanism. Each cable was connected to Joint B at one end and a fixed steel beam anchored to the strong floor at the other end. The safety cables had enough slack so that they did

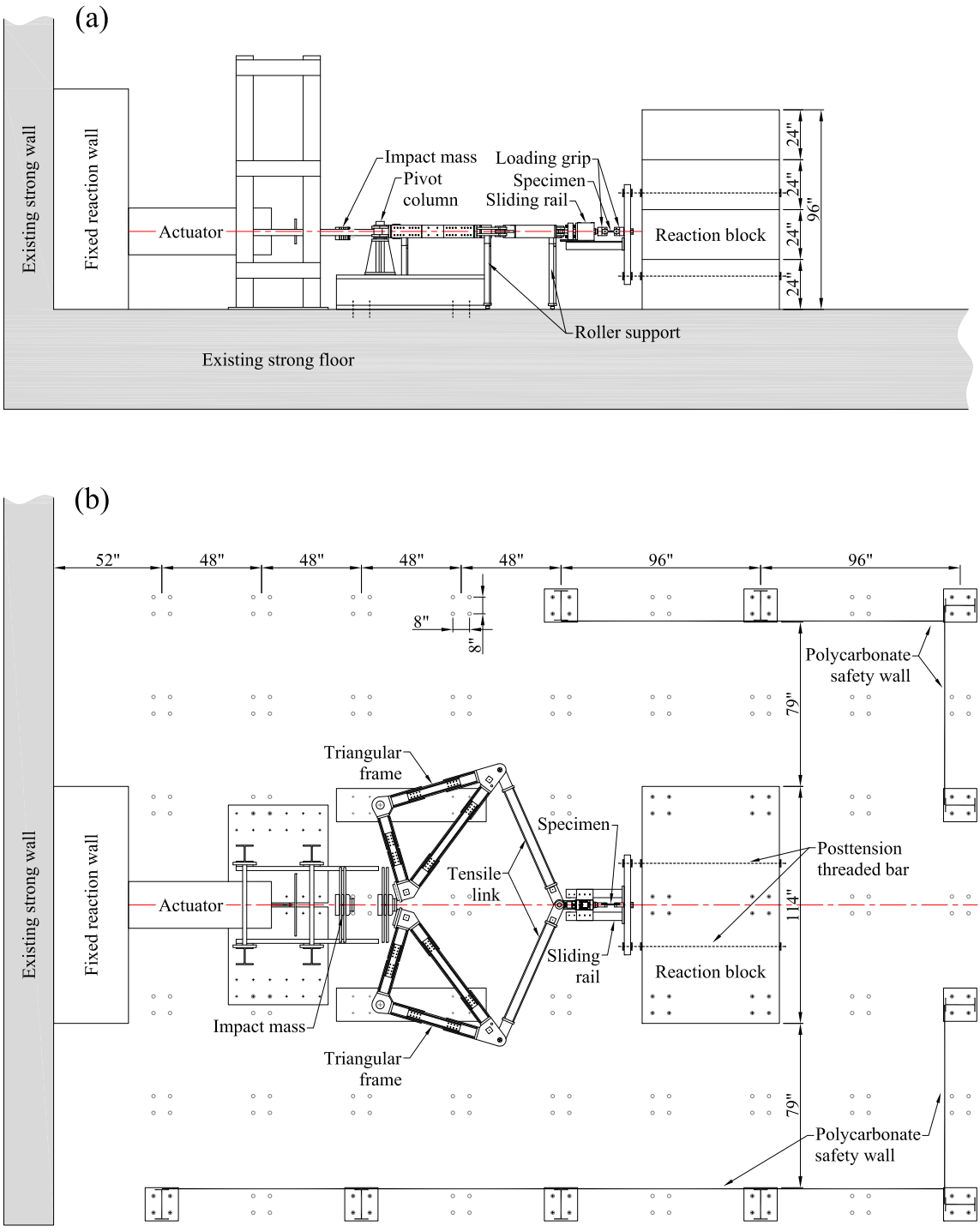

Figure 75: Overall configuration of the high-loading-rate tensile testing system installed in the testing area: (a) side view and (b) plan view (units: inch).

not provide any resistance during tests. However, if excessive displacement happened in the inverter mechanism, the safety cables would engage and provide additional reaction force to the system. Sand bags were placed around the foundation beams and below the impact mass rails to mitigate the potential damage caused by the dropping impact mass. High-speed cameras and additional lighting were mounted onto tripods on the side of the inverter mechanism and specimen assembly.

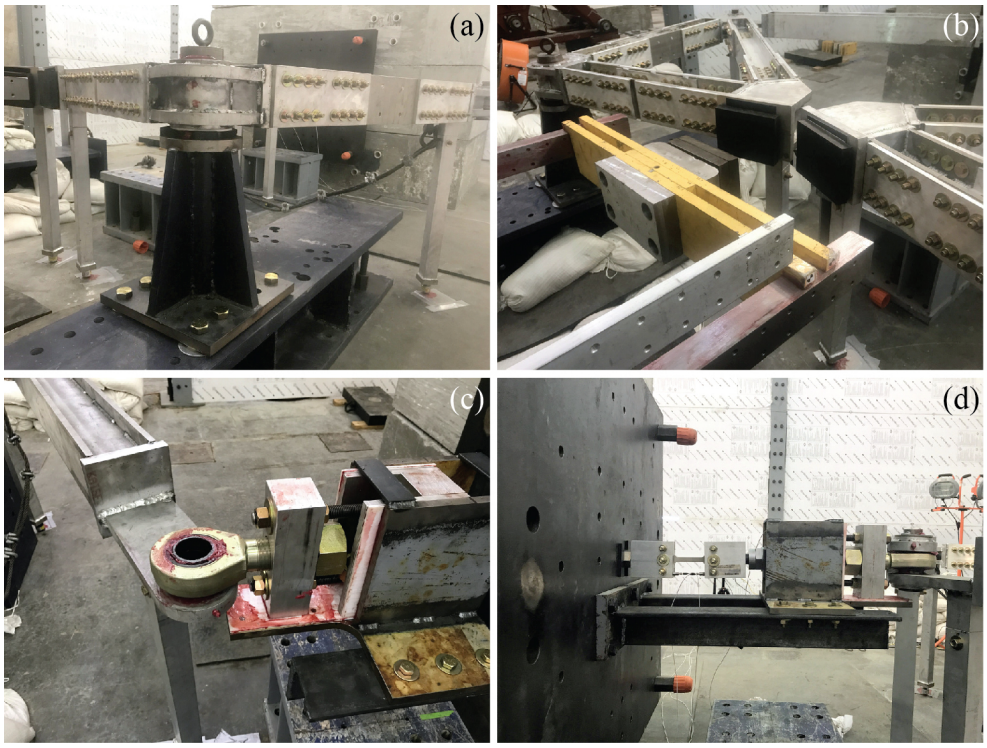

Figure 76: Photos of the testing system during and after installation

As shown in Figure 76(a), the pivot columns were leveled by shims and washers to ensure that the rotation plane of the inverter frames was as close to the horizontal plane as possible. Neoprene shim plates were also inserted between Joint A and the flange plate of the pivot column to adjust height of the inverter frame. Ball transfers at the bottom of the roller supports were adjusted by threading in-to or out-of the end plate to match the final height of the inverter frame. Figure 76(a) also shows the stainless steel sheet with lubricant attached to the floor under each roller support to reduce friction. Safety cable was connected to Joint B through a shackle and an eye bolt as shown in 76(a). Both the impact plate of Joint B and the front surface of impact mass were covered with neoprene

pads as shown in Figure 76(b). The purposes of attaching neoprene pads were to avoid direct impact between metal materials and adjust the time duration of the impact loading. The ball joint connector inside the sliding rail is shown in Figure 76(c). Grease lubricant was applied onto the plastic sheet on the T-shaped plate of the sliding rail and on the side of the ball joint connector. Figure 76(d) shows the specimen assembly with an aluminum bolted flat tensile specimen installed.

4.5 Validation tests

The high-loading-rate tensile testing system was validated and calibrated before actual tests on SMA-based components. Several aluminum specimens were tested to assess the performance of this new testing system. The instrumentation and the data acquisition system were also examined in these validation tests. The behaviors and responses of the testing system obtained in the validation tests were then used as the benchmark in the calibration of a finite element simulation discussed in Section 4.6.

4.5.1 Experimental design of the validation tests

Aluminum bolted flat tensile specimens were used in the validation tests. All specimens were cut from one aluminum 6061 alloy plate with a thickness of 12.7 mm (0.5 inch) by a water jet. As Figure 77 shows, the gage length of the specimen was 76.2 mm (3 inch), and the cross section of the specimen was 12.7 mm × 12.7 mm (0.5 inch × 0.5 inch).

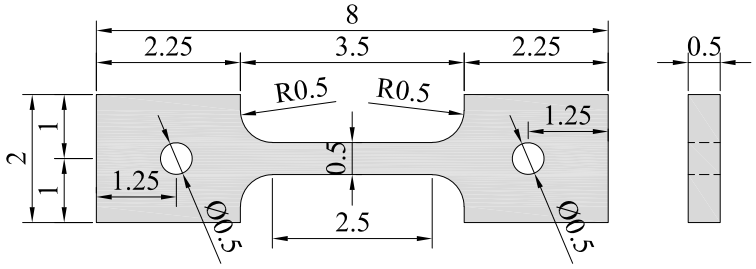

Figure 77: Design of the aluminum tensile specimen used in validation tests (units: inch).

A total of five specimens were tested using the new high-loading-rate tensile testing system in six tests. The specimen in the first test was repeatedly used in the second test. Impact mass, impact velocity, and slack distance were the three key parameters of initial

conditions. These input parameters for all the tests are listed in Table 3. The test numbers were named based on initial conditions. The first upper case letter, A, B, and C, represented three combinations of impact mass and impact velocity. The following lower case letter, a and b, represented different slack distances under the same impact mass and impact velocity.

Table 3: Initial conditions of validation tests on aluminum specimens.

Test No.	Impact mass (kg)	Targeting impact velocity (m/s)	Slack distance (mm)
A-0	139.82	5.0	12.7
A	139.82	5.0	12.7
B-a1	87.12	5.0	12.7
B-a2	87.12	5.0	12.7
B-b	87.12	5.0	6.35
C	87.12	7.0	0

4.5.2 Experimental results of the validation tests

For each test, deformation, force, energy, and impulse were obtained from measured results. The methods of processing and interpolating test results were introduced step by step for Test A-0 and Test A. The results for rest of the tests were handled with the same methods.

4.5.2.1 Experimental results of Test A-0

Test A-0 was the first shake down test of the new testing system. Since the performance and response of the inverter mechanism were untested, excess safety measures were taken to protect both personnel and instruments. The PCB 227C piezoelectric load cell was replaced with a high-strength steel threaded bar with similar length to avoid potential damage to the load cell. That was possible if the force transformed from the inverter mechanism reached beyond the load cell's maximum capacity, which was 133.4 kN (30 kip). The Miro M310 camera was fastened to a tripod that was safely attached to a scissor lift, which can be operated remotely on the ground. Before the test, the scissor lift raised the camera above the top of the safety wall, from where the camera monitored the overall movement of the inverter mechanism. The Miro C110 camera was positioned on the side of the specimen

assembly to capture the displacements of the loading grips.

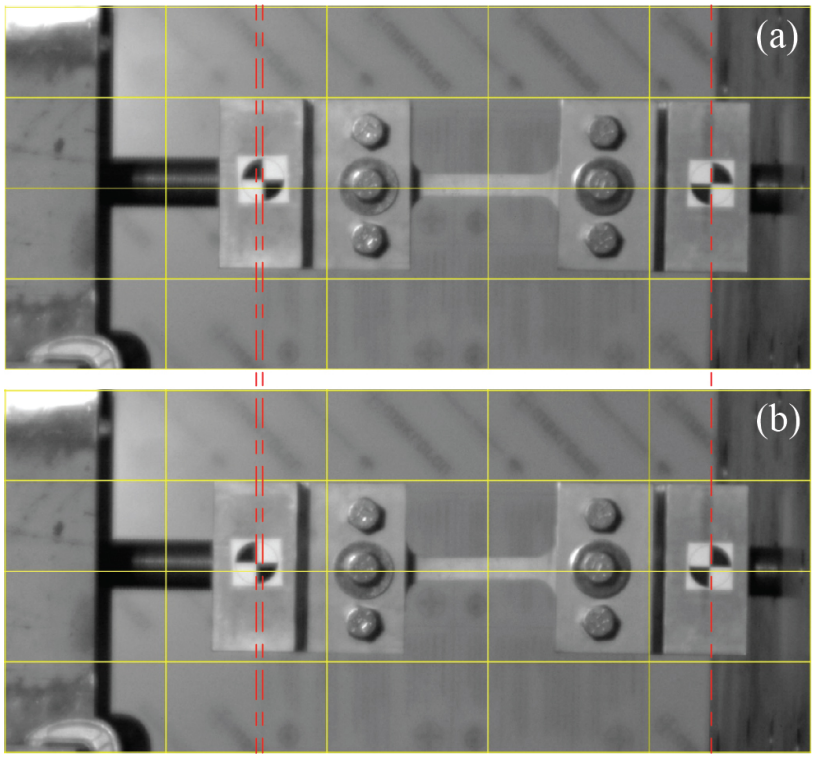

Figure 78: Displacement of targets in Test A-0 in captured high-speed video: (a) before test and (b) when specimen reached its maximum deformation.

Before testing, 25.4 mm (1 inch) diameter targets were attached onto each loading grip. From the video captured by the Miro C110 camera, the displacements of the targets were obtained using Pro-Analyst motion analysis software. Figure 78 shows the frames from the video captured by the Miro C110 camera. Red dashed reference lines were added to exhibit the movement of the targets on the loading grips. Clearly visible movement of the loading grip at the moving end was observed.

The deformation of the specimen was calculated as the displacement of the input loading grip minus the displacement of the output displacement as plotted in Figure 79. The maximum deformation of the specimen was 3.57 mm, and the residual deformation after the peak deformation was around 1.5 mm. Because the specimen assembly was connected to the external mounting plate by a nut on the back of the mounting plate, only the movement away from the mounting plate was restricted. As a result, after the specimen reached its maximum deformation, the entire specimen assembly bounced back, changed its direction

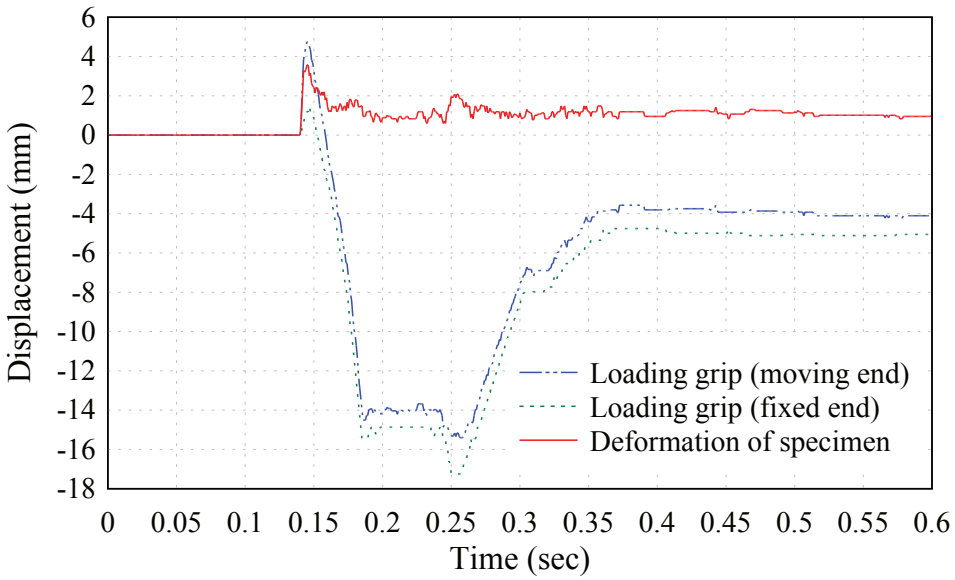

Figure 79: Displacement of the loading grips and deformation of specimen in Test A-0.

of movement, and struck back onto the mounting plate. That bouncing back and impacting onto the mounting plate corresponded to the increasing negative displacement of the loading grips from time 0.16 s to 0.25 s. After the specimen assembly impacted onto the mounting plate, it bounced back again, moved away from the mounting plate, and eventually stopped. These corresponded to the decreasing negative displacement from time 0.25 s to the end of the test.

Figure 80 shows the deformation time history of the specimen during loading and unloading. The deformation result had a frequency of 1,200 s^{-1} because the video was taken by the 1,200 fps Miro C110 camera. Therefore, the time interval Δt of the displacement time history was 1/1,200 s, which equaled 0.00083 s.

The dashed line in Figure 80 was the linear regression result of the loading part. As this line shows, the loading part had a nearly constant deformation rate $\dot{u}$ of 1,320 mm/s. The intended 12.7 mm (0.5 inch) slack distance was effective in obtaining a constant loading rate. Since the gage length L of the specimen was 63.5 mm (2.5 inch), the average nominal strain rate was calculated as

$$\dot{\varepsilon} = \frac{\dot{u}}{L} = \frac{1,320\,\text{mm}\cdot\text{s}^{-1}}{63.5\,\text{mm}} = 20.8\,\text{s}^{-1} \tag{63}$$

As expected, this nominal strain rate belongs to intermediate strain rates ranging from

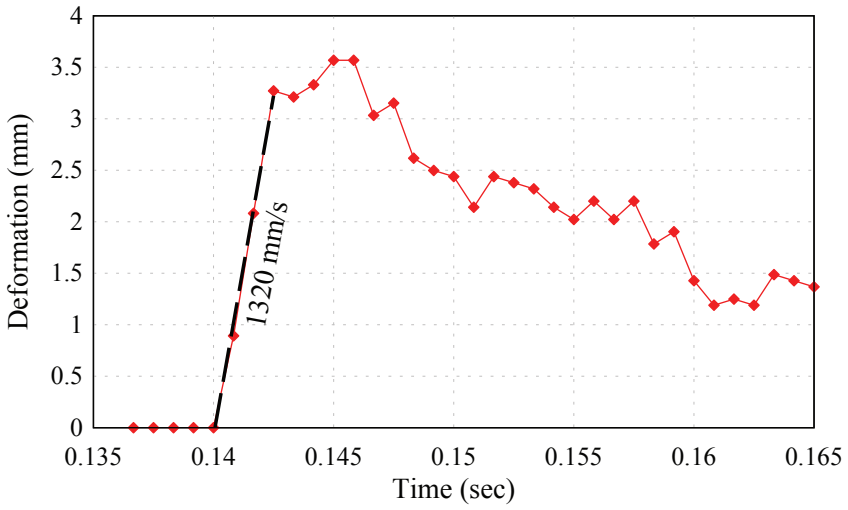

Figure 80: Deformation of the specimen in Test A-0.

1 to 100 s^{-1}.

4.5.2.2 Experimental results of Test A

Base on the results of Test A-0, it was reasonable to assume that the force during the test was under 133.4 kN (30 kip), which was the maximum allowable force of the PCB 227C piezoelectric load cell. Therefore, the load cell was installed onto the system for Test A. Camera Miro M310, which had a higher sampling rate of 4,100 fps, was set to capture the response of the specimen assembly. The other camera, Miro C110, with a lower sampling rate of 1,200 fps, was relocated to monitor the movement of the impact mass.

With the same method as Test A-0, the deformation of the specimen in Test A was obtained from the video captured by Miro M310 camera. Because of the switch in cameras, the sampling rate of the deformation was increased from 1,200 fps in Test A-0 to 4,100 fps in Test A. The time interval Δt for Test A was decreased to 2.44×10^{-4} s accordingly. As shown in Figure 81, the deformation rate of the specimen is $1,423$ m/s corresponding to an average strain rate of $22.4\,s^{-1}$.

The sampling rate of the PCB 227C load cell was set at 50 kHz. The measured force results are shown in Figure 82. To remove the noise in the measured data caused by high frequency oscillations, the force data was filtered with a low pass Butterworth filter. The cutoff frequency was set as 4 kHz, which was the upper frequency limit suggested by the

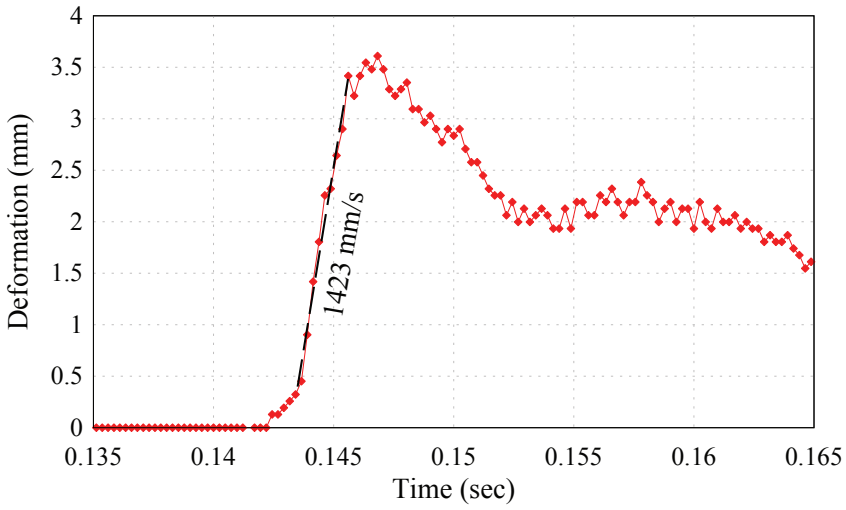

Figure 81: Deformation of the specimen in Test A.

manufacturer of the piezoelectric load cell. Figure 82 demonstrates that the filter effectively removed the high frequency noise while at the same time did not affect the overall force data.

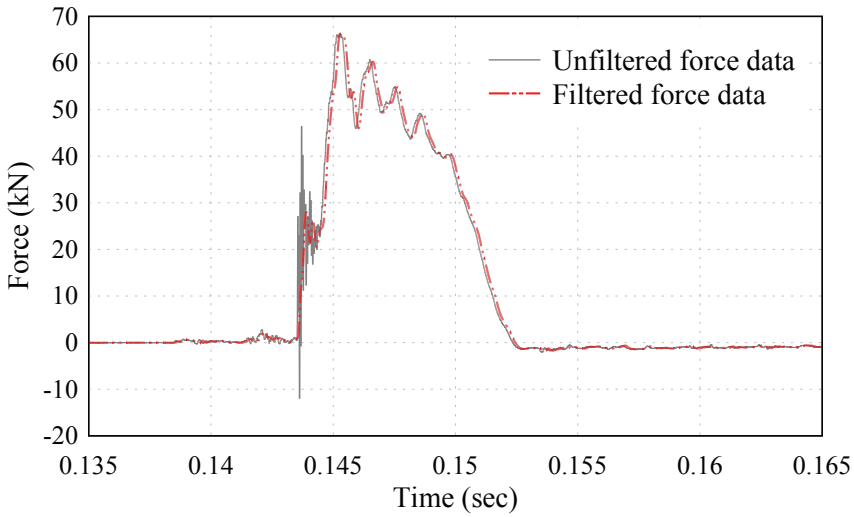

Figure 82: Unfiltered and filtered force results in Test A.

The camera and the load cell were controlled by the same DAQ system, and their measured results were synchronized to the same elapsed time. As a result, the deformation and the force of the specimen at each corresponded time point were obtained. Figure 83 shows both the deformation and the force time history in the same plot. The deformation

and force both increased from zero to peak values approximately in constant rates. After that, the force decreased back to zero again with some oscillations. Because the specimen was loaded beyond its yield strain, plastic deformation had already developed. Rather than decreased all the back to zero, the deformation only dropped back to the value of residual deformation, which was around 2 mm.

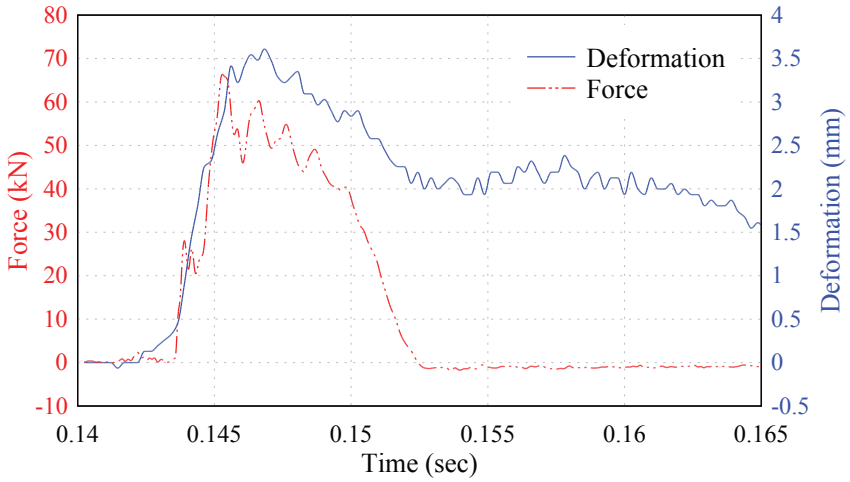

Figure 83: Force and deformation time history of the specimen in Test A.

From deformation, u, force, P, and time, t, the energy, E, absorbed by the specimen was calculated as

$$E = \int P du \tag{64}$$

and the impulse, I, applied onto the specimen was calculated as

$$I = \int P dt \tag{65}$$

The calculated energy and impulse of the specimen in Test A are plotted in Figure 84(a) and Figure 84(b), respectively.

As shown in Figure 84(a), the energy increased from zero at 0.1436 s, when the specimen started to deform, and reached to peak energy at 0.1468 s, when the specimen reached its peak deformation. After that, energy decreased from its peak value of 121 kN·mm to a steady value of 72 kN·mm, which was the remaining plastic energy that was absorbed by the specimen. The difference between the peak energy of 121 kN·mm and the plastic energy of 72 kN·mm was the elastic energy of 49 kN·mm released during elastic unloading.

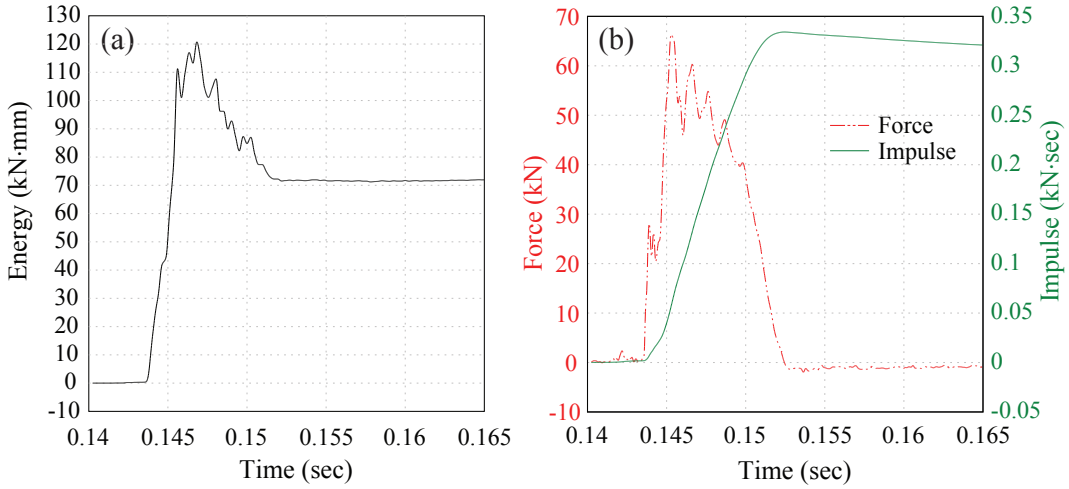

Figure 84: Energy and impulse time history of the specimen in Test A.

As shown in Figure 84(b), because impulse was calculated as the intergration of force, the impulse started increasing when the force of the specimen started to increase at 0.1436 s and reached its peak value of 0.334 kN·s when the force dropped back to zero at 0.1525 s. After that, the impulse decreased and eventually dropped back to zero.

4.5.2.3 Experimental results of Test B-a1 and B-a2

As shown in Table 3, Test B-a1 and B-a2 had identical initial conditions, including impact mass, impact velocity, and slack distance. Compared with Test A, Test B-a1 and B-a2 had a reduced impact mass. Other initial conditions were all the same as Test A. Figure 85 and Figure 86 show the deformation, force, energy, and impulse results of Test B-a1 and Test B-a2, respectively.

In Test B-a1, the specimen started to deform at 0.1562 s and reached its peak deformation of 2.57 mm at 0.1602 s. Tensile force and energy also reached their peak values at this time. The peak force was 53.46 kN, and the peak energy was 65.07 kN·mm. After that, the deformation declined to a permanent residual deformation of 0.85 mm, and the energy dropped to plastic energy of 15.5 kN·mm, both at 0.1656 s. At that time, the tensile force dropped back to zero, and the impulse reached its peak value of 0.258 kN·s. After that, the deformation, force, and energy remained the same while the impulse eventually declined to zero.

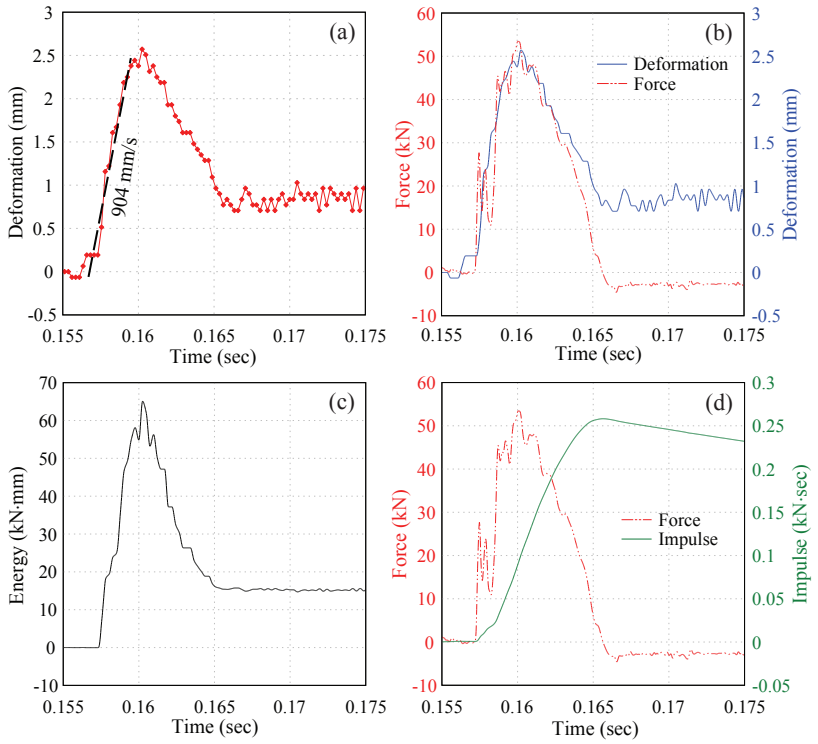

Figure 85: Experimental results of Test B-a1: (a) deformation, (b) force, (c) energy, and (d) impulse of the specimen.

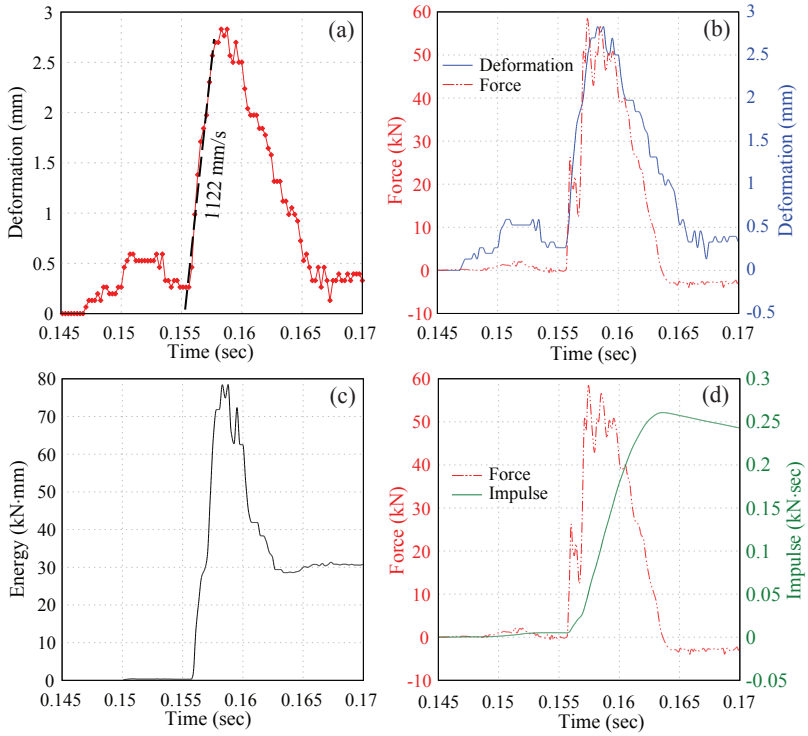

Figure 86: Experimental results of Test B-a2: (a) deformation, (b) force, (c) energy, and (d) impulse of the specimen.

In Test B-a2, the specimen started to deform at 0.1468 s. However, the force did not increase at that time, indicating that this deformation was related to the closing of some initial gaps caused by misalignment in the test setups of the specimen assembly rather than the deformation of the specimen itself. At 0.1556 s, force started to increase, and the specimen started to be loaded. The specimen reached a peak force of 58.49 kN at 0.1574 s. The deformation reached its peak value of 2.83 mm, and the energy reached its peak value of 65.07 kN·mm, both at 0.1583 s. Then the tensile force dropped back to zero, and the impulse reached its peak value of 0.261 kN·s, both at 0.1636 s. The deformation declined to a permanent residual deformation of 0.39 mm, and the energy dropped to plastic energy of 30.8 kN·mm.

4.5.2.4 Experimental results of Test B-b

As shown in Table 3, Test B-b1 had the same impact mass and impact velocity as Test B-a1 and B-a2. However, the slack distance of Test B-b was reduced to 6.35 mm (0.25 inch). Figure 87 shows the results of Test B-b.

In Test B-b, both the deformation and the force started to increase at 0.1536 s. The deformation reached its peak value of 2.78 mm, and the energy reached its peak value of 83.05 kN·mm, both at 0.1568 s The force reached its peak value of 56.34 kN at 0.1564 s. The deformation then declined to its permanent residual value of 1.40 mm, and the energy dropped to plastic energy of 51.2 kN·mm, both at 0.1618 s. Around that time, tensile force dropped back to zero, and the impulse reached its peak value of 0.283 kN·s.

4.5.2.5 Experimental results of Test C

For Test C, the impact velocity was increased to 7.0 m/s and the slack distance was decreased to zero. The impact mass was the same as Test B-a1, B-a2, and B-b. Figure 88 shows the results of Test C.

In Test C, the deformation started to increase at 0.1221 s while the force started to increase before the time 0.12 s. That was because Test C had zero slack distance and the increase of displacement at the very beginning was slower than previous tests with slack distances. Therefore, the increase of deformation fell behind the increase of force. The

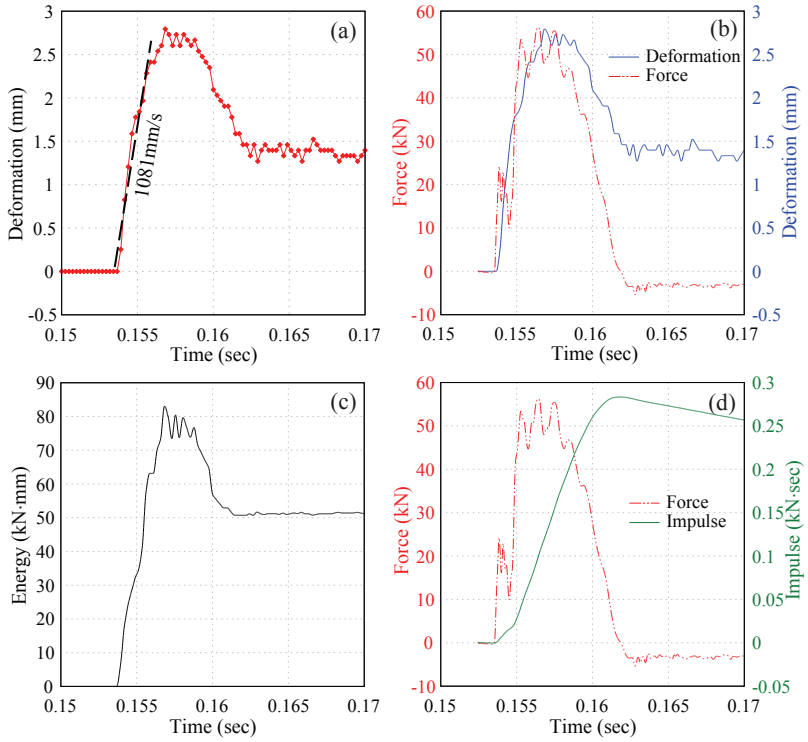

Figure 87: Experimental results of Test B-b: (a) deformation, (b) force, (c) energy, and (d) impulse of the specimen.

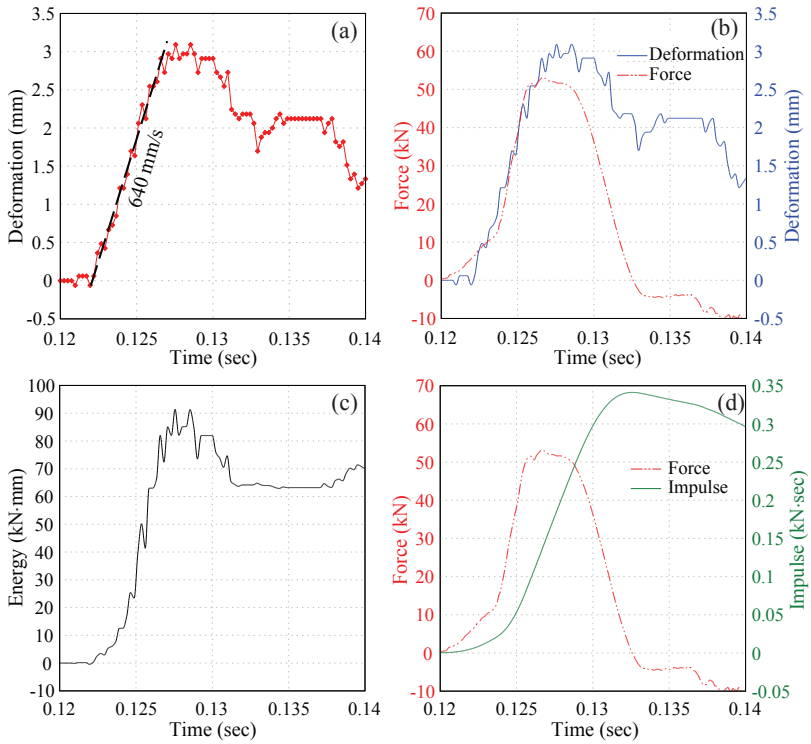

Figure 88: Experimental results of Test C: (a) deformation, (b) force, (c) energy, and (d) impulse of the specimen.

specimen reached its peak force of 91.39 kN at 0.1267 s and reached its peak deformation of 3.09 mm and peak energy of 91.39 kN·mm both at 0.1276 s. The deformation then declined to its permanent residual value of 2.12 mm, and the energy dropped to plastic energy of 63.2 kN·mm. At the time 0.1326 s, tensile force dropped back to zero, and the impulse reached its peak value of 0.341 kN·s.

4.5.2.6 Summary of the experimental results

The test results of these validation tests showed the same pattern. Both deformation and force started to increase and reached peak values roughly at the same time. Energy also reached its peak value at that same time as deformation. After that, deformation and energy started to decline until reached their permanent residual values. At that time, force dropped back to zero, and the impulse reached its peak value. Then force, deformation, and energy remained the same while the impulse started to decline until it eventually decreased to zero.

The results of all five validation tests are listed in Table 4.

Table 4: Summary of experimental results of validation tests.

Test result	Symbol	Unit	A	B-a1	B-a2	B-b	C
Peak deformation	u_{total}	mm	3.61	2.57	2.83	2.78	3.09
Residual deformation	u_p	mm	2.05	0.85	0.39	1.40	2.12
Deformation rate	$\dot{u}$	mm/s	1423	904	1122	1081	640
Peak force	$P_{\max}$	kN	66.36	53.46	58.49	56.34	53.23
Peak impulse	$I_{\max}$	kN·s	0.334	0.258	0.261	0.283	0.341
Peak energy	E_{total}	kN·mm	120.75	65.07	78.48	83.05	91.39
Plastic energy	E_p	kN·mm	72.0	15.5	30.8	51.2	63.2
Elastic energy	$E_{total} - E_p$	kN·mm	48.75	49.6	47.7	31.85	28.19

4.5.3 Validation of the experimental results

The experimental results from different instruments were compared with each other to verify the accuracy of measurements. The measured responses of the specimen were also compared with theoretical estimation to validate the experimental design of this new testing system.

4.5.3.1 Validation of the impact velocity measurement

Two 12.7 mm (0.5 inch) targets were attached onto the lateral surface of the support blocks of the impact mass. The impact velocity was verified by the displacement time history of these targets obtained from the high-speed camera video. Figure 89 shows the frames of the moving impact mass during tests.

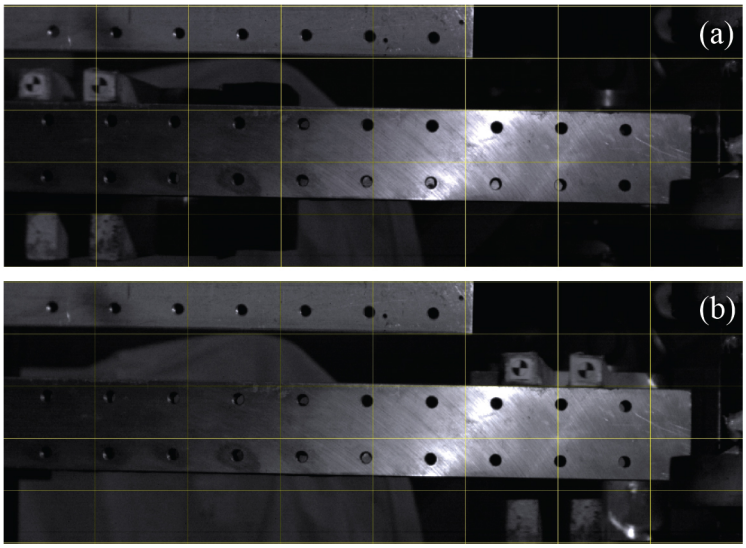

Figure 89: Frames of the impact mass moving along the rail from high-speed camera video.

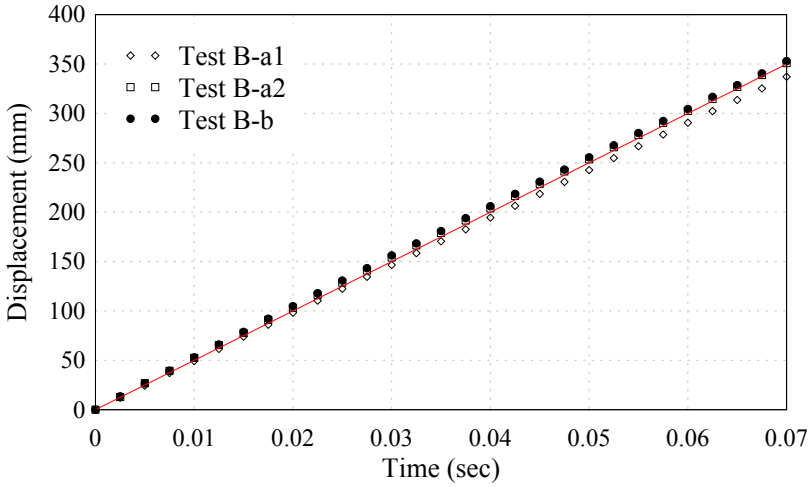

Figure 90: Displacement of the impact mass in Test B-a1, B-a2, and B-b.

Figure 90 shows the measured displacement of the impact masses of Test B-a1, B-a2, and B-b1 with synchronized time. The impact velocities from the videos were close to the

target velocity 5 m/s, which is also shown in Figure 90 as a solid line. This comparison shows that the high-speed actuator generated desired impact velocity in a controllable and repeatable manner.

4.5.3.2 Validation of the residual deformation

The residual deformation measurements were validated by measuring the deformed specimens after tests. For example, in Test A, the residual deformation obtained from the motion tracking results of high-speed video was 2.05 mm. This was confirmed by measuring the increased length of the specimen after test as shown in Figure 91.

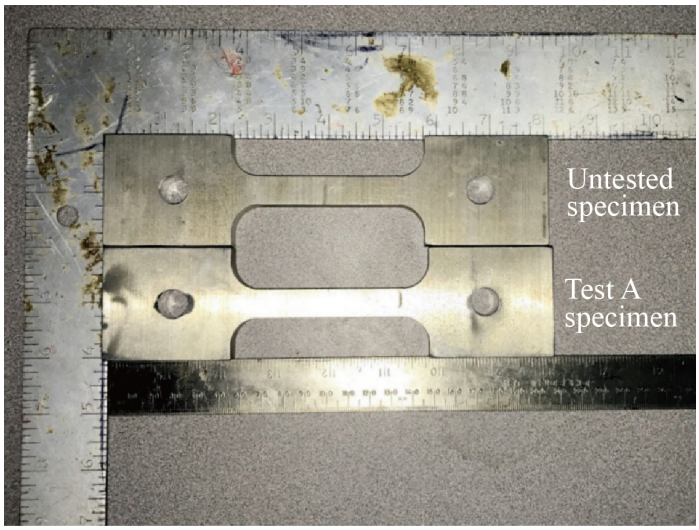

Figure 91: Photo of the comparison between an untested specimen and the specimen tested in Test A.

4.5.3.3 Validation of stress-strain results

Assuming the stress and strain were uniformly distributed along the section area and the gage length of the specimens, from the measured deformation, u, and force, P, the nominal stress, σ, and nominal strain, ε, were derived as

$$\sigma = \frac{P}{A_{section}} \tag{66}$$

and

$$\varepsilon = \frac{u}{L_{gage}} \tag{67}$$

The nominal stress and strain relations from Test A, Test B-a1, Test B-a2, and Test B-b are plotted in Figure 92 with average nominal strain rates labeled. Because of the oscillation of force data at the beginning portion of the loading process, the stress-strain curve at the beginning also oscillated around the actual value. Based on the assumption that the material was in the linear elastic range when the strain was very low, the stress-strain at the very beginning can be re-constructed by elongation of the stress-strain curve back from high strain range. These re-constructed linear stress-strain relations are shown as dotted lines in Figure 92. Each specimen was elongated under a constant loading rate. Because the elastic modulus was related to the loading rate, a constant loading rate indicated a constant elastic modulus. Therefore, the assumption that stress-strain around the very beginning can be re-constructed using the same elastic modulus was valid.

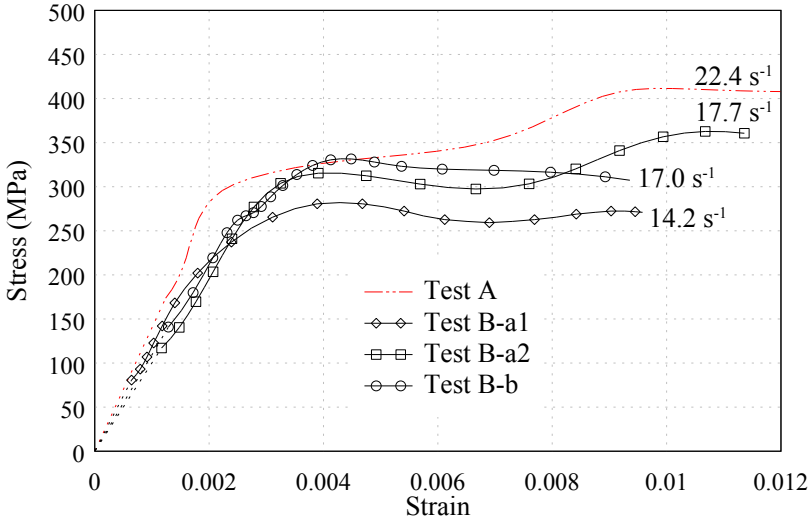

Figure 92: Nominal stress and strain results obtained in Test A, B-a1, B-a2, and B-b.

From Figure 92, the elastic modulus and the 0.2% offset yield strength were calculated and were listed in Table 5. Although the differences in average nominal strain rates were not significant, the yield strength still showed the tendency to increase as the strain rate increased. Aluminum 6061 alloy has a nominal elastic modulus of 68.95 GPa (10,000 ksi) and a nominal yield strength of 275.79 MPa (40 ksi). Compare with quasistatic nominal material properties, the elastic modulus under intermediate strain rates were significantly higher. The yield strength also increased when the loading rate increased from quasistatic to

Table 5: Elastic modulus and yield strength results from validation tests.

Test	Average nominal strain rate (s^{-1})	Elastic modulus (GPa)	0.2% offset yield strength (MPa)
Test A	22.4	139.99	329.9
Test B-a2	17.7	100.21	308.9
Test B-b1	17.0	109.31	327.2
Test B-a1	14.2	125.35	281.5

intermediate strain rates. For example, in Test A, the elastic modulus was 103% more than the quasistatic elastic modulus while the yield strength was 20% more than the quasistatic nominal yield strength. This increase in yield strength confirmed with the adoption of dynamic increase factor (DIF) in current blast design [100].

4.5.3.4 Validation of energy results

Energy results from experimental data were verified with theoretical estimations. The total energy density and plastic energy density were estimated from measured deformation and nominal material properties.

For example, in Test A, the peak total deformation u_{total} was 3.61 mm and the residual plastic deformation u_p was around 2.05 mm as shown in Figure 83. Therefore, the total nominal strain of the specimen was

$$\varepsilon_{total} = \frac{u_{total}}{L} = \frac{3.61\,\text{mm}}{63.5\,\text{mm}} = 0.0569 \tag{68}$$

The plastic strain was

$$\varepsilon_p = \frac{u_p}{L} = \frac{2.05\,\text{mm}}{63.5\,\text{mm}} = 0.0323 \tag{69}$$

The nominal elastic modulus and yield strength of aluminum 6061 alloy were estimated as 68.95 GPa (10000 ksi) and 275.8 MPa (40 ksi), respectively. The yield strain was estimated as

$$\varepsilon_y = \frac{275.8\,\text{MPa}}{68.95\,\text{GPa}} = 0.0040 \tag{70}$$

Assuming the stress-strain behavior of aluminum 6061 alloy was a elastic-perfectly plastic relation, the total strain energy, which was the energy per unit column, was estimated

as

$$
\begin{aligned}
e_{total} &= \frac{1}{2}\sigma_y\varepsilon_y + \sigma_y(\varepsilon_{total} - \varepsilon_y) \\
&= \frac{1}{2}(275.8\,\text{MPa})(0.0040) + (275.8\,\text{MPa})(0.0569 - 0.0040) \\
&= 15.127 \times 10^{-3}\,\frac{\text{J}}{\text{mm}^3}
\end{aligned}
\tag{71}
$$

The plastic strain energy was estimated as

$$
\begin{aligned}
e_p &= \sigma_y\varepsilon_p \\
&= (275.8\,\text{MPa})(0.0323) \\
&= 8.903 \times 10^{-3}\,\frac{\text{J}}{\text{mm}^3}
\end{aligned}
\tag{72}
$$

The theoretical estimated ratio of plastic to total strain energy was calculated as

$$
\frac{e_p}{e_{total}} = \frac{8.903 \times 10^{-3}\,\frac{\text{J}}{\text{mm}^3}}{15.127 \times 10^{-3}\,\frac{\text{J}}{\text{mm}^3}} = 0.589 \tag{73}
$$

This theoretical estimation was then compared with the experimental results. From Figure 84(a), the total energy E_{total} was 120.75 kN·mm, and the plastic energy E_p was 72.0 kN·mm. The ratio of plastic to total energy from experimental results was

$$
\frac{E_p}{E_{total}} = \frac{72.0\,\text{kN}\cdot\text{mm}}{120.75\,\text{kN}\cdot\text{mm}} = 0.596 \tag{74}
$$

The plastic to total energy ratios from theoretical estimation and experimental results matched each other within 1.2% difference. Using the same method, the theoretical estimated ratio of strain energy e_p/e_{total} and the experimental ratio of energy E_p/E_{total} were calculated for each test. As shown in Figure 93, the experimental ratios were close to their corresponding theoretical ratios, indicating that the measured experimental results were reasonable from the aspect of energy.

4.5.4 Effect of initial testing conditions on test results

The investigation of the relations between initial test conditions and final test results can provide deeper understanding of the testing system and better guidelines on the decisions of test conditions in future tests. For example, if a certain target of peak deformation needs to be achieved while the current test result has a lower peak deformation than that certain

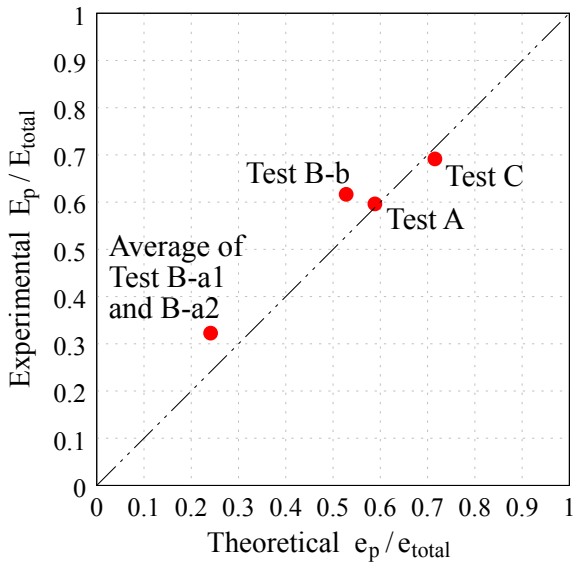

Figure 93: Ratio of plastic energy to total energy from validation tests.

target, guidelines on how to adjust initial conditions are certainly needed. These guidelines reduce the number of iterations in the trial-and-error process because the subsequent test is selected to be on the direction towards that certain target rather than just selected as a random guess.

The initial conditions were determined by three input parameters: impact mass, impact velocity, and slack distance. The input impulse, I_{input}, and input energy, E_{input}, were calculated directly from the impact mass, m_{impact}, and impact velocity, v_{impact} as follows:

$$I_{input} = (m_{impact})(v_{impact}) \tag{75}$$

$$E_{input} = \frac{1}{2}(m_{impact})(v_{impact})^2 \tag{76}$$

Since Test B-a1 and B-a2 had the same initial conditions, their results were averaged as Test B-a. The initial conditions of the tests are listed in Table 6.

4.5.4.1 Deformation

Deformation results of all validation tests were plotted in Figure 94. Time zero was the time when the high-speed actuator started to launch the pushing plate. The specimen in Test C started to deform the earliest because Test C had the highest impact velocity. Therefore, the impact mass in Test C took the least amount of time to travel across the length of the

Table 6: Input impulse and energy of validation tests.

Test No.	Impact mass (kg)	Impact velocity (m/s)	Slack distance (mm)	Input impulse (N·s)	Input energy (N·m)
A	139.82	5.0	12.7	699	1748
B-a	87.12	5.0	12.7	436	1089
B-b	87.12	5.0	6.35	436	1089
C	87.12	7.0	0	523	1568

rail and strike into the inverter mechanism. Additionally, Test C had a zero slack distance so that the specimen started to deform immediately when the ball joint connector started to move.

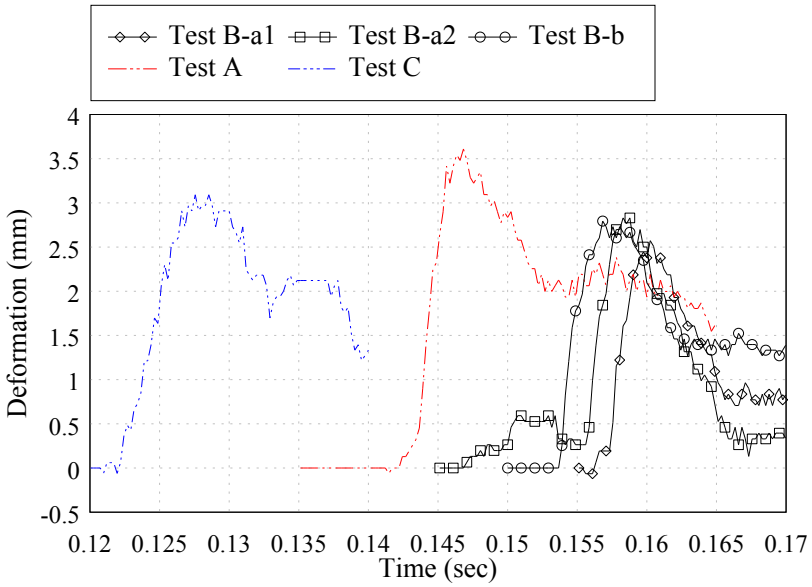

Figure 94: Compare of deformation in the validation tests.

Test A, B-a1, B-a2, and B-b had similar impact velocities so they had similar elapsed time when the impact mass struck the inverter mechanism. However, since Test A had a larger impact mass and, thus, larger impulse, the rotation and movements of the inverter mechanism in Test A were faster, and the ball joint connector started to move earlier. Therefore, Test A had an earlier t_1 than Test B-a1, B-a2, and B-b, where t_1 was the time when ball joint connector started to move as defined in Figure 71. That explained why the specimen in Test A started to deform after Test C but before the rest of the tests.

For the rest of the three tests, since they had the same impact mass and impact velocity, they all had similar t_1. However, t_2, the time when the loading grip at the moving end started to move as defined in Figure 71, of Test B-b was earlier than that of Test B-a1 and B-a2 because Test B-b had a shorter slack distance. Therefore, the ball joint connector in Test B-b engaged with the input nut earlier. As mentioned in Table 3, the slack distance in Test B-b was 6.35 mm (0.25 inch) and in Test B-a1 and B-a2 was 12.7 mm (0.5 inch), respectively. The time difference caused by the 6.35 mm difference in slack distances was not significant since the ball joint connector already accelerated to a relatively high velocity after traveling the 6.35 mm distance. It did not take much extra time to travel another 6.35 mm distance. That is the reason the deformation-time curves of Test B-a1, B-a2, and B-b were close to each other with differences of less than 0.002 s.

The maximum deformations of specimens in these tests were found to have a linear relation with the input impulse as shown in Figure 95. This was just a preliminary observation which needs to be verified by more tests. Nevertheless, this potential relation indicated that increasing input impulse can be a reasonable starting point to increase maximum deformation.

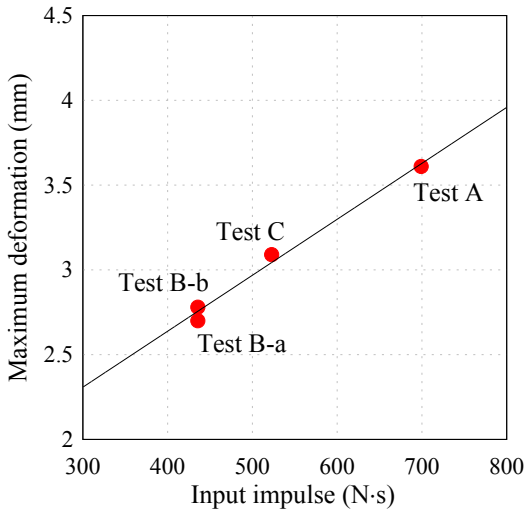

Figure 95: Relation between maximum deformation and input impulse.

4.5.4.2 Loading rate

The loading rate was unquestionably affected by the input impulse and energy. However, it was also significantly affected by the slack distance. As discussed in Section 4.3.7, the slack distance played a key role in achieving a constant loading rate. The testing results also corroborated this effect of slack distance. For example, with the same impact mass, the impact velocity in Test C was 40% higher than those in Test B-a1, B-a2, and B-b, indicating that Test C had a much larger input impulse and input energy. Nevertheless, the loading rate in Test C was around 30% lower than those in Test B-a1, B-a2, and B-b. The main reason was that Test B-a1 and B-a2 had a 12.7 mm and B-b had a 6.35 mm intended slack, respectively. However, Test C had no slack at all. As explained in Section 4.3.7, when the specimen in Test C started to be deformed by the ball joint connector, the velocity of the loading grip was still very low. In contrast, when the specimens in Test B-a1, B-a2, and B-b started to deform, the velocity of the ball joint connector was considerably high since it already accelerated through the slack distance and built up a larger momentum to strike on the input nut.

4.5.4.3 Force

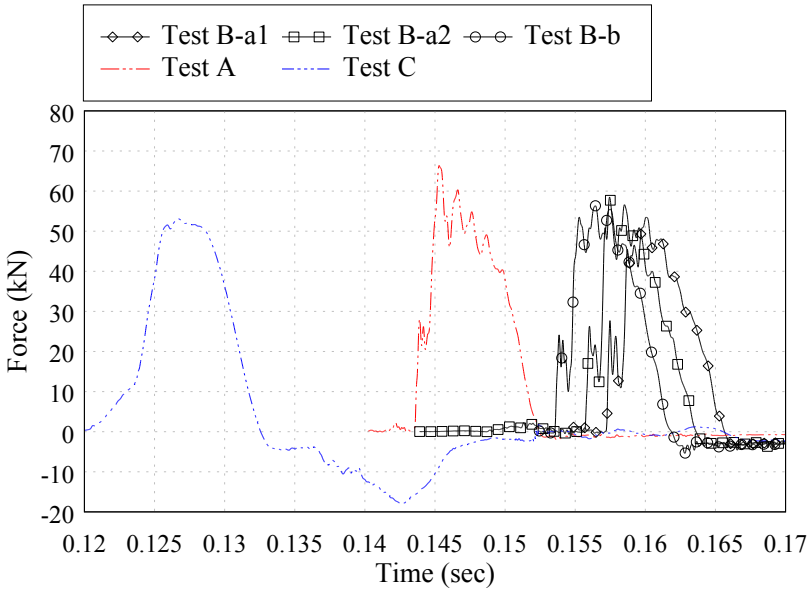

Figure 96: Compare of force in the validation tests.

Figure 96 shows the force results of all five tests. Although these tests had different input impulse and energy, the maximum forces were close to each other and relatively independent of the input impulse or energy. The deformation and derived strain in Figure 92 proved that the specimens in all these tests yielded. Therefore, the maximum force of the specimen was limited by the yield strength of the material and, thus, independent of the input impulse or energy.

4.5.4.4 Impulse

The impulses applied onto the specimen during the tests are plotted in Figure 97. Higher impact velocity tended to apply more impulse onto the specimen as the comparison between Test A and Test C indicated. Compared with Test C, Test A had 33.6% higher input impulse and 11.5% higher input energy. Nevertheless, Test C still had 2.1% higher impulse on the specimen than that of Test A mainly because its impact velocity was 40% higher.

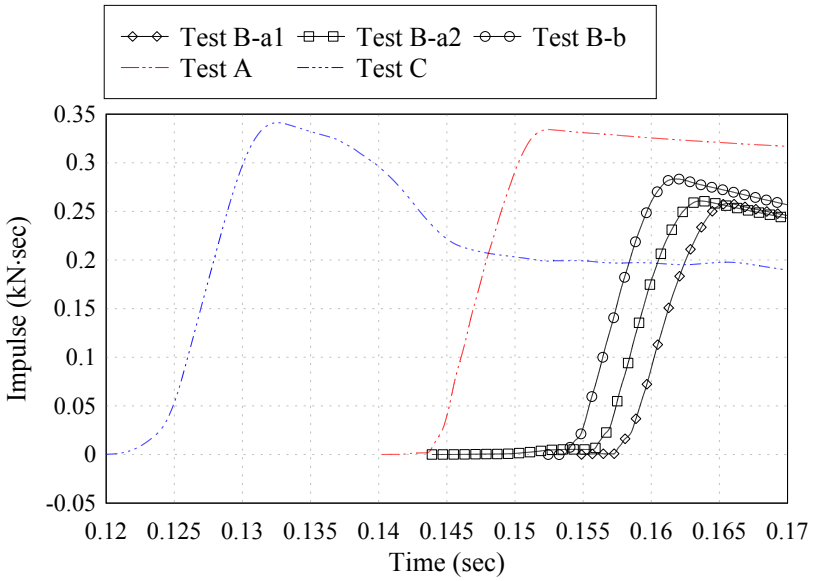

Figure 97: Compare of impulse in the validation tests.

If the stiffness of the inverter mechanism was extremely high, and the friction and damping inside the system were extremely low, the impulse on the specimen would be very close to the input impulse of the impact as demonstrated by Newton's cradle [59]. However, because of inevitable friction and damping in this large-scale testing system, only part of the input impulse actually transmitted onto the specimen. For example, the input impulse from

the impact mass of Test B-b was 435.6 N·s while the impulse applied onto the specimen in Test B-b was 283 N·s. The ratio between the impulse at specimen to the input impulse from the impact mass for Test B-b was 65%, indicating that 35% of the input impulse was lost because of friction and vibration. For all the validation tests, the ratios between the impulse on the specimen to the input impulse varied from 48% to 65% as shown in Table 7. This ratio was mainly determined by the properties of the inverter mechanism and, thus, was independent of the magnitude of input impulse. Since the only difference between Test B-a and Test B-b was the slack distance, the higher ratio of Test B-b showed that the change of slack distance increased the amount of impulse that transmitted to the specimen.

Table 7: Ratio between the measured impulse and the input impulse in validation tests.

Test No.	Total input impulse I_{input} (N·s)	Measured impulse at specimen $I_{\max}$ (N·s)	$\frac{I_{\max}}{I_{input}}$
Test A	699.1	334	47.8%
Test B-a	435.6	260	59.7%
Test B-b	435.6	283	65.0%
Test C	609.8	341	55.9%

4.5.4.5 Energy

Figure 98 shows the energy results of all the tests. Compared with the total input energy in Table 6, only a small portion of the energy was transferred onto the specimen and turned into the internal energy of the specimen when elongating the specimen beyond yielding. For example, in Test A, the total input energy was 1,748 N·m, which equaled the kinetic energy of the impact mass before striking onto the system, while the energy applied onto the specimen was 121 N·m. The ratio between the energy on specimen to the total input energy was 6.9%. For all of the validation tests, this ratio varied from 4.3% to 7.6% as shown in Table 8.

Once the energy was transmitted from the input impact into the specimen, some part of the energy contributed to the permanent deformation of the specimen while other part of

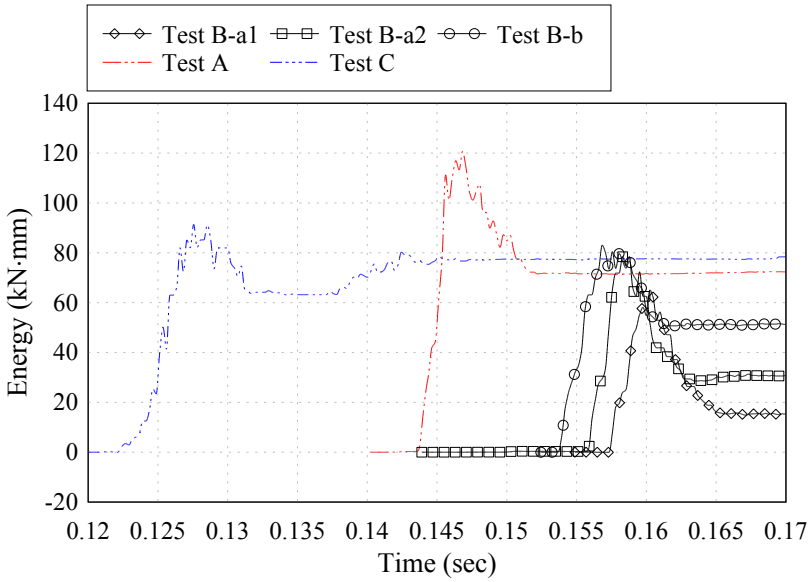

Figure 98: Compare of energy in the validation tests.

the energy was eventually released during elastic unloading. The ratio between the plastic energy to the total energy indicated the effectiveness of the system producing permanent plastic deformation on the specimen. The experimental results and the theoretical estimation of this ratio were already discussed in Section 4.5.3.4. As shown in Figure 93, this ratio of Test B-b was around 0.57, two times the ratio of Test B-a, which was around 0.28. Compared with Test B-a, Test B-b had the same impact mass and impact velocity. The only difference between Test B-a and Test B-b was the slack distance, which significantly affected the ratio of plastic energy to total energy. This again corroborated that the design

Table 8: Ratio between the measured energy and the input energy in validation tests.

Test No.	Total input energy E_{input} (J)	Measured energy at specimen $E_{\max}$ (J)	$\frac{E_{\max}}{E_{input}}$
Test A	1748	120.75	6.9%
Test B-a	1089	71.78	6.6%
Test B-b	1089	83.05	7.6%
Test C	2134	91.39	4.3%

of the intended slack distance provided flexibility and versatility in test results.

4.6 Finite element simulation of the tensile testing system

As introduced in Section 4.2.2, the trial-and-error process in the open-loop control was optimized by replacing some trial tests with finite element simulations, which were both time-effective and cost-effective. However, to ensure that the finite element simulation produced reasonable results, the methods of simulation had to be verified and calibrated based on experimental results.

In this research, a finite element model including the impact mass, the inverter mechanism, and the specimen assembly with an aluminum bolted flat tensile specimen was constructed in Abaqus/Explicit to simulate the validation tests. The simulated results were then compared to the experimental results presented in Section 4.5.2 and the methods of the finite element simulation were adjusted accordingly to improve the finite element model so that the simulated results matched closer to experimental results.

4.6.1 Methods of FE simulation

Figure 99 shows the finite element model of the tensile testing system in Abaqus/Explicit. Because of symmetry, only half of the system was modeled. Symmetric boundary conditions were enforced on all the surfaces within the center symmetric plane to ensure that the behavior of the half model was similar to that of a whole model.

To reduce the complexity of the finite element simulation, only ten parts of the system were modeled explicitly. As shown in Figure 99, following the sequence of force transmission, these ten parts were the impact mass, the triangular frame, the pivot rod, the clevis pin between triangular frame and tensile link, the tensile link, the clevis pin between tensile link and ball joint connector, the ball joint connector, the loading grip at moving end with load cell, the specimen, and the loading grip at the fixed end.

All the other parts of the system were simplified to boundary conditions or reaction forces. For example, the sliding rail for the ball joint connector was modeled as displacement constraint on the corresponding surfaces of the ball joint connector. The only gravity load of the inverter mechanism was its self weight which was approximately 360 kg (800 lbs). This gravity load was relatively small compared with the impact force and, therefore, was

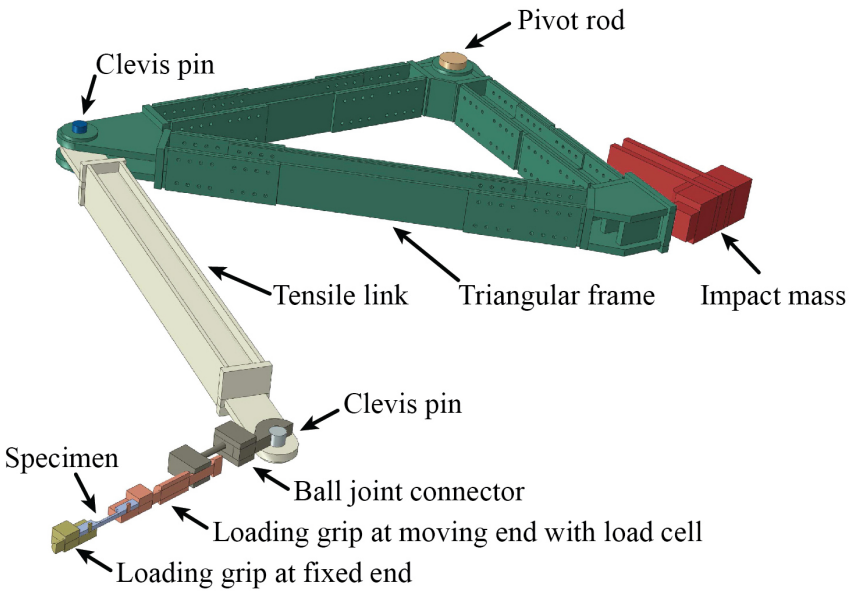

Figure 99: FE model of the high-loading-rate tensile testing system in Abaqus/Explicit.

neglected in the finite element simulation. The roller supports resisting the gravity load were simplified as boundary conditions with a displacement constraint in the direction of the gravity load.

The triangular frame of the inverter mechanism was actually composed of several parts, including joints, built-up members, and splice plates. To maintain an acceptable computing efficiency, this triangular frame was modeled as a single part justified by the excessive strength provided by high-strength bolts and splice plate at the connections. Similarly, each of the ball joint connector and loading grips was also modeled as a single part.

A predefined field of velocity was assigned to the impact mass at the beginning of the simulation to provide the impact velocity. All the interactions between parts were modeled as general contact in Abaqus/Explicit. To simulate the energy loss and dissipation throughout the system, a penalty friction formulation with a friction coefficient of 1.35 was assigned to all these interactions.

The model was analyzed with two different mesh sizes: a coarse mesh as shown in Figure 100(a), which had less computing demands and was used in the calibration process, and a fine mesh as shown in Figure 100(b), which had more computing demands and was used to confirm the results from the coarse mesh . The coarse mesh and fine mesh had

a global element size of around 15 mm and 7.5 mm, respectively. The density of mesh in the irregular geometry regions such as the hole connection, the ball joint, and the bolt hole on the specimen, was increased. The element type was chose as C3D8R with enhanced hourglass control.

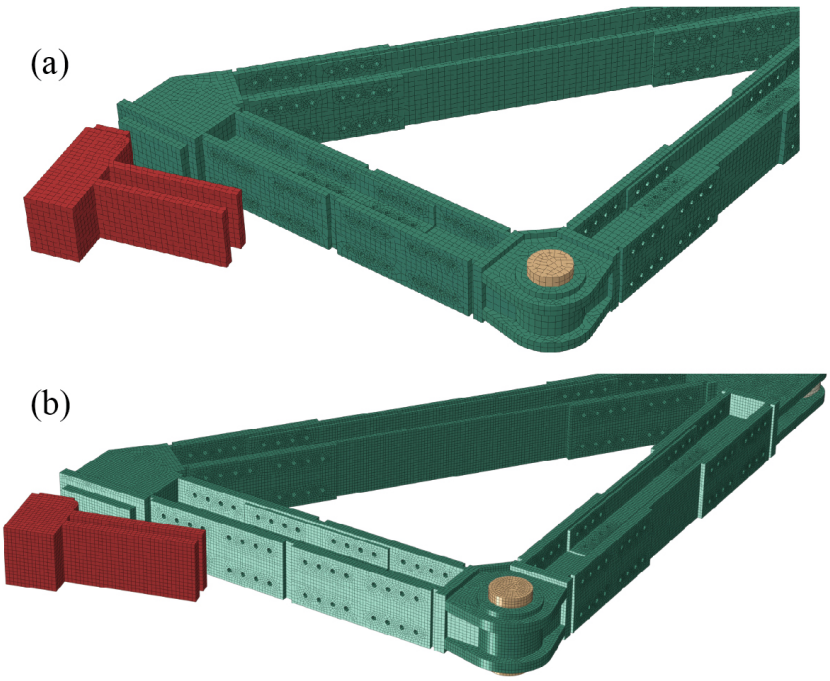

Figure 100: Mesh size of the FE model: (a) coarse mesh and (b) fine mesh.

4.6.2 Material constitutive models in the FE simulation

4.6.2.1 Aluminum 6061 alloy

Aluminum 6061 alloy material of both the testing system and the specimen was simulated using a Johnson-Cook rate-dependent plastic model. The parameters for this material model are listed in Table 9.

The static yielding stress in this Johnson-Cook plastic model is determined as

$$\sigma^0 = \left[A + B\left(\bar{\varepsilon}^{pl}\right)^n\right]\left(1 - \hat{\theta}^m\right) \tag{77}$$

where $\bar{\varepsilon}^{pl}$ is the equivalent plastic strain and $\hat{\theta}$ is a dimensionless temperature which equals zero when current temperature is lower than $\theta_{transition}$, one when current temperature is higher than θ_{melt}, and linear interpolation from zero to one when current temperature is between $\theta_{transition}$ and θ_{melt}.

Table 9: Input parameters of aluminum material model in FE simulation.

Modeling parameter	Input value	Unit
Mass density	2.7×10^{-9}	$10^3\,\mathrm{kg/mm^3}$
Young's modulus	70,000	MPa
Poisson's ratio	0.33	
A	289.6	MPa
B	203.4	MPa
n	0.35	
m	1.34	
Melting temperature, θ_{melt}	925.37	K
Transition temperature, $\theta_{transition}$	294.26	K
C	0.011	
$\dot{\varepsilon}_0$	1	s^{-1}

Considering rate dependency, the yield stress in this material model is derived as

$$\bar{\sigma} = \sigma^0 \left[1 + C \ln \left(\frac{\dot{\bar{\varepsilon}}^{pl}}{\dot{\varepsilon}_0} \right) \right] \tag{78}$$

4.6.2.2 Neoprene

Neoprene pads attached to the surface of the impact mass an the impact plate on triangular frame were simulated as a neo-Hookean hyperelastic material. The neoprene material used in the testing system was estimated to have a shear modulus, G, of 600 kPa and a bulk modulus, E_b, of 1,000 MPa.

The material parameters, $C10$ and $D1$, were calculated as

$$C10 = \frac{G}{2} = \frac{600\,\mathrm{kPa}}{2} = 0.3\,\mathrm{MPa} \tag{79}$$

$$D1 = \frac{2}{E_b} = \frac{2}{1000\,\mathrm{MPa}} = 0.002\,\frac{1}{\mathrm{MPa}} \tag{80}$$

The parameters for this hyperelastic material model are listed in Table 10.

4.6.3 Results of finite element simulation

The deformations of the specimens were subtracted from the FE simulated results and were compared with experimental results. The initial conditions, including impact mass, impact velocity, and slack distance, in the FE simulation were kept the same as the corresponding

Table 10: Input parameters of neoprene material model in FE simulation.

Modeling parameter	Input value	Unit
Mass density	1.5×10^{-9}	$10^3\,\mathrm{kg/mm^3}$
C10	0.3	MPa
D1	0.002	MPa^{-1}

experimental tests. Figure 101 plotted the deformation time history from both experimental results and FE simulated results for Test A, B-a, B-b, and C.

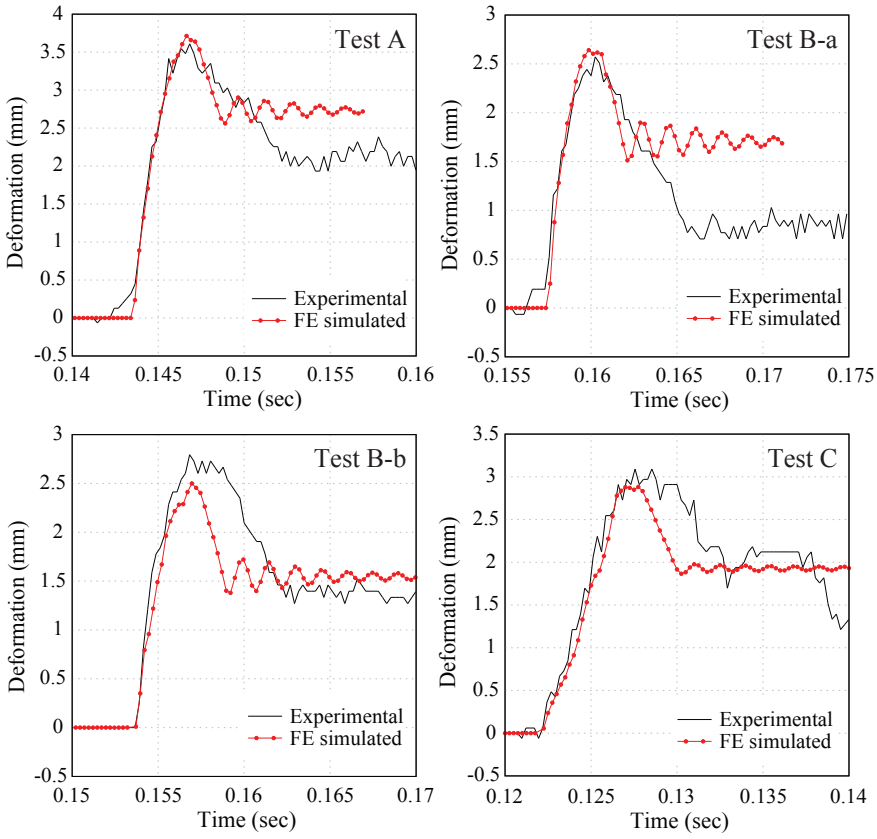

Figure 101: Comparison of the simulated deformation and experimental deformation for Test A, B-a, B-b, and C.

The FE simulation started a short time period before the impact mass struck onto the triangular frame so the simulated results had different time zero as experimental results. To compare these two results, the elapsed time of simulated results were shifted to match the experimental results. The FE simulated results had a time interval of 0.00025 s and a total duration of 0.03 s.

As shown in Table 11 and Table 12, the simulated total deformations matched the experimental results within a tolerance of approximately 10% while the simulated deformation rates matched the experimental results within a tolerance of approximately 18%. This indicated that the FE simulation captured the basic behavior of the testing system and, thus, can roughly predict the test results for trial tests. Different combinations of initial conditions can be assessed using this FE simulation, and more proper initial conditions for a certain testing target can be chosen. With the aid of this FE simulation, the trial-and-error iterations in high-loading-rate testing can be optimized.

Table 11: Comparison of experimental and FE simulated results of deformation in validation tests.

Test No.	Experimental (mm)	FE simulated (mm)	Difference
A	3.61	3.71	2.8%
B-a	2.70	2.64	-2.2%
B-b	2.78	2.50	-10.1%
C	3.09	2.88	-6.8%

Table 12: Comparison of experimental and FE simulated deformation results of deformation rates in validation tests.

Test No.	Experimental (mm/s)	FE simulated (mm/s)	Difference
A	1,423	1168	-17.9%
B-a	1,013	1087	7.3%
B-b	1,081	918	-15.1%
C	640	622	-2.8%

4.7 Summary

In this research, a new type of high-loading-rate tensile testing system was designed and constructed. Design challenges such as inverter mechanism, open-looped control, inertia effect, and requirements of adaptability were handled with proper measures. The entire process of design, fabrication, and installation of the testing system was documented in

detail.

To verify and calibrate this new tensile testing system, a series of high-loading-rate tensile tests on aluminum bolted flat tensile specimens were conducted. The deformation and force of the specimens were directly obtained from measured data. The responses of the specimens including energy and impulse were derived and analyzed. Test results were verified by comparing the measurements from independent instruments and by comparing the test results to theoretical estimations. Stress-strain relations of the aluminum specimens under varied strain rates from 14.2 to 22.4 s^{-1} were successfully obtained from these validation tests.

This research also conducted an investigation on the relation of initial conditions and final results of the tests. This investigation can provide guidelines on how to adjust initial conditions to meet a certain target, such as a certain peak energy or a certain deformation rate. In addition, this research included a finite element simulation of the testing system. Calibrated by the experimental results, this FE simulation can capture the behavior of the testing system within acceptable tolerance and can be used as a prediction tool for tests using this system.

In conclusion, this new high-loading-rate tensile testing system is capable of testing tensile specimens under intermediate strain rates and obtain reasonable test results in a controllable and repeatable manner. This system is adaptive and versatile to accommodate various types of specimens. As a result, it has a great potential as a new experimental technique.

CHAPTER V

HIGH-LOADING-RATE TENSILE TESTS OF SMA SPECIMENS

5.1 Introduction

To investigate the rate-dependency of SMA materials, this research conducted a series of tensile tests on various SMA specimens using the new high-loading-rate tensile testing system developed in Chapter 4. The types of SMA specimens included round tensile specimen, bar with threaded-end, and ring. Loading grips for each type of specimen were designed and fabricated to connect the specimen to the testing system. The test results, including deformation, force, energy, and impulse were obtained from measured data, and force-deformation or stress-strain relations were derived from experimental results. These results were then compared with the counterpart from quasistatic tests to evaluate the rate dependency of SMA materials.

5.2 Experimental design

The testing methods and data processing were similar to the validation tests described in Chapter 4. This research conducted high-loading-rate tensile tests on three types of specimens: round tensile specimens (Coupon), threaded-end bar specimen (Bar), and ring-shaped specimens (Ring). The initial conditions for each test on SMA specimens are listed in Table 13. The same SMA ring was repeatedly tested in Test Ring-1 and Ring-1.

Most of the SMA specimens were clamped by friction connections rather than attached by bolted connections as in the validation tests discussed in Chapter 4. As a result, slack distance in most of the tests was selected as zero since friction connections usually required initial tensile forces for pre-loading. Non-zero slack distance can be achieved by adding additional self-tensioning mechanism onto the loading grips. In current research, most of the tests had a zero slack distance, and most of the specimens were pre-tensioned to provide enough clamping force at the loading grips.

Table 13: Initial conditions of high-loading-rate tensile tests on SMA specimens.

Test No.	Impact mass (kg)	Targeting impact velocity (m/s)	Slack distance (mm)
Coupon-1	87.12	5.0	0
Coupon-2	87.12	5.0	0
Bar	87.12	7.0	0
Ring-1	87.12	5.0	0.5
Ring-2	87.12	7.0	0

5.2.1 Specimens

5.2.1.1 SMA round tensile specimens (Coupons)

Two SMA coupons were tested using the new high-loading-rate tensile testing system. Figure 102 shows the dimension of these two specimens. Both specimens had the same section diameter of 12.7 mm (0.5 inch). Coupon-1 had a gage length of 53.34 mm (2.1 inch), which was slightly shorter than the 60.96 mm (2.4 inch) gage length of Coupon-2. Figure 103 shows the photo of these two specimens.

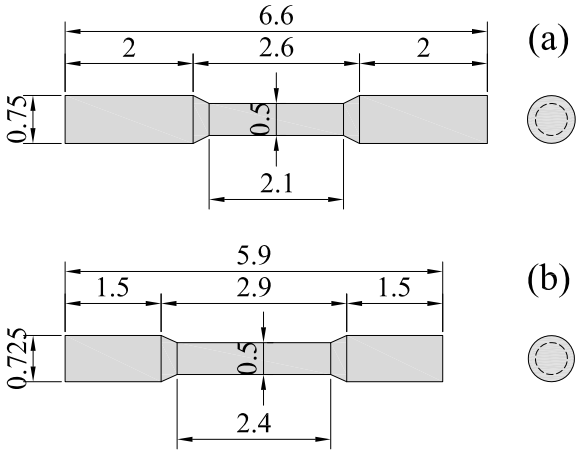

Figure 102: Design of SMA Coupon specimens: (a) Coupon-1 and (b) Coupon-2 (units: inch).

5.2.1.2 SMA threaded-end bar specimen(Bar)

One SMA threaded-end bar with a gage length of 297.8 mm (11.725 inch) and a diameter of 21.6 mm (0.85 inch) was also tested. Two custom-made threaded nuts matching the threads at the ends of this bar were used to connect the bar to the specimen assembly. The

Figure 103: Photo of SMA Coupon specimens.

dimensions of this specimen are shown in Figure 104 and a photo of this specimen is shown in Figure 105.

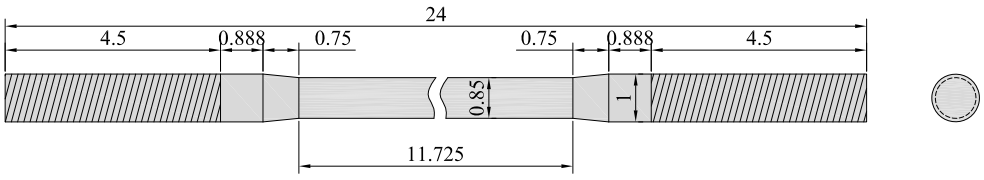

Figure 104: Design of SMA Bar specimen (unit: inch).

Figure 105: Photo of SMA Bar specimen.

5.2.1.3 SMA Ring

The SMA ring was the same specimen in the quasistatic cyclic loading test described in Chapter 3. The same ring as shown in Figure 14 was tested repeatedly in Test Ring-1 and Ring-2 under two different impact velocities: 5 m/s and 7 m/s.

5.2.2 Loading grips

As introduced in Section 4.2.4, only the loading grips needed to be changed to accommodate different types of specimens. For each type of specimen, a corresponding pair of loading grips were designed and fabricated to connect the specimens to the specimen assembly.

5.2.2.1 *Loading grips for SMA Coupons*

To apply tensile forces onto the round tensile specimens firmly and safely, wedge clamps with V-shaped notches were utilized as shown in Figure 106. The end of the round tensile specimens was inserted into the hollow space surrounded by the two V-shaped notches of two wedge clamps. Then the wedge clamps were pre-loaded to push against each other, clamping the specimen in the middle with friction. In this research, two pairs of wedge clamps from an existing MTS servo-hydraulic testing machine were adopted to clamp the round tensile specimen.

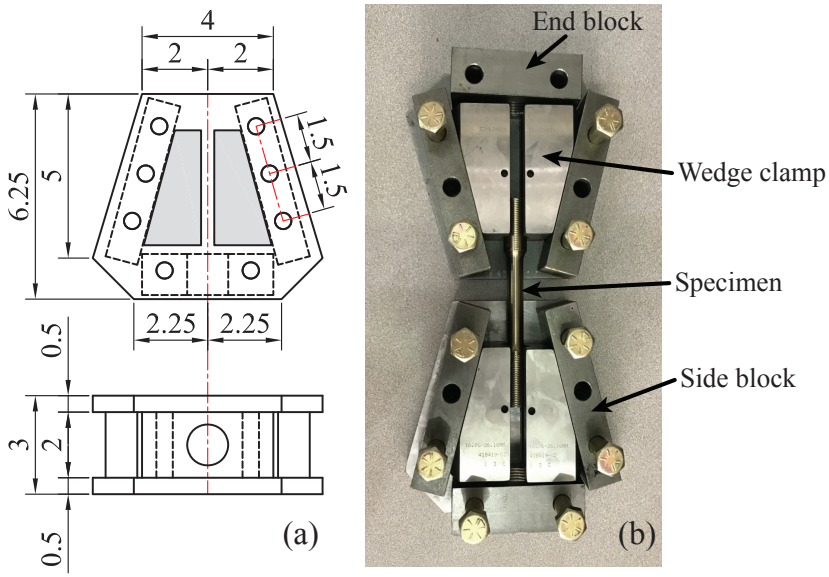

Figure 106: Design of loading grips for SMA Coupon specimens: (a) top and side view and (b) photo of assembly (units: inch).

As discussed in Section 4.2.3, the weight and stiffness of loading grips considerably affected the test results. Loading grips using wedge clamps in conventional servo-hydraulic testing machines usually had large self weight. Besides, these grips did not have the threaded connection that fit the universal connections for the specimen assembly in this new tensile testing system. Therefore, custom-made loading grips which can work with the existing wedge clamps were designed and fabricated.

As shown in Figure 106(a), two hexagon 12.7 mm (0.5 inch) thick steel plates were fabricated as the top and bottom plates. Two steel side blocks positioned in an angle

matching the inclined angle of the existing wedge clamps were bolted between the top and bottom plates as shown in Figure 106(b). To clearly demonstrate the clamping mechanism, the top plates were not included in Figure 106(b). An additional steel end block was bolted between the top and bottom plates, parallel to the end surface of the wedge clamps. The top and bottom plates, the side blocks, and the end block formed a box which held the wedge clamps in the middle. The end block had a 31.75 mm (1.25 inch) diameter through threaded hole so that a threaded bar can be turned all the way in and can push the wedge clamps firmly against the inner surfaces of the side blocks. The other end of this threaded bar was then connected to the load cell at the moving end or the mounting plate at the fixed end.

Figure 107 shows the entire specimen assembly with the SMA round tensile specimen installed onto the testing system. The specimen was pre-loaded by turning the threaded bars into the loading grips. As a result, the wedge clamps inside the loading grips were pushed against the side blocks. The specimen was then firmly gripped in the middle of these wedge clamps. A 25.4 mm (1 inch) diameter target was attached on the side of each loading grip.

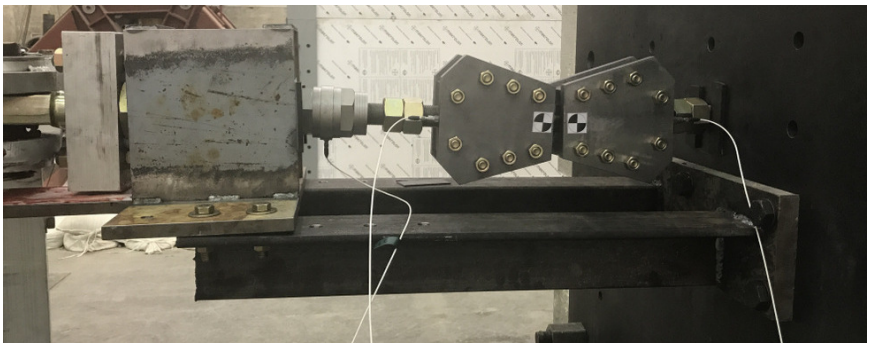

Figure 107: Photo of the specimen assembly with SMA Coupon specimen installed.

5.2.2.2 Loading grips for SMA Bar

Since the SMA Bar specimen had threads at both ends, it can be connected to the system relatively easily with the aid of custom-made nuts. However, the 25.4 mm (1 inch) diameter thread size was not the same as the 31.75 mm (1.25 inch) diameter thread size in the load cell and the specimen assembly. Therefore, a special thread adapter was fabricated from

a custom-made nut and a 31.75 mm (1.25 inch) diameter threaded bar. The moving end of the SMA rod was connected to the load cell through this thread adapter, and the fixed end of the SMA rod was secured to the back side of the external mounting plate by the other custom-made nut. Seven 12.7 mm (0.5 inch) targets were attached to the surface of the rod with a center-to-center spacing of 38.1 mm (1.5 inch). The gage length of this SMA Bar specimen was selected as 228.6 mm (9 inch), which was the distance between the two outermost targets.

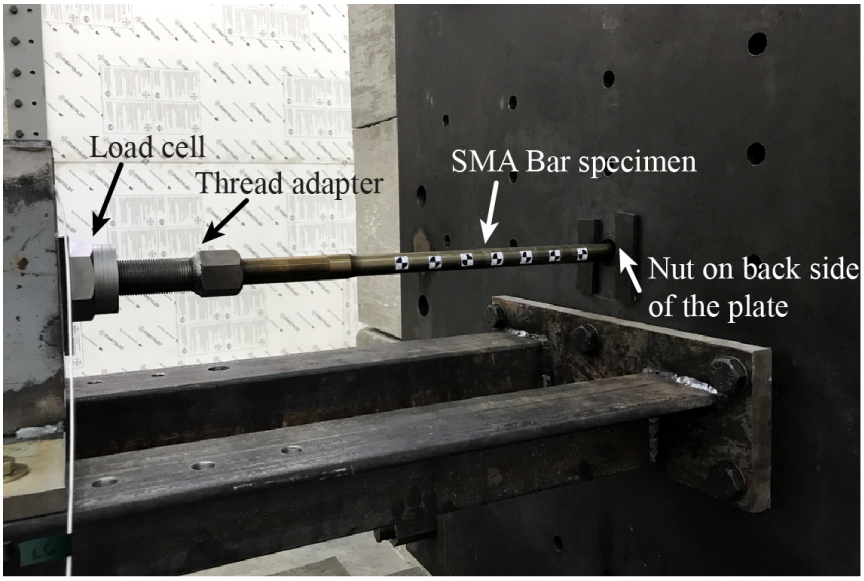

Figure 108: Photo of the specimen assembly with SMA Bar specimen installed.

5.2.2.3 Loading grips for SMA Ring

Figure 109 shows the design of the loading grips for the SMA Ring specimen. An aluminum cylinder with a diameter of 50.8 mm (2 inch) was placed inside the SMA ring with the lateral surface firmly against the inner surface of the ring. The cylinder was connected to an aluminum rectangular block by two 19.05 mm (0.75 inch) diameter high-strength steel thread bars. The rectangular block had a 31.75 mm (1.25 inch) diameter hole in the center. A 31.75 mm (1.25 inch) diameter threaded bar went through this hole and connected to the load cell at the moving end or the mounting plate at the fixed end.

The SMA ring was fixed by the loading grips as shown in Figure 110. Targets with a diameter of 25.4 mm (1 inch) were attached to the flat surface of each aluminum cylinder.

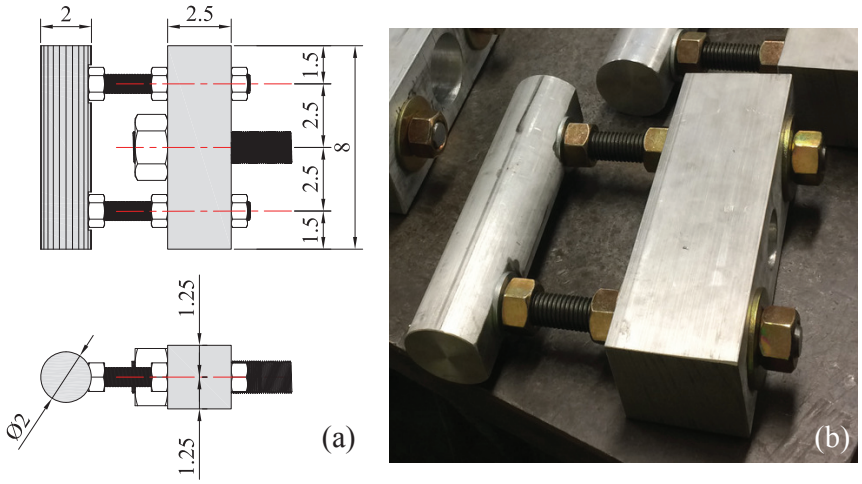

Figure 109: Design of loading grips for SMA Ring specimen: (a) top and side view and (b) photo of the loading grip (units: inch).

Additional 12.7 mm (0.5 inch) diameter targets were attached to the surface of the ring to monitor the deformation in the direction perpendicular to the impact direction.

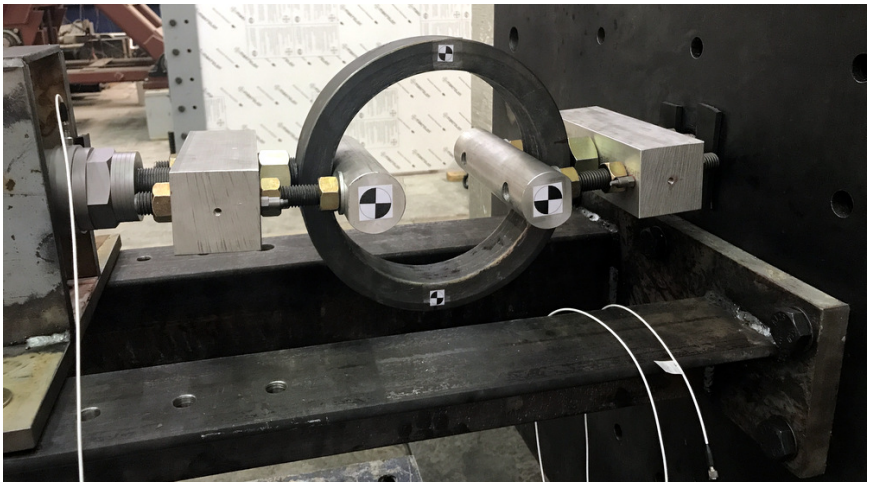

Figure 110: Photo of the specimen assembly with SMA Ring specimen installed.

5.3 Experimental results

5.3.1 Experimental observations

The deformation, force, energy, and impulse of each test were obtained using the same methods as described in Section 4.5.2.

5.3.1.1 Test results of SMA Coupons

The deformation of the SMA Coupon specimen was captured by the high-speed camera as shown in Figure 111. The video was then processed using the same motion tracking software as introduced in Section 4.5.2.

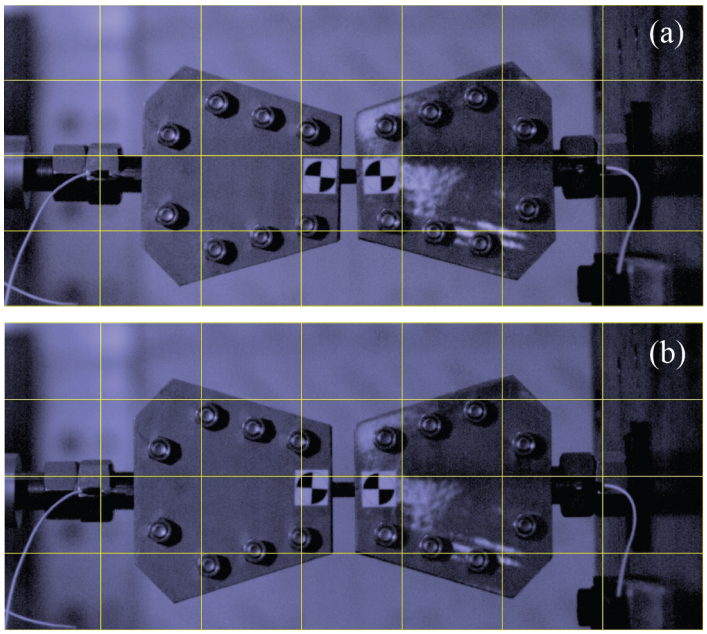

Figure 111: Screen shots of SMA Coupon specimen from high-speed camera video: (a) before test and (b) at peak deformation during test.

The test results, including force, deformation, energy, and impulse, of the specimen Coupon-1 and Coupon-2 were plotted in Figure 112 and Figure 113, respectively.

In the test of SMA Coupon-1, the specimen started to deform at 0.1512 s and reached its peak deformation of 3.61 mm at 0.1602 s. At that time, the energy also reached its peak value of 59.84 kN·mm. The force reached its peak value of 30.24 kN at 0.1599 s. Then the force dropped back to zero, and the impulse reached its peak value of 0.220 kN·s, both at 0.1656 s. The deformation dropped back to zero at 0.1740 s. After that, the impulse eventually declined to zero.

Similar responses were observed in the test of SMA Coupon-2. The specimen started to deform at 0.1507 s and reached its peak deformation of 5.82 mm at 0.1641 s. At that time, the energy also reached its peak value of 61.07 kN·mm. The force reached its peak value of 25.24 kN at 0.1634 s. After that, the force dropped back to zero, and the impulse reached

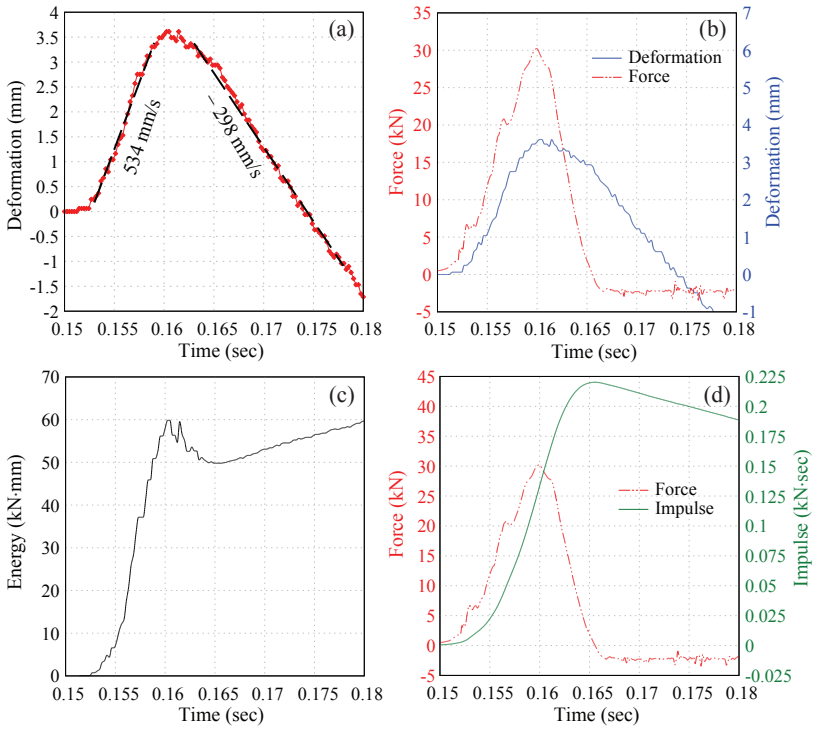

Figure 112: Experimental results of Test SMA Coupon-1: (a) deformation, (b) force, (c) energy, and (d) impulse of the specimen.

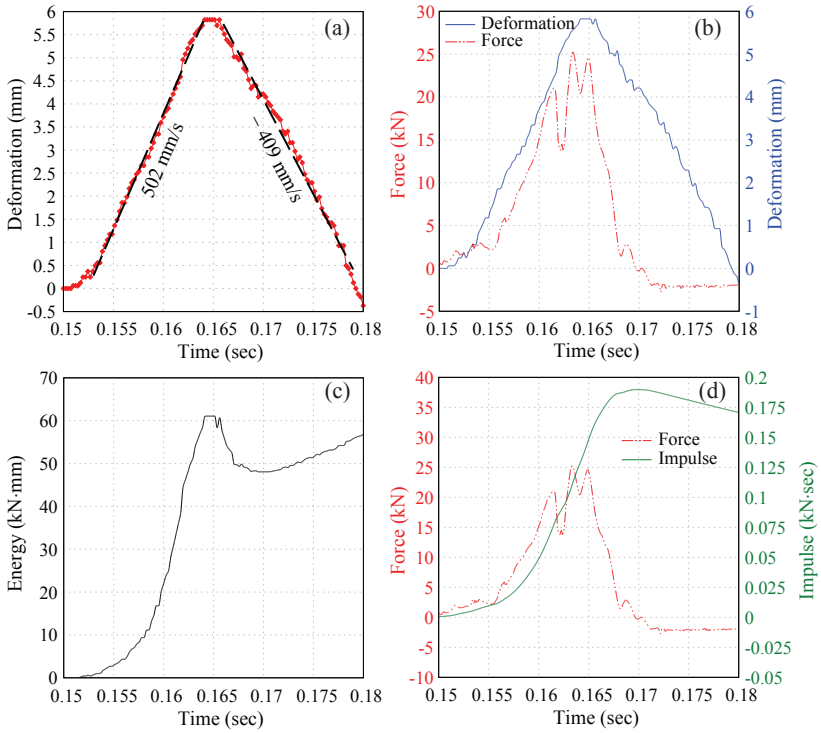

Figure 113: Experimental results of Test SMA Coupon-2: (a) deformation, (b) force, (c) energy, and (d) impulse of the specimen.

its peak value of 0.190 kN·s, both at 0.1695 s. The deformation dropped back to zero at 0.1793 s. After that, the impulse eventually declined to zero.

The deformation rates of these two tests were 534 mm/s and 502 mm/s, respectively. These deformation rates corresponded to average nominal strain rates of 10.0 s^{-1} and 8.2 s^{-1}, respectively. The strain rates achieved in these two test fell into the range of intermediate strain rates as expected. The peak deformation of SMA Coupon-1 was 3.61 mm, corresponding to a peak average strain of 0.068, while the peak deformation of SMA Coupon-2 was 5.82 mm, corresponding to a peak average strain of 0.095. The superelasticity of the SMA material was exhibited by the decreasing tendency of the deformation when the force dropped back to a constant level after unloading. The input energy of these two tests were similar while the deformation of Coupon-2 was larger than that of Coupon-1, indicating that the stiffness of Coupon-2 was lower. This lower stiffness of Coupon-2 was also corroborated by its lower peak force of 25.24 kN compared with the higher peak force of 30.24 kN of Coupon-1.

Since these two tests had identical initial conditions including impact mass, impact velocity, and zero slack distance, the total input energy and impulse were also identical. These two specimens were in the same shape with similar sizes, indicating their responses tended to be similar. As a result, the energy and impulse applied to the specimens were expected to be similar. This similarity was corroborated by the experimental results. The peak energy in these two tests were 76.14 J and 69.05 J, respectively, and the peak impulse were 0.220 kN·s and 0.190 kN·s, respectively.

Because of the design of the wedge clamps, when the specimen assembly bounced back after the peak deformation, the wedge clamps may detach from the surface of the side blocks, and the specimen may disengage from the wedge clamps. As a result, during part of the unloading process, the displacement of the targets no longer represented the deformation of the specimen since sliding had already occurred between the specimen and the wedge clamps. This also explained the increasing of energy after the peak deformation.

5.3.1.2 Test results of SMA Bar

Figure 114 shows the test results of SMA threaded-end bar specimen. In this test, the specimen started to deform at 0.1293 s and reached its peak deformation of 0.83 mm at 0.1344 s. At that time, the energy also reached its peak value of 23.85 kN·mm. The force reached its peak value of 48.53 kN at 0.1346 s. After that, the force dropped back to zero, and the impulse reached its peak value of 0.284 kN·s, both at 0.1401 s. The deformation also dropped back to zero at 0.1401 s

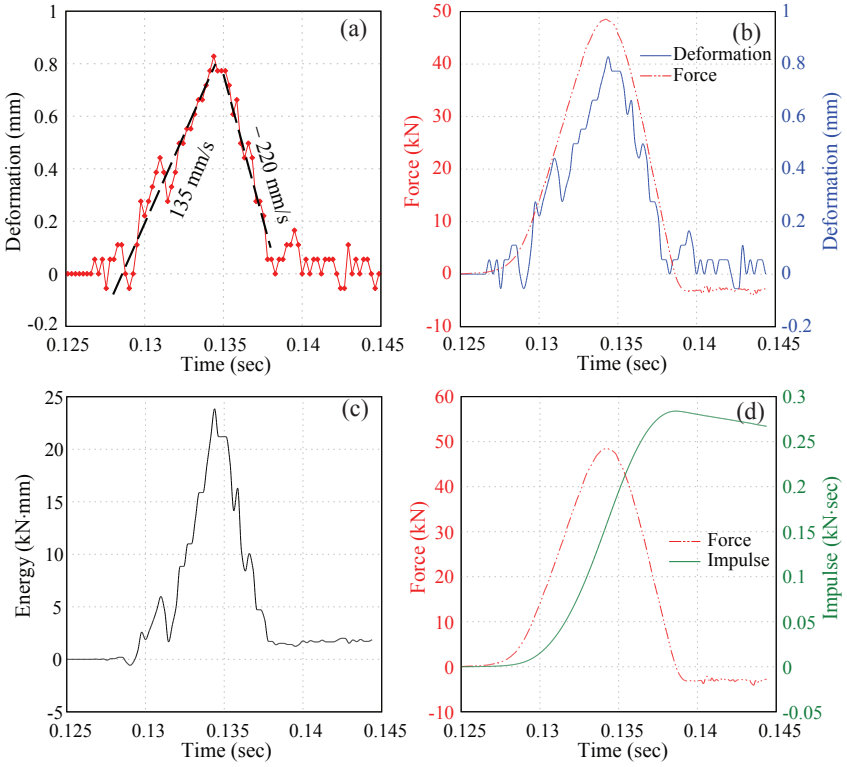

Figure 114: Experimental results of Test SMA Bar: (a) deformation, (b) force, (c) energy, and (d) impulse of the specimen.

Because of the larger cross section area and, thus, larger stiffness, the deformation rate of this test was 135 mm/s, which was significantly lower than other tests. The average nominal strain rate was 0.6 /s^{-1}. The 48.53 kN peak force was higher than SMA Coupons while the 0.83 mm peak deformation was lower than SMA Coupons, which again confirmed the high stiffness of this threaded-end bar.

The time duration of loading and unloading of SMA Bar was around 0.009 s, which was

significantly shorter than the 0.022 s duration time in SMA Coupon-1. Although the loading time was shorter, the impulse of SMA Bar was still 29% higher than that of Coupon-1 because of its higher stiffness and higher force. Nevertheless, because the small peak deformation of 0.83 mm only corresponded to an average strain of 0.0036, the SMA material in SMA Bar did not reach the AM_s point. As a result, the phase transformation of SMA materials did not start, and the SMA Bar was still in elastic range. This explained why the SMA Bar had such a low amount of dissipated energy, which was only 31.3% of that of Coupon-1.

5.3.1.3 SMA ring

Figure 115 shows the frames of the SMA ring before and during the test. The diameters of the targets attached to the aluminum cylinders inside the ring were 25.4 mm (1 inch). The 12.7 mm diameter targets on the ring remained in a same vertical line, indicating that the ring was stretched without obvious rotation or other undesired movement.

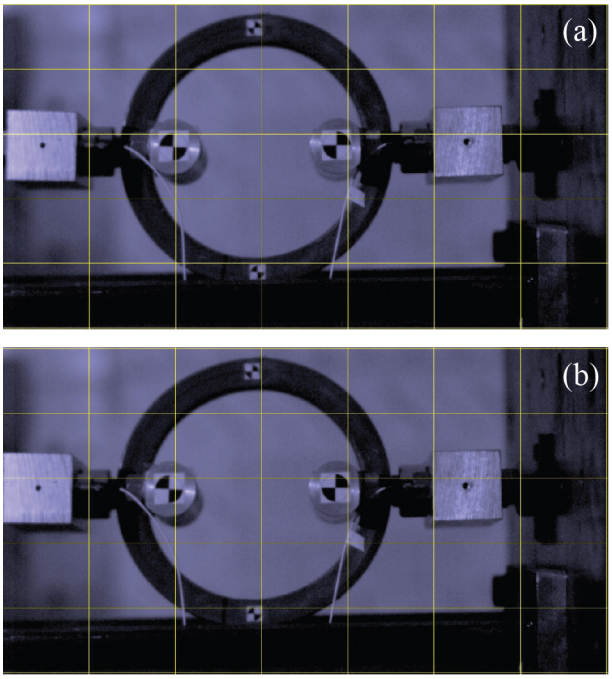

Figure 115: Frames of SMA ring specimen from high-speed camera video: (a) before test and (b) at peak deformation during test.

The test results of SMA Ring-1 and SMA Ring-2 were plotted in Figure 116 and Figure 117, respectively.

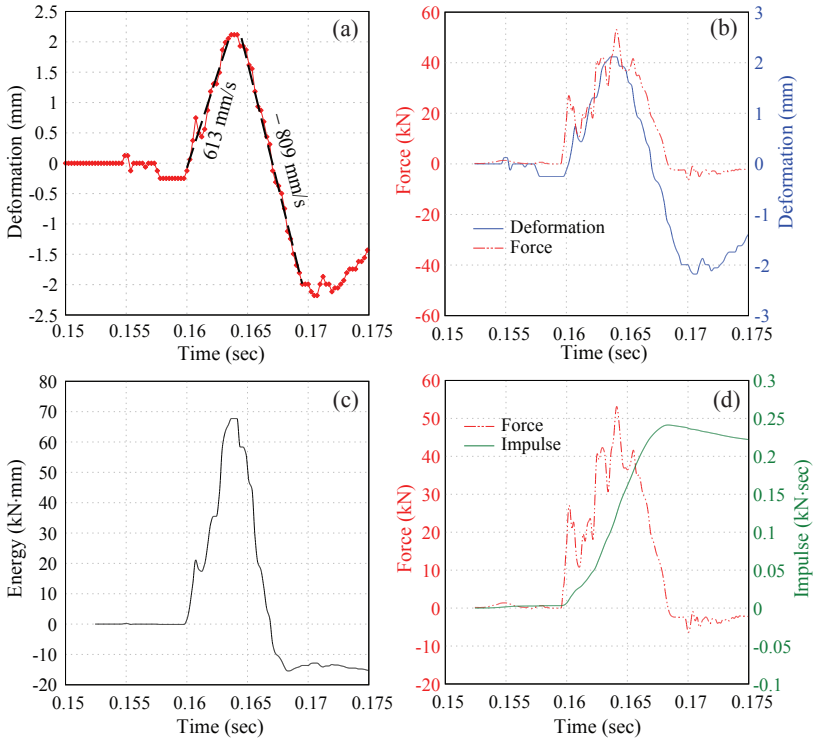

Figure 116: Experimental results of Test SMA Ring-1: (a) deformation, (b) force, (c) energy, and (d) impulse of the specimen.

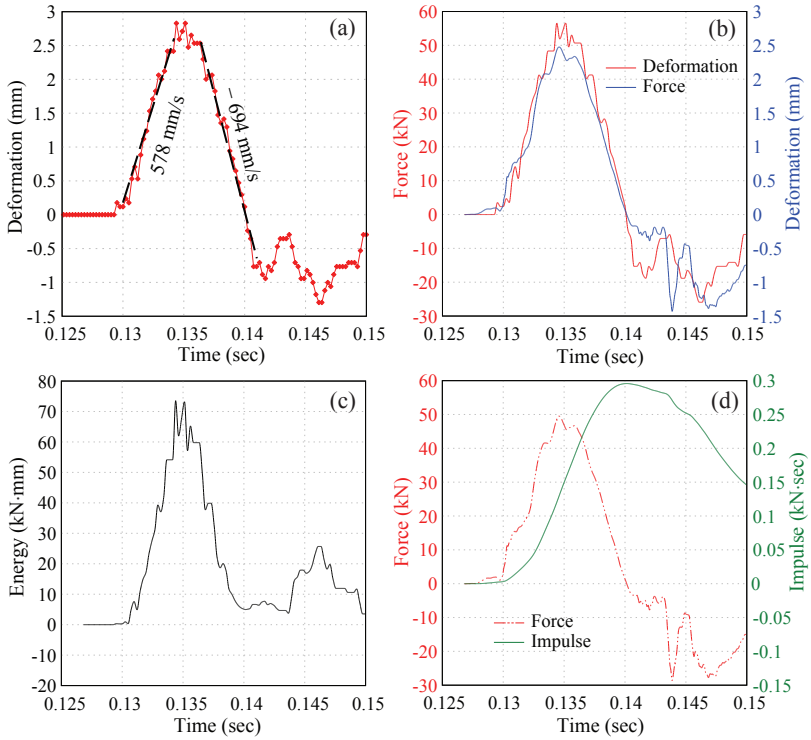

Figure 117: Experimental results of Test SMA Ring-2: (a) deformation, (b) force, (c) energy, and (d) impulse of the specimen.

In the test of SMA Ring-1, the specimen started to deform at 0.1601 s and reached its peak deformation of 2.12 mm at 0.1636 s. The energy also reached its peak value of 67.72 kN·mm at that time. Then the force reached its peak value of 53.15 kN at 0.1641 s. After that, the force dropped back to zero, and the impulse reached its peak value of 0.241 kN·s, both at 0.1684 s. The deformation dropped back to zero at 0.1670 s.

Similarly, in the test of SMA Ring-2, the specimen started to deform at 0.1293 s. At the time 0.1344 s, the specimen reached its peak deformation of 2.83 mm and peak energy of 73.14 kN·mm. The force reached its peak value of 49.52 kN at 0.1346 s. After that, the force dropped back to zero, and the impulse reached its peak value of 0.296 kN·s, both at 0.1401 s.

Although Ring-1 had a lower impact velocity than Ring-2, the deformation rate of 613 mm/s in Ring-1 was still higher than 578 mm/s in Ring-2 because of the 12.7 mm (0.5 inch) slack distance in Ring-1. The 53.15 kN peak force in Ring-1 was also higher than 49.52 kN in Ring-2. These results again corroborated the effectiveness of the intended slack in the experimental design. Nevertheless, because Ring-2 had higher impact velocity and, thus, higher input impulse and energy, the impulse and energy at the specimen of Ring-2 were 22.8% and 8.6% higher than those of Ring-1, respectively.

5.3.2 Discussion of results

The test results of all SMA specimens are summarized in Table 14.

5.3.2.1 Ratio of impulse at specimen to total input impulse

The total input impulse and the impulse measured at the specimens for each test are listed in Table 15. These ratios varied from 43.6% to 55.3%, indicating that approximately half of the input impulse was transmitted into the specimen while the other half was dissipated through friction and vibration. The ratio in these tests on SMA specimens was similar to that in validation tests on aluminum specimens because this ratio was mainly determined by the properties of the inverter mechanism.

Table 14: Summary of the experimental results of high-loading-rate tensile tests on SMA specimens.

Test result	Symbol	Unit	Coupon-1	Coupon-2	Bar	Ring-1	Ring-2
Diameter	d	mm	12.7	12.7	0.83	-	-
Gage length	L	mm	53.34	60.96	297.8	-	-
Peak deformation	u_{total}	mm	3.61	5.82	0.83	2.12	2.83
Deformation rate	$\dot{u}$	mm/s	534	502	135	613	578
Strain rate	$\dot{\varepsilon}$	s^{-1}	10.0	8.2	0.6	-	-
Peak force	$P_{\max}$	kN	30.24	25.24	48.53	53.15	49.52
Peak impulse	$I_{\max}$	kN·s	0.220	0.190	0.284	0.241	0.296
Peak energy	E_{total}	kN·mm	59.84	61.07	23.85	67.72	73.56

5.3.2.2 Ratio of energy at specimen to total input energy

The total input energy and the energy measured at the specimens of each test are listed in Table 16. This ratio varied from 1.1% to 6.2% and decreased as the input energy increased. This was partly because the energy at the specimen was considerably affected by the properties of specimens. As a result, excessive input energy did not necessarily increase the energy applied onto the specimen.

5.3.2.3 Stress-strain results of SMA Coupons and Bar

From the deformation and force results of the tests on SMA Coupon specimens and Bar specimen, assuming that the stress and strain were uniformly distributed across the section of the specimens, the average nominal stress and strain were obtained. Figure 118 shows the stress and strain curves of specimens SMA Coupon-1 and SMA Bar. The stress-strain of Coupon-1 clearly exhibited the flag-shaped curve as discussed in Section 2.1.4. The stress plateau and the second increase after the plateau indicated the ongoing phase transformation and the completion of that transformation. Because the specimen disengaged with the loading grips caused by the limitation of the clamping mechanism, the stress-strain relation of the unloading part was not accurately captured in the test.

Although the peak force of SMA Bar was 60% larger than that of Coupon-2, the peak stress in SMA Bar was still lower because its cross section area was 189% larger than that

Table 15: Ratio between the measured impulse and the input impulse in high-loading-rate tensile tests on SMA specimens.

Test No.	Total input impulse I_{input} (N·s)	Measured impulse at specimen $I_{\max}$ (N·s)	$\frac{I_{\max}}{I_{input}}$
Coupon-1	435.6	220	50.5%
Coupon-2	435.6	190	43.6%
Bar	609.8	284	46.6%
Ring-1	435.6	241	55.3%
Ring-2	609.8	296	48.5%

Table 16: Ratio between the measured energy and the input energy in high-loading-rate tensile tests on SMA specimens.

Test No.	Total input energy E_{input} (J)	Measured energy at specimen $E_{\max}$ (J)	$\frac{E_{\max}}{E_{input}}$
Coupon-1	1089	59.84	5.5%
Coupon-2	1089	61.07	5.6%
Bar	2134	23.85	1.1%
Ring-1	1089	67.72	6.2%
Ring-2	2134	73.56	3.4%

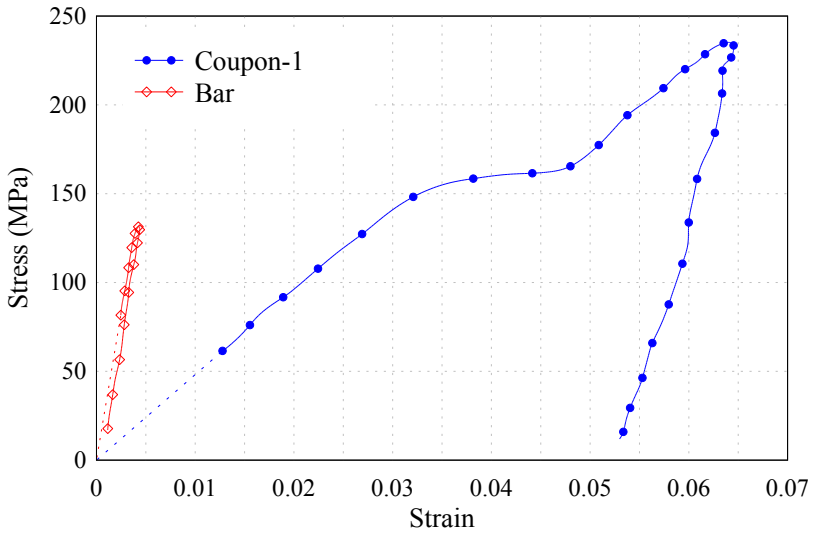

Figure 118: Stress-strain results of SMA Coupon-1 specimen and SMA Bar specimen.

of Coupon-2. SMA material in Bar specimen did not reach the stress plateau yet and did not start the phase transformation. Thus the stress-strain curve of SMA Bar was nearly a linear relation, which also explained the low amount of energy measured at the SMA Bar specimen.

5.3.2.4 Comparison of force-deformation of SMA ring in quasistatic test and high-loading-rate test

Force-deformation relations of SMA Ring-1 and Ring-2 are plotted in Figure 119, which also includes the force-deformation from quasistatic cyclic loading test discussed in Chapter 3. For this non-prismatic ring-shaped specimen, average strain rates were not applicable. The deformation rates in the diametric direction were adopted to represent the loading rates. As mentioned in Section 3.2.3, the velocity of the actuator in the quasistatic test was set as 12.7 mm/min, which corresponded to a 0.09 mm/s deformation rate on the diametric direction of the SMA ring. The loading stiffness in quasistatic test was 7.59 kN/mm while the loading stiffnesses in high-loading-rate were 31.13 kN/mm and 16.34 kN/mm for Ring-1 and Ring-2, respectively.

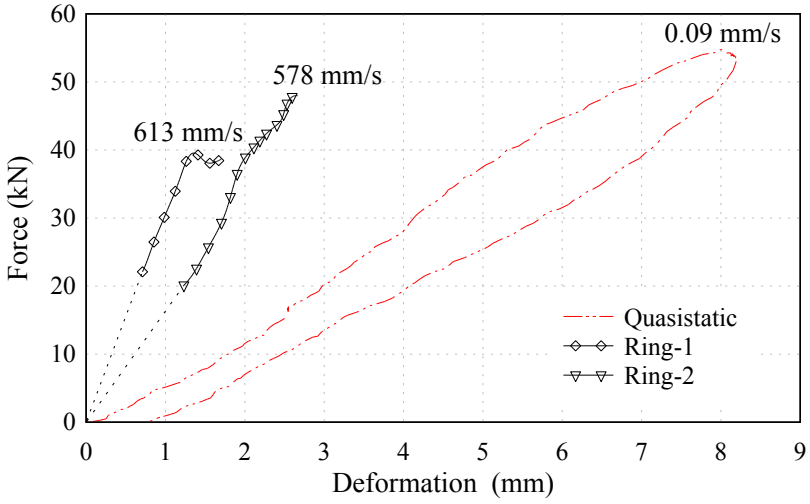

Figure 119: Comparison of force-deformation of SMA ring under different loading rates.

This comparison showed that the stiffness of the SMA ring increased as the loading rate increased, which was in accordance with the conclusions of various previous research [20, 96, 119]. Because this ring specimen was not prismatic, the strain at different regions

of the ring changed dramatically as shown in Figure 26. As loading rate and input energy increased, the regions completed the phase transformation in the SMA ring also increased. As a result, the strain distribution also changed because SMA materials exhibited different stress-strain behaviors during and after phase transformation. The differences in the loading stiffnesses of SMA rings were partly caused by this stress and strain re-distribution inside the ring rather than totally caused by the rate dependency of SMA material itself.

5.4 Summary

In this research, various SMA specimens were tested under constant deformation rates, which corresponded to constant intermediate strain rates. SMA round tensile specimens with diameters of 12.7 mm (0.5 inch) were elongated under strain rates of approximately 10 s^{-1}. An SMA ring specimen was tested by the high-loading-rate tensile testing system with a loading rate 6,500 times higher than that of the quasistatic test in Chpter 3. The comparison between the results of this ring under different loading rates clearly exhibited the rate dependency of SMAs. Stress-strain relations of the SMA material from tests of round tensile specimens and threaded-end bar were also derived. These test results showed the rate dependency of SMA materials under tensile loading and corroborated the conclusions of previous research. These tests also proved that this new high-loading-rate tensile testing system was effective in assessing rate-dependent materials. Part of the test results, such as the deformation measurement in unloading part of SMA round tensile specimens, were compromised by the limitation of the current experimental design.

CHAPTER VI

CONCLUSIONS AND RECOMMENDED FUTURE RESEARCH

6.1 Conclusions

6.1.1 Development of a high-loading-rate testing system

One of the main outcomes of this research is the development of a high-loading-rate tensile testing system, which is capable of elongating tensile specimens under constant loading rates corresponding to intermediate strain rates between 1 to 100 s^{-1}. This testing system is designed to be adaptive and versatile to accommodate a variety of specimens with different shapes, sizes, and materials. The following conclusions and significant observations are made from the experimental testing:

- This new high-loading-rate tensile testing system applied tensile forces onto specimens with the loading grip at the moving end traveling at a constant velocity. This constant velocity of loading grip corresponded to a constant deformation rate of the specimens.

- The constant deformation rates of specimens were converted into constant average strain rates varied between 0.6 to 22.4 s^{-1}, which fall into the category of intermediate strain rates as expected. This bridged the gap between quasistatic strain rates obtained from conventional servo-hydraulic testing machines and high strain rates obtained from typical Kolsky bar tests.

- The stress-strain curves of aluminum specimens in validation tests showed rate dependency as expected. Elastic modulus and yield strength increased as loading rate increased, which was corroborated by previous studies. These tests verified that the results of this new system were valid and reasonable.

- The tensile testing system can conduct tests with the same initial conditions repeatedly, indicating that it can test a batch of identical material specimens and characterize material properties with comparable results and statistical analysis.

- The deformation and force responses were directly measured without the need of assuming a uniformly distributed stress and strain inside the specimen as in Kolsky bar tests, indicating that this system can test specimens with non-prismatic sections and multiple materials. The force-deformation behavior of potential proof-of-concept structural components and devices can be assessed by this tensile testing system.

- The responses of the testing system can be estimated by a finite element simulation. The FE simulated results of the deformation of aluminum specimens in validation tests matched the experimental results within acceptable tolerances. This FE simulation is helpful in choosing the input parameters and decreasing the number of iterations in the entire testing process.

6.1.2 Investigation of the rate dependency and other properties of SMA materials

The other important outcome of this research is the investigation of material properties, especially rate dependency, of SMAs and potential applications of SMA-based devices in the field of structural engineering such as seismic mitigation and blast protection. The following conclusions and significant observations are made from the experimental testing:

- As shown in the cyclic loading tests discussed in Chapter 3, SMA-based seismic bracing system exhibited acceptable residual story drift even subject to a maximum of 3.5% story drift. SMA specimen also showed little residual deformation in high-loading-rate tensile tests discussed in Chapter 5. This corroborated that SMAs introduced significant re-centering ability to structures under both seismic and blast events.

- SMAs can also dissipated considerable amount of input energy, as shown in both cyclic loading test discussed in Chapter 3 and high-loading-rate tensile tests discussed in Chapter 5.

- The stress-strain relations of SMAs were dependent on loading rates. For example, the stiffnesses of the same SMA ring under deformation rates of 613 mm/s and 0.09 mm/s were 31.13 kN/mm and 7.59 kN/mm, respectively. The stiffness in the high-loading-rate test was 4.4 times of that in cyclic loading test under the quasistatic strain rate.

6.2 Recommended future research

6.2.1 Future improvement and application of the high-loading-rate tensile testing system

Several aspects of the tensile testing system can be improved so that it can have more potential applications. Such improvements are listed as follows:

- The aluminum welded joints of the inverter mechanism can be replaced with welded steel or cast steel joints to increase the strength and stiffness. Therefore, higher impact energy can be applied to the input end of the inverter mechanism safely, and higher loading rates and peak deformations can be achieved at the output end connecting to the specimen assembly.

- The neoprene pads working as a pulse shaper in this research can be replaced with other materials so that the duration of the loading can be further tailored. The pulse shaper can also be multiple layers of different materials, such as copper, steel, and neoprene or other rubber, stacked together to provide desired peak force and duration time. Higher loading rates can be obtained with stiffer pulse shapers while constant unloading rates may be achieved with specially designed multi-layer pulse shapers.

- Pulse shapers can also be placed inside the intended slack distance so that the impact between the ball joint connector and the input nut of the load cell can be adjusted to a more desirable manner. For example, specially designed washers or tubes placed around the threaded bar at the impact location can provide more versatility on the final impulse onto the specimens.

- Digital Image Correlation (DIC) techniques can be incorporated into the testing system. Currently, only displacements of the attached targets are re-constructed by motion tracking software from high-speed videos. Because of limited resolution of high-speed cameras, large targets with a size of 12.7 to 25.4 mm (0.5 to 1 inch) were required in the tests. As a result, the total number of targets that can be attached onto the specimen assembly was limited. Only deformations in the longitudinal direction of specimens were acquired in most of the tests. With the aid of DIC techniques,

the deformations of different parts of the specimen can be captured. More comprehensive understanding of the overall responses of the specimens, especially non-prismatic specimens, can be obtained.

- Temperature-controlled environment can be added to the specimen assembly. With a specially designed retracting mechanism, a temperature-control capsule can be placed surrounded the specimen and can retract just a very short time period before the actual impact. Thus, the specimen can be maintained at a desired temperature at the time of loading and unloading. At the same time, its deformation can still be capture by high-speed cameras. Therefore, force-deformation results under different temperatures can be acquired using this tensile testing system improved with temperature-controlling ability.

- This new tensile testing system can be utilized in various future research projects such as pull-out strength of reinforcing steel in concrete, strength of steel welded and bolted connections, and bond strength between FRP components.

6.2.2 Future studies on SMA materials

This research accessed the potential applications of SMA materials in the field of seismic mitigation and blast protection by quasistatic cyclic testing and high-loading-rate tensile testing. Some potential studies on SMA materials and potential SMA-based applications are listed as follows:

- The seismic bracing system can be further improved by adopting bracing members that are stiffer than the current steel cable assemblies. With specially designed connections, tension-only behavior and no restraint on rotation can still be achieved. Hybrid designs with buckling-restrained brace (BRB) may be another option for further improvement.

- The size effect between the SMA rings and the performance of the seismic bracing system was studied with finite element simulations in this research. This can be validated by actual tests of SMA rings with various sizes. SMA-based components

other than ring shapes can also be investigated to maximize the benefit from SMA materials and optimize the seismic performance of the design.

- The loading grips for SMA specimens can be further improved to get more comprehensive results. With modified loading grips which can pre-load the wedge clamps by itself using springs or other self-tensioning mechanism, intended slack distance can be introduced into the specimen assembly. Therefore, higher loading rates on SMA specimens can be achieved. The behavior of unloading parts of SMA specimens can be captured more effectively with modified pulse shapers and momentum capturing mechanism.

- The high-loading-rate tests can be conducted under different temperatures with the aid of upgraded testing system equipped with temperature-control capsule. The interaction between strain rate dependency and temperature dependency can be explored.

- To assess the potential applications of SMAs in blast protection, besides tests on SMA tensile specimens in this research, tests on proof-of-concept SMA-based devices are also needed. For example, steel frames with SMA-strengthened joints can be designed and tested to assess the performance of SMAs under blast loading and the potential applications of SMAs in blast protection.

REFERENCES

[1] Adharapurapu, R. R., Jiang, F., Vecchio, K. S., and Gray, G. T., "Response of NiTi shape memory alloy at high strain rate: A systematic investigation of temperature effects on tension–compression asymmetry," *Acta Materialia*, vol. 54, no. 17, pp. 4609–4620, 2006.

[2] Alam, M. S., Nehdi, M., and Youssef, M. A., "Seismic performance of concrete frame structures reinforced with superelastic shape memory alloys," *Smart Struct Syst*, vol. 5, no. 5, pp. 565–585, 2009.

[3] Alam, M. S., Youssef, M. A., and Nehdi, M. L., "Exploratory investigation on mechanical anchors for connecting SMA bars to steel or FRP bars," *Materials and structures*, vol. 43, no. 1, pp. 91–107, 2010.

[4] Andrawes, B. and DesRoches, R., "Comparison between shape memory alloy seismic restrainers and other bridge retrofit devices," *Journal of Bridge Engineering*, vol. 12, no. 6, pp. 700–709, 2007.

[5] Andrawes, B., Shin, M., and Wierschem, N., "Active confinement of reinforced concrete bridge columns using shape memory alloys," *Journal of Bridge Engineering*, vol. 15, no. 1, pp. 81–89, 2009.

[6] Asai, M. and Suzuki, Y., "Applications of shape memory alloys in japan," in *Materials science forum*, vol. 327, pp. 17–22, Trans Tech Publ, 2000.

[7] ASTM F2001-05(2010), "Standard test method for transformation temperature of Nickel-Titanium alloys by thermal analysis," *ASTM International*, 2010.

[8] Auricchio, F. and Taylor, R. L., "Shape-memory alloys: modelling and numerical simulations of the finite-strain superelastic behavior," *Computer methods in applied mechanics and engineering*, vol. 143, no. 1, pp. 175–194, 1997.

[9] Auricchio, F., Taylor, R. L., and Lubliner, J., "Shape-memory alloys: macromodelling and numerical simulations of the superelastic behavior," *Computer methods in applied mechanics and engineering*, vol. 146, no. 3, pp. 281–312, 1997.

[10] Baker, W. E. and Yew, C., "Strain-rate effects in the propagation of torsional plastic waves," *Journal of Applied Mechanics*, vol. 33, no. 4, pp. 917–923, 1966.

[11] Bhattacharya, K., Conti, S., Zanzotto, G., and Zimmer, J., "Crystal symmetry and the reversibility of martensitic transformations," *Nature*, vol. 428, no. 6978, pp. 55–59, 2004.

[12] Birman, V., "Review of mechanics of shape memory alloy structures," *Applied Mechanics Reviews*, vol. 50, no. 11, pp. 629–645, 1997.

[13] Boroschek, R. L., Farias, G., Moroni, O., and Sarrazin, M., "Effect of SMA braces in a steel frame building," *Journal of Earthquake Engineering*, vol. 11, no. 3, pp. 326–342, 2007.

[14] Bruno, S. and Valente, C., "Comparative response analysis of conventional and innovative seismic protection strategies," *Earthquake engineering & structural dynamics*, vol. 31, no. 5, pp. 1067–1092, 2002.

[15] Buehler, W. J., Gilfrich, J., and Wiley, R., "Effect of low-temperature phase changes on the mechanical properties of alloys near composition TiNi," *Journal of applied physics*, vol. 34, no. 5, pp. 1475–1477, 1963.

[16] Cadoni, E., Asprone, D., and Prota, A., "High strain-rate testing of concrete and steel for the assessment of the tenza bridge under blast loading," *New trends in fractures mechanics of concrete*, pp. 627–635, 2007.

[17] Chancellor, N. B., Eatherton, M. R., Roke, D. A., and Akbaş, T., "Self-centering seismic lateral force resisting systems: high performance structures for the city of tomorrow," *Buildings*, vol. 4, no. 3, pp. 520–548, 2014.

[18] Chang, B.-C., Shaw, J. A., and Iadicola, M. A., "Thermodynamics of shape memory alloy wire: modeling, experiments, and application," *Continuum Mechanics and Thermodynamics*, vol. 18, no. 1-2, pp. 83–118, 2006.

[19] Chen, W. W. and Song, B., *Split Hopkinson (Kolsky) bar: design, testing and applications*. Springer Science & Business Media, 2010.

[20] Chen, W. W., Wu, Q., Kang, J. H., and Winfree, N. A., "Compressive superelastic behavior of a NiTi shape memory alloy at strain rates of 0.001–750 s^{-1}," *International Journal of Solids and Structures*, vol. 38, no. 50, pp. 8989–8998, 2001.

[21] Chernenko, V., Cesari, E., Kokorin, V., and Vitenko, I., "The development of new ferromagnetic shape memory alloys in Ni-Mn-Ga system," *Scripta metallurgica et materialia*, vol. 33, no. 8, pp. 1239–1244, 1995.

[22] Choi, E., Chung, Y.-S., Choi, J.-H., Kim, H.-T., and Lee, H., "The confining effectiveness of NiTiNb and NiTi SMA wire jackets for concrete," *Smart Materials and Structures*, vol. 19, no. 3, p. 035024, 2010.

[23] Conti, M., De Beule, M., Mortier, P., Van Loo, D., Verdonck, P., Vermassen, F., Segers, P., Auricchio, F., and Verhegghe, B., "Nitinol embolic protection filters: design investigation by finite element analysis," *Journal of materials engineering and performance*, vol. 18, no. 5-6, pp. 787–792, 2009.

[24] Croci, G., "Strengthening the basilica of St Francis of Assisi after the september 1997 earthquake," *Structural engineering international*, vol. 11, no. 3, pp. 207–210, 2001.

[25] Czaderski, C., Hahnebach, B., and Motavalli, M., "RC beam with variable stiffness and strength," *Construction and Building Materials*, vol. 20, no. 9, pp. 824–833, 2006.

[26] Davidson, J. S., Porter, J. R., Dinan, R. J., Hammons, M. I., and Connell, J. D., "Explosive testing of polymer retrofit masonry walls," *Journal of Performance of Constructed Facilities*, vol. 18, no. 2, pp. 100–106, 2004.

[27] De Leon, D. M., Alexandersen, J., Fonseca, J. S., and Sigmund, O., "Stress-constrained topology optimization for compliant mechanism design," *Structural and Multidisciplinary Optimization*, vol. 52, no. 5, pp. 929–943, 2015.

[28] Deng, Z., Li, Q., and Sun, H., "Behavior of concrete beam with embedded shape memory alloy wires," *Engineering structures*, vol. 28, no. 12, pp. 1691–1697, 2006.

[29] DesRoches, R. and Delemont, M., "Seismic retrofit of simply supported bridges using shape memory alloys," *Engineering Structures*, vol. 24, no. 3, pp. 325–332, 2002.

[30] DesRoches, R. and Smith, B., "Shape memory alloys in seismic resistant design and retrofit: a critical review of their potential and limitations," *Journal of Earthquake Engineering*, vol. 8, no. 03, pp. 415–429, 2004.

[31] DesRoches, R., McCormick, J., and Delemont, M., "Cyclic properties of superelastic shape memory alloy wires and bars," *Journal of Structural Engineering*, vol. 130, no. 1, pp. 38–46, 2004.

[32] DesRoches, R., Taftali, B., and Ellingwood, B. R., "Seismic performance assessment of steel frames with shape memory alloy connections. part I—analysis and seismic demands," *Journal of Earthquake Engineering*, vol. 14, no. 4, pp. 471–486, 2010.

[33] Dolce, M. and Cardone, D., "Mechanical behaviour of shape memory alloys for seismic applications 2. austenite NiTi wires subjected to tension," *International Journal of Mechanical Sciences*, vol. 43, no. 11, pp. 2657–2677, 2001.

[34] Dolce, M. and Cardone, D., "Theoretical and experimental studies for the application of shape memory alloys in civil engineering," *Journal of engineering materials and technology*, vol. 128, no. 3, pp. 302–311, 2006.

[35] Dolce, M., Cardone, D., and Marnetto, R., "Implementation and testing of passive control devices based on shape memory alloys," *Earthquake engineering & structural dynamics*, vol. 29, no. 7, pp. 945–968, 2000.

[36] Duerig, T., Pelton, A., and Stöckel, D., "An overview of nitinol medical applications," *Materials Science and Engineering: A*, vol. 273, pp. 149–160, 1999.

[37] Dutta, R., Madangopal, K., Gadiyar, H., and Banerjee, S., "Biocompatibility of Ni-Ti shape memory alloy," *British Corrosion Journal*, vol. 28, no. 3, pp. 217–221, 1993.

[38] Entemeyer, D., Patoor, E., Eberhardt, A., and Berveiller, M., "Strain rate sensitivity in superelasticity," *International Journal of plasticity*, vol. 16, no. 10, pp. 1269–1288, 2000.

[39] Erochko, J., Christopoulos, C., Tremblay, R., and Choi, H., "Residual drift response of smrfs and brb frames in steel buildings designed according to asce 7-05," *Journal of Structural Engineering*, vol. 137, no. 5, pp. 589–599, 2010.

[40] Eshghinejad, A., "Finite element study of a shape memory alloy bone implant," 2012.

[41] Fang, C., Yam, M. C., Lam, A. C., and Zhang, Y., "Feasibility study of shape memory alloy ring spring systems for self-centring seismic resisting devices," *Smart Materials and Structures*, vol. 24, no. 7, p. 075024, 2015.

[42] Fang, C., Yam, M. C., Ma, H., and Chung, K., "Tests on superelastic Ni-Ti SMA bars under cyclic tension and direct-shear: towards practical recentring connections," *Materials and Structures*, vol. 48, no. 4, pp. 1013–1030, 2015.

[43] Fatt, M. H. and Bekar, I., "High-speed testing and material modeling of unfilled styrene butadiene vulcanizates at impact rates," *Journal of Materials Science*, vol. 39, no. 23, pp. 6885–6899, 2004.

[44] Field, J., Walley, S., Proud, W., Goldrein, H., and Siviour, C., "Review of experimental techniques for high rate deformation and shock studies," *International Journal of Impact Engineering*, vol. 30, no. 7, pp. 725–775, 2004.

[45] Filiatrault, A. and Tremblay, R., "Design of tension-only concentrically braced steel frames for seismic induced impact loading," *Engineering structures*, vol. 20, no. 12, pp. 1087–1096, 1998.

[46] Gao, N., Jeon, J., DesRoches, R., and Hodgson, D., "Numerical model of an innovative damping system using superelastic shape memory alloy rings," in *Geotechnical and Structural Engineering Congress 2016*, pp. 226–238.

[47] Gao, N., Jeon, J.-S., DesRoches, R., and Hodgson, D. E., "Cyclic testing of a shape memory alloy ring device for seismic building retrofit," in *Proceedings of the Fifteenth International Conference on Civil, Structural and Environmental Engineering Computing*, p. No. 121, Civil-Comp Press, 2015.

[48] Gao, N., Jeon, J.-S., Hodgson, D. E., and DesRoches, R., "An innovative seismic bracing system based on a superelastic shape memory alloy ring," *Smart Materials and Structures*, vol. 25, no. 5, p. 055030, 2016.

[49] Graesser, E. and Cozzarelli, F., "Shape-memory alloys as new materials for aseismic isolation," *Journal of Engineering Mechanics*, vol. 117, no. 11, pp. 2590–2608, 1991.

[50] Gram, M., Clark, A., Hegemier, G., and Seible, F., "Laboratory simulation of blast loading on building and bridge structures," *WIT Transactions on The Built Environment*, vol. 87, 2006.

[51] Harding, J., *The effect of high strain rate on material properties*, vol. 4. ch, 1987.

[52] Hartl, D. J. and Lagoudas, D. C., "Aerospace applications of shape memory alloys," *Proceedings of the Institution of Mechanical Engineers, Part G: Journal of Aerospace Engineering*, vol. 221, no. 4, pp. 535–552, 2007.

[53] Hegemier, G. and Prager, W., "On michell trusses," *International Journal of Mechanical Sciences*, vol. 11, no. 2, pp. 209–215, 1969.

[54] Hodgson, D. E., Ming, W., and Biermann, R. J., "Shape memory alloys," *ASM International, Metals Handbook, Tenth Edition.*, vol. 2, pp. 897–902, 1990.

[55] Huang, B., Zhang, H., Wang, H., and Song, G., "Passive base isolation with superelastic nitinol SMA helical springs," *Smart Materials and Structures*, vol. 23, no. 6, p. 065009, 2014.

[56] Huang, W., "On the selection of shape memory alloys for actuators," *Materials & design*, vol. 23, no. 1, pp. 11–19, 2002.

[57] Huang, X. and Liu, Y., "Effect of annealing on the transformation behavior and superelasticity of NiTi shape memory alloy," *Scripta Materialia*, vol. 45, no. 2, pp. 153–160, 2001.

[58] Huh, H., Lim, J., and Park, S., "High speed tensile test of steel sheets for the stress-strain curve at the intermediate strain rate," *International Journal of Automotive Technology*, vol. 10, no. 2, pp. 195–204, 2009.

[59] Hutzler, S., Delaney, G., Weaire, D., and MacLeod, F., "Rocking newton's cradle," *American Journal of Physics*, vol. 72, no. 12, pp. 1508–1516, 2004.

[60] Idorn, G. M., "Innovation in concrete research—review and perspective," *Cement and concrete research*, vol. 35, no. 1, pp. 3–10, 2005.

[61] Indirli, M., Castellano, M. G., Clemente, P., and Martelli, A., "Demo-application of shape memory alloy devices: the rehabilitation of the S. Giorgio Church bell tower," in *SPIE's 8th Annual International Symposium on Smart Structures and Materials*, pp. 262–272, International Society for Optics and Photonics, 2001.

[62] Jani, J. M., Leary, M., Subic, A., and Gibson, M. A., "A review of shape memory alloy research, applications and opportunities," *Materials & Design*, vol. 56, pp. 1078–1113, 2014.

[63] Janke, L., Czaderski, C., Motavalli, M., and Ruth, J., "Applications of shape memory alloys in civil engineering structures—overview, limits and new ideas," *Materials and Structures*, vol. 38, no. 5, pp. 578–592, 2005.

[64] Johnson, R., Padgett, J. E., Maragakis, M. E., DesRoches, R., and Saiidi, M. S., "Large scale testing of nitinol shape memory alloy devices for retrofitting of bridges," *Smart materials and structures*, vol. 17, no. 3, p. 035018, 2008.

[65] Kainuma, R., Imano, Y., Ito, W., Sutou, Y., Morito, H., Okamoto, S., Kitakami, O., Oikawa, K., Fujita, A., Kanomata, T., and others, "Magnetic-field-induced shape recovery by reverse phase transformation," *Nature*, vol. 439, no. 7079, pp. 957–960, 2006.

[66] Kawata, K., Hashimoto, S., Kurokawa, K., and Kanayama, N., "A new testing method for the characterisation of materials in high-velocity tension," *Mechanical properties at high rates of strain, 1979*, pp. 71–80, 1980.

[67] Kleiner, M., Tekkaya, A. E., Demir, O. K., Risch, D., and Psyk, V., "A drop-weight high-speed tensile testing instrument," *Production Engineering*, vol. 3, no. 2, pp. 175–180, 2009.

[68] Kleinstreuer, C., Li, Z., Basciano, C., Seelecke, S., and Farber, M., "Computational mechanics of Nitinol stent grafts," *Journal of biomechanics*, vol. 41, no. 11, pp. 2370–2378, 2008.

[69] Koch, C. C., "Structural nanocrystalline materials: an overview," *Journal of Materials Science*, vol. 42, no. 5, pp. 1403–1414, 2007.

[70] Krawinkler, H., "Loading histories for cyclic tests in support of performance assessment of structural components," in *The 3rd International Conference on Advances in Experimental Structural Engineering*, 2009.

[71] Kurata, M., Leon, R., and DesRoches, R., "Rapid seismic rehabilitation strategy: concept and testing of cable bracing with couples resisting damper," *Journal of structural engineering*, vol. 138, no. 3, pp. 354–362, 2011.

[72] Lagoudas, D. C., *Shape memory alloys: modeling and engineering applications*. Springer Science & Business Media, 2008.

[73] Lagoudas, D. C., Ravi-Chandar, K., Sarh, K., and Popov, P., "Dynamic loading of polycrystalline shape memory alloy rods," *Mechanics of Materials*, vol. 35, no. 7, pp. 689–716, 2003.

[74] Lee, S.-H., Bakhtiary, E., Scott, D. W., Stewart, L. K., and White, D. W., "Influence of geometric parameters on the restraint of guardrail posts by asphalt mow strips," *Sustainable and Resilient Infrastructure*, vol. 2, no. 1, pp. 22–36, 2017.

[75] Lexcellent, C. and Rejzner, J., "Modeling of the strain rate effect, creep and relaxation of a Ni-Ti shape memory alloy under tension (compression)-torsional proportional loading in the pseudoelastic range," *Smart materials and structures*, vol. 9, no. 5, p. 613, 2000.

[76] Li, M., Wang, R., and Han, M.-B., "A Kolsky bar: tension, tension-tension," *Experimental Mechanics*, vol. 33, no. 1, pp. 7–14, 1993.

[77] Liang, C. and Rogers, C. A., "One-dimensional thermomechanical constitutive relations for shape memory materials," *Journal of intelligent material systems and structures*, vol. 1, no. 2, pp. 207–234, 1990.

[78] Liu, K. and Tovar, A., "An efficient 3D topology optimization code written in Matlab," *Structural and Multidisciplinary Optimization*, vol. 50, no. 6, pp. 1175–1196, 2014.

[79] Liu, Y., Li, Y., and Ramesh, K., "Rate dependence of deformation mechanisms in a shape memory alloy," *Philosophical Magazine A*, vol. 82, no. 12, pp. 2461–2473, 2002.

[80] Liu, Y., Xie, Z., Van Humbeeck, J., and Delaey, L., "Asymmetry of stress–strain curves under tension and compression for NiTi shape memory alloys," *Acta Materialia*, vol. 46, no. 12, pp. 4325–4338, 1998.

[81] Lubliner, J. and Auricchio, F., "Generalized plasticity and shape memory alloys," *International Journal of Solids and Structures*, vol. 33, no. 7, pp. 991–1003, 1996.

[82] Machado, L. and Savi, M., "Medical applications of shape memory alloys," *Brazilian Journal of Medical and Biological Research*, vol. 36, no. 6, pp. 683–691, 2003.

[83] Mahin, S. A., "Lessons from damage to steel buildings during the northridge earthquake," *Engineering structures*, vol. 20, no. 4-6, pp. 261–270, 1998.

[84] Maji, A. K. and Negret, I., "Smart prestressing with shape-memory alloy," *Journal of engineering mechanics*, vol. 124, no. 10, pp. 1121–1128, 1998.

[85] McCarthy, E., Wright, T., Padgett, J. E., DesRoches, R., and Bradford, P., "Development of an experimentally validated analytical model for modular bridge expansion joint behavior," *Journal of Bridge Engineering*, vol. 19, no. 2, pp. 235–244, 2013.

[86] McCormick, J., Aburano, H., Ikenaga, M., and Nakashima, M., "Permissible residual deformation levels for building structures considering both safety and human elements," in *Proceedings of the 14th world conference on earthquake engineering*, pp. 12–17, 2008.

[87] Meng, H. and Li, Q., "Correlation between the accuracy of a SHPB test and the stress uniformity based on numerical experiments," *International Journal of Impact Engineering*, vol. 28, no. 5, pp. 537–555, 2003.

[88] Miller, R. A. and Wood, K. D., "Formulas for the stress analysis of circular rings in a monocoque fuselage," 1933.

[89] Mirzaeifar, R., DesRoches, R., and Yavari, A., "Is the stress distribution uniform in the cross section of SMA bars subjected to uniaxial loading? Is it related to rate dependency?," in *ASME 2011 Conference on Smart Materials, Adaptive Structures and Intelligent Systems*, pp. 281–288, American Society of Mechanical Engineers, 2011.

[90] Mirzaeifar, R., DesRoches, R., Yavari, A., and Gall, K., "On superelastic bending of shape memory alloy beams," *International Journal of Solids and Structures*, vol. 50, no. 10, pp. 1664–1680, 2013.

[91] Morgan, N., "Medical shape memory alloy applications—the market and its products," *Materials Science and Engineering: A*, vol. 378, no. 1, pp. 16–23, 2004.

[92] Moser, K., Bergamini, A., Christen, R., and Czaderski, C., "Feasibility of concrete prestressed by shape memory alloy short fibers," *Materials and structures*, vol. 38, no. 5, pp. 593–600, 2005.

[93] Mott, P., Twigg, J., Roland, D., Schrader, H., Pathak, J., and Roland, C., "High-speed tensile test instrument," *Review of scientific instruments*, vol. 78, no. 4, p. 045105, 2007.

[94] Moynihan, M. C. and Allwood, J. M., "Utilization of structural steel in buildings," in *Proceedings of the Royal Society of London A: Mathematical, Physical and Engineering Sciences*, vol. 470, p. 20140170, The Royal Society, 2014.

[95] Nakashima, M., Inoue, K., and Tada, M., "Classification of damage to steel buildings observed in the 1995 hyogoken-nanbu earthquake," *Engineering Structures*, vol. 20, no. 4-6, pp. 271–281, 1998.

[96] Nemat-Nasser, S., Choi, J.-Y., Guo, W.-G., and Isaacs, J. B., "Very high strain-rate response of a NiTi shape-memory alloy," *Mechanics of materials*, vol. 37, no. 2, pp. 287–298, 2005.

[97] Nemat-Nasser, S. and Guo, W.-G., "Superelastic and cyclic response of NiTi SMA at various strain rates and temperatures," *Mechanics of materials*, vol. 38, no. 5, pp. 463–474, 2006.

[98] Nemat-Nasser, S., Isaacs, J. B., and Starrett, J. E., "Hopkinson techniques for dynamic recovery experiments," in *Proceedings of the Royal Society of London A: Mathematical, Physical and Engineering Sciences*, vol. 435, pp. 371–391, The Royal Society, 1991.

[99] Nespoli, A., Besseghini, S., Pittaccio, S., Villa, E., and Viscuso, S., "The high potential of shape memory alloys in developing miniature mechanical devices: A review on shape memory alloy mini-actuators," *Sensors and Actuators A: Physical*, vol. 158, no. 1, pp. 149–160, 2010.

[100] Ngo, T., Mendis, P., Gupta, A., and Ramsay, J., "Blast loading and blast effects on structures–an overview," *Electronic Journal of Structural Engineering*, vol. 7, no. S1, pp. 76–91, 2007.

[101] Orton, S. L., Chiarito, V. P., Rabalais, C., Wombacher, M., and Rowell, S. P., "Strain rate effects in cfrp used for blast mitigation," *Polymers*, vol. 6, no. 4, pp. 1026–1039, 2014.

[102] Owens, A. T. and Tippur, H., "A tensile split hopkinson bar for testing particulate polymer composites under elevated rates of loading," *Experimental Mechanics*, vol. 49, no. 6, pp. 799–811, 2008.

[103] Ozbulut, O. E., Hurlebaus, S., and DesRoches, R., "Seismic response control using shape memory alloys: a review," *Journal of Intelligent Material Systems and Structures*, p. 1045389X11411220, 2011.

[104] Paiva, A. and Savi, M. A., "An overview of constitutive models for shape memory alloys," *Mathematical Problems in Engineering*, vol. 2006, 2006.

[105] Paiva, A., Savi, M. A., Braga, A. M. B., and Pacheco, P. M. C. L., "A constitutive model for shape memory alloys considering tensile–compressive asymmetry and plasticity," *International Journal of Solids and Structures*, vol. 42, no. 11, pp. 3439–3457, 2005.

[106] Paret, T. F., Freeman, S. A., Searer, G. R., Hachem, M., and Gilmartin, U. M., "Using traditional and innovative approaches in the seismic evaluation and strengthening of a historic unreinforced masonry synagogue," *Engineering Structures*, vol. 30, no. 8, pp. 2114–2126, 2008.

[107] Parlinska, M., Clech, H., Balta, J., Michaud, V., Bidaux, J.-E., Manson, J.-A., and Gotthardt, R., "Adaptive composites with embedded shape memory alloys," *Le Journal de Physique IV*, vol. 11, no. PR4, pp. Pr4–197, 2001.

[108] Ramesh, K. T., "High rates and impact experiments," in *Springer handbook of experimental solid mechanics*, pp. 929–960, Springer, 2008.

[109] Rund, M., Procházka, R., Konopík, P., Džugan, J., and Folgar, H., "Investigation of sample-size influence on tensile test results at different strain rates," *Procedia Engineering*, vol. 114, pp. 410–415, 2015.

[110] SAC Joint Venture, "Protocol for fabrication, inspection, testing, and documentation of beam-column connection tests and other experimental specimens," *Rep. No. SAC/BD-97/02*, 1997.

[111] Santillo, M., *Fracture and Crack Propagation Study of a Superficial Femoral Artery Nitinol Stent*. PhD thesis, MS Thesis, Pavia University, 2008.

[112] Seelecke, S. and Muller, I., "Shape memory alloy actuators in smart structures: Modeling and simulation," *Applied Mechanics Reviews*, vol. 57, no. 1, pp. 23–46, 2004.

[113] Sharabash, A. M. and Andrawes, B. O., "Application of shape memory alloy dampers in the seismic control of cable-stayed bridges," *Engineering Structures*, vol. 31, no. 2, pp. 607–616, 2009.

[114] Sharpe, W. N., *Springer handbook of experimental solid mechanics*. Springer Science & Business Media, 2008.

[115] Shaw, J. A., Churchill, C. B., and Iadicola, M., "Tips and tricks for characterizing shape memory alloy wire: part 1—differential scanning calorimetry and basic phenomena," *Experimental Techniques*, vol. 32, no. 5, pp. 55–62, 2008.

[116] Shaw, J. A. and Kyriakides, S., "Thermomechanical aspects of NiTi," *Journal of the Mechanics and Physics of Solids*, vol. 43, no. 8, pp. 1243–1281, 1995.

[117] Shin, M. and Andrawes, B., "Emergency repair of severely damaged reinforced concrete columns using active confinement with shape memory alloys," *Smart Materials and Structures*, vol. 20, no. 6, p. 065018, 2011.

[118] Sierakowski, R., "Strain rate behavior of metals and composites," in *Convegno IGF XIII Cassino 1997*, 1997.

[119] Song, B. and Chen, W., "Loading and unloading split hopkinson pressure bar pulse-shaping techniques for dynamic hysteretic loops," *Experimental Mechanics*, vol. 44, no. 6, pp. 622–627, 2004.

[120] Song, G., Ma, N., and Li, H.-N., "Applications of shape memory alloys in civil structures," *Engineering Structures*, vol. 28, no. 9, pp. 1266–1274, 2006.

[121] Soul, H. and Yawny, A., "Self-centering and damping capabilities of a tension-compression device equipped with superelastic NiTi wires," *Smart Materials and Structures*, vol. 24, no. 7, p. 075005, 2015.

[122] Speicher, M., DesRoches, R., and Leon, R. T., "Cyclic testing of a shape memory alloy-based articulated quadrilateral bracing system," in *Proceedings of International Symposium on Steel Structures*, pp. 698–705, KSSC.

[123] Speicher, M., Hodgson, D. E., DesRoches, R., and Leon, R. T., "Shape memory alloy tension/compression device for seismic retrofit of buildings," *Journal of materials engineering and performance*, vol. 18, no. 5-6, pp. 746–753, 2009.

[124] Speicher, M. S., DesRoches, R., and Leon, R. T., "Experimental results of a NiTi shape memory alloy (SMA)-based recentering beam-column connection," *Engineering structures*, vol. 33, no. 9, pp. 2448–2457, 2011.

[125] Stalmans, R., Van Humbeeck, J., and Delaey, L., "The two way memory effect in copper-based shape memory alloys—thermodynamics and mechanisms," *Acta metallurgica et materialia*, vol. 40, no. 11, pp. 2921–2931, 1992.

[126] Stewart, L. K., Gao, N., Pezzola, G., Sanborn, M., Sanborn, K., Nail, A., and Loreto, G., "Georgia institute of technology laboratory for blast, shock and impact," in *Proceedings of the 7th International Conference on Advances in Experimental Structural Engineering*, p. No. 685, AESE, 2017.

[127] Stewart, L., Freidenberg, A., Rodriguez-Nikl, T., Oesterle, M., Wolfson, J., Durant, B., Arnett, K., Asaro, R., and Hegemier, G., "Methodology and validation for blast and shock testing of structures using high-speed hydraulic actuators," *Engineering Structures*, vol. 70, pp. 168–180, 2014.

[128] Stoeckel, D., "Shape memory actuators for automotive applications," *Engineering Aspects of Shape Memory Alloys*, p. 283, 1990.

[129] Sun, X. and Khaleel, M. A., "Dynamic strength evaluations for self-piercing rivets and resistance spot welds joining similar and dissimilar metals," *International journal of impact engineering*, vol. 34, no. 10, pp. 1668–1682, 2007.

[130] Talischi, C., Paulino, G. H., Pereira, A., and Menezes, I. F., "Polymesher: a general-purpose mesh generator for polygonal elements written in matlab," *Structural and Multidisciplinary Optimization*, vol. 45, no. 3, pp. 309–328, 2012.

[131] Talischi, C., Paulino, G. H., Pereira, A., and Menezes, I. F., "Polytop: a matlab implementation of a general topology optimization framework using unstructured polygonal finite element meshes," *Structural and Multidisciplinary Optimization*, vol. 45, no. 3, pp. 329–357, 2012.

[132] Tanaka, Y., Himuro, Y., Kainuma, R., Sutou, Y., Omori, T., and Ishida, K., "Ferrous polycrystalline shape-memory alloy showing huge superelasticity," *Science*, vol. 327, no. 5972, pp. 1488–1490, 2010.

[133] Van Humbeeck, J., "Non-medical applications of shape memory alloys," *Materials Science and Engineering: A*, vol. 273, pp. 134–148, 1999.

[134] Van Langenhove, L. and Hertleer, C., "Smart clothing: a new life," *International journal of clothing science and technology*, vol. 16, no. 1/2, pp. 63–72, 2004.

[135] Wang, X., "Shape memory alloy volume fraction of pre-stretched shape memory alloy wire-reinforced composites for structural damage repair," *Smart materials and structures*, vol. 11, no. 4, p. 590, 2002.

[136] Wilde, K., Gardoni, P., and Fujino, Y., "Base isolation system with shape memory alloy device for elevated highway bridges," *Engineering structures*, vol. 22, no. 3, pp. 222–229, 2000.

[137] Wilson, J. C. and Wesolowsky, M. J., "Shape memory alloys for seismic response modification: a state-of-the-art review," *Earthquake Spectra*, vol. 21, no. 2, pp. 569–601, 2005.

[138] Wuttig, M., Li, J., and Craciunescu, C., "A new ferromagnetic shape memory alloy system," *Scripta materialia*, vol. 44, no. 10, pp. 2393–2397, 2001.

[139] Yang, C.-S. W., DesRoches, R., and Leon, R. T., "Design and analysis of braced frames with shape memory alloy and energy-absorbing hybrid devices," *Engineering Structures*, vol. 32, no. 2, pp. 498–507, 2010.

[140] Ye, J., Mishra, R. K., Pelton, A. R., and Minor, A. M., "Direct observation of the NiTi martensitic phase transformation in nanoscale volumes," *Acta Materialia*, vol. 58, no. 2, pp. 490–498, 2010.

[141] Youssef, M., Alam, M., and Nehdi, M., "Experimental investigation on the seismic behavior of beam-column joints reinforced with superelastic shape memory alloys," *Journal of Earthquake Engineering*, vol. 12, no. 7, pp. 1205–1222, 2008.

[142] Zegard, T. and Paulino, G. H., "Bridging topology optimization and additive manufacturing," *Structural and Multidisciplinary Optimization*, vol. 53, no. 1, pp. 175–192, 2016.

[143] Zhang, S., "Building from the bottom up," *Materials Today*, vol. 6, no. 5, pp. 20–27, 2003.

VITA

Nan Gao was born in Jinan, China in 1987. He earned a Bachelor's degree in Civil Engineering from Tongji University in 2008. After that, he worked as a structural engineer in Shanghai, China, where he participated in various design projects, most of which were high-rise concrete buildings. He also worked in several seismic retrofit projects after the 2008 Sichuan Earthquake. In 2012, he became a registered professional structural engineer in China. In 2013, he started his graduate studies at the Georgia Institute of Technology. He works as both research assistant and teaching assistant, and he teaches undergraduate concrete design courses as instructor of record at Georgia Tech. Nan is expected to graduate with a PhD degree from Georgia Tech in 2017, and he is planning to continue his teaching and research in academia. Nan is also an active popular science author who maintains blogs and social medias written in Chinese focusing on the introduction and popularization of structural engineering with over 150,000 subscribers, most of whom are engineering students. In his free time, Nan enjoys running and woodworking.